PRECONCENTRATION WITH METAL-ORGANIC FRAMEWORKS AS ADSORBENTS FOR AIRBORNE EXPLOSIVES AND HAZARDOUS MATERIALS

A STUDY USING INVERSE GAS CHROMATOGRAPHY

Dissertation zur Erlangung des naturwissenschaftlichen Doktorgrades

doctor rerum naturalium (Dr. rer. nat.)

der Fakultät für Chemie und Pharmazie

der Julius-Maximilians-Universität Würzburg

vorgelegt von

Diplom-Chemiker Max Rieger

aus Bad Mergentheim

Würzburg, 2018

“I will not deny, but possibly it might be reduced to a narrower Compass than it is; and that some Parts of it might be contracted: The way it has been writ in, by Catches, and many long Intervals of Interruption, being apt to cause some Repetitions. But to confess the Truth, I am now too lazy, or too busy to make it shorter. “

- John Locke “An Essay Concerning Human Understanding”, 1690

As well as non-literal: Mark Twain, George Bernard Shaw, Voltaire, Blaise Pascal, Johann Wolfgang von Goethe, Winston Churchill, Cato, Cicero, Bill Clinton, and Benjamin Franklin.

Eingereicht bei der Fakultät für Chemie und Pharmazie am

05. November 2018

Gutachter der schriftlichen Arbeit:

1. Gutachter:	Prof. Dr. Klaus Müller-Buschbaum
2. Gutachter:	Prof. Dr. Robert Luxenhofer

Prüfer des öffentlichen Promotionskolloquiums:

1. Prüfer:	Prof. Dr. Klaus Müller-Buschbaum
2. Prüfer:	Prof. Dr. Robert Luxenhofer
3. Prüfer:	Prof. Dr. Volker Engel

Datum des öffentlichen Kolloquiums:

15. Februar 2019

Doktorurkunde ausgehändigt am:

_____

Table of contents

Abstract

Sensitivity and selectivity remain the central technical requirement for analytical devices, detectors and sensors. Especially in the gas phase, concentrations of threat substances can be very low (e.g. explosives) or have severe effects on health even at low concentrations (e.g. benzene) while it contains many potential interferents. Preconcentration, facilitated by active or passive sampling of air by an adsorbent, followed by thermal desorption, results in these substances being released in a smaller volume, effectively increasing their concentration.

Traditionally, a wide range of adsorbents, such as active carbons or porous polymers, are used for preconcentration. However, many adsorbents either show chemical reactions due to active surfaces, serious water retention or high background emission due to thermal instability. Metal-organic frameworks (MOFs) are a hybrid substance class, composed inorganic and organic building blocks, being a special case of coordination polymers containing pores. They can be tailored for specific applications such as gas storage, separation, catalysis, sensors or drug delivery.

This thesis is focused on investigating MOFs for their use in thermal preconcentration for airborne detection systems. A pre-screening method for MOF-adsorbate interactions was developed and applied, namely inverse gas chromatography (iGC). Using this pulse chromatographic method, the interaction of MOFs and molecules from the class of explosives and volatile organic compounds was studied at different temperatures and compared to thermal desorption results.

In the first part, it is shown that archetype MOFs (**HKUST-1**, **MIL-53** and **Fe-BTC**) outperformed the state-of-the-art polymeric adsorbent **Tenax® TA** in nitromethane preconcentration for a 1000 (later 1) ppm nitromethane source. For **HKUST-1**, a factor of more than 2000 per g of adsorbent was achieved, about 100 times higher than for **Tenax**.

Thereby, a nitromethane concentration of 1 ppb could be increased to 2 ppm. High enrichment is addressed to the specific interaction of the nitro group as by iGC, which was determined by comparing nitromethane's free enthalpy of adsorption with the respective saturated alkane. Also, **HKUST-1** shows a similar mode of sorption (enthalpy-entropy compensation) for nitro and saturated alkanes.

In the second part, benzene of 1 ppm of concentration was enriched with a similar setup, using 2nd generation MOFs, primarily **UiO-66** and **UiO-67**, under dry and humid (50 %rH) conditions using constant sampling times. Not any MOF within the study did surpass the polymeric **Tenax** in benzene preconcentration. This is most certainly due to low sampling times – while **Tenax** may be highly saturated after 600 s, MOFs are not. For regular **UiO-66**, four differently synthesized samples showed a strongly varying behavior for dry and humid enrichment which cannot be completely explained. iGC investigations with regular alkanes and BTEX compounds revealed that confinement factors and dispersive surface energy were different for all **UiO-66** samples. Using physicochemical parameters from iGC, no unified hypothesis explaining all variances could be developed.

Altogether, it was shown that MOFs can replace or add to state-of-the-art adsorbents for the enrichment of specific analytes with preconcentration being a universal sensitivity-boosting concept for detectors and sensors. Especially with iGC as a powerful screening tool, most suitable MOFs for the respective target analyte can be evaluated. iGC can be used for determining "single point" retention volumes, which translate into partition coefficients for a specific MOF × analyte × temperature combination.

Deutsche Kurzdarstellung

Empfindlichkeit und Selektivität bleiben die zentralen technischen Anforderungen an analytische Geräte, Detektoren und Sensoren. Speziell in der Gasphase können die Konzentrationen von Gefahrstoffen sehr niedrig sein (z. B. Explosivstoffe) oder bereits bei niedrigen Konzentrationen schädigende Auswirkungen auf die Gesundheit aufweisen (z. B. Benzol) während sie viele potenzielle Interferenzien enthält. Präkonzentration, die durch aktives oder passives Sampling von Luft durch ein Adsorbens, gefolgt von einer Thermodesorption realisiert wird, setzt diese Substanzen effektiv in einem kleineren Volumen frei, was zu einer Erhöhung der Konzentration führt.

Üblicherweise wird hierfür eine breite Auswahl an Adsorbentien wie Aktivkohlen oder poröse Polymere verwendet. Jedoch weisen viele Adsorbentien entweder chemische Reaktionen wegen aktiver Oberflächen, starke Wasserretention oder hohe Hintergrundemission wegen thermischer Instabilität auf. Metal-organic frameworks (MOFs) sind eine hybride Substanzklasse, ein Spezialfall der porösen Koordinationspolymere, die aus anorganischen und organischen Baugruppen aufgebaut sind. Sie können für spezifische Anwendungen wie Gasspeicherung, Trennung, Katalyse, Sensorik oder Wirkstofftransport maßgeschneidert werden.

Diese Arbeit befasst sich hauptsächlich mit der Untersuchung von MOFs bei der thermischen Anreicherung für luftgetragene Detektionssysteme. Eine Methode zur schnellen Untersuchung von MOF-Analyt Interaktionen wurde entwickelt und angewendet, die inverse Gaschromatographie (iGC). Mit dieser pulschromatographischen Methode wurde die Interaktion von MOFs und Molekülen aus der Klasse der Explosivstoffe sowie Klasse der flüchtigen organischen Verbindungen (VOCs) in der Gasphase bei verschiedenen Temperaturen untersucht und mit Thermodesorptionsmessungen verglichen.

Im ersten Teil der Arbeit würde gezeigt das Modell-MOFs (**HKUST-1**, **MIL-53** und **Fe-BTC**) den polymeren Standard **Tenax® TA** beim Anreichern von Nitromethan an einer 1000 (später 1) ppm Nitromethan Quelle übertrafen. Im Fall von **HKUST-1** konnte ein Faktor von 2000 pro Gramm erreicht werden, etwa 100-fach höher als für **Tenax**. Auf diese Weise könnte eine Nitromethan Konzentration von 1 ppb auf 2 ppm erhöht werden. Diese hohen Anreicherungsfaktoren entstammen vermutlich der hohen spezifischen Wechselwirkung der Nitrogruppe mit den MOFs. Diese wurden durch iGC beim Vergleich von Nitromethans freier Adsorptionsenthalpie mit dem entsprechenden gesättigten Alkan ermittelt. **HKUST-1** weist auch einen ähnlichen Adsorptionsmodus (Enthalpie-Entropie Kompensation) für Nitro- und gesättigte Alkane auf.

Im zweiten Teil der Arbeit wurde die Anreicherung von 1 ppm Benzol, mit einem ähnlichen Aufbau und anderen MOFs, hauptsächlich **UiO-66** und **UiO-67**, unter trockenen und feuchten (50 %rF) Bedingungen bei konstanten Samplingzeiten, untersucht. Hierbei konnte kein MOF das polymere **Tenax** beim Anreichern von Benzol übertreffen. Dies liegt vermutlich an den niedrigen Samplingzeiten – während **Tenax** nach 600 s bereits stark gesättigt ist, gilt dies nicht für MOFs. Im Fall von **UiO-66** zeigten vier Proben unterschiedlicher Herkunft ein stark unterschiedliches Verhalten bei trockener und feuchter Anreicherung welches nicht vollständig erklärt werden kann. iGC Untersuchungen mit gesättigten Alkanen und BTEX-Verbindungen konnten aufzeigen, dass räumliche Beschränktheitsfaktoren und dispersive Oberflächenenergien für alle vier Proben unterschiedlich waren. Mit physikochemischen Parametern aus iGC-Messungen konnte jedoch keine einheitliche Hypothese zum Unterscheiden der Proben entwickelt werden.

Insgesamt konnte gezeigt werden, dass MOFs bestehende Adsorbens-Standards zum Anreichern von bestimmten Analyten ersetzen oder erweitern können, wobei

Präkonzentration ein Konzept ist, welches universell die Empfindlichkeit eines Detektors oder Sensors steigern kann. Insbesondere mit iGC als mächtiges Werkzeug zur Vorselektion können passende MOFs für die entsprechenden Zielanalyten evaluiert werden. Ebenso kann iGC auch zur Bestimmung von Einzelpunkt Retentionsvolumen, welche Verteilungskoeffizienten für eine bestimmte MOF × Analyt × Temperatur Kombination entsprechen, genutzt werden.

1 Introduction

Trace detection plays a significant role in many fields, starting from monitoring very toxic, instantly harming chemicals, to impurities in semi-conductor industry and drug detection in forensics. [1]–[3] Emerging, although striking in relevance, explosive detection in the gas phase has also become a subdivision of trace detection caused by the rising significance of so called improvised explosive devices (IEDs) and home-made explosives (HMEs).[4]

Within 2016, more than half of all terrorism-related incidents were related to explosives. [4] With an increasing number of incidents every year, international and organized terrorism is on the rise. Along with an increasing globalized world, e.g. international airport traffic, this problem is further emphasized. Dubai, being presumed as the airport with the most international passengers (more than 77 million in 2015) per year, showed an annual increase in 10.5 % in 2015. [5] Especially with the increased availability of explosives via the route of home-made explosives, inhibition thresholds for incidents involving explosives are expected to be lower nowadays. [6] As compared to traditional bulk detection of explosives (using terahertz or X-Ray screening), gas phase detection can be done unnoticed and passive, ideal for public or pre-checkpoint monitoring.

However, for a reliable and sensitive detection in the gas phase, advances in the underlying detection itself have to be made. The performance of analytical and sensing methods is mainly characterized by two technical factors, sensitivity and selectivity. Sensitivity is often described in terms of the methods limit of detection (LOD [7], [8]), being the lowest concentration where a signal can be repeatedly discriminated from baseline noise and a quantification is possible. This sensitivity is in most cases strongly analyte (the molecule to be detected) dependent, e.g. a flame ionization detector (FID [9],

[10]) is not capable of detecting nitrogen as nitrogen will show no interaction with the detector.

Selectivity [7], [11], [12] is another arbitrarily complex issue to be addressed. If a detector response does not allow for a selective readout, no discrimination from other existing substances with a detector sensitivity (so called interferents [13], [14]) is possible, which renders an identification of relevant target analytes (e.g. hazardous substances) impossible. There are several methods [7], [8] that can provide for analyte identification, including spectrometry (array of e.g. infrared wavenumber absorption intensities) or chromatography (separation of the sample itself based on chromatographic retention mechanisms). Another concept is a highly selective (low cross-interfering [13], [15]) detection system utilizing host-guest binding induced change in material properties that are monitored by a transducer (like enzyme-substrate binding based biosensors). However, absolute selectivity cannot be achieved, as any host molecule holds an unknown affinity for other potential guest molecules, just as a mass-spectrometers channel will be triggered by the corresponding fragment, regardless of its specific origin.

To illustrate this interference issue, Figure 1 depicts the constituents of air in different concentration regions. [16], [17]. At volume percent level, air is composed of two main compounds, nitrogen (ca. 78 vol%) and oxygen (ca. 21 vol). Below 1 % vol and above 1 ppm_V (parts per million, 10^{-6}) there are 6 compounds, below 1 ppm_V and above 1 ppt_V (parts per trillion, 10^{-12}), there are even 15 different compounds, mainly chlorofluorocarbons below 1 ppb_V (parts per billion, 10^{-9}) and hydrogen, nitrous oxide, carbon monoxide and Xenon between 1 ppb_V and 1 ppm_V.

Generally, sensitivity and selectivity are both gaining significance as the limit of detection is shifted towards lower concentrated regions. The number of potentially detector-

interfering substances is strongly increasing, while the concentration of the analyte to be detected is decreasing.

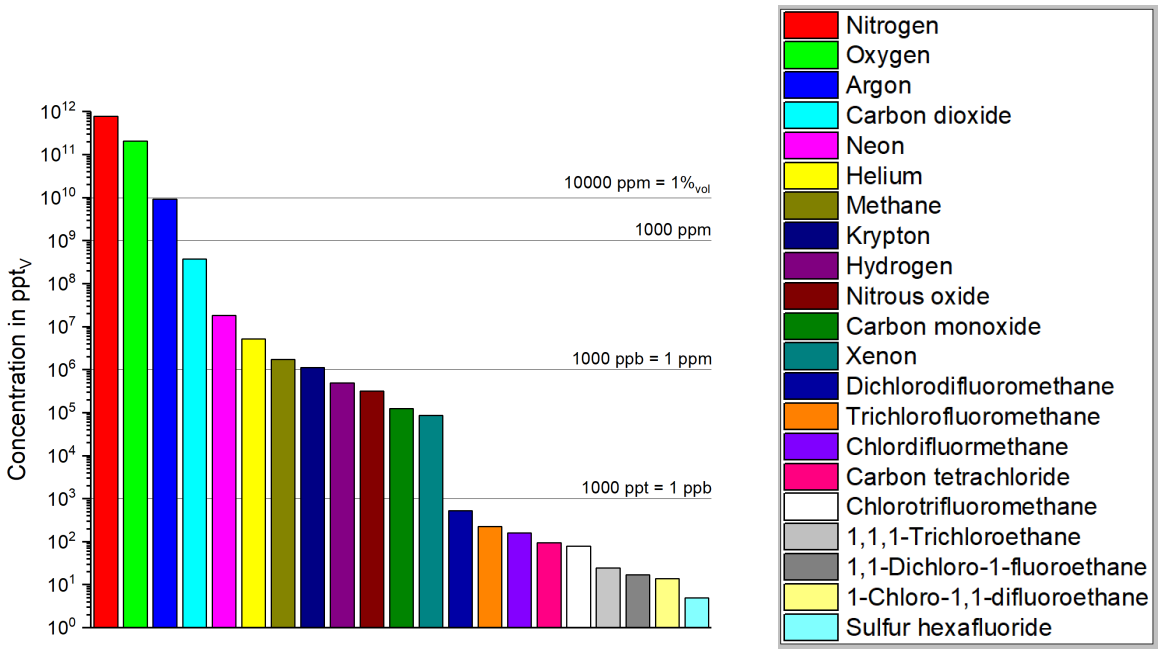

Figure 1. Barcharts of components contained in dry atmospheric air on a volumetric basis. Values taken from [16], [17] and converted to parts per trillion (10^{-12}) of volume (ppt$_V$).

The shown atmospheric air values (Figure 1) are globally averaged ones – respective concentrations may vary from location to location, especially beneath 1 ppm of concentration. Especially indoors, at industrial sites and at public places – even below 1000 ppm – completely different backgrounds (composition of interferents with respect to the analyte to be detected) are to be expected. How low a demanded detection limit can be, becomes apparent when explosives or explosive substances are considered.

Most explosives possess very low vapor pressures, which automatically hampers their airborne trace detection (Figure 2) [7], [18] with e.g. trinitrotoluene (TNT) having a saturation vapor pressure of 4 to 20 parts per billion (ppb) at ambient conditions.[19] Other regular detection strategies are bulk detection [20] using X-Ray scanners as well as swabbing techniques, where trace amounts of solid materials are directly detected using IR, Raman or Ion mobility spectrometry (IMS) methods. [7], [21] Figure 2 gives an overview of vapor pressures of typical explosives and precursors. It can be seen, that

organic substances like HMX (octogen) or HNS (hexanitrostilbene) possess extremely low vapor pressures of 10^{-9} to 10^{-6} parts per trillion (ppt), being even lower than that of inorganic salts such as ammonium nitrate (AN) or ammonium perchlorate (AP). [22]

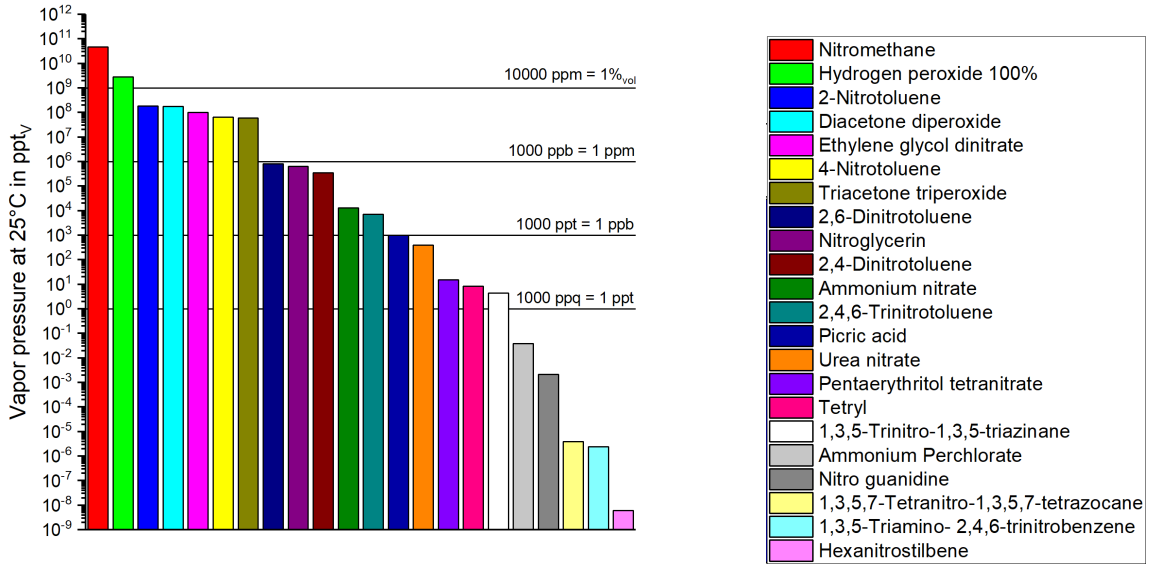

Figure 2. Vapor pressure examples for various explosives. Data taken from Östmark et al. [22] Units converted to parts per trillion (10^{-12}) of volume (ppt_V).

In relevant environments (e.g. checkpoint situations at an airport), most state-of-the-art detection systems show a significantly higher false-alarm rate (FAR [23], [24]) as compared to lab environment due to occurrence of multiple interferents. These systems are in most cases highly trained, evaluated and optimized against a specific set of relevant explosives using multivariate data analysis or pattern recognition algorithms.

Many systems are featuring mass spectrometry or ion mobility spectrometry [25]–[27] in order to provide a substance related separation as an additional dimension for their algorithms. [28] These systems often suffer long regeneration times after an alarm as their interior is contaminated by substances exhibiting low vapor pressures. [21] When low concentrations values are to be expected, adsorptive enrichment provides for a controlled enrichment when the material parameters (e.g. temperature-dependent partition coefficients) are known. Furthermore, by materials design, interferents can be

excluded from the enrichment procedure by means of chemical (functional groups) or spatial (kinetic diameters) features.

Another substance class, where trace detection plays a major role are volatile organic compounds (VOCs [29], [30]). The continuous monitoring of indoor occurring, long-term hazardous VOCs, e.g. benzene, with reasonably priced and accurate sensors is also about the become a field of trace detection. In conjunction with the advances in distributed sensor networks and algorithms, it will be possible to dramatically reduce the energy consumption for indoor ventilation and dedicate it to reasonable places and time periods. Also, the identification of VOC emitting materials becomes viable this way.

Most VOCs – especially the ones of relevance for this work – possess by far larger vapor pressures as compared to explosives. For example, benzene exhibits a vapor pressure of 100 hPa at room temperature, i.e. 10 vol. Still, benzene is a carcinogenic substance that poses a threat to health at much lower concentrations. [31] As of 2008, the lower assessment threshold for benzene is set to 2 $\mu g\ m^{-3}$ by the European Parliament and the council of the European Union. [32] Even at 1 $\mu g\ m^{-3}$ of benzene the geometric mean of excess lifetime risk of leukemia is at $6 \cdot 10^{-6}$ and increases to 10^{-4} at 17 $\mu g\ m^{-3}$. [30], [33]–[35] Other prominent VOCs that are considered as threat to human health are formaldehyde, naphthalene, polycyclic aromatic hydrocarbons (PHAs) as well as carbon monoxide and nitrogen dioxide. In general, VOCs are the main cause of the sick building syndrome and long-term exposure can cause damage to the respiratory system and skin. Indoor sources for benzene may reach from domestic cooking stoves (developing countries) but also furniture and paint emission as well as cleaning agents and, most significantly, tobacco smoke. Outdoor emissions of benzene are mainly associated with transport (65%) and industry (32%) [29] and provide the baseline concentration for indoor benzene concentrations. [35] Especially indoors, emitted by a particular source,

VOC concentrations may accumulate and reach even higher levels of concentrations. [36] At a mean benzene indoor air concentration of 10 µg m^{-3}, typically, further VOCs are simultaneously present, such as toluene, n-decane, limonene, o-xylene p-dichlorobenzene as well as m- and p-xylene (80, 20, 30, 10, 10 and 20 µg m^{-3}, respectively). Obviously, regular "outdoor air" interferents like e.g. carbon monoxide carbon dioxide and hydrocarbons are also on the list of possible interferents. [29], [37] Concentrations of respective VOCs may be grouped to the so called TVOC (total VOC) indicator, with CO_2 at several hundred ppm being a major component of this indicator. This indicator is supplied by many available sensor systems – however it lacks the capability to discriminate between low threat (e.g. hexane) and high threat (e.g. benzene) VOCs. If only a TVOC descriptor (ppm order of magnitude) is used to assess indoor air quality or to decide whether a buildings ventilation system should run or not, the ventilation will run if no hazardous materials (at ppb level) are present or it will not run even if hazardous substances (at ppb level) are present. To determine hazardous substances early enough and allow according countermeasures, it is necessary to specifically determine hazardous VOCs. As they already pose a threat to health at ppb-level concentrations, their enrichment prior to detection is also a key concept to be explored and discussed in this work.

Altogether, due to high heterogeneity and (scenario dependent) increasing multiple occurrence of several analytes at the ppm-ppb to ppt levels, air is one of the most complicated and time-consuming matrices to analyze or monitor.

This work deals with using thermal concentration enrichment (preconcentration) to enhance both, the sensitivity and selectivity of common analytical methods and systems for airborne trace detection. With the extension of detection systems by reliable preconcentration, advances in new sensitive detection applications will be supported.

Examples for such applications are health screening by breath analysis and mold detection. In both cases, a characteristic VOC background is present and allows an early detection of diseases or threats. [38], [39] The general concept of preconcentration (adsorptive enrichment) is explained in the following section (1.1).

1.1 Adsorptive enrichment and preconcentration

For using adsorptive enrichment, state-of-the-art sampling techniques (tube sampling, SPME etc.) result from varying requirements in the underlying scenarios. However, the basic concept is similar in all cases. It is illustrated in Figure 3. Effectively the substance amount is concentrated on the adsorbent by adsorption, followed by a thermally induced desorption in a small timespan, leading to a temporal, spatially focused high concentration of the analyte.

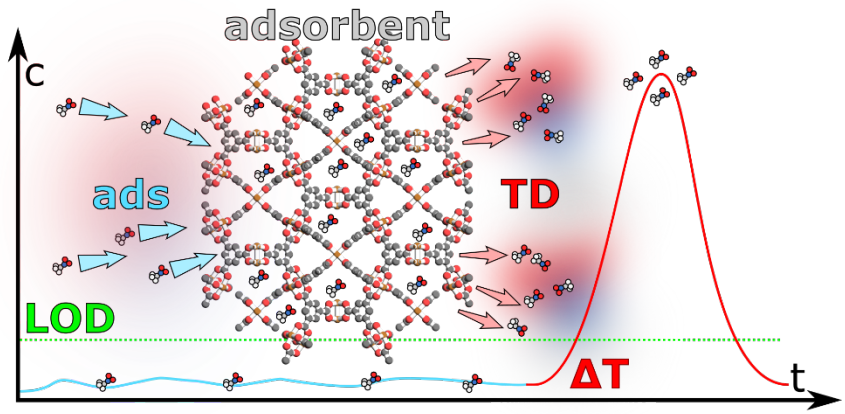

Figure 3. Schematic depiction of sampling a low concentration (blue line) of guest molecules (left) over a period of time on an adsorbent (middle) via adsorption (ads). After sampling, the adsorbent temperature is increased (ΔT) and a rapid desorption (thermal desorption, TD) of guest molecules (right) into a small gas volume leads to a strong temporal increase in concentration (red line). Overall, the limit of detection (LOD) of the analytical device is exceeded.

This temporary high concentration spot allows for a qualitative identification of the analyte as well as a retroactive quantitative calculation of the analyte concentration.

In many cases, it is not possible to directly analyze drawn samples in-field but later in a laboratory. In that case, it must be excluded that storage itself does change the qualitative and quantitative composition of the sample. Of course, these requirements do also apply for the down streamed desorption and analysis. [40], [41] Sampling itself can be divided into active and passive sampling. While using passive sampling, mass-transport of relevant components (analyte as well as interferents) is determined solely by diffusion, in active sampling a convective flow is used to pass the air sample through an adsorbent tube or a membrane.

Passive sampling is mostly used in terms of workplace substance monitoring, i.e. in a dosimeter-like fashion (integrative sampling). [42] For this application, they may be badge or tube-like, often supplemented by semi-permeable membranes in order to prevent e.g. humidity contact. [43] While badge-like passive samplers are more likely to be solvent-desorbed for analysis, tube-like ones can in most cases directly be used in thermal desorption enrichment. However, there are known influences of meteorological conditions on diffusive transport and this directly impacts any quantification based on passive sampling. [44]

In active sampling, the sample atmosphere to be investigated is drawn through a packed bed of at least one adsorbent that shows a high affinity towards the compound(s) of interest. [40], [41] Determined by the specific breakthrough volume – the amount of gas required to elute the specific compound through one gram of sorbent at the respective temperature – and the sampling speed (in volume per time), sampling intervals can range from minutes to hours, allowing for increased (monitoring) or decreased (dosimeter) temporal resolution. [45]–[47] Whereas adsorbents featuring high specific surface areas and a high micropore volume are suitable for volatile and smaller molecules like methane or permanent gases, meso- or macroporous adsorbents with low specific surface area (e.g.

Tenax®) are preferred in case of semi and non-volatile compounds. If the combination of analytes spans a wide range of volatilities, adsorbents are often combined in series, meaning one tube after another. [48]

Sample analysis after sampling can mainly be done in two ways, solvent desorption or thermal desorption. In solvent desorption, the adsorbent is washed with a defined volume of a suitable solvent. This solvent should exhibit no interference (e.g. polymer swelling) with the adsorbent and provide a high solubility for the analyte. [41], [45], [49]

In thermal desorption, the adsorbent is heated to a specific temperature and purged with a clean carrier gas towards the detection system. A simplified schematic for a possible preconcentration setup using convective transport (i.e. active sampling followed by thermal desorption) is shown in Figure 4. A packed bed of adsorbent is mounted in suitable cylindrical tubing. In the sampling mode (left picture), an air sample is conducted through this sorbent bed using e.g. a mass flow controller (MFC) and a vacuum pump. The packed bed (often referred to as trap [50], [51]) is operated at room temperature or even cooled below room temperature. The airborne molecules contained in the sample interact with the stationary phase, the adsorbent. [40], [52] They adsorb, desorb, diffuse or (in most cases unintentionally) undergo chemical reaction with the stationary phase if they are reactive. At the end of this sampling cycle, the sorbent bed “breaks through”, meaning at its exhaust, and a rise in analyte concentration is observed as its capacity for this specific or the plurality of all molecules in the air sample is depleted. Therefore, only half the breakthrough volume should be used for sampling to obtain reliable results during thermal desorption. [53] A flow controlling or monitoring is used in most cases to determine when this volume is reached and sampling is to be stopped.

Depending on the details, the thermal desorption is either carried out in the same direction as the sampling (middle scheme) or in a reclined (right scheme) fashion. In this

step (middle and right scheme in Figure 4) the trap is heated to a set temperature and a stream of clean carrier gas is purged through the packed bed. A detector (e.g. a flame ionization detector, FID) is mounted after the packed bed. [27], [54]

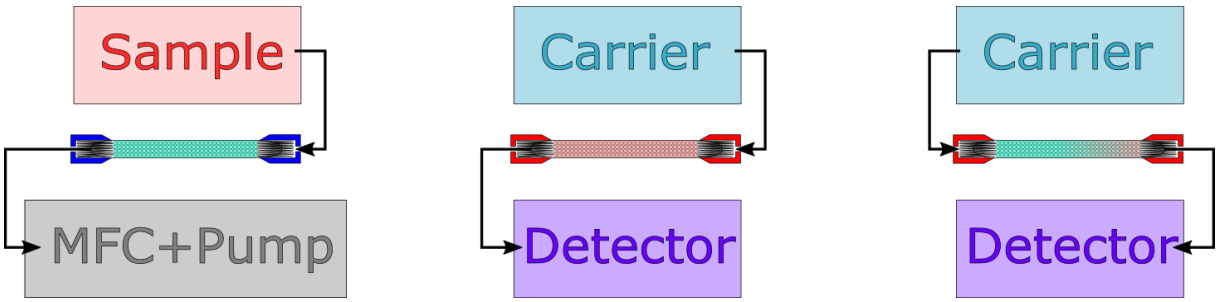

Figure 4. Sampling and preconcentration schemes using convective transport. Sampling (left) is either followed by thermal desorption in the same (middle) or reclined (right) direction. During sampling, a mass flow controller and a vacuum pump (MFC+P) are used to adjust the sampling flow.

In this case, also the gas flow needs to be determined or controlled. Using a setup like this, the prior sampled amount of analyte molecules contained in the sampled volume – leading to its concentration in this volume – is thermally desorbed in a smaller volume of carrier gas, hence increasing the analytes concentration.

If the beforehand sampled volume is known, the initial concentration of the analyte in the investigated air sample can be re-calculated. Regularly, this technique is used in conjunction with a GC-MS system. [55], [56] Directly after the thermal desorption, molecules are being trapped again (e.g. capillary cryofocusing [57]) before being eluted on the chromatographic separation column. [58]

If several physicochemical properties of the analyte and respective sorbents in the system itself are known, additional purging, separation and recollection steps may be included. [41], [59] In simpler versions using this technique, either if convection is applied or not, a sensor (called “detector” in Figure 4) is placed in the direct proximity of the trap (often referred to as “preconcentrator”). [60]–[64] When no convection is applied (e.g. the preconcentrator layer is placed on a flat heating platform [65] next to the sensor) molecule transport is merely occurring by diffusion. This sensing system design is

especially favored when it comes to cost reduction within the scope of mass production on wafer level. [66], [67].

Another technique is the so called solid phase micro extraction (SPME), a module for instrumental lab analysis. [68], [69] It is used in a similar fashion as in headspace sampling. Instead of the headspace cannula, a small sorbent coated rod is placed in a headspace vial. After a defined sampling time, it is placed in the heated injector of a GC system to release the analytes via thermal desorption.

As especially the family of explosive target molecules may contain reactive species, an important requirement for a suitable sorbent is the chemical inertness of the active surface to avoid that catalytic reactions or combustions may alter the amount sampled or lead to contaminations in the sample. Furthermore, only slight modifications of adsorbent behavior due to humidity, oxygen or carbon dioxide presence is required.

Also, the complete capture (best via physisorption) of the target analytes, meaning a sufficient loading capacity and strong interactions between analyte and sorbent to prevent a preliminary or partial breakthrough during sampling is essential.

Diversified affinities for regular occurring interferents are required to increase selectivity as well as a sufficient thermal stability of the adsorbent for (repeated) thermal desorption temperatures.

Certainly, no adsorbent will be able to meet all requirements ideally. However, there are certain material-class based trends with respect to these individual factors. The following section (1.2) will give a review about state-of-the-art adsorbents typically used in analytical science.

1.2 State-of-the-art adsorbents

There is a wide range of sorbents available being used for the preconcentration of airborne analyte containing samples. [56], [70] Conventional sorbents include both inorganic [71] and organic materials (polymers) [72], reaching from macroporous (e.g. Tenax® TA) to microporous (e.g. Zeolites) materials.

Classically, adsorbents may be grouped into three major classes[73], [74], namely:

1. Adsorbents that do not possess ions or reactive functional groups on their surface (e.g. graphitized carbon blacks (GCBs) or polyethylene).
2. Adsorbents bearing localized positive charges on their surface (carboxylate protons or exchangeable small cations), e.g. zeolites.
3. Adsorbents with localized negative charges on their surface (esters, carbonyl groups or small exchangeable anions) like coated (e.g. polyethylene glycol) or functionalized (e.g. nitrile) carbon blacks or polymers from group one.

Only the first group of adsorbents will show a non-specific interaction with any group of molecules. The other two groups will only show a non-specific interaction with guest (probe) molecules, that show an approximately spherical shape and almost no dipole moment (i.e. inert gases or saturated hydrocarbons).

Purely inorganic materials (e.g. silica gel, alumina or zeolites) have active surfaces that render them hydrophilic, leading to water condensation in relevant environment – an often undesirable effect that occurs for adsorbents from group 2 or 3. [41], [53], [55] There are only few examples of zeolites being used as sampling materials [62], [71], [75], [76], in all cases directly in a preconcentrator fashion in conjunction with a sensing device. Zeolites are more likely to be used as a coating for gas sensors. [77]–[79] Mesoporous, inorganic, non-zeolitic sorbents (e.g. based on MCM-41 or polydimethylsiloxane) were shown to be able for the quantitative, reversible capture of light gases [80] and terpenes.

[81] Other purely inorganic materials, like silica-based sorbents, are in some cases template-synthesized to match the spatial imprint of target analytes, e.g. TNT. [82], [83] This approach of template-synthesis is also frequently used with organic polymers, so called molecularly imprinted polymers (MIPs). There are examples of MIPs being used as tube sampling material [72], [84], SPME [15] or sensor coating. [7] This concept works better the larger the desired guest molecules are, because the interaction imprint or group complementarity (called pharmacophore in drug design, where agents are designed for a specific interaction in an enzymes active site) is a combination of several specific interactions. [85]–[87] This generally leads to these concepts being prevalent in the liquid phase as larger molecules (e.g. antibiotics or dyes) show low volatility (e.g. boiling point) in the gas phase. [15], [88]

As in practical scenarios, water adsorption and interference is a main problem to overcome, the most commonly used adsorbent materials for the sampling of organic vapors are porous polymers like the ones from the “Tenax®”, “Chromosorb®” or “HayeSep®” product families. Most of these polymers can be classified as type 1 or 3 adsorbents, depending on the monomers used for their formation.[74] A different frequently used class is carbon-based adsorbents, e.g. carbon molecular sieves like Carboblack (synthetic) or naturally based activated carbon like “Anasorb CSC”, a coconut charcoal. Most of them are class 3 adsorbents, whereas highly pure graphitized carbon blacks are group 1 adsorbents. Altogether, they exhibit a wide variety of specific surface areas, polarities and potentially analytes they can be used for. [41], [52], [53] Also their maximum desorption temperature and resulting background emission is different for these state-of-the-art adsorbents. Detailed property overviews of commercially available sorbents are given in [41], [89] and [40].

The Tenax series (e.g. Tenax® TA or Tenax® GR) is the most prominent class of porous polymers used for gas sampling, even though they cause problems regarding their thermal stability and resulting background emission. [41], [48], [53] Another disadvantage is the small specific surface area, which renders it unsuitable for high volatile analytes as well as chemical decomposition reactions with highly reactive species like nitrogen dioxide. [48] A clear advantage is the hydrophobicity, suppressing water adsorption. [48] There are many examples of Tenax being used for gas sampling including monoterpenes, halocarbons, aromatics, hydrocarbons and applied in micro fabricated preconcentrators. [90]–[92] Tenax is generally composed of poly-(2,6-diphenyl-p-phenylene oxide). Tenax GR is a mixture of regular Tenax and graphitized carbon black. [40] Due to higher specific surface area adsorbents from the Chromosorb family (Chromosorb® 101, 102 or 106) are often used as alternative to Tenax. Along with HayeSep P and Porapak P, they are polystyrene based polymers, e.g. Chromosorb 106 being a polystyrene-divinyl-benzene copolymer. [40], [41] Chromosorb was shown being able to sample and enrich airborne high volatile organic compounds due to its higher specific surface area. [93]. Also pesticide sampling was demonstrated. [94]

Carbon-based adsorbents can mainly be subdivided into three major groups: Activated carbons, carbon molecular sieves and graphitized carbon blacks. Their collective range of specific surface area is between 300 and 4000 $m^2\ g^{-1}$. [95] They all show a high temperature stability as compared to porous organic polymers. [40], [41]

Activated carbon (AC) presents the most widely used among the three carbon-based materials, with industrial application and production being documented since the 19th century. [95] Anasorb CSC is an example for a commercially available active carbon adsorbent. Due to the high content of micro- and mesopores, the resulting specific surface areas are in the range of 800 to 1500 $m^2\ g^{-1}$. Usually, broad pore size distributions are

tailored via the controlled carbonization and subsequent activation of carbon containing starting products, such as different natural polymers. Generally, pore sizes can be shifted towards the mesoporous (for liquid phase application) or towards the microporous (for gas phase application) region. [95]

Owing to the carbonization and the choice of natural products as starting material, several functional groups (hydroxyl, carboxyl) are to be found on the heterogeneous surface of activated carbons. This allows for irreversible surface reactions as well as significant water adsorption. [41], [96] Altogether, the choice of starting materials leads to a broad variation in physical properties of activated carbons.

Carbon molecular sieves (CMS) possess less surface bound oxygen than activated carbons, suppressing its water adsorption as compared to them. [97] They are usually formed by the controlled pyrolysis of suitable synthetic polymers, like polyvinylchloride (PVC). Also, the coating of commercially activated carbons with carbonized thermosets represents an early approach to produce CMS. [95] Generally, they are comprised of small cross-linked crystallites that strongly contribute to the micropore content of the material and render their pore size distribution narrow. [40], [74]

Commercially available families, like Carboxen or Carbosieve show micropore volumes from 0.19 to 0.5 ml g^{-1} and surface areas reaching from 387 to 1054 m^2 g^{-1}. The increased content of micropores as compared to activated carbons makes them more suitable for the adsorption of smaller molecules, e.g. light hydrocarbons. However, they still have several different functional groups (or metal traces) on their surface, leading to chemical reactions with specific analytes. [98] Consequently, they still show a significant water adsorption. LOLOL

The third class of carbon-based materials is graphitized carbon blacks (GCB), predominantly non-polar adsorbents with a homogeneous surface area and a high carbon

content of above 99%. [74] They are prepared by heating regular carbon blacks under an inert gas atmosphere to 3000 °C and above. Due to the high degree of carbonization, they lack micropores and show surface areas between 5 and 560 $m^2 g^{-1}$. [40] They also show a high thermal stability and low water adsorption. [40] Overall, they can be used in very humid environments and newer generations like Carbograph 5 or Carbosphere, showing higher specific surface areas, are even suitable for sampling smaller molecules like acrolein. [49] Also, the already low amount of polar sites can be further reduced by conditioning the adsorbent before sampling. [74], [99]

Hardly surprising, there is no universal, i.e. optimal sorbent for every analytical task. The large diversity in chemical and textural features goes along with a list of advantages and drawbacks. While adsorbents exhibiting larger micropore volume and specific surface area (being referred to as strong [40]) are used for more volatile adsorbents, meso- and macroporous adsorbents are more suitable for semi-volatiles and high-boilers.

A more general problem for many sorbents is their lack of chemical and textural uniformity and definedness. This is especially vital for natural-based active carbons but also carbon-based materials that are derived via similar routines. [40], [98] Also, water adsorption remains a problem for all but graphitized carbon blacks (GCB) that in turn possess low specific surface areas.

Polymer-based adsorbents all suffer thermal stability problems and produce a hardly acceptable background signal during desorption. However, their water adsorption is on average lower than that of carbons. Structure-deterministic, microporous materials like zeolites are purely inorganic, exhibit a high affinity for humidity and a tendency to catalyze chemical reactions. However, showing a good tailorability, chemical robustness and large specific surface areas, they provide a good starting point to develop new materials.

Recently, many interesting substance classes have emerged, such as porous, crystalline polymers, graphene [100] and single/multi walled nanotubes [101]. Metal-organic frameworks (MOFs) [102]–[104] belong to the class of porous coordination polymers, along with covalent organic frameworks [105], the latter do not contain metals. All these materials, being porous in nature, are promising new candidates for thermal enrichment by sampling. Especially, the possibility to tailor their pore system and functionality via synthesis allows for a affinity driven structure optimization to selectively match specific guest molecules (analytes). Due to the high textural and chemical versatility of MOFs alone, the focus of this thesis is dedicated to them. Regularly, a comparison towards state of the art Tenax TA was drawn.

1.3 Objectives and challenges

The scope of this thesis is the investigation and application of metal-organic frameworks as new materials for trace gas enrichment. This method can generally enhance any gas-phase based detection system (such as IMS, MS or FID) in terms of sensitivity and selectivity.

As the range of MOF is large and includes several levels of dimensionality, such as metals, linkers and additional functionality, interpenetration and defects, it is necessary to evaluate them under standardized conditions. Full-scale testing in this case would require the implementation of MOFs in a sensor system that includes a whole range of additional parameters (diffusion distances, sensor elements characteristics and the MOF application itself). Therefore, individual results lack transparent results and a straightforward evaluation is complex. The investigation and evaluation of MOFs as sampling materials for trace gas analysis should therefore be standardized using a technique that is capable to yield materials parameters that directly affect the sorption behavior.

Inverse gas chromatography is a method that directly yields retention volumes that resemble partition coefficients of guest molecule MOF combinations at specific temperatures. These retention volumes directly influence the performance in a preconcentration setup, i.e. the ratio of the carrier gas volumes from that guest molecules are sampled (adsorption) and thermally desorbed afterwards. As regular chromatographic techniques and equipment can be used, the process can also be automated to suppress the human factor and run 24/7. Individual iGC parameters should be chosen carefully and linear, reliable ranges must be found for each combination of MOF and probe molecule. This combination furthermore includes carrier gas flows, temperatures and column design. Ranges of these parameters need to be explored prior optimizing them. If the experimental procedure is standardized, MOF materials can be investigated and compared on a universal basis, e.g. for high adsorption enthalpies with the analyte molecules of interest. If these requirements are met, Henry constants, enthalpies and entropies of adsorption as well as selectivities can be derived, allowing for an in-depth thermodynamic characterization. While the former ones directly yield information with respect to the device parameters (sampling time, capacity at infinite dilution and optimal desorption temperature), the latter one can be used to address selectivity. Furthermore, iGC can be used to investigate the materials stability with respect to temperature and temperature cycles, a parameter that is especially important for a MOF layer in a sensor system that is used for monitoring.

If iGC proves to be a suitable screening method, it will be possible to correlate the respective results with full-scale thermal desorption experiments. A more detailed view and understanding of the individual sorption processes (guest molecules times MOFs, both having their respective structural and chemical features) is possible with iGC. It may

be possible to obtain specific trends that are caused by structural or chemical complementarity or exclusion during the sorption process.

Furthermore, effects that cannot be explained by regular analytical techniques (specific surface area, XRPD pattern) can be explained using iGC, as the interaction with several chemical different molecules at zero coverage is assumed to be specific and sensitive to small changes in structure.

The analyte classes to be addressed in this thesis are mainly two families: Explosives (e.g. explosive precursors) and volatile organic compounds (VOCs). Explosives were chosen because they are relevant for security applications and checkpoint situations, and VOCs were chosen, as some molecules of these families pose a danger to health even at low concentrations.

The main result chapters of this thesis deal with the concept of utilizing 1st generation MOFs (e.g. HKUST-1) on adsorptive enrichment for nitro alkane (e.g. nitromethane) sampling. The principle of iGC is used as a prescreening method prior to more time consuming thermal desorption experiments. The enrichment of benzene with 2nd generation MOFs (e.g. UiO-66) is shown thereafter. After thermal desorption experiments under humid and dry conditions, iGC is used to gain further insight in the adsorption mechanisms. Additional linker deficiency calculations from TGA investigations are included in the discussion.

2 General part

2.1 Metal-organic frameworks

About 30 years before gaining widespread attention among the scientific community, in 1965, the first mention of a new class of metal-organic polymers, coordination polymers were reported. TOMIC used multidentate (di- tri- and tetradentate) carboxylic ligands and various metals (e.g. Zinc, Iron and Uranium) to form highly temperature stable new compounds with a high metal content. [106] Also in 1965, BIONDI reported crystalline but polymeric compounds comprised of tricyanomethanide (a planar, tridentate ligand) and Copper(II) ions. [107] In the early 1990s, materials featuring Cu(I) ions and cyano-funtionalized tetraphenylmethane (a non-planar, tetradentate ligand) were reported. [108]

Today, these compounds could mistakenly be referred to as metal-organic frameworks (MOFs), because they lacked one important criterion, permanent porosity. The structure of one of the most famous MOF structure, MOF-5 (structural details in section 2.1.1), consisting of Zinc and terephthalate linkers, exhibiting permanent porosity, i.e. no structural collapse after solvent removal, was published in 1999 by the YAGHI group. [109] In the same year, the structure of the well-known MOF HKUST-1, aka MOF-199 (see section 2.1.1), composed of Copper and trimesate linkers, featuring different pore apertures was published. [104]

Three years later, the whole concept of reticular chemistry and design featuring various carboxylate linkers was further elaborated by the YAGHI group. [102] The term metal-organic framework itself was introduced in 1995. [110] Also, the first possible applications of MOFs were explored at that time, namely the storage of methane. [111] A short time later, the French research group of FÉREY reported the synthesis and characterization of a MOF featuring large pores. Also, as compared to isoreticular MOFs

(IRMOFs) being composed of identical nodes but spatially different linkers, e.g. MOF-5, the structure of MIL-47 exhibited high surface area as well as a back then unparalleled chemical and thermal stability. [112] Today, the Cambridge Crystallographic Data Centre [113] contains several ten thousand different MOF structures [114] with specific surface areas up to more than 6,000 $m^2 g^{-1}$. [115]

According to IUPAC, a MOF is a "a coordination network with organic ligands containing potential voids." [116] The last criterion is an important one: Without potential voids, specific surface area and micropore-content is neither permanent (open frameworks), nor can they form due to temperature change, guest molecules or other external stimuli (dynamic systems). This definition also underlines that MOFs do not have to be crystalline, a requirement that was a central one in a former MOF definition originating from YAGHI. [117]

In the early days of MOF research, there was a personal urge of many research groups to categorize and brand the new structures. Starting as a new material class in the existing zeolite community, MOFs were labeled with a 3-letter prefix system, followed by a number. This prefix represents the research facility or group of their origin, such as MIL (Materials of Institute Lavoisier), MOF (metal-organic framework, YAGHI group, e.g. MOF-5), ZIF (Zeolitic imidazolate framework, YAGHI group, e.g. ZIF-8), HKUST (Hong Kong University of Science & Technology, e.g. HKUST-1), UiO (University in Oslo, e.g. UiO-66) or DUT (Dresden University of Technology, e.g. DUT-5). [118]

Given the fact that MOFs are not only comprised of a large amount of different metals (or metal clusters) but also of a much larger part of organic molecules, the resulting plurality of possible structures seems almost unlimited. This vast variety of pore topologies and functional diversity but on the other side chemical uniformity and crystallinity has lighted the synthesis, exploration and technical application of MOFs ever since.

A review of MOF synthesis, activation, post-synthetic-modification and further processing is given in the appendix (section 6.1). A review of selected MOF applications, such as gas storage, gas and vapor separation as well as MOFs in chromatography, air purification and selected optoelectronic applications is also given in the appendix (section 6.3).

2.1.1 Structural features of MOFs

As already implied by their name, MOFs consist of (at least) two key components, metal centers and organic ligands. Cations or cationic clusters of mostly transition metals act as "nodes", i.e. being connected by the organic ligands (linkers). [117] Both, the metal nodes and the linkers are referred to as secondary building blocks (SBUs) in the design and construction of MOFs. SBUs are part of a concept that uses simplified, topological models for both, nodes and linkers for the sake of clarity and visualization. [119], [120]

Metal nodes can have various geometric forms, such as linear, angled, triangle, square planar, tetrahedral or quadratic bipyramidal, generally showing coordination numbers ranging from 2 to 10. Figure 5 gives an overview of common metal SBUs in different representations. [119], [121]

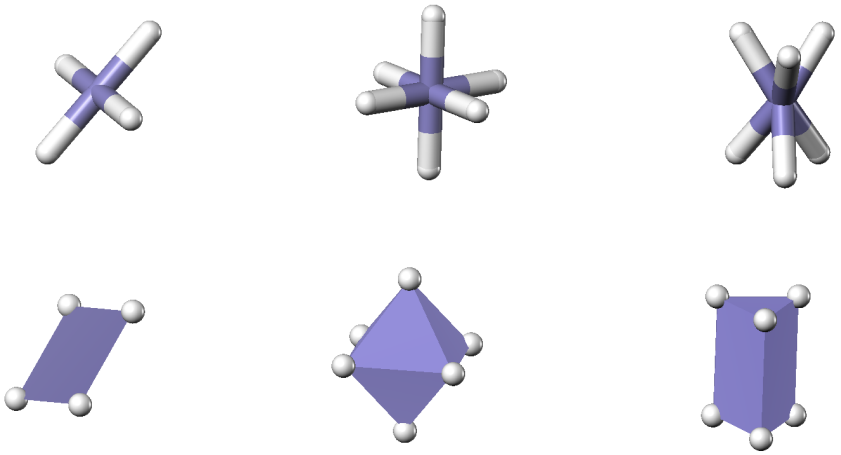

Figure 5. Representations of different MOF nodes. From left: $Cu_2(CO_2)_4$, $Zn_4O(CO_2)_6$ and $O(OH)_3Cr_3(CO_2)_6$. Top: Representation of the node in the MOF net. Bottom: Shapes enclosed by the carbon atoms of the carboxylate group.

From a preparative point of view, using metal salts that mimic the geometric arrangement of the desired metal building block, like zinc(II)-oxo-acetate (basically representing a hexa-acetate coordinated Zn_4O structure) can be helpful for the MOFs nucleation and growth. It is also possible to have multiple metal nodes in one MOF, if they are compatible in terms of connectivity and topological parameters. Either in the sense of different oxidation states, such as porphyrine-connected Co(II) and Co(III) species in PIZA-1 (porphyrinic illinois zeolite), or different metals, such as mixed Cu-Cd nodes in $Cu(PYAC)_2$ (PYAC = 3-(4-pyridyl)pentane-2,4-dionato) based MOFs. [122], [123] Recently, this was further developed by incorporating up to 10 different metals into one structure in MOF-74. [124] The basis for this mixed-metal MOF was the famous Mg-MOF-74 structure, i.e. Mg(DOBDC) (DOBDC = dihydroxy terephthalic acid) featuring a bidentate linker.

Linkers occur in different forms, such as neutral, anionic as well as cationic, with the latter being least prevalent. [117], [119] To arrange for permanent porosity after guest molecule removal (activation), rigidity of the framework linkers is needed

If linkers show rotatory degrees of freedom, flexibility within the structure cannot be excluded. Therefore, in most cases, aromatic linkers are used due to their rigidity and stability. Alkane-based backbones of linkers are rarely to be found. More importantly, linkers need to be multi-dental, to adequately connect the metal nodes. [119], [121]

Anionic bidentate linkers like deprotonated terephthalic acid (benzene-1,4-dicarboxylate, often referred to as BDC) or neutral linkers like 4,4′−dipyridyl are key building blocks for a large variety of MOF structures. [125], [126] Deprotonated trimesic acid (benzene-1,3,5-tricarboxylate, BTC) is such a prominent linker which is to be found in HKUST-1, coordinating linear Cu_2 clusters in a “paddlewheel” fashion. [104], [127]

The systematical design using equal metal nodes (Zn_4O tetrahedrons) and various linkers was demonstrated by YAGHI with the so called IRMOF series – IR meaning isoreticular or

reticular isostructures. [117], [119] Reacting differently in terms of length, rigidity and shape, carboxylate linkers with zinc nitrate, MOF structures exhibiting different crystal density and pore volume were synthesized. Figure 6 gives and overview of common linkers and their node abstractions.

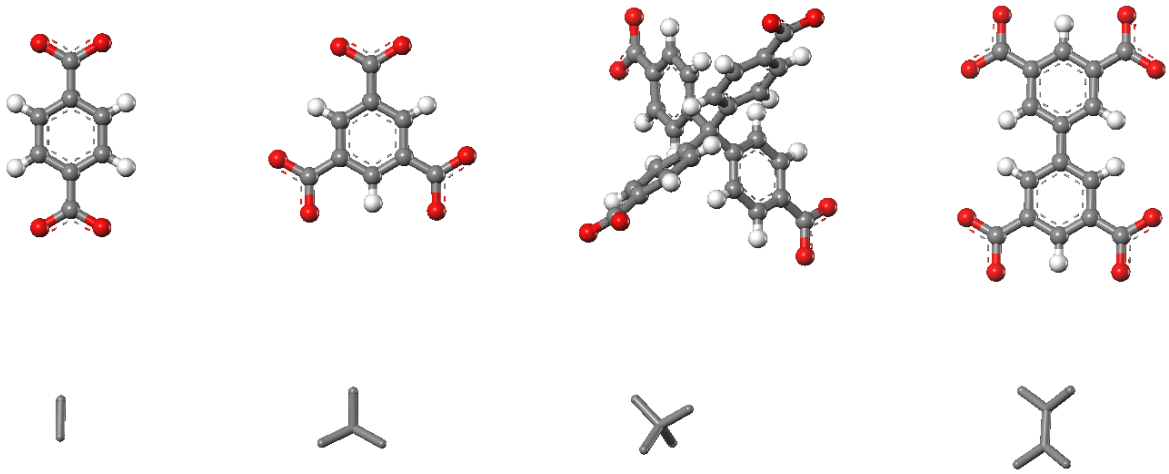

Figure 6. Examples of carboxylate-based linkers in MOFs (top) as well as their abstraction as nodes of the MOF net (bottom). While the ditopic BDC (terephthalate) linker is only abstracted as a link (without a node), the tetratopic linker on the right (biphenyl-tetracarboxylate) would be abstracted as two nodes of the resulting net. In case of the trimesate (BTC) linker, the node is in the center of the benzene ring, in case of the tetraphenylmethane-based linker the intended node is located at the tetrahedral carbon.

Moreover, the occurrence of multiple linkers in one framework is possible. The resulting structures are referred to as multi component (MC) [128] or multivariate (MTV) [121] MOFs, in the latter case meaning that various functionalities can be incorporated in one structure for example to be applied in multi-step catalysis.

A prominent example is the pillar-linking of 2D sheets of metal-porphyrine to a 3D structure using 4,4′−dipyridyl linkers besides the porphyrine linkers used to form the 2D sheets. [129] DABCO (1,4-diazabicyclo[2.2.2]octane) is also a prominent linker for joining 2D MOF sheets, especially in case of epitaxially grown, surface mounted MOFs, so called SURMOFs. [130], [131]

The interactions that provide for the frameworks stability and structure comprise mainly coordinative covalent bonds between linkers and metal clusters, with a varying fraction of ionic contributions. [132], [133] However, also other interactions like metal-metal

interactions between the metals of a cluster, or hydrogen bonds between the linkers are to be observed. [134], [135] Generally, structures featuring higher coordination numbers show higher stabilities, while vacancies lead to higher reactivity. Also, higher coordination numbers establish a steric barrier for guest molecules to enter the framework and interact with the metal nodes.

Another component, being present in metal organic frameworks, are guest molecules. These guest molecules may be solvent molecules, reactant, modulator or template molecules from synthesis, if the material is not activated properly. [126], [136] For means of catalysis or adsorption, guest molecules may also be deliberately added to the structure after synthesis. [137], [138] Depending on the structural regularity of guest molecules, their occurrence may be visible in crystal structure patterns. [138]

Since nature will always occupy void spaces and vacant surfaces by means of adsorption to minimize the overall systems energy, even properly activated MOFs will show guest molecules if they are exposed to the atmosphere. Often, water or carbon dioxide molecules do occur as guest molecules. [139]

A further aspect, or structural feature generally reducing pore volume and complicating characterization is possible interpenetration of MOF structures. When two nucleations start very close to each other, the resulting structures are only physically, not chemically linked together. [119], [121] They cannot be separated in a topological sense, i.e. without breaking bonds. This is only to be observed, when the potentially interpenetrating nucleation fits the pore of the primary structure.

As with MOF structures themselves, the interpenetration does also have a dimensionality. Not all MOF structures show the same tendency towards interpenetration. [140] For some systems, the degree of interpenetration can even be controlled via synthesis parameters, such as temperature and reactant ratios. [141]

Altogether, given a large amount of metals and a larger number of organic linkers, combined with postsynthetic modification and the intended use of guest molecules, the degrees of freedom encountered by materials design seem almost endless. The following section gives a brief overview of prominent MOF structures and their structural features, selected for the investigation in this thesis.

MOF structures of relevance for this work

Except for MOF-5, the following MOFs are an exemplary extract of MOFs used in this thesis. Render pictures were produced from CIF files of the respective primary literature cited in the paragraphs.

An easy to understand structure from the isoreticular series of MOFs, is MOF-5 (IRMOF-1, Figure 7). [109] MOF-5 is comprised of Zn_4O^{6+} metal clusters that are hexa-coordinated by terephthalate linkers (BDC^{2-}). Each Zn atom in the tetrahedral Zn_4O cluster is coordinated towards the central oxygen atom in the center of it.

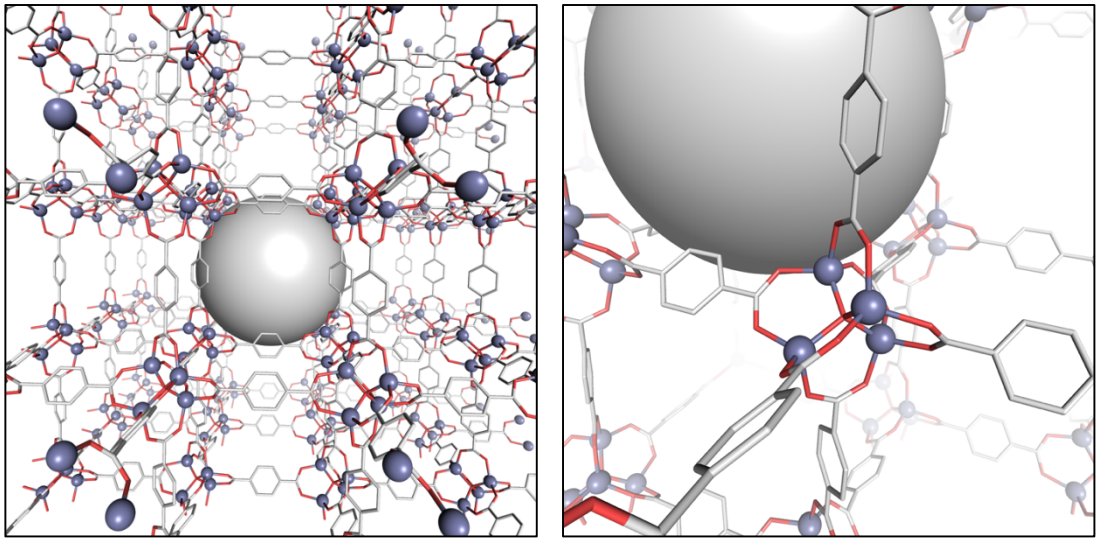

Figure 7. Pore system (left) and metal-node (right) view of MOF-5. Benzene hydrogen atoms omitted for clarity. Zn atoms are shown as violet spheres, oxygen atoms in red, carbon atoms in light grey.

Additionally, each Zn atom is coordinated by three carboxylate oxygens (each from a different BDC linker), leading to a total coordination number of four. The tetrahedral coordination environment of the central oxygen (by four Zn atoms) is expanded towards

an octahedral coordination environment of the Zn part of the node (by 6 BDC linkers). The result is one type of uniform pores with diameters of 7.5 Å to 8 Å in a cubic Bravais lattice. [102], [142] The structure is zero-dimensional (0D) and shows a Langmuir surface of about 2,900 $m^2\ g^{-1}$. [143]

Using different bidentate linkers (e.g. biphenyl-dicarboxylic acid) of different length, the pore diameters, free volume and crystal density can be tailored with free volumes from 55.8 to 91.1 volume percent. [102] Using larger linkers, bulky side groups have to be introduced in order to provide for stability and permanent porosity after post-synthetic activation. [144]

Another prominent yet structurally different MOF selected for this thesis, is MIL-53(Al) (Figure 8). It contains linear trans $Al_x(OH)_x$ chains that corner share these groups. [145]

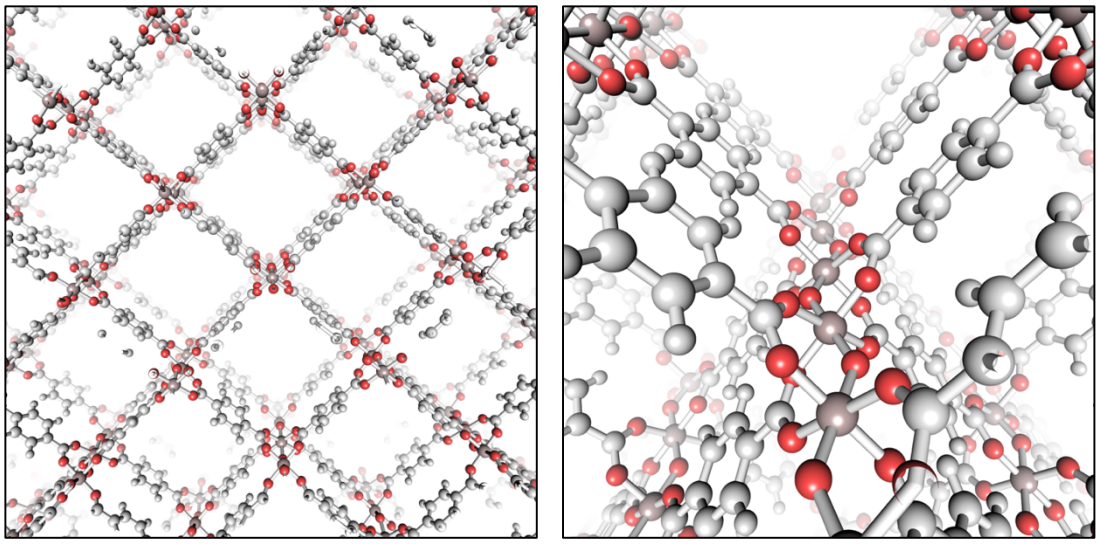

Figure 8. Pore system (left) and Al(OH) metal-node chain (right) in MIL-53(Al) in the ht-form (open framework). Oxygen atoms in red, Al atoms in pale red, hydrogen and carbon atoms in light grey. Hydrogen atoms at Al-connecting OH groups omitted for clarity.

The missing four oxygen atoms (to form an $AlO_4(OH)_2$ octahedra) are supplied by the BDC ligands that bridge Al nodes along this direction in an alternating fashion. The framework exists in different forms, depending on activation, temperature and guest molecule pressure. In all forms, it is one dimensional (1D). [143] The pore system has (with the pore channels in z-direction) a diamond shape (in the xy plane), with varying angles. The

BDC-Al-BDC angle varies from 70.9° in MIL-53 in the as synthesized (as, orthorhombic) form to 75.1° in the activated high temperature (ht, orthorhombic) form to 42.7° in the activated low temperature (lt, monoclinic) form. [145]

This behavior is also referred to as the breathing effect of MIL-53. The pore diameters change from 7.3 × 7.7 Å (as) to 8.5 × 8.5 Å (ht) towards 2.6 × 13.6 Å (lt). [142] The ht-form shows a Langmuir surface area of 1,590 m^2 g^{-1}. MIL-53(Al) is commercially provided by BASF under the trade name Basolite A100.

HKUST-1 (Figure 9) is probably one of the most widely studied MOFs. [104] It contains copper $(Cu_2)^{2+}$ clusters (z-axis) that are coordinated by four trimesate (BTC^{3-}) linkers in the xy-plane, forming the so-called paddlewheel shape. The sum formula of the blue-colored substance is Cu_3BTC_2.

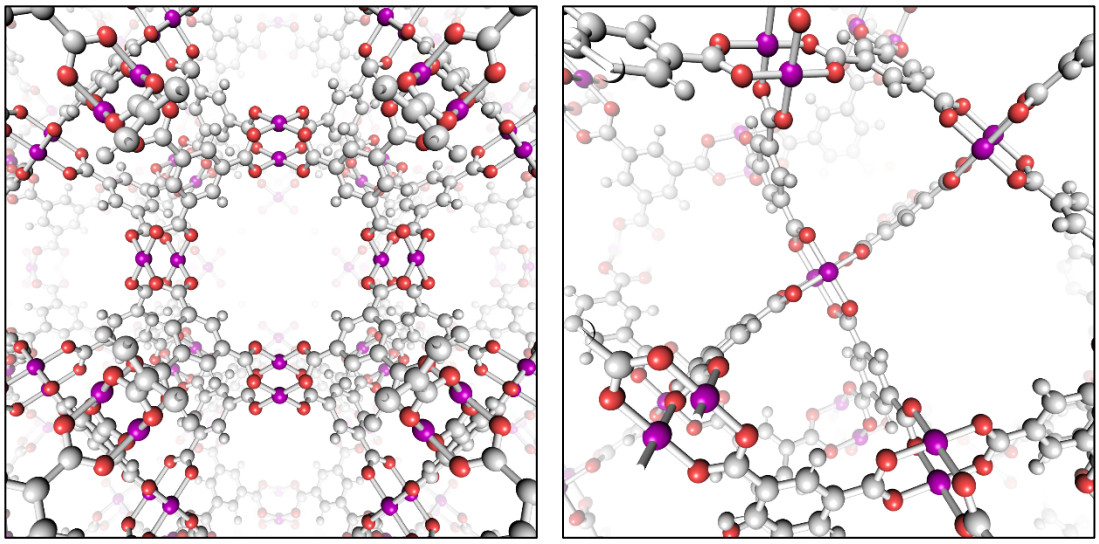

Figure 9. Pore system (left) and trimesate (BTC) coordinated Cu_2 node (paddlewheel) SBU view (right) of HKUST-1. Cu atoms in purple, oxygen atoms in red, hydrogen and carbon atoms in light grey.

As compared to MOF-5 and MIL-53, HKUST-1 shows vacancies at the Cu_2 clusters, also referred to as open metal sites. These coordination sites significantly improve the gas adsorption features of HKUST-, especially for polar gases and water. Because of its 3D structure, three different pores (5.5 Å, 11.1 Å and 13.1 Å) are observed showing a geometric surface area of 2,352 m^2 g^{-1} and apparent BET surface areas of 1,500-2,200 m^2 g^{-1}. [146] Due to the accessibility of open metal sites in the largest pore, this pore

also shows the highest hydrophilicity. [147] It is commercially sold by BASF under the trade name of Basolite C300.

With respect to its composition Fe-BTC (Basolite F300) can be compared to HKUST-1 as Fe-BTC is composed of an interconnected network of iron metal (Fe^{+3}) coordinated with trimesate linkers. However, the exact nature of the structure remains unknown, although a distorted variant of MIL-100 was suggested. [148], [149]

UiO-66 (Figure 10) can be considered as a second-generation MOF material although the structure itself can be extended to a whole material series. [150] UiO-66 type MOFs consist of zircon oxide based $Zr_6O_x(OH)_{8-x}$ clusters, that are connected to a maximum of 12 ditopic (BDC in the most basic case) linkers.

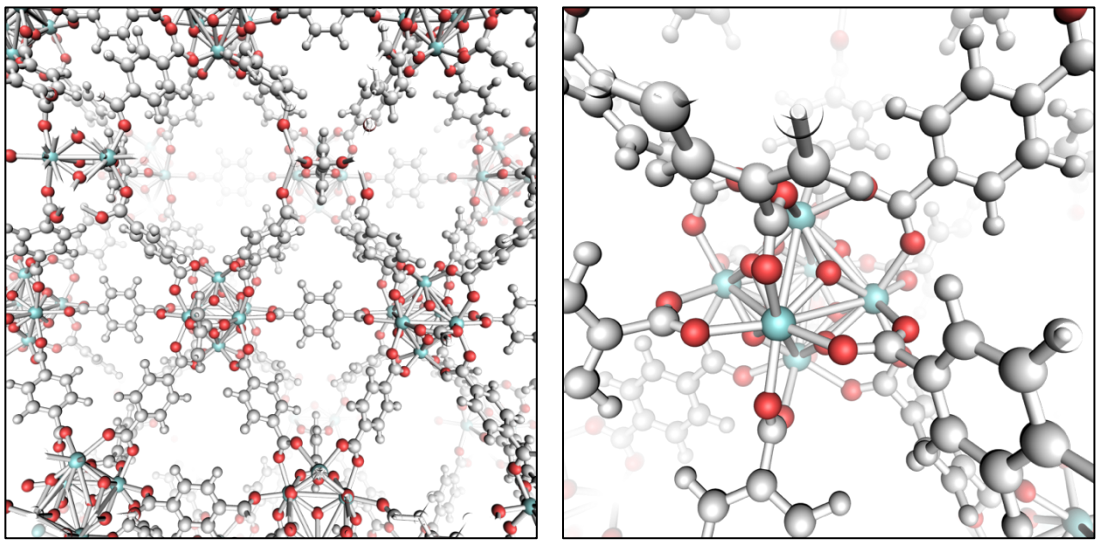

Figure 10. Pore system (left) and 12-fold BDC coordinated $Zr_6O_{8-x}(OH)_x$ node (right) of UiO-66(BDC). Zr atoms in pale blueish green, oxygen atoms in red, carbon and hydrogen atoms in light grey.

The ratio of hydroxyl towards oxy ligands on the cluster itself depends on the activation temperature and environmental conditions. The shape of the octahedral cluster is distorted due to further dihydroxylation under vacuum at 300 °C towards a more compact Zr_6O_6 cluster. [151] The geometric surface area is 1,247 $m^2\ g^{-1}$, apparent BET surface areas are between 500 and 1,200 $m^2\ g^{-1}$. [146] UiO-66 exhibits two types of microporous cages (tetrahedral 8 Å and octahedral 11 Å) connected by microporous, triangular windows of 5 to 7 Å. As compared to many other MOFs, UiO-66 shows high thermal stability and

chemical stability (water and acids), however it is unstable under basic conditions. If it is defect free, its pore system is hydrophobic. [152], [153] By using larger linkers, e.g. biphenyl-based BPDC, the frameworks pore size can be extended like in UiO-67 (octahedral pore 23 Å and tetrahedral pore 11.5 Å). [154]

A non-carboxylate based MOF compound was selected from the group of zeolitic imidazolate frameworks (ZIFs), namely ZIF-8 (Figure 11). [155] It consists of zinc (Zn^{2+}) nodes that are tetraedrically coordinated by four methyl imidazolate (^{Me}Im) linkers.

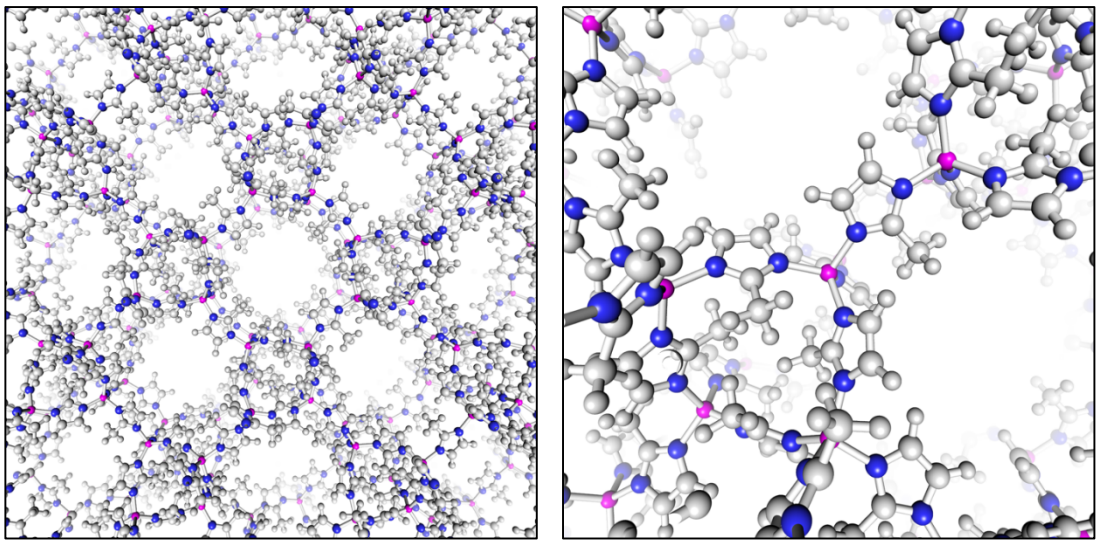

Figure 11. Pore system (left) and Zn($^{MeI}m)_4$ cluster view (right) of ZIF-8. Zn atoms in magenta, nitrogen atoms in blue, hydrogen and carbon atoms in light grey.

Methyl imidazolate is a bidentate linker with a negative charge that contains two nitrogen atoms that allow for coordinate bonds towards then zinc nodes. The Zn-(^{Me}Im)-Zn angle is close to 145°, which is comparable to Si-O-Si angles in common zeolites. In fact, ZIF-8 shows a sodalite (SOD) like topology, that is related to its stability. It shows a pore diameter of 11.6 with 3.4 windows connecting them. [155] Geometric surface areas of 1,947 $m^2\ g^{-1}$ and apparent BET surface areas of 1,300 to 1,800 $m^2\ g^{-1}$ are typical. The pore system is hydrophobic, due to Zn nodes being sterically shielded, and size exclusion is observed, although rotational linker flexibility provides for larger molecules entering the pore system. [146], [155]

2.1.2 Characterization of MOF structures

As MOFs are crystalline, porous solids, the two most basic and widespread methods to characterize MOFs are X-Ray powder diffraction (XRPD) [156] patterns and nitrogen adsorption/desorption experiments using the Brunauer-Emmett-Teller (BET) [115], [157] model. While the former provides information on the crystallinity and phase purity of the material, the latter gives direct evidence for porosity and the data to calculate the specific surface area. [139]

Another characterization possibility is thermogravimetric analysis (TGA) which can provide information on the thermal stability if decomposition products are volatile or in combination with differential scanning calorimetry (DSC) to investigate endothermic or exothermic processes within the MOF upon heating, e.g. phase changes. TGA can furthermore help to assess the Water content (especially hydrophilic MOFs) [158] and estimate the pore volume by prior solvent loading (shown for NU-1000) [139]. Also, the linker-coordination number towards the metal nodes can be estimated using TGA investigations. [151] It was done in this work for UiO-66 MOFs (section 4.2).

Diffuse reflectance infrared Fourier transform spectroscopy (DRIFTS) can be applied for a comparison of infrared band patterns for infrared active chemical groups. [159], [160]

Inductively coupled plasma optical emission spectroscopy (ICP-OES) [161], [162] is often used to determine elemental ratios within MOFs, as well as purity assessment of the bulk sample [139]

Nuclear magnetic resonance spectroscopy (NMR) [163], [164] is either used to assess the bulk sample purity, quantifying the linker ratios in multi component MOFs or even for the measurement of diffusion constants of volatile guest molecules within the MOF. [165], [166]

Scanning electron microscopy (SEM) provides for crystal or particle sizes and exterior particle morphology (in contrast to dynamic light scattering investigations) [167] or in conjunction with energy dispersive X-ray spectroscopy (EDX) to investigate elemental homogeneity and spatial dispersion. [168]

Single crystal X-Ray diffraction [127], [169] determines absolute structural information and is furthermore important for calculating pore volumes by molecular modelling [170], [171]. Also, resulting coordinate files are a starting point for large scale screening of MOF databases [172]–[175]

It is furthermore possible to exploit other techniques or the interaction with guest molecules itself for the characterization. Examples are water stability testing (at varying pH values) to assess the integrity and stability of MOFs. [176], [177] A different approach that will be discussed in section 2.3 is inverse gas chromatography, exploiting the quantification of MOF-guest or probe molecule interaction in the gas phase. A short overview of applied characterization methods in this thesis is given in the appendix (6.2).

2.1.3 MOF stability

As compared to other industrially relevant adsorbents, e.g. zeolites, the mechanical, thermal or chemical (especially with respect to water or humidity) stability of MOFs is still considered a critical property in different application scenarios. [150], [177]–[180] Stability in relevant environment represents, along with the synthesis costs (as compared to carbons and zeolites), one of the major obstacles for MOFs to successfully being implemented in technical applications. Basically, all demonstrated potential MOF applications (storage, separation, sensing etc.) are limited by the water or humidity stability of MOFs or their thermal stability. Mechanical stability is more of a concern when particle shaping, membrane manufacturing and coating is considered. [181]–[183]

Water stability

Especially “first generation” MOFs, i.e. MOF-5, suffer from strong water instability. As water molecules enter the pore system, they coordinate a metal of a node, displacing the organic linker in many cases irreversibly (e.g. in case of a bidentate linker by going from η^2 to η^1 and finally to η^0-coordination). After successive steps, only hydroxyl- or water-coordinated clusters and protonated linkers remain, consequently the porosity and surface area are permanently lost. [178], [184], [185]

The successful coordination-replacement (or attack) of a water molecule towards a MOF metal SBU contains several facets, mainly the pore systems hydrophobicity (kinetic), the linker-metal bond strength (thermodynamic stability) and the steric shielding of the linkers with respect to the metal nodes (kinetic stability).

In the most basic attack of a water molecule, featuring a transition state with an energetic height of E1, a hydrophobic MOF would feature a higher transition state barrier (E2). Its energetic location is higher than for the first transition state because additional repulsion (for example caused by a $-CF_3$ group) needs to be overcome for the reaction to proceed. This directly influences the respective time constants for the decomposition reaction, being lower for the hydrophobic one.

If a pore system itself shows an exclusion effect for water, only the exterior surface may be the target of degradation by water molecules. Excellent examples for this feature are anionic nitrogen containing linker-based MOFs, namely ZIF-8. It does even withstand soaking of aqueous 8 mol l^{-1} sodium hydroxide solution at 100 °C. The pore system or its aperture (size limiting windows) does not allow for small water clusters to enter the pore system. [155] Also other compounds from the zeolite-like MOF (ZMOF) family show this behavior. [185] The incorporation of hydrophobic groups in MOF structures does also follow the strategy to prevent the buildup of water clusters in the pores. [184], [185]

Another important factor is the bond-strength between the building blocks itself being determined by several other factors. The thermodynamics of the water-MOF reaction are governed by enthalpic and entropic factors. Metal-linker bond strengths are mainly determined by the valences of the metals and the metal-linker bond strength (simplified, the metal-carboxylate-oxygen bond). Also the amount of linker-coordination vacancies, i.e. Lewis base sites, often referred to as denticity or topicity is stability multiplicator as multiple bonds have to be broken to entirely disconnect a linker from the framework. [146] Just like in multi-step organic reactions, every intermediate step features different thermodynamic quantities and kinetic activation barriers.

It is evident that metal clusters exhibiting higher metal ionization, such as Ti(IV) and Zr(IV) as well as Al(III) and (Cr(III) compared to Zn(II) or Cu(II), do generally form more stable structures. [185], [186] With a higher metal ionization, the bond strength of a comparable metal oxide is increased as well as the bond strength of a carboxylate-based coordination compound. [187]–[189] Using bivalent metal oxide bond-strengths, the relative water stability queue of MIL-101 (Cr-O, 374 kJ mol^{-1}) > HKUST-1 (Cu-O, 372 kJ mol^{-1}) > MOF-5 (Zn, 365 kJ mol^{-1}) can be explained. With isostructures showing identical valency, the superior stability of MIL-53 (Al, Al_2O_3, 514 kJ mol^{-1}) as compared to MIL-53 (Cr, Cr_2O_3, 447 kJ mol^{-1}) can be explained similarly. [187]

Steric factors, like shielding of the linker with respect to the metal nodes depicts more of a kinetic stability enhancement. Sidechains (like -F, $-CF_3$ or $-OCF_3$) directly attached to the linker provide for an increased activation barrier that needs to be passed to successfully attack or coordinate towards the metal cluster. [178], [184], [190] A prominent example is Banasorb-22, a zinc-based MOF using a 2-trifluoro-methoxy terephthalic acid linker. [191] It can structurally be compared to MOF-5. From a thermo-analytical perspective, three different binding sites for water, occurring at 65, 110 and 200 °C (in MOF-5) were

reduced to just one at 60 °C (in Banasorb-22), evidenced by normalized differential curves from TGA. The water stability was improved as compared to regular MOF-5: After one week of exposition to steam over boiling water, the BET surface areas was reduced by 81%, while regular MOF-5 was reduced by 98% within 5 minutes. Modifications like this do also reduce the pore volume and specific surface area. [191]

Also, a higher coordination number (like $Zr_6O_x(OH)_{8-x}$-BDC_{12} UiO-66 as compared to Zn_4O-BDC_6 MOF-5) increases kinetic stability by avoiding water cluster buildups near the metal centers. [177], [179], [184] Ligand flexibility can have positive impacts on the water stability as well as negative ones. Considering torsional rotations in BDC linkers – rotations occurring at frequencies of MHz at room temperature in UiO-66 – this creates additional steric bulkiness in case of UiO-66. In Case of MIL-53 (Al), the temperature and guest molecule dependent breathing behavior may lead to water clusters coming near metal centers as consequence of this flexibility. [184]

A comprehensive overview of the thermodynamic and kinetic stability of MOFs is given in the literature [184], [185], as well as systematic studies of MOFs in aqueous solution at varying pH values. [179] In the latter study, MIL-101 (Cr) and UiO-66 (Zr) remained stable (confirmed by XRPD and BET measurements) at pH value of 4 and 12 in liquid water for 3 days to 2 months. Both MOFs successfully passed the steam-test performed in this study. Furthermore, MIL-101 (Cr) showed stability in aqueous solution at pH 0 for 2 months. Aluminum based MIL-53 and copper based HKUST-1 showed only slight or no steam stability, respectively.

Thermal stability

Thermal degradation of MOFs follows in most cases a simplistic mechanistic pathway: node-linker bond breakage followed by the combustion of the organic linker. Therefore, the thermal stability is governed by the linker-node bond strength and the number of

linkers per node. [185] Other mechanisms that are related to thermal degradation are anaerobic linker dehydrogenation, graphitization or amorphization. Similar to water stability, using higher valency metal nodes (such as Al(III) or Zr(IV) ions) will enhance the metal-linker bond strength and consistently the thermal stability. [185] Framework interpenetration and incorporating linker sidechains is also a strategy to improve thermal stability of MOFs. Varying amounts of linkers connected to an identical node are seen for the $Zr_6O_x(OH)_{8-x}$-BDC_{12} SBU that occurs in e.g. UiO-66. In UiO-66, featuring a BDC linker, 12 linkers per node are possible. Using a BTC linker in MOF-808, the structure only contains 6 linkers per node. Other structures featuring eight (PCN-222) or ten (MOF-802) linkers per node are possible. Also in UiO-66, due to non-ideal synthetic conditions, linker-node coordination numbers lower than 12 are often to be observed that directly alter the behavior in TGA experiments. [192], [193]

Plotting the activation energy for one water molecules first attack versus the temperature stability, a stability map for first generation MOFs was established. [187] This study from 2009, being older than the above cited one from 2016 [179], dealt mostly with the earlier generation of MOFs (e.g. ZIF-8, MOF-5 and MIL-53(Al)). Therefore, the top-performers within the older study, do (from a point of stability) depict the bottom line in the newer study. Generally, the qualitative dichotomy of porosity and stability is evident.

Improving MOF stability

As already mentioned in the synthesis section (6.1), there are also non-molecular-level post-synthetic methods available to alter MOF stability with regards to water stability. One possible method is partial calcination using an inert gas and a heating source. The outer shell of the MOF is converted into a metal or metal oxide containing porous carbon that shows water-repellent properties. [194] Using this approach, the water-labile MOF-5 showed a 99% retention of its specific surface area after 14 days at ambient conditions.

[194] Regular MOF-5 shows a loss of 72% after 14 days. It must be noted, that the specific surface area of the pristine material was already diminished by a factor of 2 by this procedure. XRPD patterns were sustained as well. Using different heating ramp endpoints, a thickness-variation of the calcinated shell was possible. Complete calcination was already demonstrated as a method to prepare zirconia, alumina, copper and zinc containing carbons, being applied in catalytic reactions and exhibiting lower surface areas as compared to the MOF starting material. [195]–[199]

A different approach to modify the water stability of MOF materials is the application of a water-repellent polymer on the exterior surface area, being hydrophobic in nature. A possible polymer is poly-dimethylsiloxane (PDMS). By placing MOF powders in vacuum at elevated temperatures (235 °C), a thin coating of PDMS was deposited on the exterior surface area, rendering e.g. MOF-5 hydrophobic. As compared to calcination methods, a complete retention in specific surface area was observed using this method. [200] After 1 day at ambient conditions, MOF-5 showed a decrease in specific surface area of only 9%, HKUST-1 showed no change at all. This approach is sadly not applicable towards thermal desorption as used in this work, because during desorption, PDMS will be desorbed as well, contaminating detectors and/or columns.

2.1.4 Sampling and enrichment using MOFs

The same features of MOFs that make them promising candidates for gas storage (high surface area and pore volume, review in the appendix, 6.3.1) [201], [202] combined with the imposed selectivity (e.g. tailorable pore-sizes and chemical groups, review in the appendix, 6.3.2 and 6.3.3) [51], [119], [203] render them ideal candidates for active or passive sampling applications to temporarily enrich gaseous analytes of low concentrations.

One of the first applications directly targeted the enrichment of an airborne chemical warfare simulant DMMP (dimethylmethyl phosphonate) by IRMOF-1(MOF-5) by placing it into a gas-sampling loop (0.06 µl volume). [51] Using sampling times of only 4 seconds, preconcentration factors of above 5,000 were observed for DMMP. Selectivity, being arbitrarily complex to assess, was demonstrated by measuring the enrichment factor for toluene which was three orders of magnitude lower than for DMMP. DMMP sources containing sub-ppm levels were used. As compared to MOF-5, Tenax® TA only showed preconcentration factors of around two. The high capacity of IRMOF-1 for DMMP (0.95 g per g of MOF) combined with the strong dipole-dipole interactions explain this high enrichment factors and selectivity over aromatic toluene as well as n-dodecane.

An example for offline-sampling (using sorbent tubes for sampling followed by storage and a later analysis in the lab) was the preconcentration of atmospheric formaldehyde using MOF-5. No chemical derivatization of formaldehyde was needed prior to detection using a GC-MS system. [204] MOF-5 provided for 53 and 73 stronger preconcentration factors as compared to state-of-the-art adsorbents Tenax® TA and Carbograph 1TD, respectively. Even though MOF-5 suffers humidity instabilities it was possible to realize in-field sampling at humidities of 45% with formaldehyde recovery rates of 90% after 72 h of storage between sampling and analysis. Also the long-term repeatability was investigated. After 200 cycles, no significant loss of sampling efficiency was observed. Not only the high surface area of MOF-5 but also the Zn metal sites are assumed to be responsible for this behavior. A capacity of 32 µg of formaldehyde for 300 mg of MOF-5 was determined. The detection limit using this method was 0.6 µg m^{-3} (240 ppt) with a calibration curve linearity of three orders of magnitude. In a more recent study using optimized parameters and conditions and MOF-5 as adsorbent, it was shown to be even

possible to quantify formaldehyde concentrations down to 10.1 ppb from a 20 ml sample volume, i.e. 0.25 ng. [205]

A different sampling application of MOFs is solid phase microextraction (SPME). A substrate, mostly a stainless-steel wire, is coated with adsorbent. This wire is protected within the canula of an SPME extraction unit and can be moved out of the canula for sampling (e.g. after the canula has pierced a septum of a headspace vial). It is possible to sample from both the gas phase or the liquid phase. Thermal desorption in combination with GC and a suitable detector is used for the analysis of the adsorbed substances. Especially, the MIL-class of MOFs showing aqueous stability was investigated for their usage as SPME materials. [206]–[209] Analytes of interest were chloro-aromatics, BTEX (benzene, toluene, o-, m- and p-xyelene as well as ethylbenzene) compounds and polycyclic aromatic hydrocarbons (PAHs), pesticides as well as synthetic musks.

In most cases, MOFs are being attached to the fiber using poly dimethylsiloxane (PDMS) or similar adhesives. The extraction of benzene homologues from the gas phase using MOFs as SPME adsorbent was demonstrated using HKUST-1 as a hydrothermally grown film. A high fiber-to-fiber reproducibility (RSD was below 10%), enrichment factors for over 19,000 for benzene and over 110,000 for p-xylene were reported. Detection limits ranging from 8.3 to 23.3 ng l^{-1} for all benzene homologues were possible using this method (GC-FID).

2.2 MOFs and sorption

In most cases of application and application-driven research, MOFs are investigated and evaluated due to their porosity and tailorability, i.e. the possibility to synthesize crystalline and chemically defined model systems. Therefore, gas storage and separation were, at least in the early days of MOF research, the most promising fields of research and engineering. [169], [181], [210] Later, concepts for solid-phase extraction, sensing and drug delivery were explored. [211]–[218] Except for some rare cases, all these application fields demand the permanent porosity of MOF structures and/or their specific sorption behavior.

In general, one can distinguish two main sorption processes, dynamic and static sorption processes, at either low or high coverage. Moreover, competitive sorption may occur in relevant environments, where in most cases water adsorption is present, resulting in multi-component sorption, whose investigation is arbitrarily complex. [219], [220] Regarding single component sorption, the sorption process on/in porous materials comprises several steps and species. Figure 12 gives an overview of the main species and processes involved in adsorption processes.

In the nomenclature of IUPAC, the mobile phase is called adsorptive (the guest molecule, e.g. hydrogen), while the solid phase (host material, e.g. active carbon or a MOF) is referred to as adsorbent. Adsorption is a surface-based process. [73], [221], [222] Once being adsorbed on the surface of the adsorbent, the original guest molecule (adsorptive in its non-bound state) is called the adsorbate. This process is related to, but not to be confused with absorption, where a guest molecule (referred to as permeate) is dissolved and/or permeates through a solid (host material), like gaseous water molecules in organic polymers. [223]–[225] The process of permeation can be divided into an adsorption process, followed by a diffusion process. While the first step represents a surface based

related process, the latter refers to the volume of the material. Both processes, however, belong to the class of sorption processes. Desorption describes the process of an adsorbate (or permeate) leaving the surface or bulk material, which is an endothermic process.

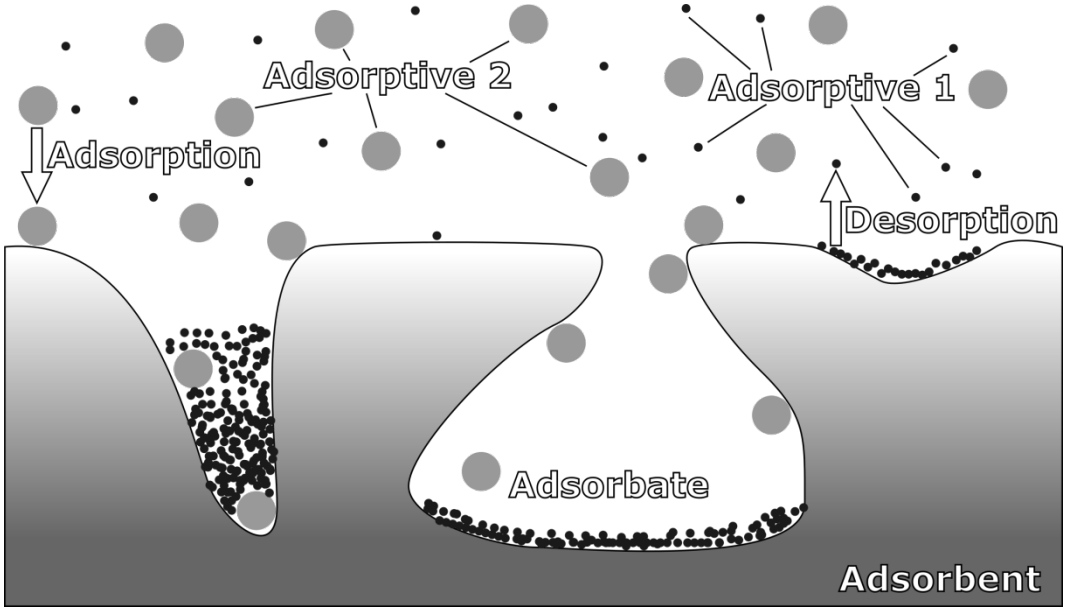

Figure 12. Overview of relevant species and processes in the sorption process.

Generally, adsorption is a direct consequence of the adsorbents surface energy. As compared to a non-porous bulk material, surface atoms lack an atomic or molecular neighboring partner (which they tend to have in the bulk phase) to complement their ionic, covalent, coordinative or metallic bonds potentials. As surface-localized molecules or atoms lack these immediate neighbors, they can attract bypassing guest molecules (adsorptives).

Although the exact composition, compensation and direction of interaction strongly relies on the species involved, the processes may be split into physisorption and chemisorption. While in the former case, only non-covalent interactions (van-der-Waals forces, hydrogen bonding as well as electrostatic forces) steer the thermodynamics of adsorption, in the latter case chemical bonds are formed upon adsorption and must be broken upon desorption. Physisorption features adsorption energies in the range of the enthalpy of

condensation (4 to 40 kJ mol^{-1}), and no change of the surface and adsorbate is observed after desorption. [157], [226] Adsorption energies in case of chemisorption are usually one order of magnitude higher than for physisorption (e.g. 50-500 kJ mol^{-1}) and, in most cases, irreversible. [9], [221]

2.2.1 Thermodynamics of adsorption

During adsorption, the kinetic energy of the guest molecule either leads to its reflection by the surface (elastic in nature) or its kinetic energy (adsorption energy) is transmitted to the adsorbent in case of adsorption. Due to this fact, adsorption represents an exothermic process. If an adsorbed molecule (adsorbate) accumulates enough energy, it may as well leave the surface again, showing the reversible nature of adsorption, mostly found for physisorption processes.

Figure 13 gives an overview of different potential energy curves with respect to adsorptive-adsorbent distances (r). For a flat surface, a common, Morse-like potential can describe the distance-potential energy relationship. [227], [228] With increasing distance from the surface, the potential energy converges to zero due to adsorption. [229]

This is partially fulfilled in a macropore, or when the guest molecules dimensions are negligible as compared to the pore aperture (Figure 13, left). In a mesoporous system, a guest molecule can approach two pore walls on either side resulting in a double-minimum potential (Figure 13, middle).

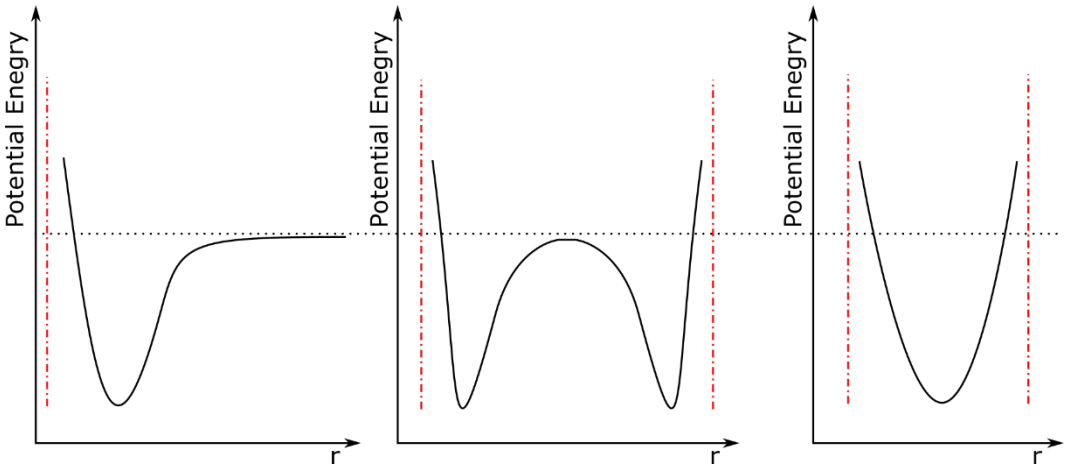

Figure 13. Interaction potentials of an adsorptive and a surface in several pores. Left: a macropore or nonporous surface, middle: mesopores, right: micropore. The distance of the adsorptive towards the adsorbent surface is depicted by r.

In a micropore, or when the guest molecule most tightly fits the pore, only one minimum is found (Figure 13, right). [230] A further distancing (of the guest molecule) from one pore wall (in order to find a lower energy minimum) will result in more repulsive forces from the opposed pore wall, therefore increasing the overall potential energy. If the adsorbent surface is entirely covered with adsorbate molecules, it is referred to as monolayer, i.e. the layer that is formed based on the 1:1 interaction of the adsorbent and adsorbate molecules. Therefore, in case of chemisorption processes, only a monolayer is formed. The next layer is then based on physisorption and adsorbate-adsorbate interaction, which is (except for very reactive adsorptives) non-covalent. Under ideal conditions and the assumption that all interactions are homogeneous, the minimum of these potential energy curves directly refers to the vertical position of the first monolayer.

2.2.2 Adsorption isotherms

Aiming to quantify adsorption processes with various adsorbent/adsorbate combinations, adsorption isotherms are used. An adsorption isotherm is a plot showing the uptake of adsorbate molecules at constant temperature (mostly normalized in terms of 1 g of sorbent) as a function of exerted relative guest molecule pressure (in p/p_0). The

ordinate value is mostly normalized towards 1 g of adsorbent, units may be moles, weight or volume units. The resulting shapes of the isotherms can yield information about the nature of interaction during adsorption, the relative pore-adsorbate dimensions and allow for the calculation of the specific surface area using different theoretical models. According to IUPAC, isotherm shapes can be classified into 6 major types, I to IV (see Figure 14). [231]

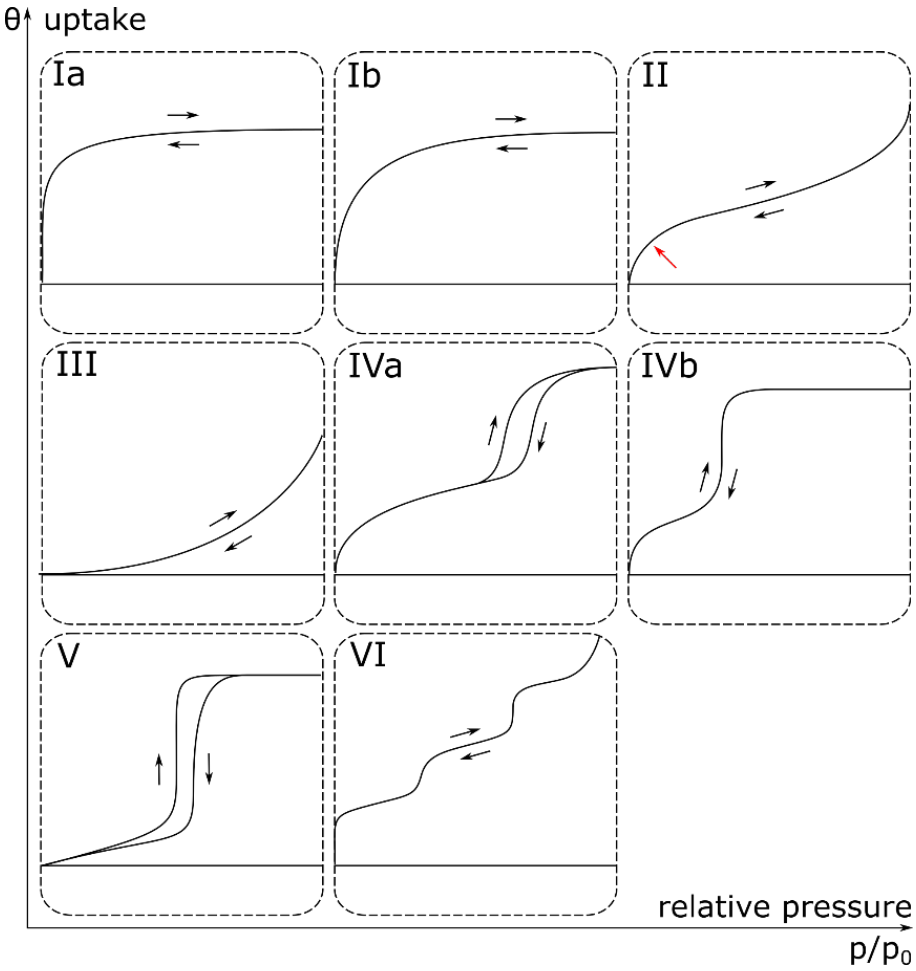

Figure 14. Adsorption isotherm types according to IUPAC. [231] Abscissa represents partial pressure (relative towards saturation vapor pressure, p/p_0) and ordinate the uptake (gravimetric, molar or volumetric, θ).

Reversible type I isotherms show a characteristic concave shape with a horizontal asymptotic limit. They are mostly observed for either chemisorption (e.g. catalyst surfaces) or microporous materials (e.g. zeolites and MOFs). In case of chemisorption, the large increase starting at low pressures is due to a monolayer formed by chemical reaction. After this monolayer is formed, further pressure increase will only result in

adsorbate-adsorbate interaction, being less attractive. In case of microporous materials, this strong increase at low pressures is due to micropore filling, with the asymptotic limit being directly restricted by the accessible pore-volume and an overlap of the potential energy curves (Figure 12, right curve). Further pressure increase will result in adsorbate-adsorbate repulsion. While for narrow micropores, type Ia isotherms are observed for nitrogen adsorption at 77 K, type Ib isotherms are predominant for broader distributed micropores and narrow mesopores.

Type II isotherms, also being reversible in nature, are observed for non-porous or macroporous adsorbents. A knee at lower relative pressures indicates the complete monolayer coverage. At higher pressures multilayers are formed. If for a fictive type II isotherm system adsorbent-adsorbate interactions are low in comparison to adsorbate-adsorbate interactions a type III isotherm is observed. A knee (red arrow in Figure 14) at lower relative pressures is not observed as even before the monolayer coverage local multilayers are formed at energetically preferable sites. Type III isotherms are convex with respect to the relative pressure axis.

Type IV isotherms are typically observed for mesoporous materials, e.g. molecular sieves or porous metal oxides. The adsorption behavior is not only determined by the adsorbent-adsorbate interaction but also by the adsorbate-adsorbate interaction, i.e. molecules in the condensed state. The monolayer-multilayer formation on the mesopores walls, which marks the starting point for further adsorption, is similar as for Type II isotherms (knee). This initial step is followed by pore condensation. The result is the formation of a liquid-like phase within the mesopores below the regular condensation point of the gas (when $p/p_0 = 1$). A characteristic for type IV isotherms is the horizontal asymptotic limit, as for Type I isotherms. In case of a IVa isotherm, a hysteresis loop can be observed when comparing adsorption and desorption isotherms.

The origin of hysteresis is the metastability of multilayers during adsorption, i.e. not being in thermodynamic equilibrium with their environment. As the evaporation process itself does not contain a nucleation step, the desorption curve is equivalent to a (reversible) liquid-vapor or liquid-gas transition. Hence, the desorption branch of a hysteresis loop is in thermodynamic equilibrium if the pores are filled with condensate beforehand. Hysteresis can be observed when the pore aperture exceeds a certain limit, e.g. 4 nm for argon adsorption at 87 K in cylindrical pores. Below this pore size limit, depending on the adsorbate as well as the temperature, a IVb type isotherm is observed. In this case, no hysteresis is observed. Type IVb isotherms are characteristic for conical pores as well as tapered cylindrical mesopores, i.e. mesopores that show smaller access-windows.

Type V isotherms show a shape that is like type III isotherms in the low to moderate p/p_0 region. Weak adsorbent-adsorbate interactions are overlapped by strong adsorbate-adsorbate interactions at higher pressures that will cause adsorbate clustering, followed by pore condensation at higher pressures. A typical example is water adsorption on hydrophobic micro- and mesoporous adsorbents.

Type VI isotherms have a stepwise and reversible progress. They can be observed on highly uniform surfaces, e.g. argon adsorption on graphitized carbon blacks. In this case, the step height directly correspondents to the respective adsorbate capacity of each layer, the gradient of each step transition is depending on the adsorbent-adsorbate combination as well as the temperature.

2.2.3 Isotherm models

As mentioned before, using adsorption isotherms and different theoretical models, the specific surface area (SSA) for a given adsorbent can be calculated. In this work, the model of Brunauer, Emmett and Teller (BET) was used for the calculation of the adsorbents specific surface area. Another, simpler model is the Langmuir model. The simplest model,

that can be used to describe an adsorption isotherm, is a linear model, the Henry isotherm, formally resembling Henry´s law.

$$\theta = K_H \cdot p_G \qquad (1)$$

Where θ is the uptake in mol kg^{-1}, p_G is the adsorptives pressure in Pa and K_H is the Henry constant in . The Henry isotherm is only capable of describing the initial part of an adsorption isotherm correctly. It can also be used to describe systems at low surface coverages. [232] If the surface is heterogenic, adsorbates will interact with the most energetic adsorption sites first. This aspect will be further discussed in the inverse gas chromatography (iGC) section (2.3.1 and 2.3.3). Figure 15 gives a short overview of Henry regions at low pressures, being extended towards a Langmuir and BET isotherm model.

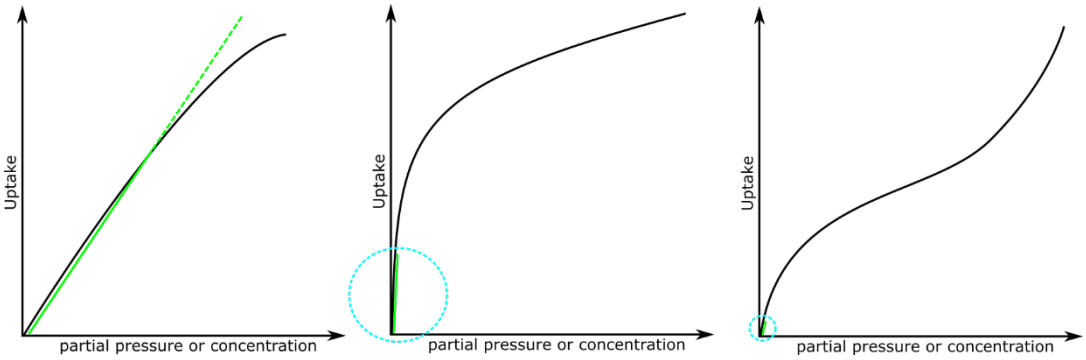

Figure 15. Adsorption isotherm with increasing (from left to right) partial pressure or concentration range. The Henry (linear) region is highlighted with a green line and a blue circle in each area of the isotherm. Left: Henry region with deviations at higher pressures. Middle: Langmuir-type isotherm with Henry region at lower pressures. Right: BET-type isotherm with Henry region in the lower pressure region.

Langmuir isotherm model

In the Langmuir model, a single monolayer adsorption is assumed, i.e. no multilayer adsorption. This monolayer is formed by uniform gas particles, showing no intermolecular interaction, i.e. no adsorbate-adsorbate interaction. After adsorption, the gas molecules are in an immobile state. The adsorbents surface is considered homogeneous. N_m adsorption vacancies exist in total (monolayer), N_i are occupied by adsorbate molecules. The total coverage θ is given by:

$$\theta = \frac{N_i}{N_m} = \frac{[G_{ad}]}{[S_0]} \tag{2}$$

Alternatively, $[S]$ is the concentration of vacant sites (e.g. in $1/nm^2$) and $[G_{ad}]$ is the concentration of adsorbed molecules of G (e.g. in $1/nm^2$). A kinetic derivation of the Langmuir equation uses two equations that describe the adsorption and desorption process:

$$r_{ads} = k_{ad} \cdot p_G \cdot [S] \tag{3}$$

$$r_{des} = k_{de} \cdot [G_{ad}] \tag{4}$$

where r_{ad} and r_{de} are the rate constants for the adsorption and desorption, respectively, p_G is the partial pressure of gas G above the surface. As under equilibrium conditions r_{ad} and r_{de} are equal and both equations may be rearranged to:

$$k_{ad} \cdot p_G \cdot [S] = k_{de} \cdot [G_{ad}] \tag{5}$$

and further simplified towards:

$$\frac{k_{ad}}{k_{de}} = \frac{[G_{ad}]}{p_G \cdot [S]} = K_{eq}^G \tag{6}$$

where K_{eq}^G represents the equilibrium constant for the adsorption of G on the adsorbent. As there is a total concentration of monolayer adsorption sites $[S_0]$, being a sum of $[G_{ad}]$ and $[S]$ the equation becomes

$$\begin{aligned}[S_0] = [S] + [G_{ad}] &= \frac{[G_{ad}]}{p_G \cdot K_{eq}^G} + [G_{ad}] \\ &= \frac{1 + p_G \cdot K_{eq}^G}{p_G \cdot K_{eq}^G}[G_{ad}]\end{aligned} \tag{7}$$

As the coverage ratio is defined by (2), the above term can be rearranged to:

$$\frac{[G_{ad}]}{[S_0]} = \frac{p_G \cdot K_{eq}^G}{1 + p_G \cdot K_{eq}^G} = \theta \tag{8}$$

Inverting this equation, a linearized form of the Langmuir isotherm is established.

$$\frac{[S_0]}{[G_{ad}]} = \frac{1 + p_G \cdot K_{eq}^G}{p_G \cdot K_{eq}^G} \rightarrow \frac{1}{[G_{ad}]} = \frac{1 + p_G \cdot K_{eq}^G}{p_G \cdot K_{eq}^G \cdot [S_0]} = \frac{1}{[S_0] \cdot K_{eq}^G} \cdot \frac{1}{p_G} + \frac{1}{[S_0]} \quad (9)$$

By plotting $\frac{1}{[G_{ad}]}$ vs $\frac{1}{p_G}$ the linear regressions intercept can be converted to $[S_0]$ or N_m, while the slope yields K_{eq}^G. It should be noted that a non-linear regression will generally lead to better fitting results. With the molecular cross-sectional area (CSA) A_G of the adsorbate (also called probe molecule) known, the specific surface area may be calculated:

$$S = [S_0] \cdot A_G = N_m \cdot A_G \quad (10)$$

The Langmuir equation does describe type I isotherms accordingly well. It lacks a quantitative picture for chemisorption, as homogeneity of reactive materials is not given, and reactions only take place at chemically reactive sites. For microporous materials, where the predominant mechanism is the filling of micropores, monolayers and resulting capacities are difficult to determine.

Brunauer-Emmett-Teller (BET)isotherm model

In fact, during physical adsorption at low pressures, the most energetic adsorption sites will be covered first. If the surface is chemically homogeneous, these sites are within narrow pores, where pore wall potentials overlap, i.e. allowing adsorbates to interact with several walls at the same time. Another place where this is possible are edges and steps within the surface.

If the material itself is heterogeneous, e.g. containing heteroatoms (due to impurities) or functional groups, this will also lead to varying adsorption potentials and to possible overlapping sites, being preferred for adsorption. Less energetic sites are also covered with adsorbate molecules at this stage, however, the average residence time is lower as compared to high energy sites. Bypassing adsorbate molecules will hence, with a

particular probability, adsorb on already adsorbed guest molecules. This leads to localized multilayers before the whole adsorbent surface will be covered with exactly one monolayer. [221], [226]

The BET (named after Brunauer-Emmett-Teller) [157] theory extends the Langmuir model by several assumptions. First of all, molecules of the first (localized) layer provide for adsorption vacancies for second and higher layers. Second, the upmost layer of a multilayer (or the first layer of a monolayer) is always in thermodynamic equilibrium with the gas phase and the adsorption enthalpy for a second layer of adsorbate is equal to the latent heat of condensation of the adsorbate. Also, completely vacant sites coexist with mono- and multilayers and the adsorption layer does not exhibit a uniform thickness. Lastly, the adsorbate has liquid like behavior, i.e. near saturation vapor pressure, the vapor condenses as a liquid exhibiting infinite number of adsorbed layers

The Langmuir equation is used as a starting point and further extended.

$$k_{ad} = k_{de} \tag{11}$$

$$k \cdot p_G \cdot \theta_0 \cdot A_1 = N_m \cdot \theta_1 \cdot \nu_1 \cdot e^{-\frac{-E_1}{RT}} \tag{12}$$

$$k = \left(\frac{N_a}{2 \cdot \pi \cdot M \cdot R \cdot T}\right)^{0.5} \tag{13}$$

On the adsorption side of the equation, p_G is the adsorbates vapor pressure, θ_0 is the fraction of unoccupied surface on the adsorbent and A_1 is the condensation coefficient, the probability for a molecule to become permanently adsorbed by the surface after a collision. [221], [233]

On the desorption side N_m is the number of molecules in the monolayer, θ_1 is the surface fraction covered with the first layer (monolayer), ν_1 is the adsorbates frequency normal to the surface. The exponential term represents a probability factor that the adsorbed molecule carries enough energy to overcome the attractive potential of the surface.

For the definition of the factor k, N_a is the Avogadro number, M the adsorbates molecular weight, R the universal gas constant and T the absolute temperature in K.

For the second layer, the kinetic equilibrium would be:

$$k \cdot p_G \cdot \theta_1 \cdot A_2 = N_m \cdot \theta_2 \cdot \nu_2 \cdot e^{-\frac{-E_2}{RT}} \qquad (14)$$

or more general:

$$k \cdot p_G \cdot \theta_{n-1} \cdot A_n = N_m \cdot \theta_n \cdot \nu_n \cdot e^{-\frac{-E_n}{RT}} \qquad (15)$$

BET theory assumes that the variables ν_n, A_n and E_n are constant for the second and following, higher layers, i.e. the adsorption and desorption characteristics of gaseous and liquid nitrogen being constant. For the layers near the surface this assumption may be flawed because of polarization effects, however, for higher layers, it becomes more and more realistic. After the second layer, E is replaced by the heat of condensation E_c. So finally, for the first layer it is:

$$k \cdot p_G \cdot \theta_0 \cdot A_1 = N_m \cdot \theta_1 \cdot \nu_1 \cdot e^{-\frac{-E_1}{RT}} \qquad (16)$$

and for second and higher layers:

$$k \cdot p_G \cdot \theta_{n-1} \cdot A = N_m \cdot \theta_n \cdot \nu \cdot e^{-\frac{-E_C}{RT}} \qquad (17)$$

After several mathematic substitutions and transformation, the BET equation is derived in its final form:

$$\frac{1}{W\left(\left(\frac{p_0}{p}\right)-1\right)} = \frac{1}{W_m \cdot C} + \frac{C-1}{W_m \cdot C} \cdot \left(\frac{p}{p_0}\right) \qquad (18)$$

and the general form, in cases where the pore size limits the number of layers that can be built up:

$$\frac{N}{N_m} = \frac{W}{W_m} = \frac{C}{\left(\left(\frac{p_0}{p}\right) - 1\right)} \cdot \frac{\left(1 - (n+1) \cdot \left(\frac{p}{p_0}\right)^n + n \cdot \left(\frac{p}{p_0}\right)^{n+1}\right)}{\left(1 + (C-1) \cdot \left(\frac{p}{p_0}\right) - C \cdot \left(\frac{p}{p_0}\right)^{n+1}\right)} \quad (19)$$

With W being the surface coverage or amount of adsorbend gas, W_m being the monolayer coverage or the amount of gas adsorbed for monolayer coverage,p the gas pressure, p_0 the saturation gas pressure and C the BET constant, which depends on the temperature and the gas/solid system investigated.Furthermore, in the general form, n depicts the layer number.

with $n \to \infty$ this term is reduced to the above derived form of the BET equation while for $n = 1$ it equals the Langmuir equation. A plot of $\frac{1}{W\left(\left(\frac{p_0}{p}\right)-1\right)}$ vs $\left(\frac{p}{p_0}\right)$ will yield a straight line in the region of $0.05 \leq \frac{p}{p_0} \leq 0.35$. W_m, the weight amount of the monolayer W_m and the BET constant C can be calculated from the intercept i and the slope s of this plot:

$$W_m = \frac{1}{s+i} \quad (20)$$

$$C = \frac{s}{i} + 1 \quad (21)$$

For many microporous materials $0.05 \leq \frac{p}{p_0} \leq 0.12$ is used as pressure range. [234] It is essential that the intercept is positive and that C has a positive, large value. Furthermore, the BET equation fitting should only be done in the range, where the term $n \cdot \left(1 - \frac{p}{p_0}\right)$ continuously rises with $\frac{p}{p_0}$ and the value corresponding to W_m needs to be located within

this selected BET range. Even if all these criteria are fulfilled, the BET surface area from a type I isotherm should not be treated as a realistic probe-molecule derived accessible surface area. Surface areas derived by the BET method provide a useful and adsorbent specific fingerprint in terms of an apparent surface area. [231], [235]–[238]

2.2.4 Kinetics of adsorption

Along with thermodynamic driving forces for adsorption, there are kinetic ones, i.e. how fast involved equilibria are established. A guest molecule within a bulk volume flow enters the laminar zone in the close vicinity of an adsorbent particle (see Figure 16). This process is referred to as film diffusion. In case of a non-porous adsorbent, molecules will diffuse through this laminar film and be adsorbed on the exterior surface area of the adsorbent particle. [239] They exhibit, if not strongly chemisorbed, a specific mobility via surface diffusion.

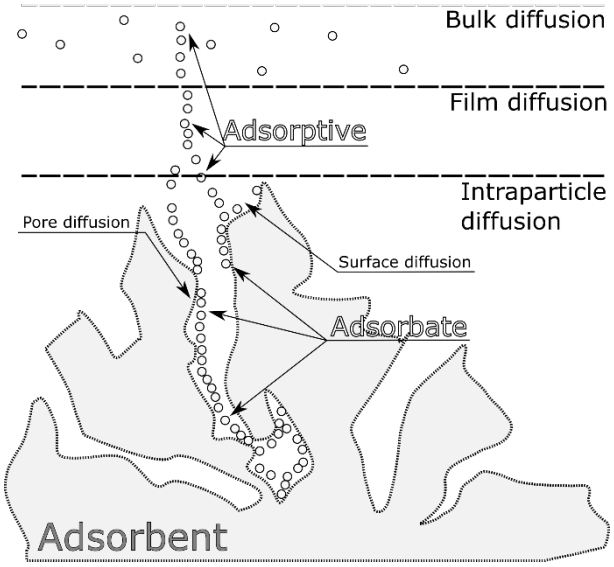

Figure 16. Diffusion pathways for a guest molecule according to [240]. Adsorptives and adsorbates as white, black outlined particles. Interparticle diffusion between multiple particles, beginning beyond intraparticle diffusion regime, is omitted.

If the particle is porous, intraparticle or pore diffusion is possible, where the guest molecule diffuses into the interior pore system of the particle. These phenomena of mass transport can be divided and described using several levels of model theories as

experimental data will always contain a complex interplay of several diffusion regimes. [165], [241]–[246]

Using molecular modelling, intraparticle diffusion constants can be determined by analyzing the root mean squared deviation (RMSD) of a guest molecules position (center of mass) in a framework over time in a molecular dynamics (MD) simulation. [247], [248] Two approaches are possible to determine diffusion constants, either the slope of a RMSD vs time plot or the hopping rate, i.e. the reciprocal difference in time for static positions of the guest molecule in the framework.

Generally, diffusion constants in the bulk phase and the laminar film zone are usually higher as compared to surface diffusion, where an adsorbent is visually hopping between several interaction potentials. In pores, especially narrow pores, the amount of lateral interactions with adsorption sites or rather their interaction potentials are increased leading to even lower diffusion constants. [249]

Separation

The diffusion coefficient or diffusivity for a given adsorbent/adsorbate system is influenced by steric, kinetic and equilibrium mechanisms or factors. The combination of these factors does directly affect the capability of an adsorbent for a separation process of different adsorbates.

Steric separation mechanisms are based on the pore size and geometry of the adsorbent and the guest molecule(s) spatial features. Size exclusion (e.g. in chromatography) as a result of the guest molecules molecular dimensions or minimal molecular diameters being too large for the aperture of the adsorbents pores, represents a classic example for steric factors. [250], [251]

Kinetic factors, often referred to as molecular sieving, are based on the guest molecules exhibiting varying diffusivities in a pore system. The above-mentioned affinity of the guest

molecules towards the adsorbents interaction potential landscape, i.e. high affinities (high desorption barriers) leading to longer local residence (retention) times at these adsorption sites is a major cause for different diffusion constants.

Generally, it can be stated that if steric factors are negligible, the guest-molecules exhibiting a lower affinity towards the adsorbent will show a higher mobility, i.e. diffusion constant in this area or region. Therefore, in a chromatographic set-up (i.e. iGC) they will show lower retention times and specific retention volumes as compared to molecules showing higher affinities and smaller diffusion constants.

A third factor are equilibrium mechanisms. In any adsorption process, depending on the adsorbate capacity of a given adsorbent, equilibrium is reached at a specific adsorbate loading. Both, kinetic and steric effects will combine and determine at which point of an adsorption process this capacity will be exhausted. Together with the adsorption capacity this determines the timeframe that is needed to reach the adsorption equilibrium. [252]

In case of metal-organic frameworks, a different kinetic factor gains importance, namely a structural transition, e.g. the gate-opening mechanism, that is imposed by guest molecules entering the pore system. A transition from a closed and non-microporous to an open microporous system can be observed at specific threshold pressures. [252], [253]

In MOF applications, a complex interplay of all these factors can be observed, e.g. in separation, chromatography and sensing. The following chapter gives an overview of MOF applications with respect to various fields.

2.3 Inverse gas chromatography

Whether being used at industrial scale or for analytical purposes, chromatography exploits the different interaction of guest molecules (probe molecules or analytes in the mobile phase) with a column material (thin layer, packed or liquid layer, the stationary phase). This different interaction (due to different adsorption isotherms and kinetic factors) leads to a different retention behavior for all analytes conducted through the column, finally resulting in their separation. In linear, ideal chromatography, a volume element V is moving though the column with a constant linear velocity u. The volume element V consists of two parts (phase spaces), the mobile phase V_m and the stationary phase V_s (see Figure 17). Their ratio is also called phase ratio β_V, a partition coefficient.

$$\beta_V = \frac{V_m}{V_s} \tag{22}$$

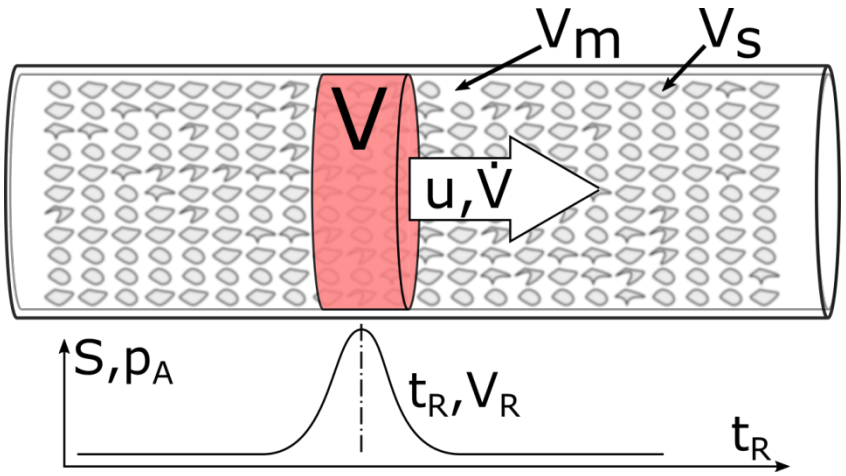

Figure 17. Basic terms in ideal chromatography. Top: mobile phase V_m and stationary phase V_s as well as linear velocity u and volume element V. Bottom: chromatogram with a single Gaussian peak. Retention time (t_R or retention volume V_R by multiplication with volumetric flow $\dot{V}$) on x-axis, detector signal (S, ideally proportional to vapor pressure (p_A) of substance) on y-axis.

The spatial dimension on this volume element is chosen in a fashion that a complete equilibrium between the stationary and mobile phase is reached with respect to the mobile phases residence time in this element. If this is fulfilled, the volume element is

referred to as equilibrium stage or theoretical plate. The concentration profile of any substance is, in the most basic version, a Gaussian bell curve:

$$T(x,t) = e^{\frac{-x^2}{4 \cdot D \cdot t}} \tag{23}$$

T will yield the temporal concentration of a substance with x relating to the spatial coordinate in m, t relating to time in s and D to the diffusion constant in $m^2\ s^{-1}$. However, the signal intensity will drop due to mass conservation. The variance (σ) of a peak can directly be derived from its full width at half maximum (FWHM). It can be used to calculate the amount of separation steps N and the height of a theoretical plate H when the length of the column L is known.

$$N = \left(\frac{t}{\sigma}\right)^2 \tag{24}$$

$$H = \frac{L}{N} \tag{25}$$

The variance, also referred to as second moment of the peak, can be used to assess the column performance and optimize it using e.g. van-Deemter plots. [254] These plots show the relationship of the linear or volumetric flow and the height of a theoretical plate hence can be used to optimize the flowrate. But it can also be used to calculate physicochemical properties of the column material, as the van-Deemter equation contains several components, such as Eddy diffusion, longitudinal and mass transfer resistance terms. These components can individually be disassembled into several sub terms, effectively yielding the diffusion constants of the analyte in the mobile and the stationary phase when several system parameters are known. [254], [255]

The concept of inverse gas chromatography (iGC) – the stationary phase is the material of interest – can also be applied for the first moment of peaks. The first moment (center of mass) or peak maximum (ideally similar when the peak is symmetrical) yield the retention time (or volume) of the respective analyte and column material at a specific

temperature. Depending on the concentration area worked in (infinite dilution of finite concentration), these retention volumes can directly be converted into Henry constants, the linear part of the respective isotherm.

The big advantage of iGC is the straightforwardness and versatility of the method. If several system parameters, like packed column (or capillary column) parameters, temperature and flow are known and chosen appropriate, the retention time will directly yield several thermodynamic and kinetic constants of the system. Figure 18 gives an overview over physicochemical measurements by gas chromatography.

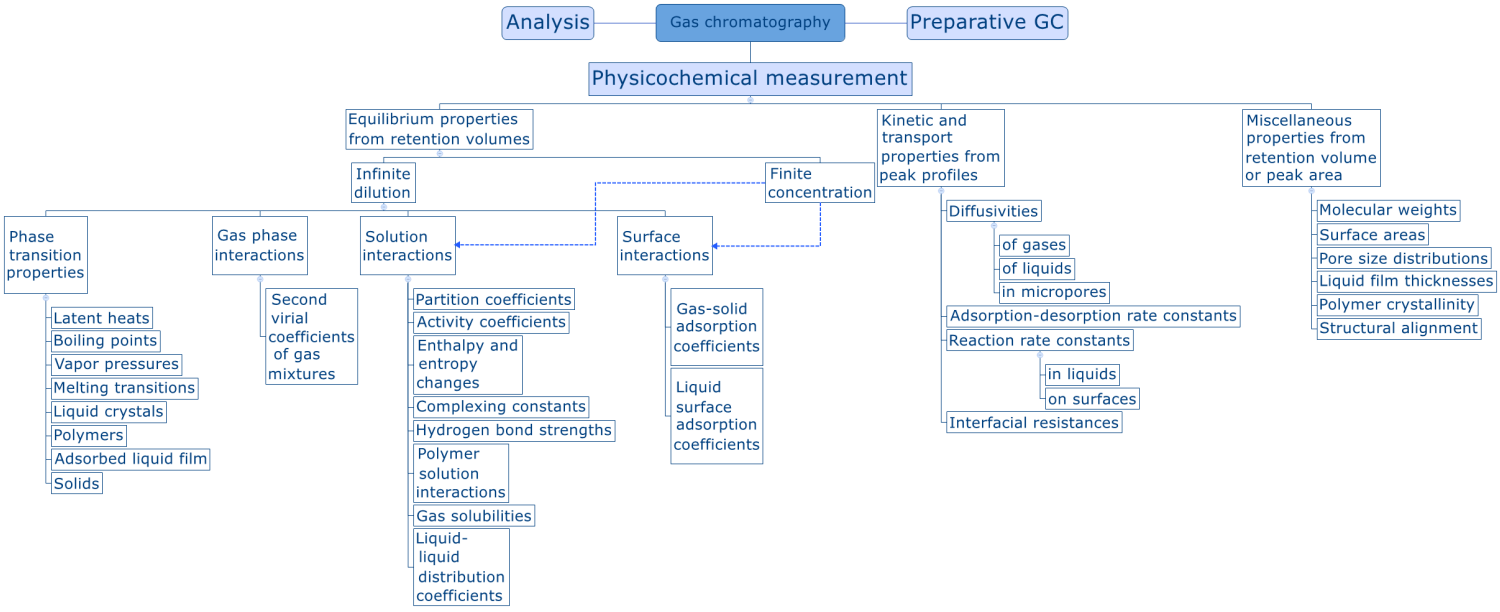

Figure 18. Selected gas chromatography methods overview, according to the overview in [9]. Note that the fields "Solution interactions" and "Surface interactions" can also be characterized using finite concentration methods, as indicated by the blue arrows.

2.3.1 Thermodynamic background

To derive thermodynamic quantities, retention volumes (partition coefficients normalized towards adsorbent mass not volume) must be determined at constant flow for varying temperatures. The relations and equations can be derived from assuming equilibrium conditions (for example the mobile phase behaves like an ideal gas mixture of carrier gas and analyte/probe molecule vapor) and considering chemical potentials for the adsorbed state (μ_s) and the state in the mobile phase (μ_G). [255], [256]

$$\mu_G = \mu_G = \mu^0(T) + R \cdot T \cdot \ln\left(\frac{p_G}{1\ atm}\right) \qquad (26)$$

Where μ^0 is the chemical potential of the adsorbate in its standard state (pure vapor at 1 atm). R denotes the ideal gas constant (8.31 J mol^{-1} K^{-1}), T the absolute temperature in K and p_G the gases absolute pressure in atm. The Gibbs free enthalpy ΔG which would be the result of 1 mol of vapor transferred from its standard state of 1 atm at the experimental temperature T to the adsorbed state (q mol per cm^3 of stationary phase) with the respective pressure p is:

$$\Delta G_{ads} = \mu_s - \mu^0(T) = R \cdot T \cdot \ln\left(\frac{p_G}{1\ atm}\right) \qquad (27)$$

With the partition coefficient (equilibrium constant):

$$K = \frac{mol\ of\ adsorbate\ per\ cm^3\ of\ solid\ adsorbent}{mol\ of\ adsorbate\ per\ cm^3\ of\ carrier\ gas\ at\ column\ T} = \frac{q_s}{c_G} \qquad (28)$$

and the ideal gas law:

$$p \cdot V = n \cdot R \cdot T \qquad (29)$$

$$c_G = \frac{n}{V} = \frac{p}{R \cdot T} \qquad (30)$$

the following relationship between K and ΔG can be established:

$$K = R \cdot T \cdot q_s \cdot e^{\left(\frac{-\Delta G_{ads}}{R \cdot T}\right)} \qquad (31)$$

As the phase ratio β equals K, multiplying K with V_s yields the net retention volume V_N.

$$V_N = R \cdot T \cdot V_s \cdot q_s \cdot e^{\left(\frac{-\Delta G_{ads}}{R \cdot T}\right)} = R \cdot T \cdot n_s \cdot e^{\left(\frac{-\Delta G_{ads}}{R \cdot T}\right)} \qquad (32)$$

Where n_s is the total amount of substance in the adsorbed state.

Further substituting:

$$\Delta G_{ads} = \Delta H_{ads} - T \cdot \Delta S_{ads} \qquad (33)$$

yields

$$V_N = R \cdot T \cdot n_s \cdot e^{\left(\frac{\Delta S_{ads}}{R} - \frac{\Delta H_{ads}}{R \cdot T}\right)} \quad (34)$$

where ΔS_{ads} and ΔH_{ads} are the differential entropy (J mol^{-1} K^{-1}) and enthalpy (kJ mol^{-1}) of adsorption. Logarithmizing finally yields:

$$\ln(V_N) = \ln(R \cdot T \cdot n_s) + \frac{\Delta S_{ads}}{R} - \frac{\Delta H_{ads}}{R \cdot T} \quad (35)$$

Where again, at infinite dilution conditions, the $\ln(R \cdot T \cdot n_s)$ term is negligibly small and can be set to zero.

$$\ln(V_N) = \frac{\Delta S_{ads}}{R} - \frac{\Delta H_{ads}}{R} \cdot \frac{1}{T} \quad (36)$$

This implies that when plotting $\ln(V_N)$ vs. $\frac{1}{T}$ (in 1/K), a linear regression line ($y = c + m \cdot x$, resembling equation (36))best described the scatter plot, as shown in Figure 19. These plots are referred to as van`t Hoff plots. Both the enthalpy (ΔH_{ads}) and entropy (ΔS_{ads}) of adsorption can be calculated by multiplication with the negative or positive value of the ideal gas constant ($\Delta H_{ads} = m \cdot -R$ and $\Delta S_{ads} = c \cdot R$).

It should be noted that adsorption enthalpies derived by this method are differential ones (defined for constant pressure and temperature). Due to adsorption processes not taking place at constant pressure, they need to be converted into an isostere (at constant coverage) adsorption enthalpy. This adjustment can be realized by adding $R \cdot T_{av}$, with T_{av} being the average experimental temperature, to $\Delta H_{ads,diff}$. [257]–[259] However, as the deviation is around 3 kJ mol^{-1} at 100 °C and this correction is usually not considered in most papers dealing with iGC and MOFs [260]–[262], it was also not done in this work to ensure for a better comparison on a standardized basis.

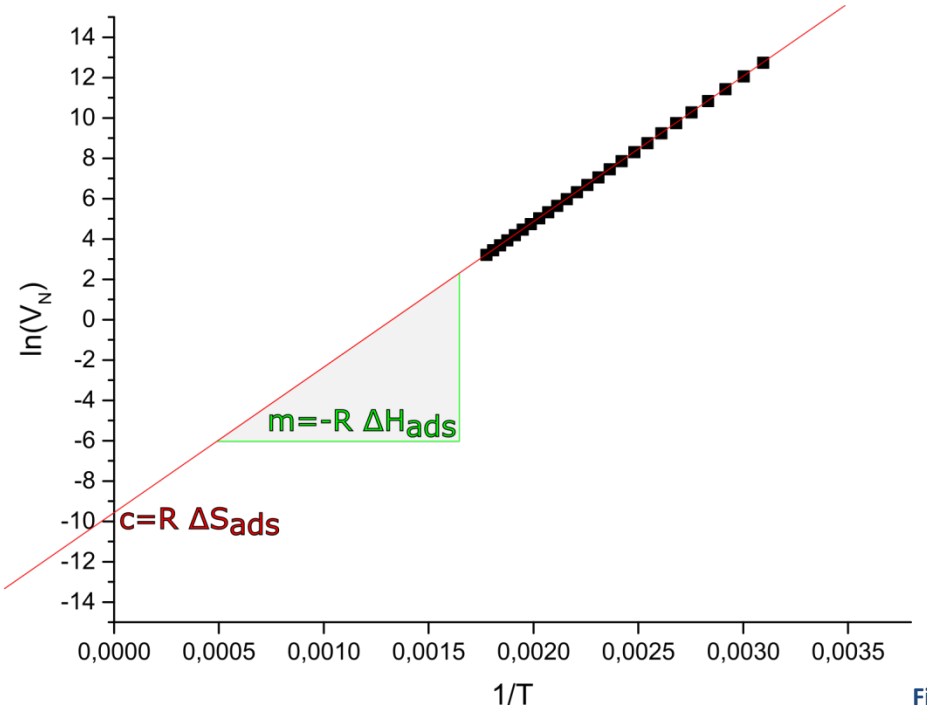

Figure 19. Example van`t Hoff plot for the determination of ΔH_{ads} ad ΔS_{ads} by linear regression from an equidistant temperature series.

This relationship assumes that ΔH_{ads} is constant with respect to temperature, hence it is only valid in a specific temperature region. For different materials, deviations from the linear trend in van´t Hoff plots can be used to determine structural changes, e.g. the glass transition temperature for polymers. [263], [264] If the constancy for ln (V_N) vs. $\frac{1}{T}$ is assured, ΔH_{ads} and ΔS_{ads} can be used to extrapolate retention volumes to e.g. room temperature, which would result in very long and unfavorable retention times causing peak broadening due to diffusion and hence loss in signal intensity.

2.3.2 Calculation of thermodynamic quantities and surface energies

Retention volumes

If adsorption equilibrium can be verified with the chosen flowrate, the specific retention volume (dead time corrected and normalized with respect to sorbent mass) can be calculated as follows:

$$V_N = \frac{j}{m} \cdot \dot{V} \cdot (t_R - t_0) \cdot \left(\frac{T_C}{T_{MFM}}\right) \quad (37)$$

$$j = \frac{3}{2} \cdot \left(\frac{\left(\frac{p_i}{p_0}\right)^2 - 1}{\left(\frac{p_i}{p_0}\right)^3 - 1} \right) \quad (38)$$

where j depicts the James Martin [9], [265] pressure drop correction, t_R and t_0 the retention times of the analyte and methane after injection (dead time in min), T_C and T_{MFM} the GC-column and mass flow meter temperatures (K), $\dot{V}$ the carrier gas flow (in ml min^{-1}) and m the packed-bed sorbent mass. For dead time correction, a substance that will show no significant retention is chosen, in most cases noble gases or methane.

The James Martin pressure drop correction j is needed to convert the carrier gas volume from one thermodynamic state (before the packed bed) to another one (after passing the packed bed) and is calculated as shown in (38), where p_i denotes the inlet and p_o the oulet pressure. [265]

Retention volumes represent a volume for a specific substance on a specific sorbent at a given temperature and are expressed in terms of volume of carrier gas that is needed to elute the analyte in a packed bed (using 1 g of sorbent) to its peak maximum, e.g. ml g^{-1}.

Specific net retention volumes V_G^0 at infinite dilution can be converted to Henry constants (K_C) by assuming ideal gas behavior for each analyte. Conversion of V_G^0 to more familiar units of K_C ( ) is done through the application of (39) in which R represents the universal gas constant and T_C the experimental column temperature. [9], [255]

$$K_C = \frac{V_N}{R \cdot T_C} \quad (39)$$

Flowrates at experimental conditions $\dot{V}_{exp}$ can be converted to normal flows $\dot{V}_{norm}$ (given in ml_n min^{-1}) when the experimental temperature T_{exp} and experimental pressure p_{exp} are known.

$$\frac{p_{exp} \cdot \dot{V}_{exp}}{T_{exp}} = \frac{p_{norm} \cdot \dot{V}_{norm}}{T_{norm}} \quad (40)$$

$$\dot{V}_{norm} = \frac{p_{exp} \cdot \dot{V}_{exp} \cdot T_{norm}}{T_{exp} \cdot p_{norm}} \quad (41)$$

with T_{norm} 0 °C and p_{norm} 1 atm, i.e. $1.013 \cdot 10^5$ Pa. For clarity, flowrates in the results sections (4.1 and 4.2) are provided in $ml_n\ min^{-1}$.

Enthalpy and entropy of adsorption

As explained in 2.3.1 and shown in (36) plotting ln (V_N) vs. $\frac{1}{T}$ (van't Hoff plot) will yield a linear relationship if ΔH_{ads} is independent from T in the chosen region. A linear regression ($y = m \cdot x + c$) will yield values and errors for both, ΔH_{ads} ($\Delta H_{ads} = m \cdot -R$) and ΔS_{ads} ($\Delta S_{ads} = c \cdot R$).

Specific and non-specific interaction

As already explained in section 2.2.1 and 2.2.4, a whole range of different interactions collude during adsorption, depending on the chemical structure of adsorbate and adsorbent. They are embodied in the respective retention volume at the given temperature or in the free enthalpy of adsorption. The standard free enthalpy change of adsorption, ΔG_{ads}, can be calculated from V_G^0 and the column temperature T_C using (42). The constant C depends on the reference state chosen (e.g. de Boer for ideal vapors and ideal adsorbed vapors). [266], [267] The respective free enthalpy of adsorption at temperature T resembles the linear combination of respective adsorption enthalpy and adsorption entropy at a specific temperature (equation (43)).

$$\Delta G_{ads} = -R \cdot T_C \cdot ln(V_N) + C \quad (42)$$

$$\Delta G_{ads} = \Delta H_{ads} - T\ \Delta S_{ads} \quad (43)$$

In general, interaction of an adsorbate with the adsorbent may be split into a non-specific and a specific term, see (44). The non-specific term is caused by London-dispersion interactions that are represented by adsorbent interaction with linear alkane probes. Specific contributions are caused by hydrogen bonding, π-π or acid-base interactions as well as Keesom and Debye interactions.

$$\begin{aligned} |\Delta G_{ads}| &= |\Delta G_{\text{interaction}}| \\ &= |\Delta G_{\text{specific}}| + |\Delta G_{\text{non-specific}}| \end{aligned} \tag{44}$$

When the non-specific component of the free enthalpy of adsorption is known, the specific component can be calculated by subtracting the free enthalpy of adsorption caused by a hypothetical probe molecule, that is only showing a non-specific, i.e. dispersive, interaction with the stationary phase. Non-branched, linear alkanes are regularly used to determine the non-specific component of the surface energy.

To provide for regression, an x-axis needs to be defined. In case of alkanes, this may be the carbon number (N_C), as many properties of n-alkanes are neatly correlated with it (polarizability, vapor pressure etc.). In case of non-alkane systems (cyclic, branched or aromatic systems) there are different descriptors used for the x-axis. While the Brookman and Sawyer method uses the boiling point T_b and the Papirer method uses the logarithmised vapor pressure ln (p_{vap}) , the Schultz method uses the cross sectional area and the liquid probe surface tension dispersive component ($a \cdot \sqrt{\gamma_L^d}$). [268], [269]

Specific energies can be used to determine the influence of functional groups, classify steric features (so called nano roughness when comparing linear and branched alkanes), acid and base donor and acceptor numbers and determine empirical factors by linear free energy relationships. [53], [219], [258], [261], [268], [270]

Dispersive component of the surface energy

The dispersive part of the surface free energy can be calculated using the method of Dorris and Gray. [271] It expresses the potential of a solid to undergo London or dispersive types of interactions. It is in general more sensible to small changes on the solid surface, e.g. its morphology than the enthalpy of adsorption.

Practically, several linear alkanes are injected and their respective retention volumes plotted according to (45).

$$\gamma_S^D = \frac{\left(G_{CH_2,n+1} - G_{CH_2,n}\right)}{4\,\gamma_{CH_2}\,N\,A_{CH_2}^2} \qquad (45)$$

where $G_{CH_2,n+1}$ is the free energy of adsorption of a n-alkanes with a carbon count of n + 1, N is the Avogadro number, $A_{CH_2}^2$ is the area occupied by one methylene group (0,06 nm^2), γ_{CH_2} is the surface tension of a surface consisting of CH_2 groups (mJ m^{-2}), which is temperature dependent. [260]

$$\gamma_{CH_2} = 35{,}6 + 0{,}058\,(20 - T) \qquad (46)$$

2.3.3 Deviations from the Henry region

Isotherm curvature

As explained in the isotherm section (2.2.3), the Henry region represents the part of the isotherm, where it is most closely resembled by a linear model, i.e. a straight line with the slope being the Henry constant. Resulting peaks at infinite dilution (zero coverage or Henry region) should by symmetric. The middle graph in Figure 20 shows a peak that is caused by a linear adsorption isotherm. The two other cases of concave and convex curvature leads to peak fronting and tailing, respectively. With smaller gas phase concentrations (c_G) both curvatures approach the linear Henry region (quasi-linear

range). Note that tailing and fronting are both accompanied by shift in the peaks center of mass (first moment) with respect to the linear-isotherm peak.

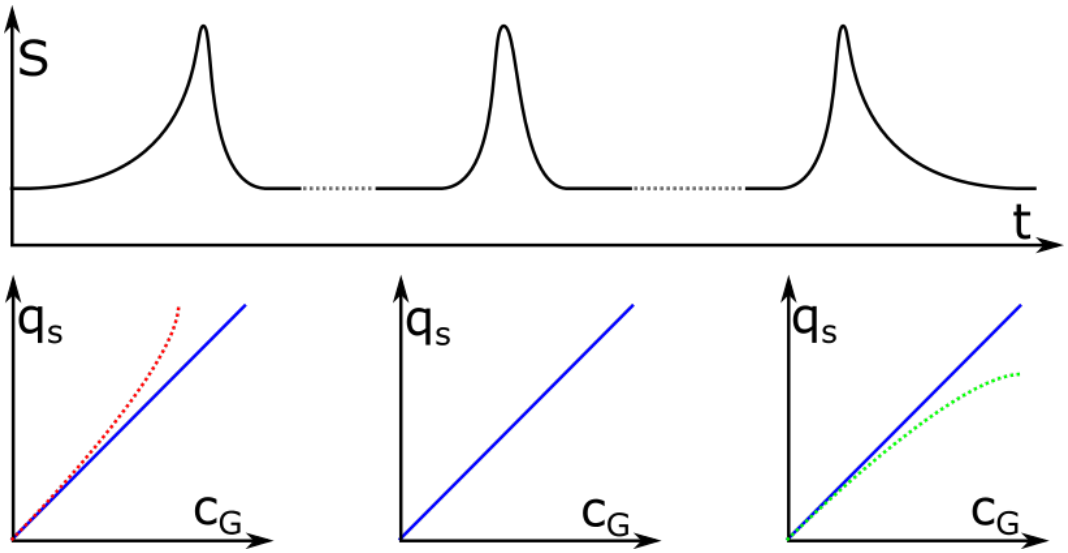

Figure 20. Influence of the isotherm shape (mobile phase concentration c_G and stationary phase concentration q_s) on the peak shape (time t and signal S). A concave curvature (left, $K= q_s/c_G$ increases with c_G) leads to peak fronting (left), while a convex curvature (right, $K= q_s/c_G$ decreases with c_G) leads to peak tailing (right). The middle picture displays a peak originating from a linear isotherm, where $K= q_s/c_G$ is constant with respect to c_G. A symmetrical peak is the result.

Two main factors cause the deviation from a linear isotherm shape, namely adsorbate-adsorbate interactions and non-homogeneous materials. Figure 21 gives a qualitative overview of different interaction energies with respect to coverage.

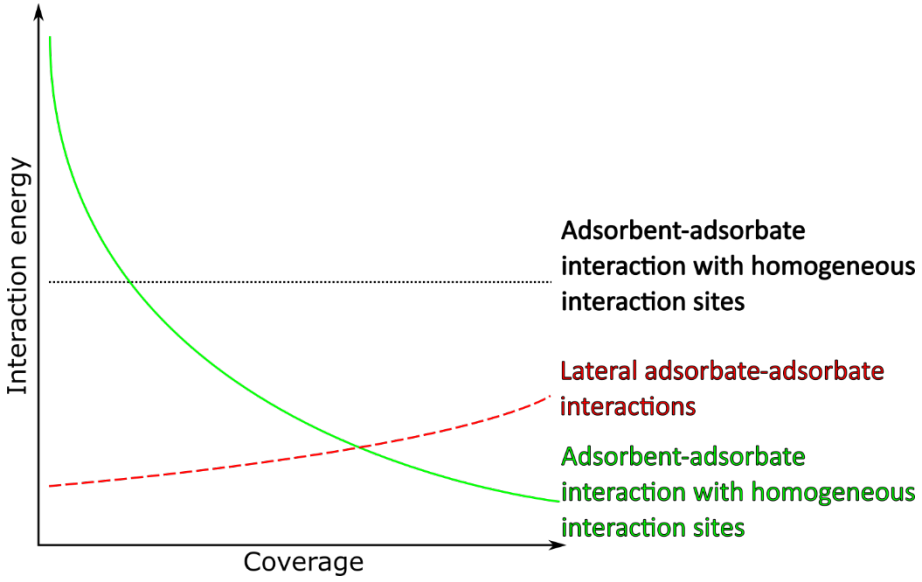

Figure 21. Schematic view of various components of interaction energy as a function of adsorbent coverage.

Adsorbate-adsorbate interactions may cause both isotherm curvatures, given that adsorbate-adsorbate interactions may be attractive or repulsive. In fact, a mixture of both will be observed experimentally.

A homogeneous material features a constant distribution of surface energy or interaction potentials. Mobile phase contained molecules (red dot in Figure 22) will interact with several interaction sites, i.e. adsorb and desorb, while passing through the column. The net retention time is simply the sum over all microscopic retention times with respect to location and time. In Figure 22, the retention time would simply be $3 \cdot t_s$.

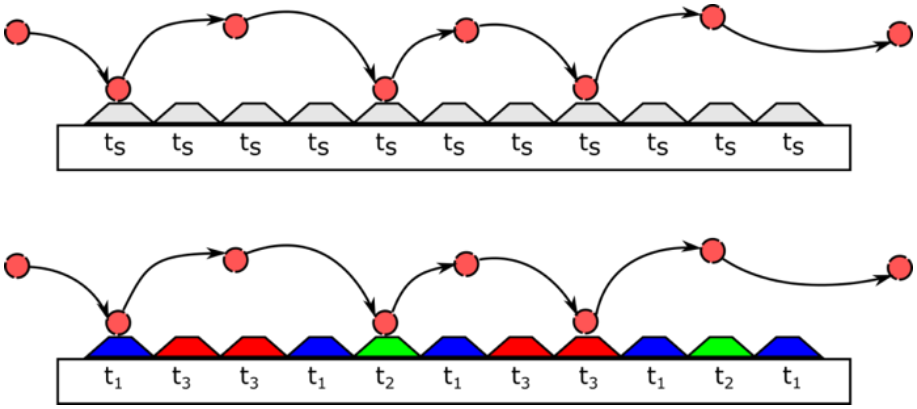

Figure 22. Schematic representation of interaction with molecules from a mobile phase molecule (red circle) on a homogeneous adsorbent featuring an equal surface energy distribution (top) and a heterogeneous adsorbent featuring several discrete adsorption sites with different surface energies (bottom).

At higher loading this picture will not change unless adsorbate-adsorbate interactions are to be considered, i.e. beyond the Henry region. For a heterogeneous adsorbent, the surface energy distribution shows rather discrete levels than continuity. A bypassing molecule will statistically interact with all adsorption sites, resulting in a total retention time of (in this case) $1 \cdot t_1 + 1 \cdot t_2 + 1 \cdot t_3$. Supposed that adsorption sites marked green will show the largest microscopic retention time t_3 but their ratio is the smallest (2 of 11), these adsorption sites will shape the retention behavior at low coverage (low mobile phase concentration). However, if the concentration is further increased, the other adsorption sites will contribute more to the overall retention, as their percentage is higher (9 of 11).

As an isotherm curvature (relative to the linear Henry isotherm) causes fronting or tailing, the Henry region can be confirmed by multiple injections with different injection volumes. If the first moment of the peak (center of mass) and the peak maximum does not shift significantly, the infinite dilution condition can be verified. As tailing may occur due to dead volumes in the GC system, the first moment or maxima shifting of peaks is the most reliable way to confirm this condition. [9], [255], [272]

Using iGC at finite concentration, the Henry region of the isotherm is gradually vanishing and increasingly more adsorption sites contribute to the overall peak shape (first, second and third moment). The afore-mentioned distribution of surface energy levels can be calculated by deconvolution of chromatographic peaks, when the single substance isotherms are known. [272]–[276]

Beyond the region of infinite dilution, not only the interaction with the high energy (causing high retention) sites, but also the interaction with other adsorption sites, determines the retention volume and peak shape. Consequently, not only the sorption behavior in the Henry region of the adsorption isotherm can be derived via iGC, but also the region at higher coverage. These isotherm measurements can be done using either a single pulse for each concentration – determining the respective retention time for each injection – or by one single injection (elution of a characteristic point, ECP). [277], [278]

This method can also be extended if a molecule series (e.g. alkanes for the determination of γ_S^D) is used instead of a single molecule. This way it is possible to determine the dispersive surface energy as a function of coverage. [279], [280] This is also possible for other material properties, such as donor and acceptor numbers or specific components of interaction.

Flowrate

Flow rates must be chosen to allow for equilibrium establishment. Therefore, the invariance of retention volume with respect to flowrate must be verified. Due to the connection V_N *and* $V_R \sim \dot{V} \cdot t_R$, t_R will have a hyperbolic shape when plotted vs. $\dot{V}$, but V_R will show a linear (ideally slope of 0) relation towards $\dot{V}$. Figure 23 shows several important parameters behavior with respect to $\dot{V}$. The hyperbolic relationship between t_R and $\dot{V}$ is shown as well as, for the larger scale with hypothetical high flow rates, its convergence towards the dead time, t_0. [9], [52], [281]

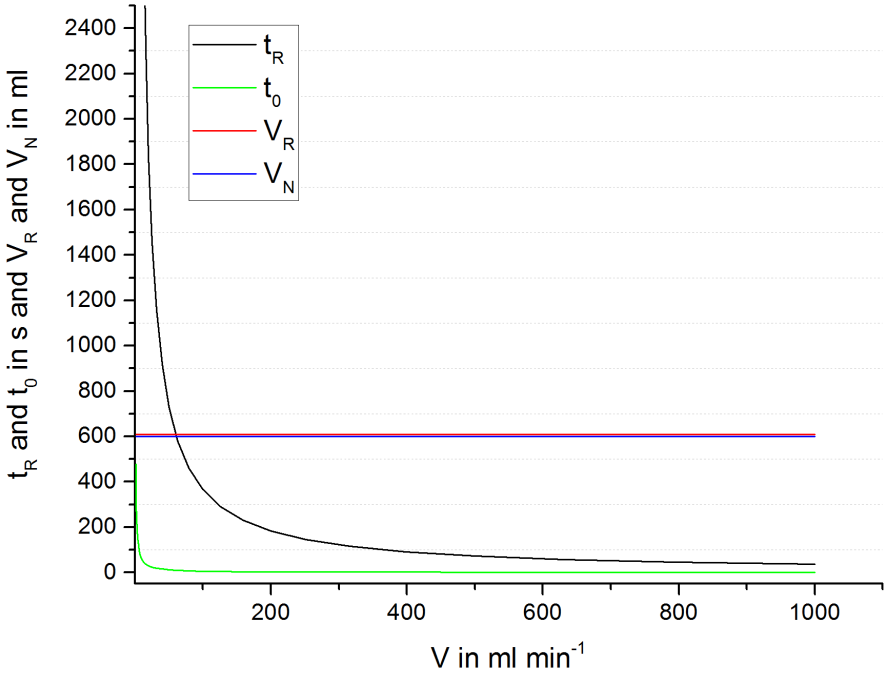

Figure 23. Hypothetical plots for the behavior of retention time (t_R), retention volume V_R, specific retention volume (V_N, (t_R-t_0) multiplied by volumetric flow) and dead time (t_0) as a function of volumetric column flow. Parameters: net retention volume (V_N = 600 ml), dead time (dead volume V_0 = 10 ml) James-Martin correction factor (j = 0.629) Column temperature (T = 473 K), flowmeter temperature (298 K). It can be seen that for large values of flow (right part of graph), t_R converges towards the dead time t_0.

This picture is idealistic and assumes that mass transfer happens on an infinitely fast scale. Under real conditions, deviations from the trend of V_N and V_R with respect to flow will be seen, especially if the chosen flow is too high.

Figure 24 shows a plot of the retention time t_R versus the reciprocal volumetric flow $\dot{V}^{-1}$. For the case of $\dot{V}^{-1}$ approaching zero, i.e. infinite volumetric flow, t_R becomes the dead

time t_0, as the timeframe for substance-specific retention is zero. For the case of $\dot{V}^{-1}$ approaching infinity, i.e. the volumetric flow approaching zero, the retention time is merely diffusion controlled, effectively leading to t_R becoming the t_{diff}. Within both extremes, a linear dependency of retention time and reciprocal volumetric flow is observed. The linear fits slope will directly yield the retention volume.

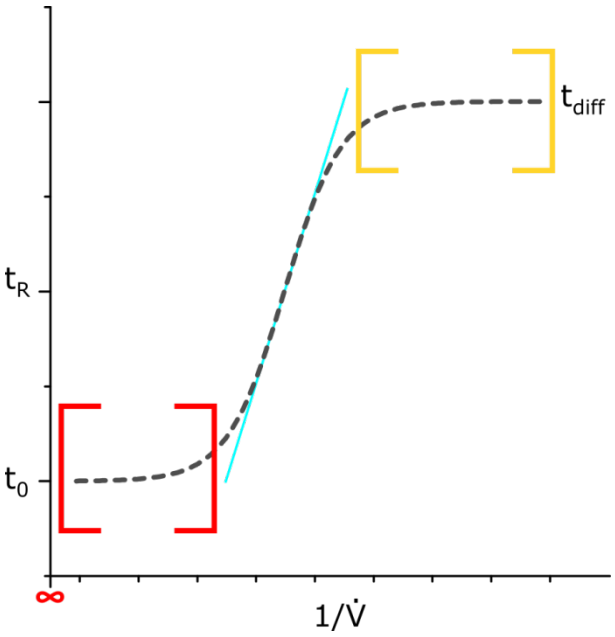

Figure 24. Schematic plot of retention time t_R vs. reciprocal volumetric flow. At infinite flow (red bracket), the retention time converges towards the dead time t_0. At zero flow, no retention occurs and mass transport is established by diffusion (yellow bracket). In the linear region (cyan line) the retention volume is simply the slope of the line.

3 Experimental section

This experimental section gives an overview of the methods and materials that were applied for the generation of the two main results chapters (4.1 and 4.2). The section is therefore subdivided into two main sections.

3.1 Preconcentration of nitro alkanes with archetype 1st generation MOFs

MOFs and Tenax were obtained from Sigma Aldrich in standard quality, Tenax was purchased as 60/80 mesh sieving fraction. All samples were characterized using thermogravimetric analysis (TGA), specific nitrogen surface area (BET-model) and X-Ray powder diffraction (XRPD) as well as particle size distribution (dynamic light scattering) prior to iGC-investigations. Details on these methods are shown in the following section (3.1.1).

Using iGC at infinite dilution (Henry region) retention volumes of various sorbent-analyte combinations at temperatures between 50 and 200 °C were obtained. They were used to calculate physicochemical properties whose underlying equations are shown in section 2.3.2. Temperature ranges of 100 to 200 °C were used to investigate alkane probes retention volumes. Further details on the GC instrumentation are also given in this section (3.1.2).

3.1.1 Adsorbent pre-characterization

As no information on purity was available all materials were pre-characterized before iGC investigations.

X-ray powder diffraction analyses data were collected on a D8 Advance from Bruker AXS, equipped with a copper tube, two 2.5° Soller collimators, anti-scatter screen, flip-stick stage and silicon strip detector in an angular range of 5, 10 or 12.5 to 65 °2θ with a step

size of 0.06°2θ. A crystallite size derivation method via XRPD peak widths is shown in [282].

A particle size distribution (PSD) was calculated as well. Dynamic light-scattering in heptane was used to obtain individual PSDs. Samples were sonicated for 10 minutes prior to measurement. Values for A100 differ from Basolite datasheets and may be attributed to agglomeration if a different solvent was used for PSDs.

For surface area determinations, all samples were prepared with a Quantachrome XeriPrep activation station at a pressure of p = 10^{-5} mbar at 200 °C for 24 h. Analyses were carried out on a Quantachrome Autosorb iQ-MP-C-System with N_2 (Linde AG, 5.0) at 77 K. For Basolites Z1200, C300 and F300, the analysis was performed according to pressure table selection for points between p/p_0 = 0,001 and p/p_0 = 0,1, while for A100 the analysis was carried out with the VectorDosing routine within the pressure range of p/p_0 =5 10^{-5} and p/p_0 = 0,2. Suitable points for multipoint BET analysis were selected with the Micropore-BET-Assistant tool and according to the Rouquerol method for microporous systems. Linear fit qualities were in all cases at least 99.98%.

Thermogravimetric analysis was done on a TGA Q5000 from TA instruments with a heating rate of 10 K min^{-1} up to 700 °C in an air atmosphere. Samples were not thermally activated prior to measurements.

IR spectra were recorded between 650 and 4000 cm^{-1} at a resolution of 4 cm^{-1} accumulating 64 scans using a diamond ATR/FT-IR spectrometer (Thermo Nicolet 6700; ATR-Durascope) with an MCT detector.

3.1.2 Inverse gas chromatography investigations

MOF powder samples were packed into inert GC-injector liners with varying inner diameters. They were plugged on both ends using silane-treated glass wool (Restek) to prevent any loss of sorbent mass during experiments. In most cases, 2 mm inner diameter

packed columns were used. All packed columns were placed in a MARKES Tube conditioner for at least 24 hours at 150 °C and a pressurized nitrogen flow at 1.2 bars (absolute) before being mounted into the iGC system. Nitrogen 5.0 was used as carrier gas without further purification. Conversions of experimental flowrates to $ml_n\ min^{-1}$ are shown in section 2.3.2.

An iGC system scheme is shown in Figure 25. Gas samples were passed through the tubings (inert steel tubing 1/16“) to the packed bed where substance-related retention occurs.

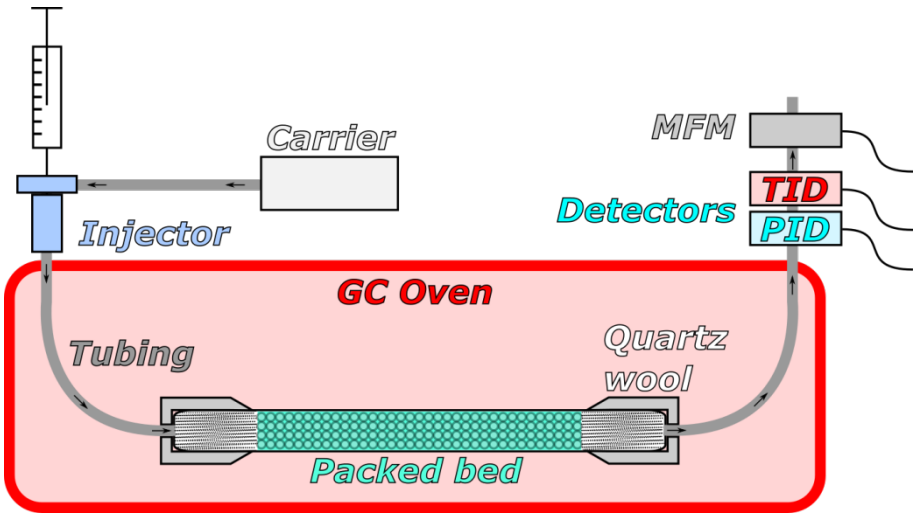

Figure 25. Schematic depiction of the iGC set-up. Vapor samples of probe molecules are injected in the carrier gas flow using a gastight syringe. They are conducted through the packed column bed (fixed with quartz wool) where the substance specific retention occurs. The probe molecules concentration is monitored using two sensors, a photoionization (PID) or thermionic ionization detector (TID) after the packed bed. The column flow is determined using a mass-flow meter (MFM) after the detectors. Pressure sensors (before and after packed bed) and electronic pressure controller (before injector) omitted for clarity.

After passing the packed bed, samples were carried to a detector system consisting of a photoionization detector (PID), a thermionic ionization detector (TID) and a thermal conductivity detector (TCD). These detectors were used to monitor analyte concentrations over time. An electronic gas-flow meter was mounted before the systems exhaust to measure overall carrier gas flow in the system. Methane 5.5 was headspace injected to determine total net retention times for every packed column.

After being heated to a suitable temperature (20-30 °C below their boiling point) in headspace vial, vapor samples of analytes (see Table 1) were collected via a headspace syringe. Typically, volumes of 50 µl were introduced into the gas flow via an injection port. Analytes were purchased from Sigma Aldrich in p.a. or analytical standard quality. Properties such as boiling point, molecular weight and heats of vaporization for all probe molecules used are given in Table 1.

Table 1. Probe molecules used in this study, sorted by analyte family. Boiling point (T_b) in °C, molecular weight (M_W) in g mol^{-1}, standard heat of vaporization (ΔH_{vap}) in kJ mol^{-1}.

Name	short	family	T_b	M_W	ΔH_{vap}	Reference
Methane	CH4	aliphatic	-161.49	16.04	8.6	[283]
Pentane	C5	aliphatic	36.1	72.15	26.1	[283]
Hexane	C6	aliphatic	69.1	86.18	31.5	[283]
Heptane	C7	aliphatic	90.1	100.21	36.1	[283]
1-Nitropropane	1NP	nitro	132	89.09	42.6	[283]
2-Nitropropane	2NP	nitro	120	89.09	40.9	[283]
Nitroethane	NE	nitro	114	75.07	41.3	[284]
Nitromethane	NM	nitro	101	61.04	38.3	[285]

For the monitoring of analyte concentrations during iGC investigations two detectors were used: A photoionization detector (PID) for hydrocarbons and a thermionic ionization detector (TID) for nitroalkanes.

Photoionization detectors (PID) use a UV lamp (usually 10.6 eV, Kr MgF_2) to ionize analytes. Analyte molecules passing this UV lamp are ionized and may undergo reactions, fragmentations and rearrangements. After being ionized, the ions pass a collector electrode. By measuring its current corresponding analyte concentrations (over a region from several ppbs to several hundreds of ppm) can be monitored. As methane (used for dead volume determination) cannot be ionized by a 10.6 eV photodiode (even at temperatures of 200 °C) a negative peak is observed. Generally, this detection process is assumed to be reversible. [286], [287]

Thermionic ionization detectors (TID) are a special case of nitrogen-phosphorus detectors (NPD). A special alkali salt bead is heated to several hundred degrees and the column outlet (N_2 or air) is mounted face-to-face with it. After thermal ionization on the surface current measurements on a nearby collector electrode directly refers to analyte-ion concentrations. This process is assumed to be only partially reversible due to the high thermal part of ionization and possibility of subsequent catalytic surface reactions after on the bead. [288], [289]

In order to establish the required flow through the packed bed of MOF, the carrier gas pressure needs to be adjusted for each MOF-temperature combination. Flows of 9.2 ml of nitrogen per minute can be achieved without the pressure drop exceeding 0.2 bar. A variation of retention volumes with carrier gas flows are seen between 9.2 and 46.1 ml_n min^{-1} and 46.1 to 92.1 ml_n min^{-1}. It is evident that even at flows of 9.2 ml_n of nitrogen per minute, gas-solid equilibrium is not entirely obtained but the influence is negligible.

In one case a pressure drop of more than 2 bar along the packed column was achieved, which led to about the double amount of retention volumes. This effect may be due to leaving the linear region of the adsorption isotherm or delayed mass transfer effects. Regularly, calculated James-Martin correction factors are assumed to compensate for this. [290] However, in this case a compensation was not possible. These values were thus excluded for later calculations and comparisons. Generally, this shows that each parameter needs to be evaluated and picked carefully prior to measurement series.

It is recommended to place pressure sensors before and after the column and to observe them carefully. During temperature programs or temperature series thermal expansion of e.g. **ZIF-8** at higher temperatures occurs. After cooling, micro channels may occur in the packed bed, resulting in lower retention times as only convective transport is occurring. A possibility to overcome this is determining the retention volume and peak shape of a

sample standard (whose retention time on **ZIF-8** is well known and reproducible) in order to confirm the packed column's integrity.

3.1.3 Micro breakthrough and thermal desorption investigations

Micro breakthrough investigations were done using a similar setup as shown for iGC. The injector part was replaced by a nitromethane reservoir of constant concentration in nitrogen carrier gas (Figure 26, left).

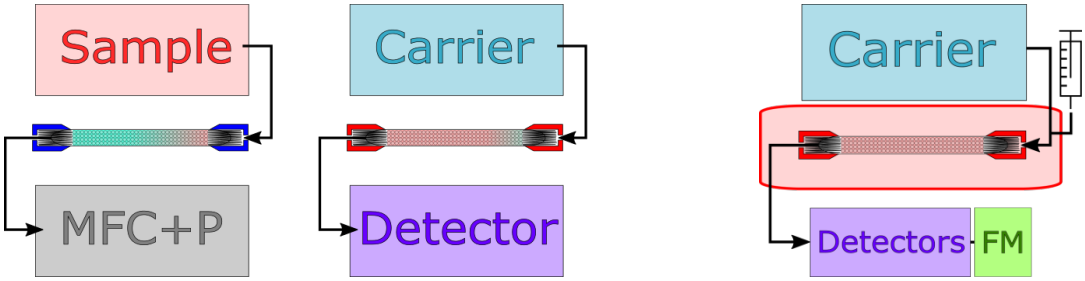

Figure 26. Left: Scheme of sampling (left) and thermal desorption set-up (right). "MFC+P" depicts a mass-flow-controller in combination with a pump, "Sample" refers to the gas-sampling bags and "Carrier" refers to carrier purge gas, controlled by a mass-flow-controller. Right: Simplified schematic (detailed schematic in Figure 25) of an iGC set-up using a carrier gas, injection port, an oven to heat the packed bed followed by detectors and a flowmeter (FM).

The packed beds exhaust was connected to a mass-flow controller and a vacuum pump to conduct the nitromethane enriched carrier gas through the packed bed. Standard gas sampling bags ("Supel™ Inert Multi-Layer Foil Gas Sampling Bags") were used as nitromethane enriched nitrogen source. Concentration explanations and calculations are shown in the appendix (section 6.4).

Equilibration times no shorter than 12 hours were chosen. A process mass spectrometer (Pfeiffer GSD 301) was introduced in between the packed bed and mass-flow controller using a T-type connector. Flows were in most cases 55.3 $ml_n\ min^{-1}$. Mass spectra were recorded using multi ion mode.

After breakthrough measurements, a constant flow of nitrogen carrier gas was passed through the column bed, while the combination of mass-flow controller and vacuum pump at the very exhaust was removed. Again, the mass spectrometer operating in multi-

ion mode was used to record the chromatograms. The temperature was increased to 200 °C to thermally desorb nitromethane from the packed beds of adsorbent.

3.2 Preconcentration of benzene with archetype 2nd generation MOFs

The Basolite® MOF **MOF-177** was obtained from Sigma Aldrich in standard quality. UiO-MOFs were obtained from several manufacturers. UiO-67, UiO-66(ADC), CAU-10 and one sample of UiO-66(BDC) (**UiO-66-d**) were obtained from the company ProfMOF. One sample of UiO-66(BDC) (**UiO-66-c**) was obtained from STREM chemicals. **ZIF-67** was obtained from MOF Technologies. A different sample of UiO-66 (**UiO-66-b**) was synthesized in batch based on a reported method [291], using molar ratios of 1:1:65:2:10 (Zr:BDC:DMF:HCl:H_2O), $ZrOCl_2 \cdot 8H_2O$ as metal and terephthalic acid as linker source. After heating at reflux for 24 h using mechanical stirring, the gel was repeatedly washed with DMF and methanol as described in the procedure. Final activation was done at 200 °C overnight. The low-coordinated UiO-66 (**UiO-66-b**) was synthesized applying a continuous synthesis process [292], using molar ratios of 1:1:98:2:20 for (Zr:BDC:DMF:HCl:H_2O) and residence times of 8 minutes at 90 °C. The same metal and linker sources but only half concentrated HCl (18.5%) were used to avoid suppression of the framework formation which would result in lower specific surface areas.

All samples were characterized using thermogravimetric analysis (TGA), specific nitrogen surface area (BET-model) and infrared spectroscopy before iGC-investigations. Details in the methods are given in 3.1.1.Thermal desorption experiments were done under dry and humid conditions, details see section 3.2.1. Using iGC in the Henry region of dilution, various sorbent-analyte combinations at temperatures between 150 and 220 °C were investigated. Thermodynamic quantitites were calculated using equations from section 2.3.2. Further details on iGC in section 3.2.2.

3.2.1 Sampling and thermal desorption investigations

Different adsorbents from different MOF families were evaluated for their capability of benzene concentration from a 1 ppm_V gas-phase source. Gas sampling bags ("Supel™ Inert Multi-Layer Foil Gas Sampling Bags" from Supelco) were used as containers for the benzene/nitrogen or benzene/nitrogen/water samples (humid conditions). Using the ideal gas law, concentrations can be adjusted by introducing respective amounts of liquid analytes prior to a 24 h equilibration phase. Bags were filled using MFCs, benzene and water amounts were injected using microliter syringes. By further diluting gas atmosphere from a bag A into a bag B, lower concentrations can be achieved.

Being placed into state-of-the-art sampling tubes, MOFs were preconditioned (200 °C for at least 24 h under nitrogen 5.0) and mounted into the setup. After a sampling period from this benzene source, sampling was stopped and the GC-oven temperature was increased to 200 °C with no flow being present. After reaching this temperature, a nitrogen purge gas was passed through the packed bed towards a mass spectrometer (Pfeiffer GSD 301 operating in multi ion mode).

In case of sampling and desorption, flows of 46.1 $ml_n\ min^{-1}$ were used and facilitated using mass flow controllers. During the sampling set-up, a vacuum pump after the MFC provides for the necessary pressure drop. A result of this setup is that the exact pressure drop along the column is not known as well as the exact flow along the packed bed. As no breakthrough curves were recorded this is rather unproblematic. During desorption, the system exhaust flow was determined to be ca. 5% lower than the purge gas flow determined by using a soap-bubble flowmeter.

3.2.2 Inverse gas chromatography studies

Sample preparation was done similar as in the first study, as well as the general usage of the GC system. Flow rates were chosen between 18.4 and 27.6 ml_n min^{-1}. In addition to the PID and TID detector, a thermal conductivity detector (TCD) was used to monitor analyte concentrations over time.

An overview of probe molecules used in this study is given in Table 2.

Table 2. Probe molecules used in this study, sorted by analyte family. Boiling point (T_b) in °C, molecular weight (M_W) in g mol^{-1}, standard heat of vaporization (ΔH_{vap}) in kJ mol^{-1}.

Name	short	family	T_b	M_W	ΔH_{vap}	Reference
Methane	CH4	aliphatic	-161.49	16.04	8.6	[283]
Hexane	C6	aliphatic	69.1	86.18	31.5	[283]
Heptane	C7	aliphatic	90.1	100.21	36.1	[283]
Octane	C8	aliphatic	125.5	114.23	41.0	[283]
Benzene	B	BTEX	80.2	78.11	33.1	[283]
Toluene	T	BTEX	110.7	94.12	38.9	[283]
o-Xylene	oX	BTEX	143.9	106.17	41.1	[283]
m-Xylene	mX	BTEX	139.2	106.17	44.7	[283]
p-Xylene	pX	BTEX	138.3	106.17	37.7	[283]
Ethylbenzene	EB	BTEX	136.2	106.17	41.8	[283]

3.2.3 MOF coatings for diffusive sampling

Alumina hotplates (3 x 3 mm) were obtainted from UST Umweltsensortechnik GmbH. Prior to deposition experiments, they were cleaned by washing them with deionized water and ethanol and placing them in an oven at 150 °C.

In case of deposition of HKUST-1 and MIL-53 on alumina hotplates, MOFs were immersed in di-n-butyl ether and sonicated for 10 minutes to disperse potential agglomerations. Drop depositions were carried out using a Nichipette EX II and a 1µl tip or glas capillary tubings. After deposition, hotplates were dried in an oven at 150 °C and 500 mbar of vacuum.

In case of silicon-based wafers, MOF particles were immersed in ethylene glycol, sonicated and loaded into a Sogolee airbrushing pistol (Double Action AirbrushPistole HP200) with a nozzle diameter of 200 µm. Heating the base of the wafer to 80-110 °C, using a magnetic stirrer with an aluminium coverage, several layers of MOF suspensions were airbrush-coated on top of silicon wafers with drying times of 1-2 minutes between each layer. Finally, wafers were placed in a vacuum oven at 150 °C and 500 mbar for several hours.

For preconcentrator testing of UST heaters, analyte containing gases were mixed in gas sampling bags according to the calculations stated in 6.4 and optionally by further diluting gas atmospheres obtained by this method. The preconcentrator modules were placed in a stainless steel measuring chamber, face-to-face with a MOSFET sensor. The gas streams exiting the chamber were monitored by a mass sprectrometer (Pfeiffer GSD 301 quadrupole MS) operated in multiple ion mode. A mass flow controller and a vacuum pump at the exhaust of the setup was used to adjust gas flows.

4 Results and Discussion

The Results and Discussion chapter is divided in two sections. The first section contains a concept and evaluation of nitro alkane preconcentration using archetype MOFs. This section was already published as a full paper in a more condensed form. [293] The second section contains the evaluation of a broader range of MOFs for BTEX compound enrichment. In contrast to the first section, enrichment under humid environment was studied as well.

4.1 Preconcentration of nitro alkanes with archetype 1st generation MOFs

In this study, the archetype commercially available MOFs **HKUST-1** (Basolite C300), **MIL-53** (Basolite A100), **Fe-BTC** (Basolite F300), and **ZIF-8** (Basolite Z1200) have been evaluated for their use as preconcentrator materials for gas-phase sensing. The results were compared to the porous standard **Tenax® TA**. The evaluation of this concept of preconcentration is based on inverse gas-chromatography (iGC) using nitro-functionalized and regular alkanes as probe molecules at infinite dilution.

As MOFs are intended to be used as gas-phase preconcentrator materials their interaction in the region of infinite dilution (zero coverage or Henry region) is of particular importance. This region resembles the linear part of a respective probe molecule sorbent adsorption isotherm. Computational studies addressing this region have shown high selectivity for the separation of BTEX mixtures (benzene, toluene, ethylbenzene and xylenes) [294] and polycyclic aromatic hydrocarbons (PAHs) as well as explosives. [295] Compared to analytical gas chromatography (GC), the roles of stationary and mobile phase are reversed. [53] The material to be investigated is placed in a packed column and gas phase samples of suitable and chemically acceptable diversified analytes are passed through this column bed (schematic and explanation in Figure 25, simplified comparison

towards breakthrough experiments in Figure 26). Interactions with the stationary phase will result in different retention times (retention volumes), peak shapes for any particular probe molecule/stationary-phase combination. [296] iGC uses standard gas-chromatographic components such as injectors, columns and detectors. It is possible to characterize non-porous surfaces and solids in terms of their surface energy and surface energy distribution, polar and disperse contributions as well as their surface heterogeneity which is also governed by crystal morphology. [277]

Traditionally, iGC is used for the characterization of non-porous materials, e.g. fibers, clays or polymers. [297]–[299] Surface chemistry mainly influences industrial processes and iGC provides a method for bulk material characterization as compared to localized methods such as AFM or contact angle measurements. Especially, for pharmaceutical formulations it is important as the pharmacology of the agent is also strongly influenced by textural and surface-chemical properties of the agent's dosage form. [300], [301]

Recently, iGC methods were applied to characterize porous materials. [277] Not only the first moment (retention volume) of the peak shape but also its second moment (FHWM and skewedness) can be analyzed to yield material properties. In the Henry region, at infinite dilution, Henry constants, enthalpies and entropies of adsorption for the materials high energy sites can be obtained analyzing the first moment of peaks. The second and higher moments can be used to derive kinetic properties, such as mass transfer coefficients, diffusion and permeability constants for the respective analyte-adsorbent combination. [268]

Recently, IRMOF-5 (MOF-5) was investigated with respect to VOC sorption. Most importantly, three different IRMOF-1 batches were compared. Generally, lower BET specific surface areas resulted in increased adsorption enthalpies and retention volumes for most adsorbates. A possible degradation phase of IRMOF-1 may be the cause for that.

The dispersive component of the surface energy (γ_S^D) determined by iGC was significantly lower as compared to purely inorganic materials. Using the Abraham linear free energy relationship (LFER) model, it could be shown that hydrogen bonding and dispersive interaction were the most dominant terms driving retention volume and adsorption enthalpies. As the Abrahams model does not contain a term for size exclusion, a negative term for polarizability was derived, which is presumably due to larger aromatics not being able to reach the binding sites featuring the strongest adsorption potential (high energy sites).

In order to make commercial off-shelf (COTS) MOFs comparable to literature results, standard analytical investigations, including X-Ray powder diffraction, particle size distributions, specific surface area and thermogravimetric analysis were carried out. Additional to iGC investigations, micro breakthrough investigations were carried out, where, compared to iGC experiments, a global equilibrium between the solid adsorbent phase and the nitromethane saturated gas phase is obtained. After breakthrough, columns were thermally desorbed and respective peak heights converted to enrichment factors.

4.1.1 MOF pre-characterization

Different analytical investigations, especially XRPD and specific surface area measurements as well as thermogravimetric analysis were carried out for the fundamental characterization and evaluation considering the quality of the commercially obtained MOFs. A summary of material specifications from the supplier (BASF) is shown in Table 3.

Table 3. List of used Basolites. Particle size d(0,5) values and surface areas from BASFs Basolite datasheet. Fe-BTCs d(0,5) was not available.

Basolite	MOF short formula	MOF name	Surface area in $m^2 g^{-1}$	Particle size distribution d(0,5) in µm
A100	Al(OH)BDC	**MIL-53** (Al)	1100-1500 (BET)	31.55
C300	Cu_3BTC_2	**HKUST-1** (Cu)	1500-2100 (BET)	15.96
F300	**Fe-BTC**	MIL-100 (Fe)	1300-1600 (BET)	n.a.
Z1200	$Zn^{Me}Im$	**ZIF-8** (Zn)	1300-1800 (Langmuir)	4.90

XRPD-patterns are in accordance with literature values for **MIL-53**, **HKUST-1** and **ZIF-8** (Figure 27). **Fe-BTC** showed only few broad reflexes in its pattern [104], [145], [155] being a result from its polycrystalline morphology with tiny crystallites and low long-range order. In addition, the signal noise ratio is poor due to iron being present. [148] **MIL-53**, **HKUST-1**, **Fe-BTC** and **ZIF-8** exhibit crystallite sizes of 16, 69, 5 and 61 nm based on XRPD peak widths as calculated using the Scherrer equation from the package DIFFRACplus TOPAS. [282], [302]

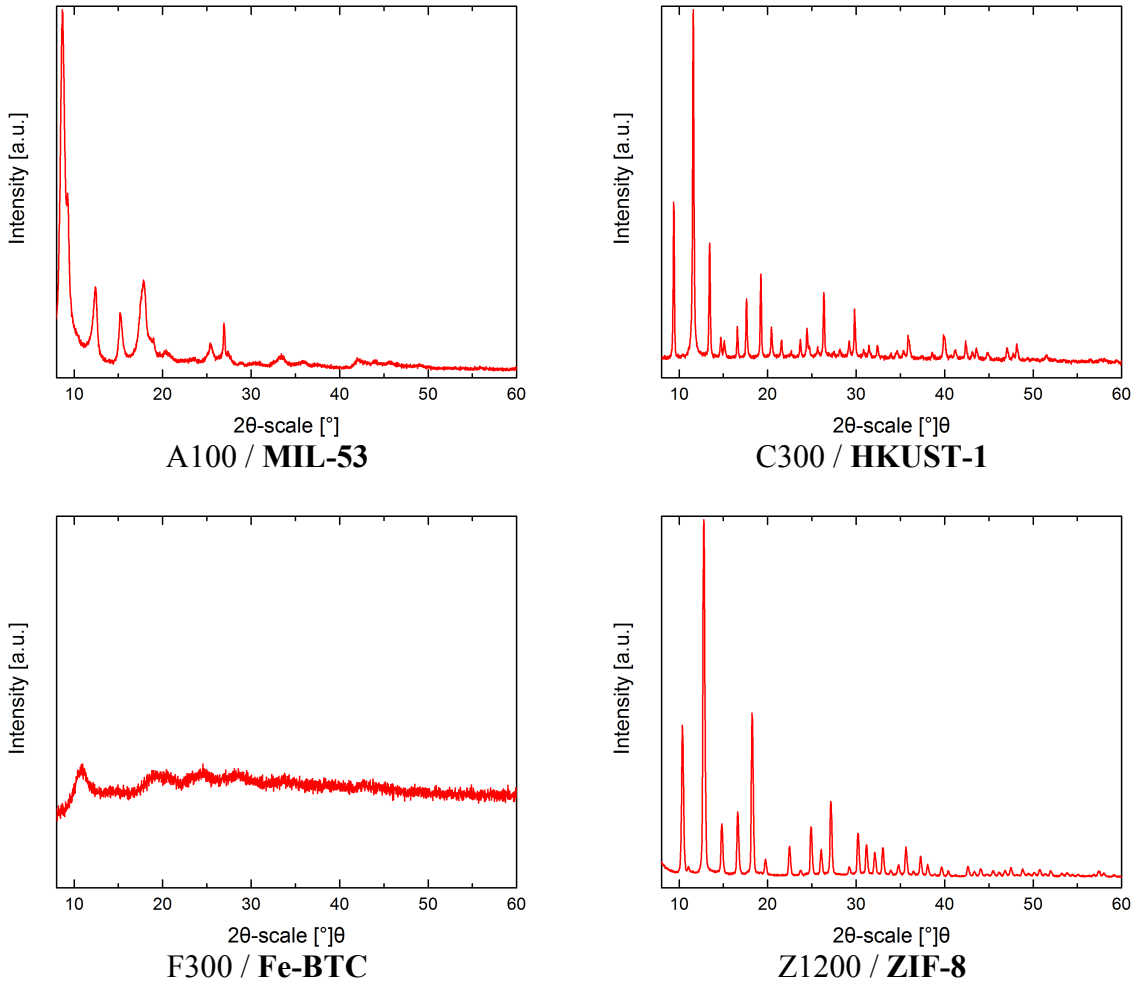

Figure 27. X-Ray powder diffractograms of Basolites prior to investigations. Reflection intensities are normalized towards maximum within respective patterns.

Regarding specific surface areas, BASF datasheets (Table 3) only provide ranges as batch-to-batch variations occur. In case of **MIL-53** (1100-1500 $m^2\ g^{-1}$, BET, measured: 1169), **HKUST-1** (1500-2100 $m^2\ g^{-1}$, BET, measured: 1689) and **ZIF-8** (1300-1800 $m^2\ g^{-1}$, Langmuir, measured: 1766) these values are within the supplied range, only **Fe-BTC** is lower (1300-1600 $m^2\ g^{-1}$, BET, measured 470) than reported. A summary is shown in Table 4.

Table 4. Summary of results obtained from particle size and surface area investigations. d(0.5), d(0.9) display the diameter threshold for 50 and 90 % of all particles being smaller than it. D[4,3] (DeBroukere mean) and D[3,2] (Sauter mean) refer to a volume or surface weighted mean diameter. All size distributions showed at least a bimodal shape.

MOF	Surface area in $m^2 g^{-1}$ (BET)	BET constant	d(0.5) in µm	d(0.9) in µm	D[4,3] in µm	D[3,2] in µm
MIL-53	1169	1608	12.47	47.99	19.84	5.97
HKUST-1	1689	34683	15.23	26.52	16.20	10.62
Fe-BTC	470	465	8.14	16.16	8.97	4.67
ZIF-8	1766	607	4.97	28.48	10.18	3.62

All MOF powders show at least bimodal particle size distributions. Ratios of maximum 1 and 2 are given in Table 4 together with d(0.5) and d(0.9) values. The latter values display a threshold diameter, with 50% and 90% of all particles being smaller than this threshold. D[4,3] (DeBroukere mean) and D[3,2] (Sauter mean) refer to a volume or surface weighted mean diameter. The Sauter mean is defined as the diameter of a spherical object that has the same volume to surface area ratio as the ensemble of particles investigated. In case of **Fe-BTC**, no values from BASF were supplied. In case of **MIL-53**, there is a difference in d(0.5) particle size that may occur from PSDs being measured in different solvents.

Thermogravimetric analysis was done to assess MOF stabilities during iGC experiments (Figure 28). While the trimesate MOFs **HKUST-1** and **Fe-BTC** showed their TGA-inflection point at 310 and 323 °C, **MIL-53** and **ZIF-8** show this point at 555 and 453 °C, respectively. It can be assumed that trimesate MOFs can be handled up to at least 200 °C. In its as received form **MIL-53** showed a ratio of 58 to 42 mass percent of *lt* to *ht* form. Structure descriptions and additional structural representations views for **HKUST-1**, **MIL-53** and **ZIF-8** are given in section 2.1.1.

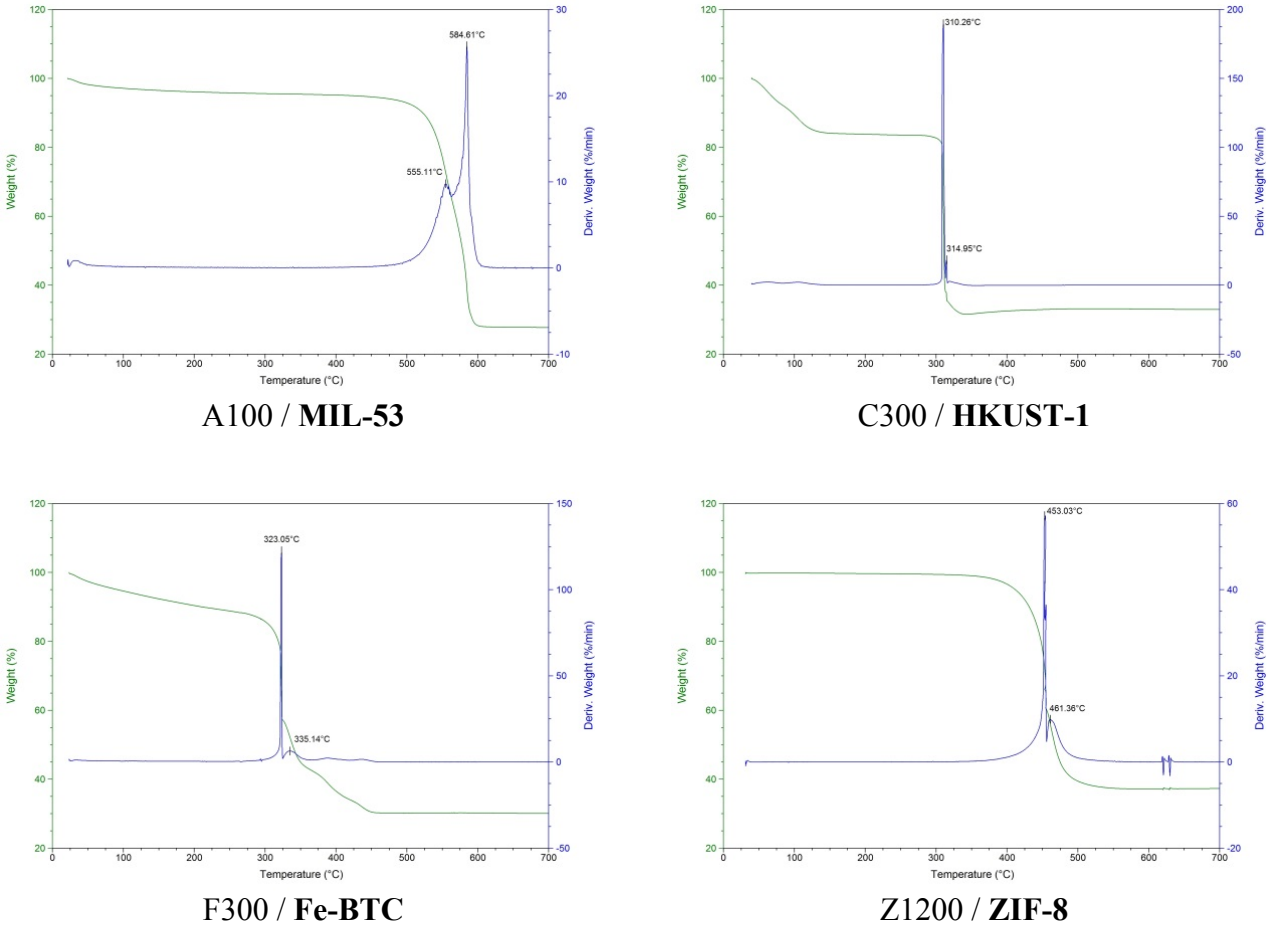

Figure 28. TGA plots of investigated Basolites. Green lines: Actual mass-loss signal. Blue line: derivative of mass loss. Measurements carried out under air (9.2 ml_n min^{-1}) with a heating rate of 10 k min^{-1} from room temperature to 700 °C.

Especially for **HKUST-1** it is important to remove adsorbed water prior to measurements (range up to 150 °C, loss of almost 20 mass percent) and it is recommended for **Fe-BTC** as well (loss of 10 mass percent up to 200 °C). **HKUST-1**s heat of solvation in water is about -70 kJ mol^{-1}. [303] **MIL-53** and **ZIF-8** can be handled up to temperatures of at least 450 and 350 °C, respectively. They show almost no physisorbed water in TGA plots.

For **Fe-BTC** (1300-1600 m^2 g^{-1}, BET, recorded: 470), the determined surface area falls below reported values. [148] This may be attributed to its poor crystallinity as shown in Figure 27. A reduced surface area due to a reduced micropore contribution to the pore volume may be the reason for that. [260] A surface area of 840 m^2 g^{-1} (BET model) was determined in the literature when a direct comparison to MIL-100 (Fe) was drawn. The crystalline analogue MIL-100 (Fe) consists of mesoporous cages of 29 and 25 Å connected

by microporous windows of 8.6 and 5.5 Å. [148] **Fe-BTC** (Basolite F300) has a polycrystalline morphology and its structure remains unknown. A distorted MIL-100(Fe) was suggested. [260], [304] With respect to many applications it cannot be directly compared to MIL-100 (Fe). Its catalytic behavior as compared to MIL-100 (Fe) was studied in the literature [148] as well as its morphological properties. [260]

Tenax® TA consists of 2,6-diphenyl-p-phenylene oxide (DPPO) polymer chains. It is considered being stable up to 350 °C and having a high water and oxygen stability as well as a low water affinity. The granular sorbent in 60/80 mesh contains particles between 180 and 250 microns. Datasheets claim a free fall density of 0.25 g ml^{-1} and a surface area of 35 m^2 g^{-1}. [305] In the literature, BET surface areas of only 20 m^2 g^{-1} and a pore volume of 2.4 ml g^{-1} were reported. The average intraparticle pore size was determined to be 200 nm, rendering it a macroporous sorbent. [92] In BET-measurements in this work, a surface area of 23 m^2 g^{-1} and a C constant of 71.3 were determined. Thermal decomposition started at 400 °C in a 10 K min^{-1} TGA measurement in air. A mass loss of 3.6% was detected between 150 and 200 °C.

4.1.2 Confirmation of the Henry region

The basis for any calculation of thermodynamic quantities is the probe molecules specific retention volumes at infinite dilution, i.e. in the Henry region. In this range the uptake is independent of the surface coverage and probe molecules interact preferably with high energy sites. The isotherm is linear and the peaks in the chromatogram are nearly symmetrical. [277] Some tailing may occur because of Eddy diffusion and resistance to mass transfer (non-equilibrium). In this study, the region of infinite dilution was confirmed by repeatedly injecting and eluting varying amounts of a given sample on the respective stationary phase (MOF). An example is shown in Figure 29 for the elution of nitromethane on **MIL-53** at 200 °C.

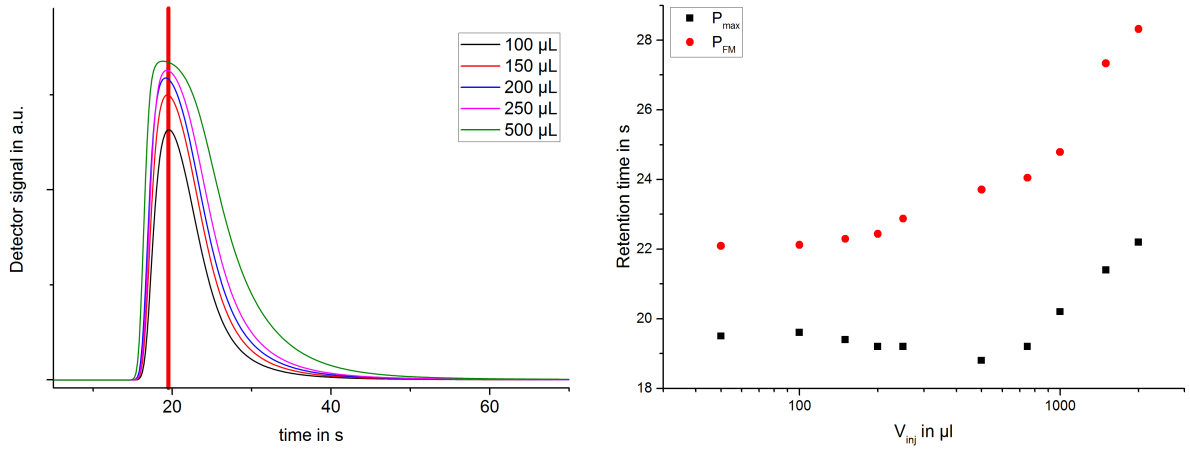

Figure 29. Left: Elution chromatograms of different injection volumes of nitromethane on MIL-53 at 200 °C. Red thick line shows peak maxima for all 5 peaks. Right: Shift of peak maxima (P_{max}) and first moment of peaks (P_{FM}) as a function of injected volumes (log-scale).

For 50 to 500 µl of injected volume, there is no significant shift in retention times (based on peak maximum). All retention times were within standard deviations of retention times (2-5%). Above 0.5 ml of volume injected, a peak broadening was observed, and a shift of the peak maximum and first moment occured. In general, peaks tailed without any MOF present in the packed bed. This may be attributed to dead volume in the connection between tubing and packed bed, such as pressure sensors and reducing unions.

4.1.3 Retention volumes and Henry constants

For a strong preconcentration effect the ratio of the sampling (low temperature) and desorption (high temperature) retention volumes (V_R or Henry constants K_C) are key parameters. This is also resembled in heats of adsorption representing the slope in a $\ln(V_R)$ vs 1/T plot. [277]

Henry constants reflect the isotherm slope in the linear region. They can be calculated from specific net-retention volumes by dividing them by $R \cdot T_C$ as shown in section 2.3.2. They resemble the amount of nitrogen required to elute the spatially distributed substance peak of respective analytes to its maximum concentration (signal) within the porous bed. A specific net retention volume is a material specific value (for a given guest

molecule-material combination) that is influenced by packing geometry, particle size and carrier gas flow as well as column pressure drop and temperature. It is similar to the inflection point of a breakthrough set-up which is a frontal technique (comparison in Figure 26). [46], [290]

It is also common to compare natural logarithms of retention volumes or Henry constants ($\ln(V_G^0)$ or $\ln(K_C)$) for a sense of review. In this study, standard errors were usually within 5-10% of absolute values. Several peaks due to successive injections with different injection volumes are shown in the left picture of Figure 29.

Values at 50 °C were measured once for all nitro compounds. Alkane lines were not recorded at 50 °C for MOFs in this study. No alkane investigations were made on the standard **Tenax® TA** as retention times were too low, even at 9.2 ml_n min^{-1} (ml_n conversion shown in section 2.3.2), to analyze them in a proper fashion.

On a sorbent comparison basis, **HKUST-1**, **MIL-53** and **Fe-BTC** showed higher retention volumes (at 50 °C) observed within the series (Figure 30). **HKUST-1** proves the peak substance for nitromethane with a value >10 l g^{-1} of sorbent, while **ZIF-8** and **Tenax® TA** show values below 1 l g^{-1} of sorbent. **ZIF-8** shows the lowest retention volumes with 125 ml g^{-1} at 50 °C and 31 ml g^{-1} at 200 °C. In a scenario of sampling at 50 °C, followed by thermal desorption at 200 °C, these values are directly related to sampling volume and thermal desorption volume, respectively. [53] **HKUST-1**, **MIL-53** and **Fe-BTC** showed higher ratios while **Tenax** and **ZIF-8** showed lower values of 4-5. Individual values at 50 and 200 °C as well as their rations are shown in Figure 30.

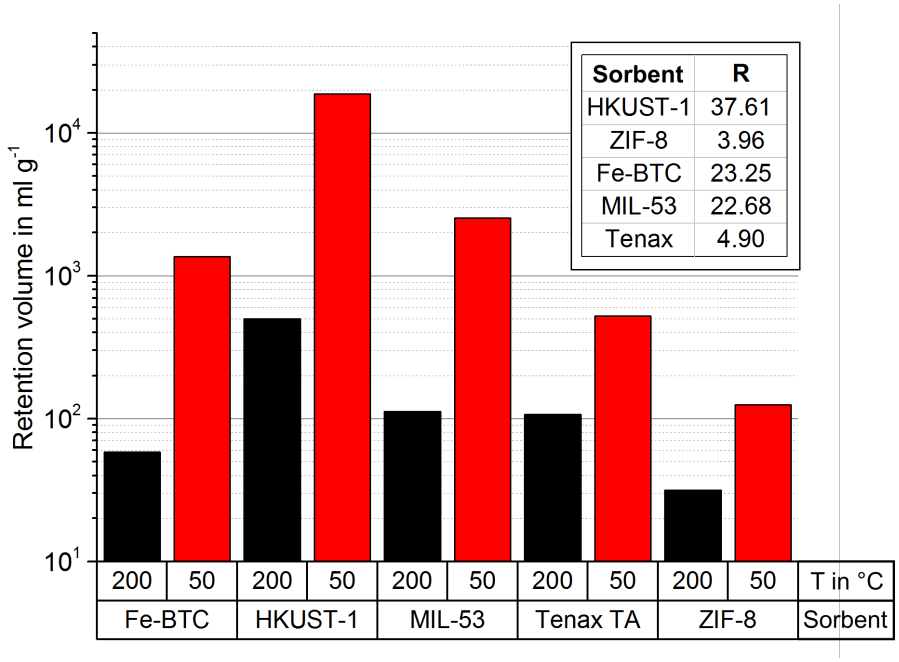

Figure 30. Retention volumes (in ml g^{-1}) of nitromethane on the four investigated MOFs and Tenax® TA at 50 and 200 °C at log_{10} scale. R represents the respective ratios of 50 °C and 200 °C nitromethane retention volumes of respective sorbents.

HKUST-1 shows a molar weight based trend for all nitro-compounds without any changes in qualitative trends throughout the temperature range studied. Linear nitropropane is always strongly favored over the branched isomer at all temperatures. At 50 °C and 100 °C nitroethane and 2-nitropropane showed almost identical Henry constants indicating that the nitro group is predominantly responsible for the retention. Nitromethane showed a Henry constant of 6.9 mmol Pa^{-1} kg^{-1} at 50 °C which is the highest among all sorbents. **Fe-BTC** shows, right after **MIL-53**, the third highest retention volume for nitromethane at 50 °C but in general a rather poor discrimination among other nitro-compounds at all temperatures. **ZIF-8** showed a strong favor for 1-nitropropane at 50 °C, this trend was maintained throughout the whole temperature series, while 2-nitropropane showed values comparable to those of nitroethane and -methane.

An explanation for this could arise from the small windows of **ZIF-8'**s pore system that prefers linear, aliphatic moieties that govern the retention. From 50 to 200 °C, a molar weight correlated order for all nitro-compounds was seen for **MIL-53**. Discrimination among nitroethane and nitropropanes is poor at 50 °C. Nitromethane´s retention volume

– after a drop from 50 to 100 °C – remain almost constant from 100 to 200 °C. This may be attributed to the increasing formation of its *ht*-form (starting at 60-80 °C as indicated in [306]) and may be additionally supported by guest molecules entering the pores. **Tenax® TA** showed an inverse molar weight based trend throughout the whole series, generally being lower in values than the MOFs. Linear 1-Nitropropane is always favored over 2-Nitropropane (Figure 31).

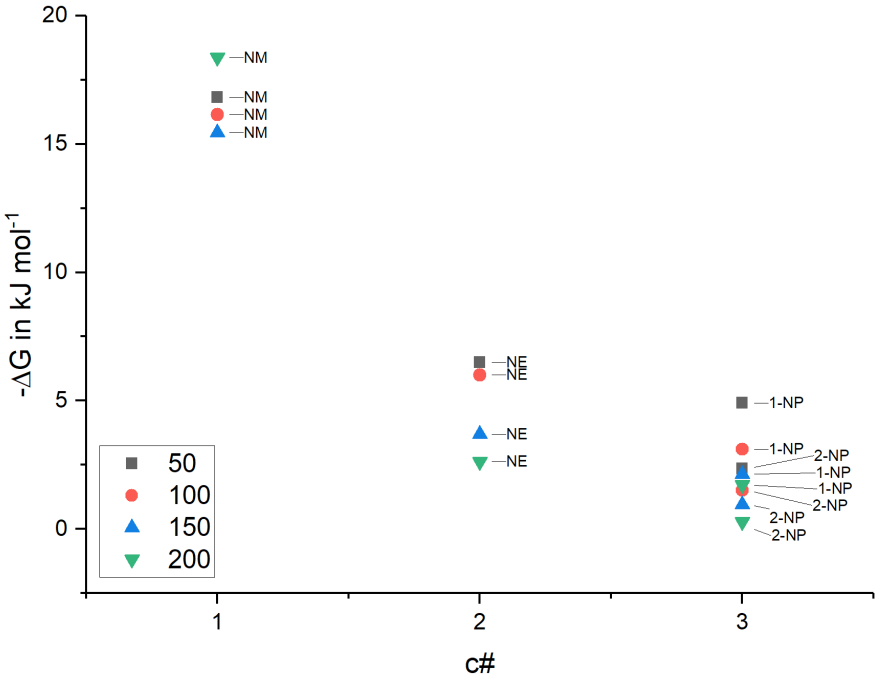

Figure 31. Carbon number plot for nitro alkanes on Tenax TA on the basis of free enthalpies of adsorption (calculation see section 2.3.2). NM: nitromethane, NE: nitroethane, 1- and 2-NP: 1- and 2-nitropropane, respectively.

Tables with logarithmised Henry constants are shown in the appendix (section 6.5.1).

4.1.4 Adsorption enthalpies

As explained, ratios of retention volumes at different temperatures (e.g. sampling volume at 50 °C or thermal desorption volume at 200 °C) are directly related to respective heats of adsorption (ΔH_{ads}). A temperature-independent adsorption enthalpy within the region where a linear regression is done is a prerequisite. Even though the temperature window was chosen wider as in other studies, regression analysis was successful. On choosing this

temperature window, relative errors in temperature measurement were also minimized. Derived enthalpies of adsorption were correlated towards thermal desorption peak heights showing that adsorption enthalpies are a key parameter for preconcentration materials screening.

Heats of adsorption (enthalpies of adsorption) were calculated from van't Hoff plots in the temperature range of 50 °C to 200 °C (100 °C to 200 °C for alkanes). This procedure is described in section 2.3.2. Looking at nitro compounds, a more general correlation with particle properties is seen for all MOFs. The smaller the majority of their particles, the higher their retention volumes and their temperature dependency, resembled in heats of adsorption. This is apparent, when the d(0.9)-value (often also referred to as D90) is considered, describing a derived diameter of a particle size distribution – 90% of the particles are smaller than this diameter (Basolite values see Table 4).

This may result from the interior pore volume being reduced as particle sizes are smaller. However, a study comparing different particles beds for one and the same MOF would be necessary to finally confirm this observation. Overall, absolute values of enthalpies of adsorption of alkanes were larger than their enthalpy of vaporization (Figure 32 and Table 1).

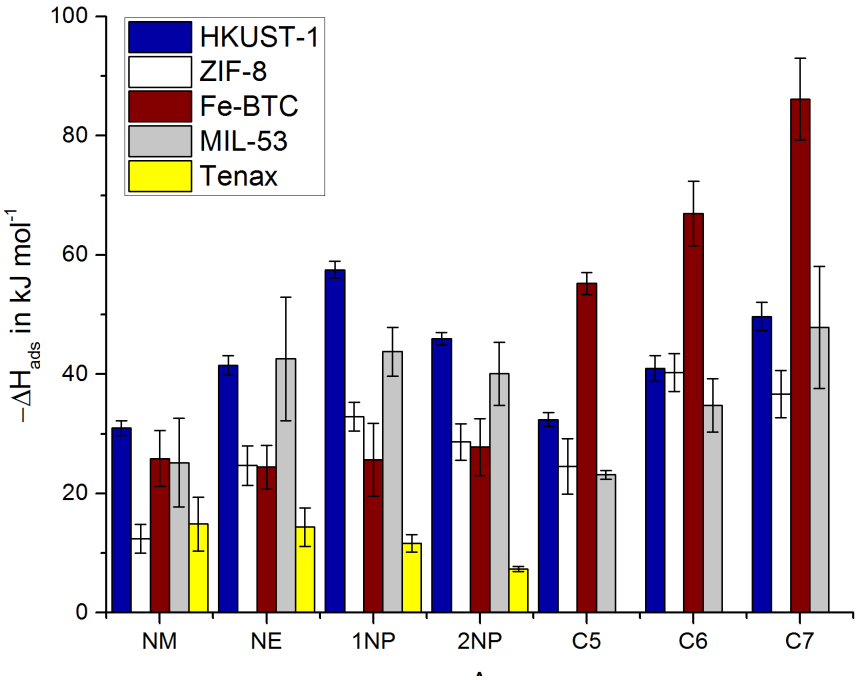

Figure 32. Enthalpies of adsorption (in kJ mol^{-1}) for regular and nitro alkanes on all sorbents investigated in this section. Analytes: nitromethane (NM), nitroethane (NE), 1- and 2-nitropropane (1NP and 2NP) as well as pentane (C5), hexane (C6) and heptane (C7).

This refers to the process of adsorption being more dominant than the process of condensation. This is different for nitro compounds. Only **HKUST-1** showed enthalpies of adsorption being larger than enthalpies of vaporization except for nitromethane. All other MOFs showed a non-enhanced interaction with nitro compounds. Considering entropies of adsorption, the smaller the pore or the smaller the void between an adsorbed molecule and the pore walls the more degrees of freedom (mostly include translational and rotational) are lost due to adsorption. The ratios of pore sizes and kinetic diameters of guest molecules can be thought of as a confinement factor. If size exclusion does not occur, the smaller this ratio is, the higher an enthalpy gain will be, whereas more entropy in terms of degrees of freedom is lost. [307]

HKUST-1 showed a clear dependence on chain length or molecular weight in case of linear alkanes with small error bars. This resembles the separation feasibilities of **HKUST-1** for linear alkanes as shown in reference [259]. For nitro-alkanes a similar trend as well as a differentiation between both nitropropane isomers was seen. This effect is due to

sterics as the enthalpy of vaporization only differs by 2 kJ mol^{-1} for 1- and 2-nitropropane. Isosteric heats of adsorption are about 15 kJ mol^{-1} higher for pentane and hexane and 5 kJ mol^{-1} higher for heptane. [258]

Entropies of adsorption are by more than 50% lower than reported in that study. Alike this study, entropies of adsorption do not change as much when going from hexane to heptane, as on going from pentane to hexane. Overall, a different experimental setup was used employing **HKUST-1** coated capillary columns with helium as carrier gas.

In this series, all entropies of adsorption were correlated to the chain length of alkanes or linear nitro-alkanes and 2-nitropropane losing the highest amount of entropy (-43.9 J mol^{-1} K^{-1}) upon adsorption. **HKUST-1'**s heat and entropy of adsorption for heptane can also be compared to the literature [260] showing a smaller difference in enthalpy of adsorption (here: -45.99 kJ mol^{-1}; reference -57.7 kJ mol^{-1}) and a bigger difference in adsorption entropy (here: -46.38 J mol^{-1} K^{-1}; reference -95.7 J mol^{-1} K^{-1}).

Looking at the compensation plot (enthalpy gain vs. entropy loss, Figure 33), nitro-alkanes (red line) show a similar slope as regular alkanes (blue line). This implicates that the nitro group does not change the frameworks mode of sorption significantly, i.e. their confinement factor Z, which is directly related to this slope. [307], [308] This factor is explained more in detail in section 4.2.4.

However, both nitropropane isomers behave differently with respect to their mode of sorption. With respect to non-specific interactions playing the key role, this is presumably a result of 2-nitropropane being bulkier, therefore showing a different adsorption mechanism reflected in its enthalpy and entropy of adsorption. If specific interactions are considered, different pk_A values of 1- and 2-nitropropane (8.98 and 7.68, respectively) [309] leading to a different behavior in hydrogen bonding, must be taken into account.

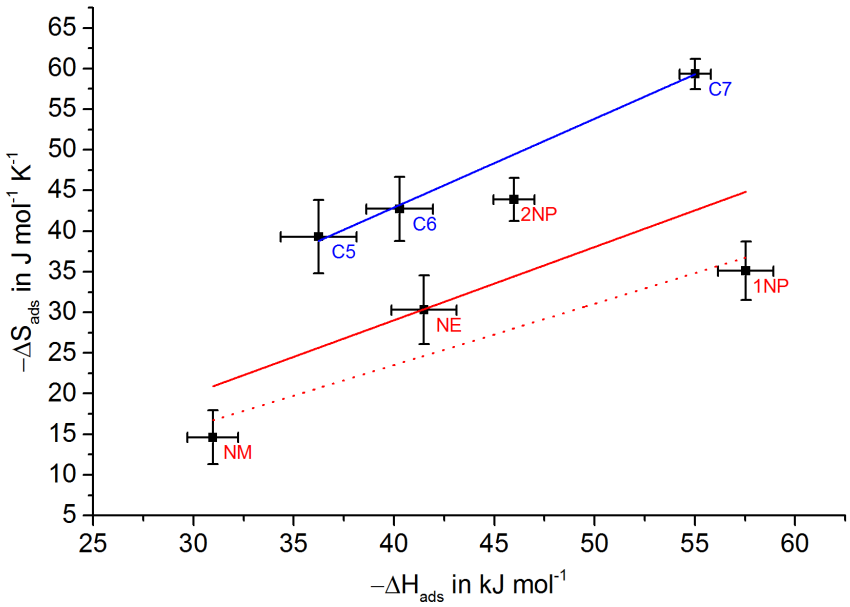

Figure 33. "Compensation effect" for alkanes and nitro-alkanes on HKUST-1. Error bars denote absolute errors from error propagation and regression analysis. Data points: Nitromethane (NM), nitroethane (NE), 1- and 2-nitropropane (1NP and 2NP), as well as pentane (C5), hexane (C6), and heptane (C7). Regression lines in blue for alkanes and in red for nitro alkanes (dashed with 2-nitropropane excluded)

ZIF-8 showed, like **HKUST-1**, small error bars for linear alkanes and a correlation to molar weight and chain length. Respective values for pentane, hexane and heptane (29.70, 36.04 and 41.58 kJ mol^{-1}) are close to literature values (investigations at approximately 250 °C): 32.74, 37.59 and 42.93 kJ mol^{-1}. [310]

Unlike **HKUST-1**, enthalpic differences in alkane series are of similar value. For the series nitromethane to 1-nitropropane a chain length depending order was observed. A molecular sieving effect for branched alkanes (namely isobutene) was already shown and discussed before [310]. Again, this shows the favor of disperse interaction in case of **ZIF-8**, probably because nitro alkanes may not sufficiently enter the pore system.

Entropies of adsorption show a chain length based increase in entropy loss upon adsorption in the alkane series when error bars are fully respected. Within the nitro series, a growing entropy loss was seen in the linear series, whereas the branched 2-nitropropane showed values between nitromethane and nitroethane. For nitromethane a

value close to zero was observed that could indicate a surface reaction with imidazolates. [311]

Fe-BTC showed comparable heats of adsorption for all four nitro alkanes. A slight increase was seen from nitromethane to nitropropane. Neither in terms of enthalpy (22-26 kJ mol^{-1}) nor in entropy (10-20 J mol^{-1} K^{-1}) a discrimination of nitro alkanes was seen even if error bars were fully respected. **Fe-BTC** showed increasingly high error bars for pentane, hexane and heptane. A linear chain length behavior of enthalpies and entropies of adsorption are seen that are reflected in values of dispersive components of the surface energy.

A comparison to heat of adsorption values of heptane given in literature [260] (-77.4 kJ mol^{-1}) reveals a difference of about 9 kJ mol^{-1} and a difference of ca. 25 J mol^{-1} K^{-1} in adsorption entropies (-158.3 J mol^{-1} K^{-1}). This difference could arise from the fact that the reference experiments were carried out in a narrower temperature window (120 to 150 °C) using helium as carrier gas. Also, the flowrates were around three times higher than in this study.

In general, polar repulsive forces (combined with poor crystallinity and hindrance for larger molecules [260]) could make the interaction with polar nitro alkanes unfavorable. A higher accessibility of open metal sites – in a distorted MIL-100(Fe) structure – should lead to a stronger interaction with polar groups such as nitro-groups, maybe even a catalytical reaction occurs. [164] This is further discussed in section 4.1.7.

Having even increasingly larger error bars, **MIL-53** showed a chain length dependent heat of adsorption for alkanes as well as nitro-alkanes. It showed comparable heats of adsorption for nitroethane as well as 1- and 2-nitropropane within respective error bars. So far, there is no knowledge of iGC-experiments using **MIL-53** up to now, only for the amino functionalized version [312] or MIL-47(V) [313]. Generally, as mentioned before,

MIL-53's flexibility (temperature and guest molecule dependent) is a major challenge, which is reflected by high error bars throughout the whole study. In case of regular alkanes, increasing entropy of adsorption is required on increasing the alkane chain length. While values of 30-40 J mol^{-1} K^{-1} for hexane and heptane seem realistic, values of below 10 for pentane seem to be a result from its low heat of adsorption and error propagation into the calculation of entropies. Tables with enthalpies and entropies of adsorption are shown in the appendix (Table 12).

For Tenax® TA, being a macroporous adsorbent, small specific surface areas lead to generally low retention volumes opposed to microporous MOFs. A partly inverse molar weight based trend is seen, with nitromethane carrying the largest enthalpy of adsorption, but also the largest error bar being reflected in an R^2 of only 0.91 in the vant'Hoff plot.

Looking at **Tenax'**s structure, a favor for the aliphatic moiety of all higher nitro homologues would be expected, however, the opposite is observed. Size exclusion may not play a role as **Tenax** is macroporous. As this observation is the result of several measurements and calculations, only impurities in **Tenax** structure maybe responsible for this behavior. Their relevance is emphasized in iGC at infinite dilution, see section 2.3.3. Nitroethane and both nitropropanes show linear vant'Hoff plots with R^2 values of greater than 0.95.

4.1.5 Free enthalpies of adsorption and surface energies

When the enthalpy and entropy of adsorption (for a respective probe molecule/sorbent combination) is known, the respective Gibbs free energy (free enthalpy) of adsorption can be calculated using their linear combination and the temperature. In this study, they have directly been calculated from retention volumes (see section 2.3.1). By plotting free energies of adsorption of linear alkanes against their respective carbon number – or other

molecular descriptors like their deformation polarizability – the non-specific component of the surface energy and thus the dispersive component of it – can be obtained from the slope of a linear regression fit. [258], [310] Along with different acid/base contributions, this component is an important material constant. Also, a comparison towards functionalized nitro-compounds – at least the ones exhibiting a linear shape – was drawn. Carbon number plots containing regular and nitro alkanes at different temperatures are shown in the appendix (section 6.5.3, Figure 63).

Non-specific component of the surface energy

In general, MOFs showed a drop in the surface energy´s dispersive component with increasing temperatures. Individual values are shown in Figure 34. This is due to entropic components of free energies of adsorption, gaining importance at higher temperatures. A weak correlation towards BET surface area and Sauter mean was found at higher temperatures (Figure 35 left and right, respectively).

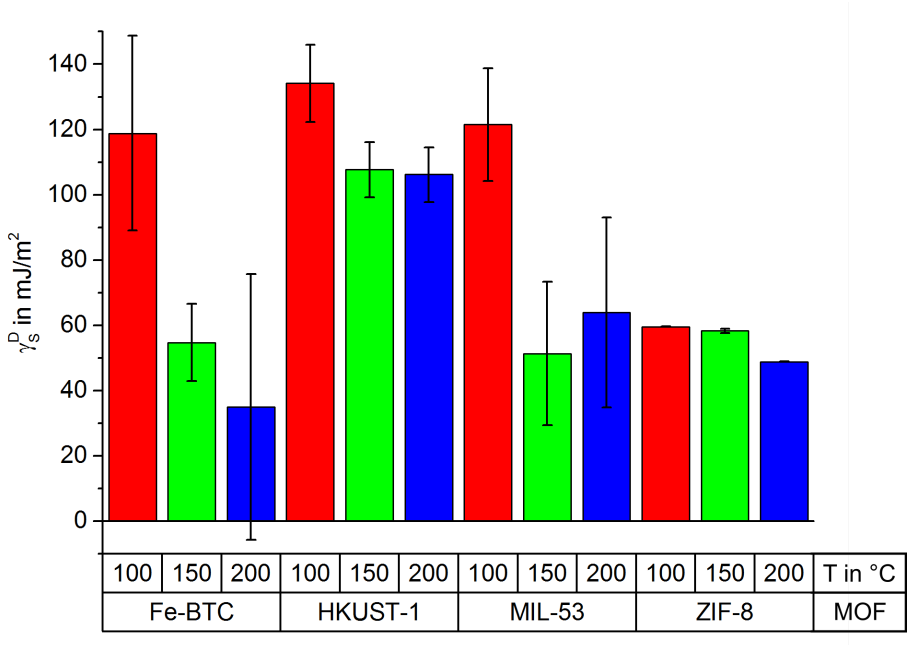

Figure 34. Dispersive component of surface energies derived from alkane lines. Error bars represent absolute errors calculated from carbon number plot slopes.

Values of **ZIF-8** are in good agreement with reported literature values, decreasing from 57.46 mJ m^{-2} at 180 °C to 44.33 mJ m^{-2} at 270 °C. [310] Values for **HKUST-1** and **Fe-BTC** can also be compared to [260] although the temperature windows only arranges for some intersection. In case of **Fe-BTC** a drop from 120 °C to 150 °C was shown, as well as constancy for **HKUST-1** within this range. This is in accordance with values reported herein. A sharp drop in dispersive surface energy is observed for **Fe-BTC**. Values at 200 °C are as low as 35 mJ m^{-2} with a large error. At 150 °C values are ca. 10 mJ m^{-2} higher than in the literature, at 100 °C there are no values to compare, however the trend is maintained with values close to **HKUST-1**. Values for **HKUST-1** show constancy at 150 and 200 °C and higher values of 134 mJ m^{-2} at 100 °C. A table with individual values is shown in the appendix (Table 13).

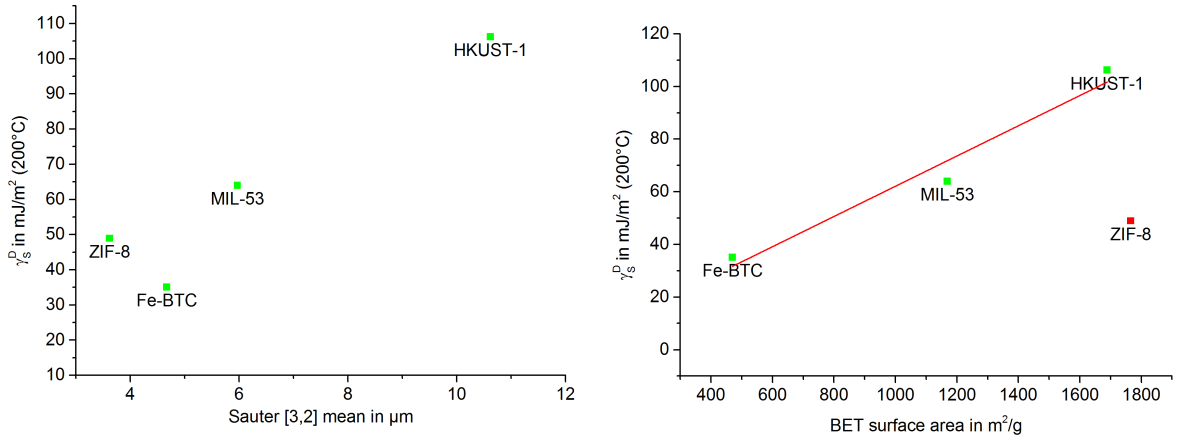

Figure 35. Left: Scatter plot of respective MOFs dispersive components of the surface energy at 473 K (200 °C) versus Sauter mean diameter (SMD). Right: Plot of the dispersive component of the surface energy at 473 K (200 °C) versus BET surface area. Regression line in red with ZIF-8 excluded for regression.

A rough correlation of BET surface area and Sauter mean towards the dispersive component of the surface energy exists, vanishing at lower temperatures. **ZIF-8** seems to represent an outlier in both series, which may be due to its different chemical nature (imidazolate linkers) or textural properties (small windows for the entrance of guest molecules). Including only terephthalic (**MIL-53**) and trimesic (**HKUST-1** and **Fe-BTC**) MOFs, R^2 increases from 0.05 to 0.99 at 200 °C in case of γ^D-BET correlations, while Sauter

mean correlations towards γ^D show an increase from 0.84 to 0.93 at 200 °C. These associations show that not only the microporous interior surface but also the external surface area – especially if a guest molecule is sterically excluded from the pore system as for **ZIF-8** – may play a major role in how the high-energy sites of a material are distributed. A table containing respective values is given in the appendix (section 6.5.4).

MIL-53 also shows a decrease towards higher temperatures. This may be due to its transition to the *ht* form that starts gradually at 60-80 °C with small time constant. [306] Between 150 °C and 200 °C, the γ^D remains constant with large errors. This could be due to structure transformation and exposure of alumina nodes towards interacting guest molecules that are nonpolar in this case. However, as the experimental setup's influence on possible *ht* to *lt* conversion kinetics is not known, this remains speculation.

Specific contribution of the nitro group

Based on free energies of adsorption, nitro alkanes can be compared towards their regular saturated hydrocarbons. The difference in free energies of adsorption between a non-functionalized hydrocarbon and a functionalized one yields the specific contribution of their structural difference, in this case the nitro group.

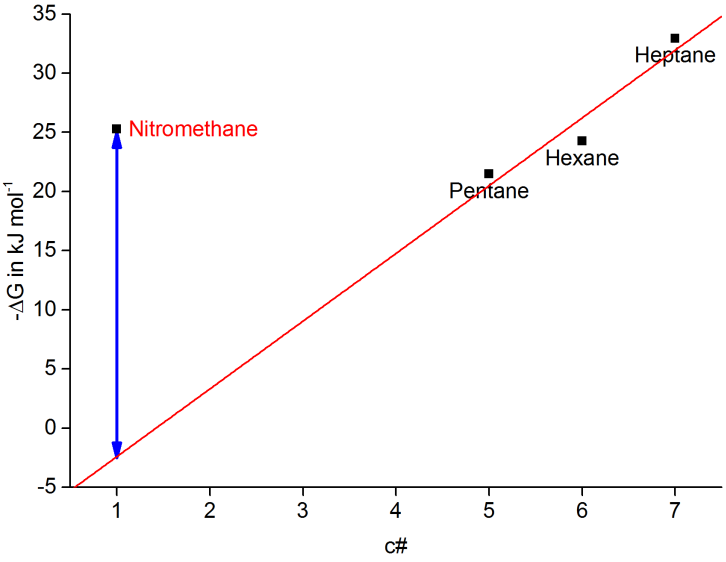

Figure 36. Determination of specific interaction of nitromethane's free energies of adsorption on HKUST-1 at 100 °C. Red line shows extrapolations of free energies of adsorption for alkanes with carbon numbers ranging from 1 to 4. Blue arrow represents specific interaction of nitromethane as compared to hypothetical methane (c#=1).

The process is schematically shown in Figure 36 and explained in section 2.3.2. All carbon number plots not shown in this section are included in the appendix (section 6.5.3, Figure 63). A linear fit in a ΔG vs. carbon number plot for a nitro-alkane series and a regular alkane series is compared at several carbon numbers – extrapolated as there is no direct carbon number overlap for both families, i.e. at carbon number 3, 4 and 5. The difference is averaged, in case of **ZIF-8**, 2-nitropropane was excluded as its branched structure lead to strong deviations in the alkane carbon number plots already. Standard errors were also calculated while averaging the differences in 3, 4 and 5 carbon number differences.

HKUST-1 and **ZIF-8** provide almost temperature independent specific contributions (in free energies of adsorption) for the nitro group in nitromethane of about 26 and 15 kJ mol^{-1}, respectively (**ZIF-8**, see Figure 37, others in Figure 63 the appendix).

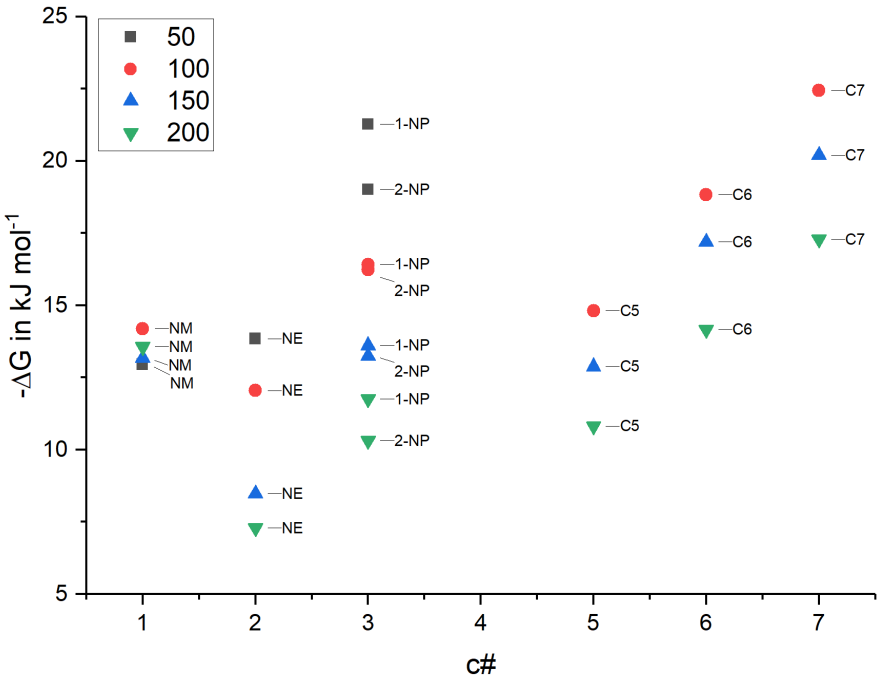

Figure 37. Carbon number plot for nitro and regular alkanes on ZIF-8 on the basis of free enthalpies of adsorption (calculation see section 2.3.2). NM:nitromethane, NE: nitroethane 1- and 2-NP: 1- and 2-nitropropane, respectively as well as C5: pentane, C6: hexane and C7: heptane.

In case of **Fe-BTC** and **MIL-53**, individual errors are large (appendix, Table 14, Table 15 and Table 16) and possibly a result of *ht* and *lt* phase mixing in **MIL-53** and a result of a chemical reaction in case of **Fe-BTC**. In most cases, the quality of linear regression based NO_2 contributions (over the whole carbon range from hypothetical methane to heptane) improved by excluding 2-nitropropane. No literature values are available for comparison. Comparing the specific NO_2 contribution to other functional groups such as halogens or ethers, the strong influence of the nitro group is emphasized. Bromoform has shown a specific interaction of only 5.70 kJ mol^{-1} on **ZIF-8** [310], tetrahydrofurane has shown values of 23.5 kJ mol^{-1} on **HKUST-1**. [258]

4.1.6 Micro breakthrough curves and thermal desorption investigations

Aiming to make iGC measurements comparable to a frontal technique like sorbent tube sampling, micro breakthrough measurements were done. Being very time consuming, for

they were done only for the analyte or major interest for explosive detection, nitromethane.

Instead of a concentration pulse being injected into a carrier gas stream, a source of known quantity and concentration of probe molecule in a carrier gas was constantly processed through the packed bed of adsorbent. In ideal, linear chromatography retention times (first moment of peaks in iGC) yield the same values obtained by analyzing the point of inflection (50% breakthrough) of a breakthrough curve.

In all cases, a gas sampling bag containing 1000 ppm_V of nitromethane was passed through a packed bed of adsorbent (40 to 60 mg). Breakthrough times were determined at different flowrates and temperatures, mostly at 55.3 ml_n min^{-1} and 100 °C. After breakthrough investigations, the packed sorbent was heated to 200 °C and purged with clean nitrogen for thermal desorption.

In a potential sensor system, a preconcentrator may be operated between room temperature and 100 °C, the first temperature being preferable for the retention of the analyte, the second one to inhibit water adsorption on the sorbent by capillary condensation, which is essential for MOFs like **HKUST-1** exhibiting sensitivity towards water adsorption. However, resulting Henry constants or retention volumes are smaller at 100 °C and the structure of HKUST-1 degrades more rapidly, which may be especially problematic in a cyclic preconcentration mode, causing a drift in the overall system sensitivity. Individual values for breakthrough and thermal desorption results are shown in Figures Figure 38 and Figure 39. It should be noted that reported breakthrough volumes are apparent values as in this setup the pressure drop along the packed bed is not known.

Using the described setup, correlations towards iGC measurements were possible. As breakthrough curves behave asymptotic and detector signals carry a particular noise

level, determining the 100% breakthrough point bears a large error. Therefore, 50% breakthrough times were converted into volumes and related towards the adsorbents mass. Peak heights and areas (within the dynamic range of the mass selective detector) were also related to respective sorbent masses.

For **HKUST-1**, additional temperatures and flow rates were tested as this MOF showed the highest adsorption enthalpy for nitromethane. This included one sampling measurement at room temperature followed by a thermal desorption at 200 °C. In order to calculate enrichment factors, peak height represents a good basis as a broad, high area peak would not enhance detector sensitivity significantly.

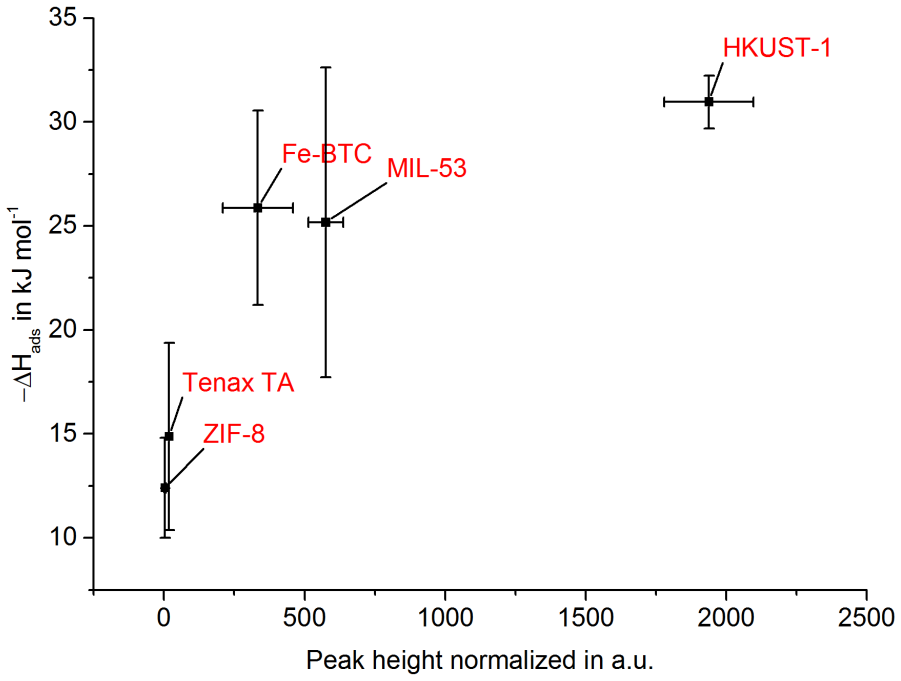

Figure 38. Correlation between nitromethane adsorption enthalpy and peak heights at thermal desorption after breakthrough investigations.

ZIF-8 showed the highest breakthrough volumes, in spite of having the lowest thermal desorption peaks. During iGC investigations packed columns of **ZIF-8** often produced high pressure drops. At breakthrough conditions, where no pre-pressure but a vacuum after the packed bed is applied, this problem gains significance, even though a system leakage can be excluded. Also, during thermal desorption investigations, repeatability was poor.

Looking at thermal desorption peak heights, a qualitative correlation towards enthalpies of adsorption from iGC experiments is evident.

Tenax® TA and **ZIF-8** show – as compared to other sorbents – no significant correlation to thermal desorption peak heights even though they show varying enthalpies of adsorption. In case of **ZIF-8**, this could be due to size exclusion effects for nitromethane as discussed in iGC experiments, meaning the interaction with nitromethane is purely occurring on the external surface area of **ZIF-8**. For **Tenax® TA** there is no mesopore or micropore contribution resulting in a different adsorption mechanism with adsorbate-adsorbate interaction playing a major role.

With error bars considered, the order of enthalpies of adsorption from iGC experiments can be directly compared with thermal desorption results with microporous adsorbents that do not exert size exclusion effects on adsorbates (see Figure 38). By normalizing peak heights to average sampling bags signal value (1000 ppm_V nitromethane) as well as sorbent mass (in g), signal enhancement factors can be calculated for each adsorbent.

As **HKUST-1** showed the by far highest desorption peak areas, closely resembled in nitromethanes enthalpy of adsorption. For further investigations of **HKUST-1**s sampling parameters, additional breakthrough and subsequent thermal desorption experiments were carried out at lower and higher temperatures for reduced flows of 9.2 $ml_n\ min^{-1}$. A large increase in breakthrough volumes was observed when the temperature was lowered to room temperature. This was also the case when the temperature was increased to 150 °C, but was likely caused by a systematic thermal compaction of packed beds and a resulting higher pressure drop.

Even at a sampling temperature of 100 °C, where water adsorption is strongly reduced, nitromethane preconcentration factors of 2850 could be achieved with this setup, i.e. $2.85 \cdot 10^5$ %. (per gram of sorbent). Normalized thermal desorption peak heights are

shown in Figure 39 and Table 5. By reducing the sampling (breakthrough) temperature from 100 °C to room temperature, desorption peak areas were increased by a factor of ca. 1.5. Also, they were diminished by a factor of ca. 142 by increasing the sampling temperature from 100 °C to 150 °C. Obviously, enrichment factors above 1000 cannot be reached even with higher amounts of MOFs in a preconcentration device, as 1000 times 1000 ppm amount to 100% partial pressure.

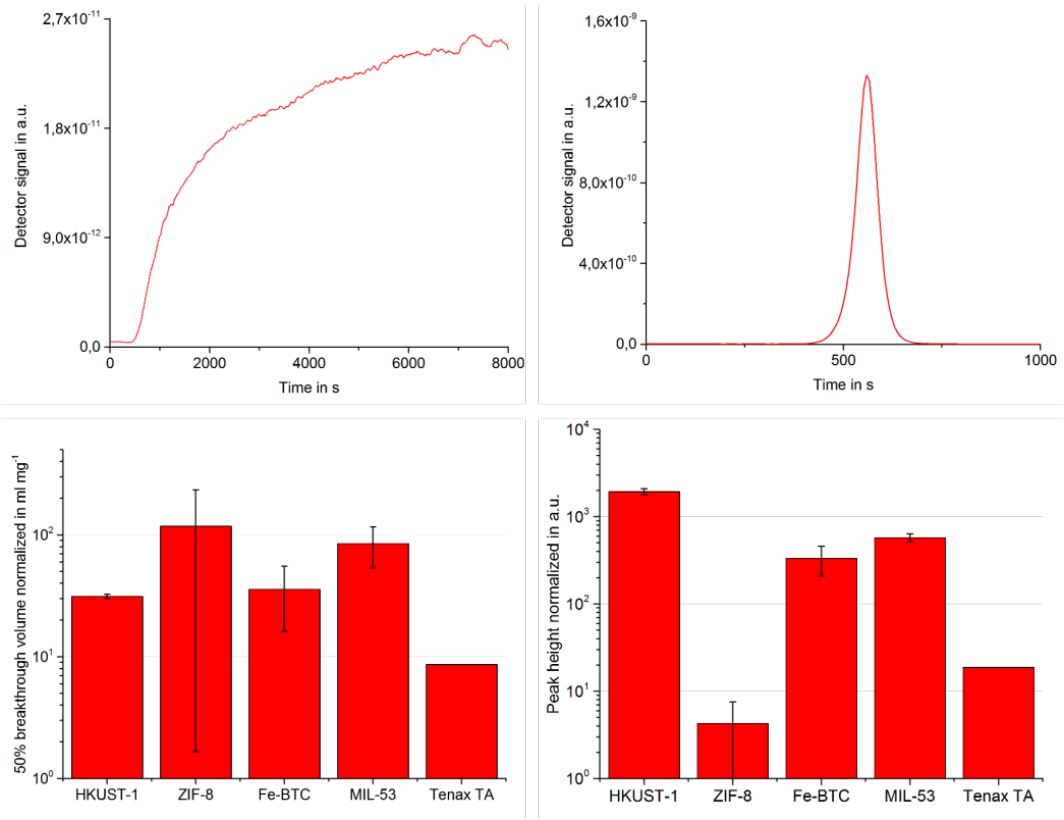

Figure 39. Upper row: Example breakthrough curves for nitromethane on 40 mg of HKUST-1 at 100 °C (left); exemplary thermal desorption peak at 200 °C (right); mass spectrometer detector signal in Amperes, using secondary electron multiplier. Lower row: Results of micro-breakthrough (left, apparent volume needed for 50% breakthrough in ml mg^{-1}) and thermal desorption experiments (right, towards 1000 ppm_V normalized peak signal); log10 scale in both graphs, therefore stretching ZIF-8's error bars.

In these experiments, **MIL-53** showed 1.7 times the thermal desorption peak height as compared to **Fe-BTC**. During iGC investigations, **Fe-BTC** showed a slightly higher ratio of 50 and 200 °C retention volume. This gap is possibly the result of a guest molecule depending breathing behavior of **MIL-53** as a more equilibrated state is established in the packed bed during breakthrough measurements.

Finally, for sampling on a 1 ppm_V nitromethane source with the same set-up as described above (flow 55.3 ml_n min^{-1}, sampling at 100 °C, desorption at 200 °C using 52 mg of HKUST-1), a preconcentration factor of 102 ± 7 was determined, i.e. raising the ion channel to a value that would be caused by an extrapolated 102 ppm nitromethane source. The derived normalized enrichment factor (1965 ± 129) is slightly lower than for 1000 ppm_V. Because the deviation is lower than 5% the preconcentration concept is shown to be extrapolated to lower concentrated target analytes of just 1 ppm.

Table 5. Enrichment factors of all adsorbents investigated in this study with respect to breakthrough experiment temperatures. Peak heights were normalized to sorbent mass (in g) and an average signal of 1000 ppm_V of nitromethane. Flowrates of 55.3 ml_n min^{-1} if not specified otherwise.

Adsorbent	Breakthrough temperature in °C	Thermal desorption peak height normalized a.u.	50% Breakthrough volume in l g^{-1}
Fe-BTC	100	334 ± 125	36 ± 20
HKUST-1	100	2051 ± 195	30 ± 5
MIL-53	100	576 ± 61.6	85 ± 8
Tenax TA	100	19 ± 2.7	9 ± 2
ZIF-8	100	4 ± 3	118 ± 31
HKUST-1, 9.2 ml_n min^{-1}	25	2850	277
	100	1939	36
	150	14	52

It could recently be shown that, in case of BTEX components, results from iGC can be modelled and experimentally compared with a preconcentrator concept using diffusive sampling (no packed bed and no carrier gas). [314] Still, using a setup as shown in breakthrough investigations, enrichment factors are assumed to be higher. It was also shown that enrichment factors based on diffusive sampling do rely on concentrations of respective sampling sources. [314], [315]

4.1.7 MOF stability

Stability remains a central prerequisite of materials used for preconcentration or sampling, especially in relevant environments. In case of a preconcentrator for a sensor system, it is more important as for a single-use dosimeter-like sampling device.

In order to evaluate MOF integrity during iGC measurements (several hundred injections at varying temperatures) their structural characteristics before and after these measurements were compared. Structural stability was investigated in terms of infrared spectra (ATR) and X-Ray powder diffraction. From IR spectra (Figure 40), a change in structure is evident when MOFs are exposed to nitro compounds at temperatures from 50 to 200 °C. The extent however, cannot be quantified.

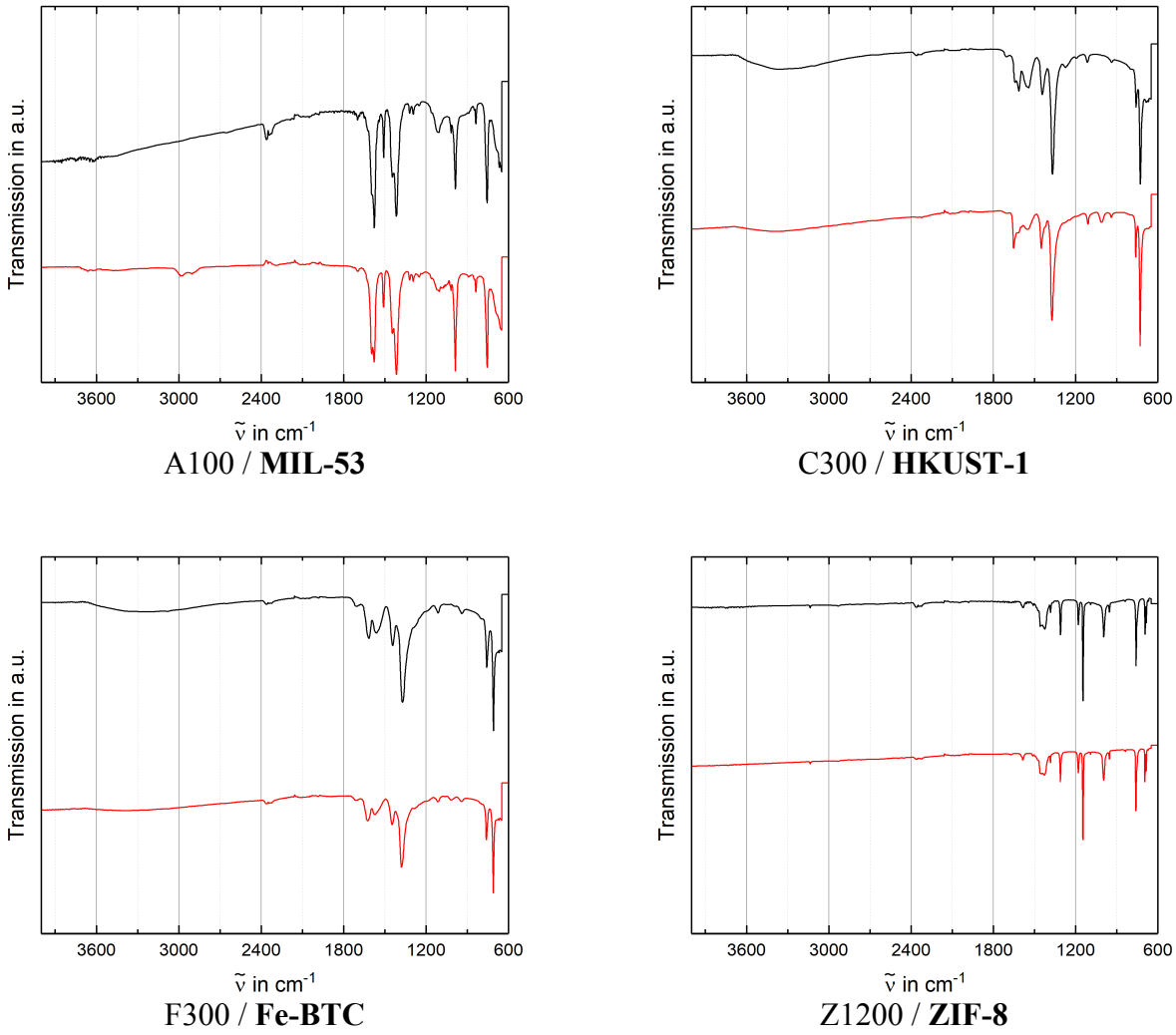

Figure 40. Infrared spectra of the MOFs used in this section. Reference spectra always shown in red.

In case of MIL-53 there is a loss of a double peak at 2900-2800 cm^{-1}, possibly relating to an increase in free carboxylic acid. In case of HKUST-1 and Fe-BTC there is a loss of peaks at 900 to 1100 cm^{-1}. As both compounds feature a trimesate linker this could also point out a reaction of the organic linker itself.

Long-term characteristics of HKUST-1

In case of using analytes from aliphatic or aromatic families no drift in retention times over a series of investigations with HKUST-1 was observed. Crystallinities and the crystallite size was maintained (shift from 69 nm to 67 via Rietveld peak widths). BET surface areas were reduced from 1689 to 1421 $m^2\ g^{-1}$.

Using nitromethane as analyte, a steady color change to almost black was observed for **HKUST-1**. As substance quantities used were not sufficiently high enough to perform XRPD or BET-measurements, an additional sample series with nitro compounds and one without was carried out at 200 °C. SEM pictures indicate a strong change in morphology for **HKUST-1** after repeated interaction with nitromethane (Figure 41).

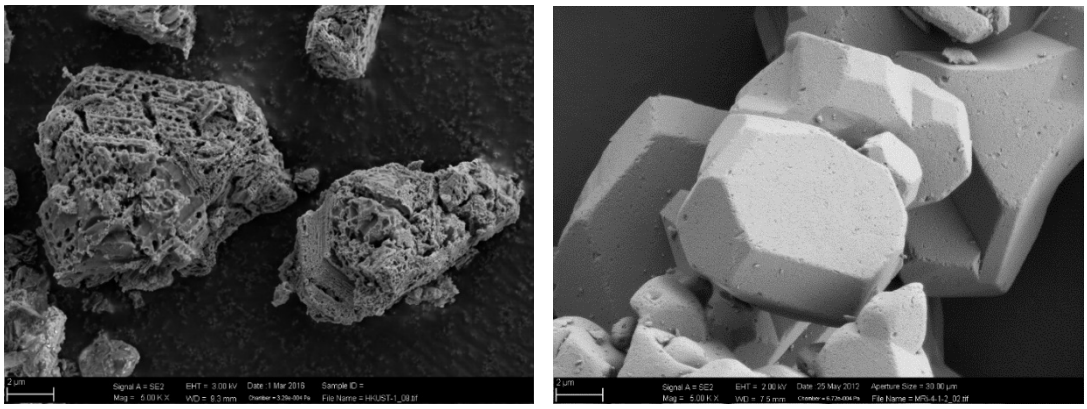

Figure 41. REM pictures of HKUST-1 crystals after nitromethane injections (left) and pristine reference material for comparison (right).

This could also be attributed to a carbonization at the outer shell of the MOF particles as discussed in [194] and [316]. As the experiments in the respective references were performed at temperatures being almost more than 200 °C higher, it is more likely to be the result of a chemical reaction of **HKUST-1** with nitromethane. SOTNIK et al. described catalytic properties of **HKUST-1** in supporting Henry reactions of nitromethane with aldehydes in solution. [317], [318] No structural change was reported when adsorbing nitromethane from the gas phase at 20 °C.

In order to further investigate the structural integrity of **HKUST-1**, several nitromethane elutions were repeated with a larger sample size of **HKUST-1**. Successive injections of nitromethane with a higher amount of MOF (60 mg) were carried out. However, no significant shift in nitromethane retention time was observed during these investigations. BET results indicate a clear loss in specific surface area during a series of subsequent nitromethane injections at 100 and 200 °C. After the iGC investigations, a specific surface area of 1118 m^2 g^{-1} was calculated, revealing a total loss of 570 m^2 g^{-1}. X-Ray

diffractograms show that the crystallinity of **HKUST-1** is maintained after nitromethane injections (Figure 42). Rietveld refinement via peak width lead to a crystallite size of 55.2 nm after 30 nitromethane injections compared to 68.9 nm before.

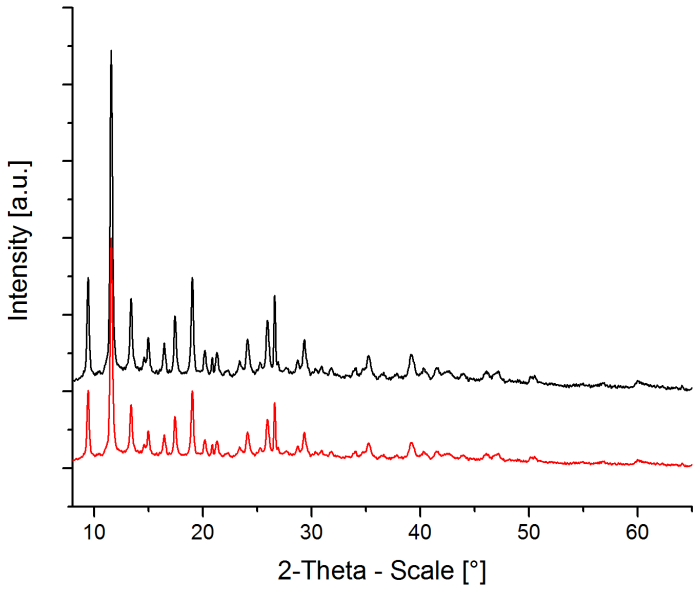

Figure 42. Comparison of XRPD diffractograms of HKUST-1 after nitromethane injections at high temperature. Red line: starting material, black line: material after several nitromethane injections at 100 and 200 °C.

As described in the literature for the example of MOF-5, there is no clear or sometimes even an inverse relationship between BET surface area and specific net retention volume.[261] It was shown that different samples of MOF-5 with varying specific surface area showed a non-significant influence of the specific surface area on several adsorption enthalpies that were calculated using retention volumes.

In case of toluene and benzene, an inverse relationship could be observed, meaning lower specific surface area resulting in an increased dependency of retention volumes and temperature. [261] A possible explanation for **HKUST-1**s behavior could also be the formation of a degradation phase on which nonpolar or aromatic molecules are more strongly adsorbed.

In order to further examine this effect, the heat of adsorption of pentane was derived during successive nitromethane injections at 200 °C. Resulting vant'Hoff plots for **HKUST-1** are shown in Figure 43.

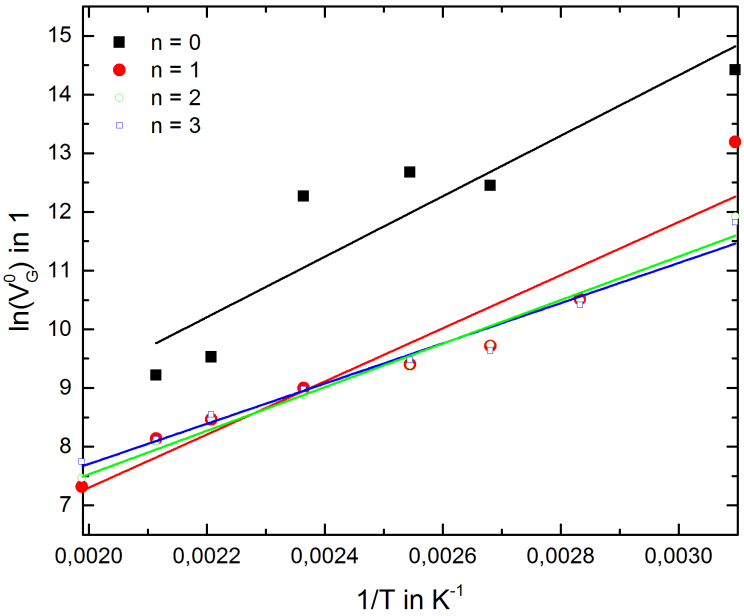

Figure 43. Vant'Hoff plot for the determination of pentane adsorption enthalpies on HKUST-1 after multiple cascades (10 injections per cascade) of nitromethane injections at 200 °C. n denotes the number of nitromethane injection cascades.

For retention volumes of nitromethane there is no clear trend even though the morphology of **HKUST-1** is clearly modified as evidenced by SEM images. After the first cascade of nitromethane injections, pentane retention volumes are generally reduced. This is directly due to the mentioned loss in specific surface area.

Resulting enthalpies of adsorption do not change by a trend but vary around 5-15% for each series. Given the hypothesis that a degradation phase was gradually developed as a result of nitromethane injections, this potential phase did after all not show a different interaction with regard to nonpolar pentane.

Adsorption behavior of Fe-BTC

It was shown in the literature, that Fe and Co show an increased potential for reactions with nitromethane in the gas phase. The mechanism features a metal insertion between the C-N bond, which is the weakest one in nitromethane (61 kcal/mol). [319] Due to small

crystallite sizes and large pores, **Fe-BTC** may accommodate for this. A range of reaction products may occur, including NO and NO_2. These fragments, in contrast to simultaneously occurring alkyl fragments with carbon numbers between 1 and 3 occurring in this reaction, can be detected by the GC-system, namely its thermionic ionization detector. This may explain almost no trend in retention times for nitro alkanes (see $\ln(V_R)$ vs. carbon number plots). The compensation plot – plotting ΔH_{ads} vs. ΔS_{ads} for respective data points in a scatter fashion – show that there is a linear correlation to be obtained for alkanes. In contrast, only a small cluster is found for nitro alkanes, where all individual compounds are located (Figure 44). The slope of a linear regression of this smaller spot is larger than the linear regression line obtained for regular alkanes, suggesting a more confined picture for nitro alkanes. Regularly, the slope of these plots is materials specific for alkanes on e.g. zeolites. [307]

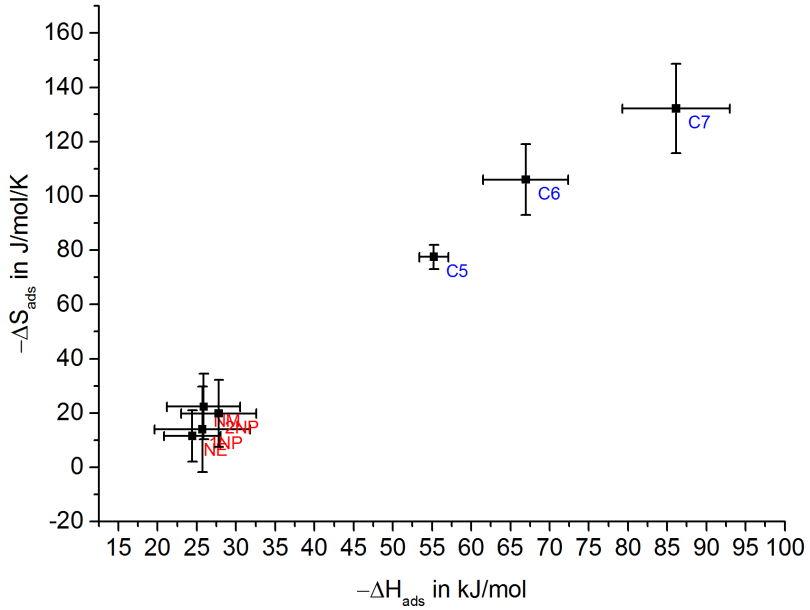

Figure 44. "Compensation effect" for alkanes and nitro-alkanes on Fe-BTC. Error bars denote absolute errors from error propagation and regression analysis. Datapoints: nitromethane (NM), nitroethane (NE), 1- and 2-nitropropane (1NP and 2NP) as well as pentane (C5), hexane (C6) and heptane (C7).

4.2 Preconcentration of benzene with archetype 2nd generation MOFs

In this section, the preconcentration concept developed in results section 4.1 is extended towards volatile organic compounds, in particular benzene. The detection of highly toxic VOCs among more or less benign VOCs is of striking relevance in many indoor air quality and health related applications. This was already elaborated in the introduction of this thesis. [29]

In this study, a wider range of MOFs was evaluated using thermal desorption of benzene at 1 ppm_V, namely **UiO-67**, **CAU-10-H**, **HKUST-1**, **MOF-177**, **ZIF-8**, **ZIF-67** and four different batches of regular (terephthalate-based) **UiO-66** as well as an acetylene-based linker version of **UiO-66**. Aiming to evaluate and investigate MOFs for the preconcentration of BTEX (benzene, toluene, o-, m- and p-xylene as well as ethylbenzene) compounds in relevant environment, thermal desorption under dry and humid conditions was chosen as method. Being the target analyte, enrichment factors of benzene were of highest interest, while the toluene, ethylbenzene and xylenes (TEX part) would be considered interferents.

The interaction of VOCs and MOFs has already been reported in the literature. [260], [320] For instance, **ZIF-8** was characterized using iGC and various VOC molecules. [310] A molecular sieving effect was observed for aromatic compounds, branched alkanes and heavily halogenated compounds. Flexibility of the **ZIF-8** framework at different temperatures was also observed for alkanes being bulkier than **ZIF-8**s pore size, which showed a significant retention volume as compared to even bulkier guest molecules, i.e. the size exclusion threshold was shifted towards larger molecular dimensions with increasing temperatures. A correlation of adsorbates dipole moments towards their retention volumes was observed, an indication for electrostatic interactions being important.

In the literature, adsorption mechanisms of VOCs in **Fe-BTC** and **HKUST-1**(Cu) were studied via iGC, using heptane, methylcyclohexane and toluene. The iGC investigations were complemented with immersion calorimetry measurements. [260] Using compensation plots derived from iGC, it could be shown that the adsorption modes of both MOFs were different with respect to enthalpy-entropy compensation. Due to the adsorbates in this case being different in chemical nature (linear, cyclic and aromatic) no common material constant can be derived from the slopes of these plots. In contrast, when regular n-alkanes were used for the characterization of zeolites, the confinement factor Z can be determined by the compensation plots (explained in section 4.2.4) of these hydrocarbons in combination with various zeolites. [307] Confinement factors do correlate well with pore sizes, which are experimentally not accessible at elevated temperatures.

In a different study, iGC was applied in conjunction with investigations at higher loadings, where adsorbate-adsorbate interactions gain relevance. For example, the C8 alkyl-aromatics separation behavior of **MIL-47**(V) could be attributed towards its different capacities (and isotherm shapes) but not to the adsorbate-adsorbent interaction at infinite dilution, which was investigated using iGC. [321] Henry constants and adsorption enthalpies determined at infinite dilution did not show a strong differentiation between the C8 isomers. When quaternary breakthrough curve investigations were recorded, this separation was clearly visible. It is, therefore, most probably due to adsorbate-adsorbate interactions and not adsorbate-adsorbent interactions.

In this study, a constant comparison to the polymer-based adsorbent **Tenax® TA** was drawn. Most of the MOFs investigated are known to have superior thermal and chemical stability, such as the UiO-series or **CAU-10**. [176], [185] Also, a comparison towards **HKUST-1** and the zeolitic imidazolate frameworks **ZIF-8** (Zn) and **ZIF-67** (Co) was drawn.

Two large-pore MOFs, namely **UiO-67** and **MOF-177** as well as four different batches of **UiO-66**, two from own synthesis and two from different commercial sources, were also investigated using benzene sampling and thermal desorption. It is known that synthesis, activation and handling conditions have a major impact on defects in MOFs [153], [164], also the interaction at low concentrations is strongly influenced by defect or high-energy sites. [261] Hence, different available sources of UiO-66 were chosen to investigate this effect. Prior to that, adsorbents were characterized via TGA, PXRD, nitrogen adsorption isotherms and infrared spectroscopy.

Benzene concentrations of 1 ppm were chosen as they can still be detected by a process mass spectrometer during sampling. This is of crucial importance if a preliminary breakthrough during sampling occurs. In contrast to the first study (4.1), sampling was not done until adsorbent breakthrough but for a particular timeframe of 10 minutes, followed by thermal desorption until the mass channel for benzene (m/z = 78) equaled the baseline level.

During sampling and thermal desorption, these four batches of **UiO-66** showed a strongly inhomogeneous behavior, which could not be explained by trends in specific surface area or linker-coordination numbers derived from TGA investigations. Therefore, these for materials were further investigated using iGC at infinite dilution and all BTEX compounds as well as regular n-alkanes. The dispersive component of the surface energy was calculated for all four UiO-66 samples and confinement factors were calculated from the enthalpies and entropies of regular alkane probe molecules.

4.2.1 MOF pre-characterization

Prior to thermal desorption and iGC investigations, all adsorbents were pre-characterized using adsorption isotherms (BET model), TGA investigations and IR spectroscopy. Pre-characterization of all adsorbents did confirm their porosity, thermal stability and

chemical functionalities (by IR spectroscopy). These datasets are especially useful for an after-sampling analysis of the adsorbents with respect to their structural integrity. Table 6 summarizes textural properties from BET measurements as well as coordination numbers for **UiO-66** type MOFs as determined by TGA (section 4.2.2).

Table 6. Properties of all adsorbents used in this study. Specific surface area (SSA), C_{BET} constant and micropore volume (V_{micro}) from BET measurements, coordination number (CN) from TGA investigations.

Adsorbent	origin	SSA in $m^2 g^{-1}$	C_{BET}	V_{micro} in ml g^{-1}	CN in 1 node^{-1}
UiO-66-a	MRT batch	847.40	586.60	0.34	7.92
UiO-66-b	Regular batch	1210.50	683.70	0.51	10.53
UiO-66-c	STREM	1049.80	2859.40	0.40	11.71
UiO-66-d	ProfMOF	1206.20	1492.10	0.47	11.53
UiO-67	ProfMOF	1188.90	3141.70	0.47	-
UiO-66(ADC)	ProfMOF	675.00	1080.60	0.28	-
CAU-10-H	ProfMOF	595.60	3246.80	0.24	-
HKUST-1	BASF	1503.90	27499.80	0.60	-
MOF-177	BASF	4134.30	698.20	1.65	-
ZIF-8	BASF	1210.60	*	0.58	-
ZIF-67	MOFtechnologies	1448.70	2019.80	0.53	-
Tenax TA	BASF	23.00	71.30	n.a.	-

* Single point SSA calculation, therefore no C constant.

4.2.2 Thermogravimetric analysis of UiO-66 type MOF samples

Due to their high thermal stability, **UiO-66** type MOFs can be characterized with respect to their coordination number (linkers per node) using thermogravimetric analysis (TGA). In TGA under atmospheric air, ZrO_2 will be the final residual decomposition product left after the main decomposition at approximately 500 °C. Consequently, relative amounts of organic component (linker) can be determined before this decomposition. [151], [154], [192] TGA plots for the four **UiO-66** type MOFs are shown in Figure 45. Further details are given in the appendix (section 6.6.1).

Certainly, linker deficiency is only one type of defect that is accompanied by others in MOFs. [164] For instance, the nature of ligands, e.g. hydroxyl or chloride ions, occupying the linker deficient sites will not only distort the coordination numbers as determined by

TGA but also show different interaction potentials with guest molecules in the framework, resulting in different adsorption behavior. Still, coordination numbers determined by TGA provide a significant material property. However, no discrimination between free, mono-coordinated and regularly coordinated linkers in the framework can be made.

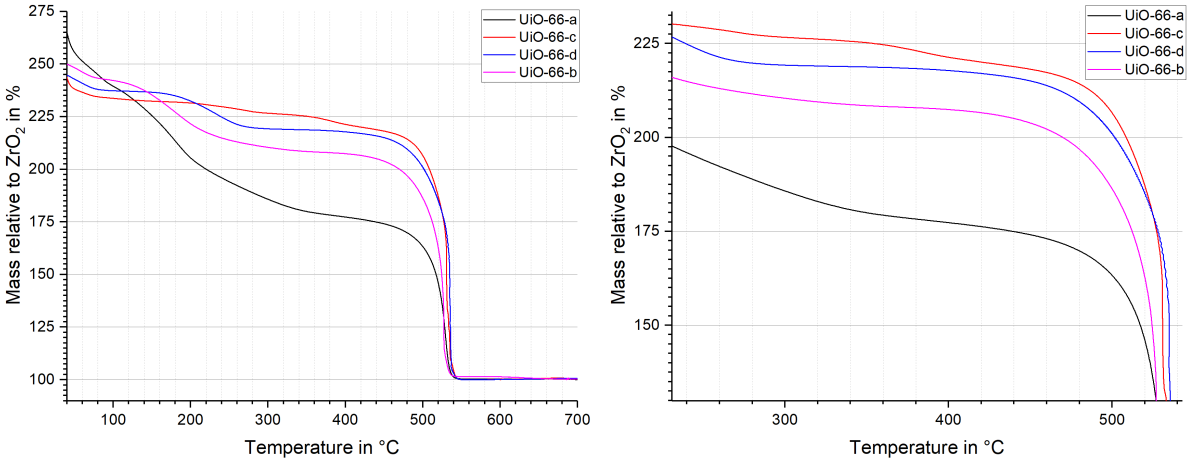

Figure 45. TGA plots for UiO-66 type samples used in this study using a heating rate of 10 K min^{-1} under air atmosphere. Left: Complete plot, right: Zoomed-in area.

Masses relative to ZrO_2 (being 100%) of **UiO-66** samples were determined at their inflection point (near 340 to 360 °C). The step at 500 °C represents the combustion of the terephthalic linker. Although dehydration of $Zr_6O_x(OH)_{8-x}$ to Zr_6O_6 can be assumed at this stage, an average coordination number was calculated using equal ratios of $Zr_6O_4(OH)_4$, Zr_6O_8 and Zr_6O_6 clusters for $m_{Cluster}$ according to the following formula:

$$n_{Linker} = 2\frac{\left(\left((m_{rel}-1)\cdot m_{Zr_6O_{12}}\right)+m_{Zr_6O_{12}}-m_{Cluster}\right)}{m_{BDC}} \qquad (47)$$

with $m_{Cluster}$ being the mass of 1 mol of the respective cluster, m_{BDC} being the mass of 1 mol of deprotonated terephthalic acid and $m_{Zr_6O_{12}}$ the molecular mass of 6 moles of ZrO_2. As linear heating rates of 10 K min^{-1} were used, an equilibration of all possible node configurations cannot be entirely assumed, as the kinetics for these processes are unknown and may not only rely on textural properties but also on solid guest molecules, as well as particle shape and size. A table with different hypothetical clusters and resulting coordination numbers is given in the appendix (Table 20).

4.2.3 Enhancement factors by thermal desorption

Sorbents were equally prepared and pre-conditioned at 200 °C to remove volatile and semi-volatile impurities before sampling and thermal desorption. Experiments were repeated at least twice with a fresh sampling tube for dry and humid conditions to avoid materials degradation, especially due to water.

Aiming to determine detector-independent preconcentration or enhancements factors (EFs) by thermal desorption, investigations needed to be standardized first. Enhancement factors are analyte-related peak heights occurring during thermal desorption, normalized towards the analyte concentration during sampling and the adsorbent mass. In this study, enhancement factors (EF) were calculated using the following formula:

$$EF = \frac{S_{peak} - S_{BL,\ source}}{S_{BL,\ source} \cdot m_{MOF}} \qquad (48)$$

With S_{peak} being the signal level at the maximum of the desorption peak, $S_{BL,\ source}$ the signal level caused by the source concentration during sampling (1 ppm_V of benzene in nitrogen carrier gas) and m_{MOF} the mass of MOF used in this sampling and desorption experiments (in g).

Looking at their TGA plots, it is evident that for most MOFs within this series, 200 °C is clearly not the maximum feasible desorption temperature. However, for **HKUST-1**, the decomposition background increases at above 220 °C that can affect the reliable detection of desorbed guest-molecules. This may also occur for other adsorbents or MOFs. Therefore, 200 °C was chosen as the universal thermal desorption temperature for all investigations.

As most MOFs show a non-negligible water retention, thermal desorption measurements were performed using dry (0 %rH) and humid (50 %rH) nitrogen 5.0) carrier gas-background, while for desorption always dry nitrogen was used. In no case, a preliminary adsorbent breakthrough within the sampling timeframe of 600 s was observed for the

benzene mass channel of m/z = 78, meaning not any adsorbent capacity for benzene was depleted during sampling.

With all adsorbents included, a neat correlation of dry and humid enrichment factors (EFs) is maintained throughout all adsorbents (Figure 46). In most cases, humid sampling environment resulted in lower error bars, i.e. stabilizing repeatability. **Tenax** is showing the peak EFs under both conditions (above 10^4). This can be explained by both, experimental parameters and materials properties.

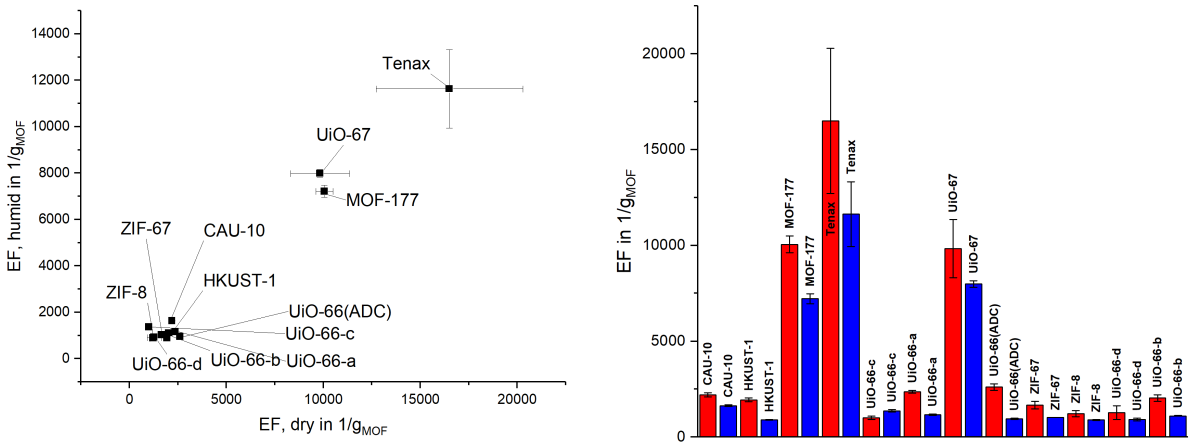

Figure 46. Left: Scatter plot of dry and humid EFs for all sorbents used in this study. Right: Barchart showing benzene EFs under dry (red, 0 %rH, i.e. pure nitrogen 5.0) and humid (blue, 50 %rH) conditions for all adsorbents used in this study. Abbreviations explained in Table 6, explanation of EF calculation in section 3.2.1, equation (48).

Contrary to the first part of the thesis, sampling was not done until sorbent saturation (analyte breakthrough prior to thermal desorption, section 4.1.6) but only for a fixed timeframe (600s). Hence, the unusual high benzene capacity of MOFs is far from being exhausted, while Tenax might be closer to saturation, a suggested by benzene retention volume determinations. [322] Benzene capacities of **HKUST-1** and **MIL-53** were determined to be two orders of magnitude higher than for Tenax, [322] which means their saturation is most likely at about 1% of **Tenax**´s saturation. Also, it was recently shown that in a non-convective sampling system, **HKUST-1** sampling times of 60 minutes for benzene are still not within saturation with respect to preconcentration factors. [314] Being only partially occupied with benzene guest molecules, re-adsorption in the

remaining unoccupied vacancies of MOFs lead to poor enrichment factors if not completely saturated (breakthrough) prior to thermal desorption. Also, being a polymeric and macroporous adsorbent with significantly lower water retention than MOFs, faster mass transport and therefore high EFs by trend an expected behavior for **Tenax**. However, the general repeatability for **Tenax** was poor, which was also observed in the literature. [40], [41]

Intermediate factors (around 10^4 for dry and $7 \cdot 10^3$ for humid conditions) are achieved using MOFs bearing larger organic linkers, namely **MOF-177** (BTB-linker, 1,3,5-Tris(4-carboxyphenyl)benzene) and **UiO-67** (BPDC-linker, 4,4′-biphenyldicarboxylic acid), which both show low water retention. The datapoint-cluster with lower enrichment factors contains all other MOFs used in this study (Figure 47).

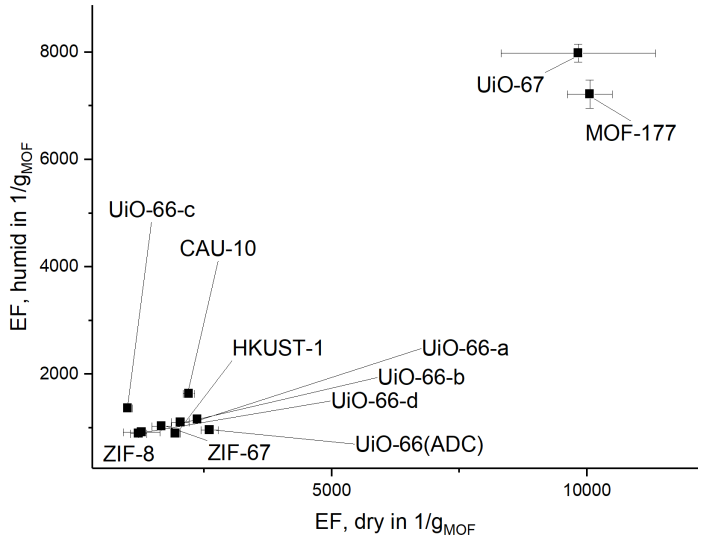

Figure 47. Scatter plot of dry and humid benzene enrichment factors (EF) for all MOFs used in this study. Abbreviations explained in Table 6, explanation of EF calculation in section 3.2.1, equation (48).

Zeolitic imidazolate frameworks **ZIF-8** (Zn) and **ZIF-67** (Co) show comparable enrichment factors of above 10^3 with **ZIF-67** showing higher ones than **ZIF-8**, likely an effect of its larger surface area as the critical pore aperture only differs by 0.1 Å. [323] **ZIF-67** loses over 38% of its EFs due to water, **ZIF-8** only 26%. Carboxylate-based non-UiO MOFs **HKUST-1** (Cu) and **CAU-10** (Al) show EFs of $1.9 \cdot 10^3$ and $2.2 \cdot 10^3$, respectively.

Humid conditions lead to a loss of 54% and 26% for **HKUST-1** and **CAU-10**, respectively. **HKUST-1** shows a higher affinity towards water than **CAU-10**, which is in agreement with literature observations. [184]

Correlations between thermal desorption and iGC experiments, as shown in the previous results chapter (section 4.1.6), seem to lose their significance in case of benzene: Retention volume ratios (value at 50 °C divided by value at 200 °C) of 216 were determined for **HKUST-1**, while only ratios of 2.7 were determined for **Tenax** in the literature. [322] This suggests **HKUST-1** may show higher EFs than **Tenax**, which is not observed here. Again, this may be due to sampling times and loadings, as discussed above.

Looking at the Zr based **UiO-66** family, a total of four different sources for **UiO-66** (BDC) were investigated, two from commercial sources and two from own synthesis (batch and using high flow rate continuous synthesis). They all show varying textural and thermogravimetric properties. They vary in specific surface area as revealed by the BET model as well as in the coordination number derived from thermogravimetric analysis. This clearly shows the parameter sensitivity in MOF synthesis.

Looking at structurally comparable MOFs (similar metal nodes ($Zr_6O_x(OH)_{8-x}$) and linkers, BDC) that only may vary in terms of guest molecules, defects (Cl^- or OH^-) and overall pore structure, a comparison in EFs is straightforward. It is evident that the coordination number (number of organic linkers per metal node, explained in section 4.2.2) and specific surface area does directly affect preconcentration capabilities, i.e. enhancement factors as illustrated in Figure 48, however, no clear connection can be established.

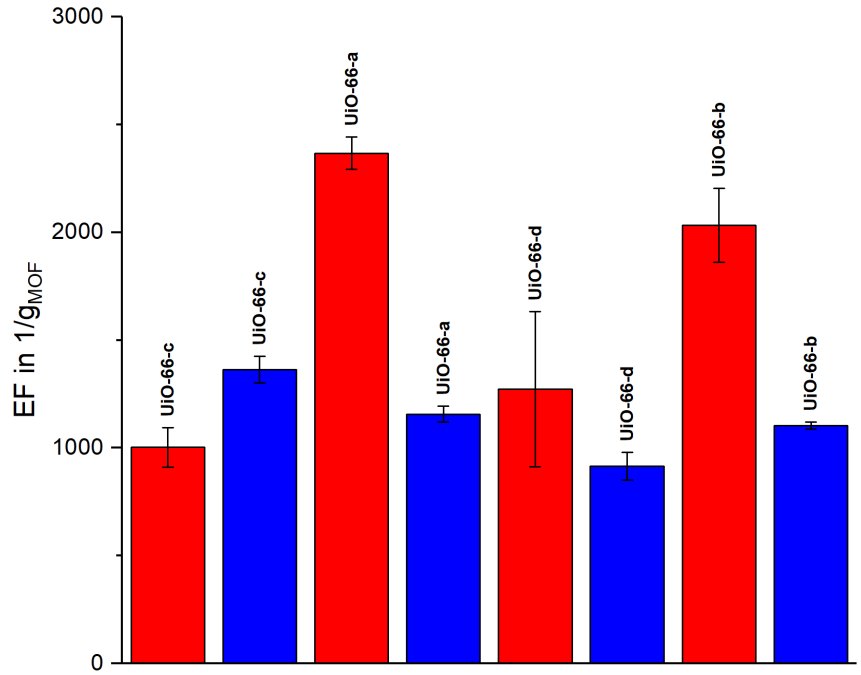

Figure 48. Barchart showing benzene EFs under dry (red, 0 %rH, i.e. pure nitrogen 5.0) and humid (blue, 50 %rH) conditions for all UiO-66 type MOFs used in this study.

While at dry conditions, the low-coordinated (**UiO-66-a**, also showing the lowest SSA, 847.4 m^2 g^{-1}) shows the highest EFs, it is greatly diminished under humid conditions (more than 50%). As the exact nature of defects is not known, but likely occupied with ionic species, atmospheric water is likely to occupy these vacancies during humid sampling, effectively competing with benzene molecules for adsorption sites. This is supported by **UiO-66-a** showing the highest water desorption peak heights of all adsorbents (appendix, section 6.6.4).

Under dry conditions, the general trend for EFs is **UiO-66-a** > **UiO-66-b** > **UiO-66-d** > **UiO-66-c**, i.e. the lowest specific surface area and linker coordination number shows the best performance while the MOFs exhibiting the highest linker coordination feature the weakest enrichment factors. It could be also due to samples **a** and **b** post-synthetic processing (washing etc.), a parameter that is not known for samples **c** and **d** from commercial sources.

This trend is changed under humid conditions: **UiO-66-c** > **UiO-66-a** > **UiO-66-b** > **UiO-66-d**. The commercial UiO-66 samples **c** and **d**, showing an almost identical specific surface areas (SSA), mark the start and end of the trend series. This supports the hypothesis that defects, resulting in either changed pore-sizes or ionic ligand species, drive the competitive adsorption of benzene and water.

In both series, the larger pore **UiO-67** shows the highest enrichment factors. **UiO-66(ADC)**, **UiO-66** with an acetylene-based linker, shows results comparable to regular **UiO-66**. The narrow pores, resulting from this short linker does not significantly change benzene adsorption/desorption.

The observed difference between dry and humid conditions is not only observed for **UiO-66-a** (lowest SSA), but also for **UiO-66-b** (highest SSA) and **UiO-66-d** (second highest SSA). Only **UiO-66-c** (1049.8 m^2 g^{-1}) shows a contrary behavior, i.e. higher EFs under humid conditions (Figure 49).

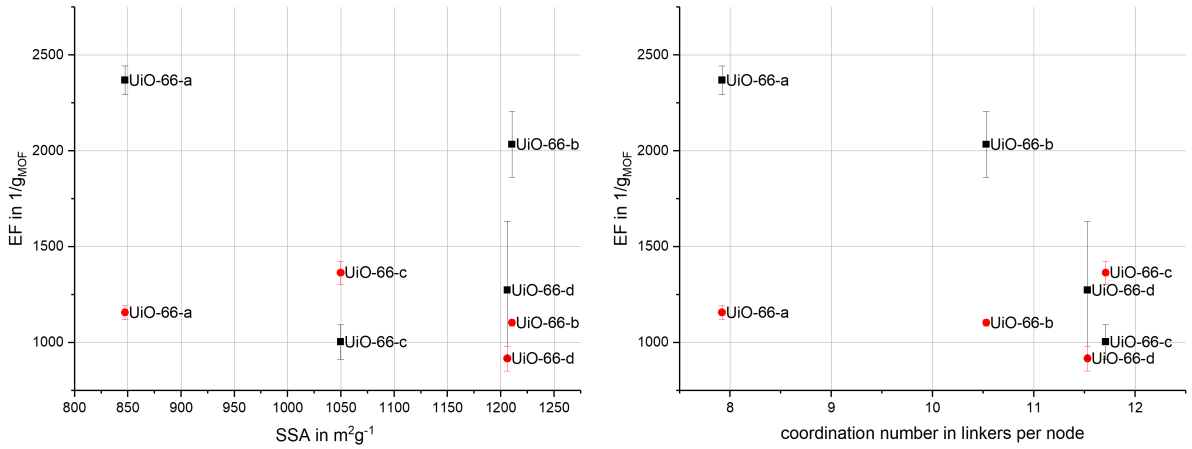

Figure 49. Scatter plots for all UiO-66 samples within this study. Left: EFs vs. specific surface area under dry (black) and humid (red) conditions. Right: EFs vs. coordination numbers under dry (black) and humid (red) conditions.

When the average coordination number (in linkers per node) as determined by TGA measurements is considered, it is evident that under dry conditions the **UiO-66** sample series follows an inverse relationship of coordination number and EFs, while at humid conditions a straight line with a small slope represents the relationship.

From this perspective, low coordination numbers seem to lead to high differences in enrichment factors during dry and wet adsorption. This behavior could be due to the pore system becoming more hydrophilic, preferring water over benzene. [152] Also, as the coordination numbers by TGA are ensemble-averaged values, they might indicate an increasing amount of undefined non-UiO-66-based porous phases, which show a higher benzene affinity as compared to **UiO-66** under dry conditions, but also a high affinity towards water. Furthermore, Figure 49 also indicates that at a specific coordination number the difference between EFs under dry and humid conditions reaches a minimum value for this UiO-66 series.

However, 50% relative humidity is still below the 80% threshold, where in defective UiO-66 structures the pore condensation of water was shown to occur. [152] Using molecular modelling and adsorption isotherms, it was also shown that different linker functionalities are capable of drastically alter the CH_4/CO_2 selectivities and affinities. [324], [325] Uncoordinated or mono-coordinated BDC linkers could increase UiO-66s favor of water as carboxylic acid is a polar functional group. This effect is emphasized using more polar or even reactive guest molecules like NO_2 for hazardous gas capture. [326]–[328] This trend is reversed when methyl groups are introduced at the linker, increasing affinities for non-polar molecules, but mainly due to additional pore-confinement and resulting adsorption potential overlap. [270]

A strong difference between **UiO-66** samples exhibiting variable coordination numbers was already observed during the sampling period. While **UiO-66-a** (example in Figure 50) as well as **UiO-66-b** and **UiO-66-d** did not show a preliminary breakthrough, **UiO-66-c**, the sample with the highest linker coordination number, did show this behavior. Moreover, a delayed increase of the water signal (mass channel 18) is observed in this case as compared to **UiO-66-a**.

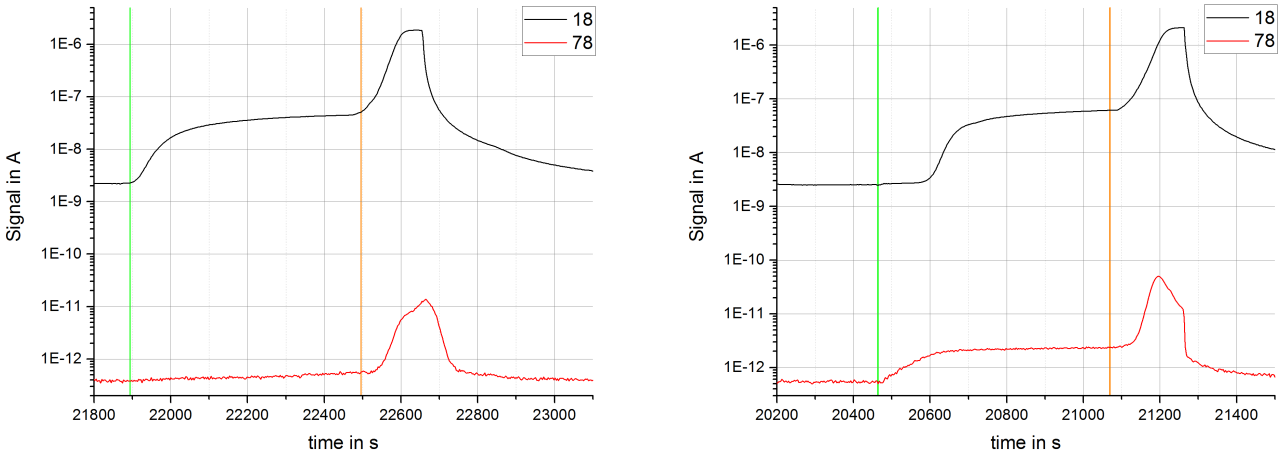

UiO-66-a **UiO-66-c**

Figure 50. Comparison of water (m/z=18) and benzene (m/z=78) mass channel signals during sampling (starting at green line) and thermal desorption (starting at the red line) for U-LC (left) and U-ST (right) using humid conditions. Left: Sampling period starting at 21900 s, temperature increase for desorption starting at 22500 s. Right: Sampling period starting at 20465 s, temperature increase for desorption starting at 21065 s.

UiO-66-d (11.53 linkers per node) and **UiO-66-b** (10.53 linkers per node) did not show this behavior. They also showed the smallest water desorption peaks within the **UiO-66**-type series under dry and humid conditions (appendix, Figure 65). With the degree of linker coordination, water and benzene competitive adsorption seems to be increased. This is the case even though high coordination numbers lead to less exposed inorganic components within the pore, which effectively shows a preferred interaction with polar water molecules. Additionally, low coordination numbers in combination with hydroxylation of the vacant sites are known to increase the adsorption of polar gases like CO_2. [153]

In case of **UiO-66**, a favor for polar guest molecules is reported to be accompanied by the increased aperture of its tetrahedral pores from 8.5 to 11.5 Å. [154] In combination, this may lead to an increased capacity for water molecules, hence delaying the point where the competitive adsorption of both adsorbates will result in a preliminary breakthrough of benzene.

This preliminary breakthrough behavior is not seen for the larger pore containing **UiO-67**. Due to its biphenyl-based linkers, pore sizes are larger (octahedral pore 23 Å and

tetrahedral pore 11.5 Å) [154] and seem to avoid this effect either by a superior capacity for water or by a strong favor for non-polar guest molecules as a result of the linkers being the major component of the pore walls. A similar mechanism is expected for **MOF-177**. [329]

However, during repeated runs, the opposite was observed, i.e. a decrease in EFs during consecutive runs under dry conditions and an increase in EFs during consecutive runs under humid conditions. Adsorbent behavior with respect to repeated runs is shown in the appendix (6.6.3). Also, a table with water signal-based (mass channel 18) EFs during thermal desorption measurements is shown in the appendix (6.6.4).

4.2.4 Inverse gas chromatography investigations

Due to their varying behavior in dry and humid benzene sampling, UiO-66 type MOFs of varying coordination numbers (**UiO-66-a**, **-b**, **-c** and **-d**) were investigated using inverse gas chromatography. BTEX compounds were chosen as aromatic probe molecules, linear alkane probes were used to indicate the non-specific interaction with the frameworks. Carrier gas flows from 18.4 to 27.6 ml_n min^{-1} were chosen. A large spreading, although general correlation towards molar weight (M_W) with respect to different probe molecules (grouped by molar weight) on all **UiO-66** adsorbents is shown in Figure 51. A molecular sieving effect can be observed for all four MOFs, although showing different slopes. While **UiO-66-d** shows a small slope, **UiO-66-c** shows a large one. Large deviations can be seen for C8-aromatics, an indication for steric effects with respect to thermal framework dynamics. Generally, **UiO-66-d** shows the highest enthalpies of adsorption for benzene, toluene and m-xylene.

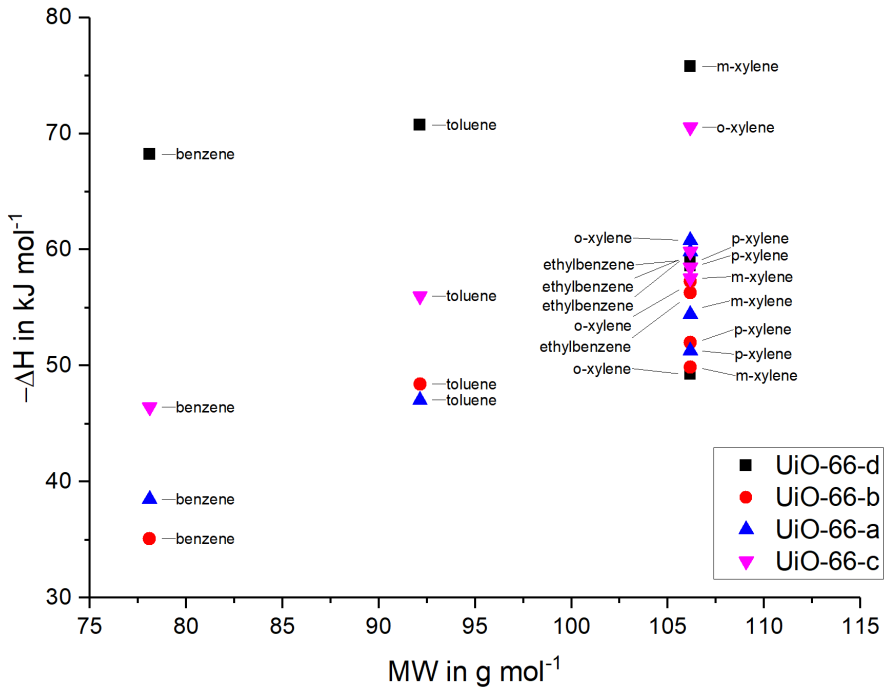

Figure 51. Enthalpies (in kJ mol^{-1}) of adsorption for all BTEX compounds by molar weight for four differently synthesized UiO-66 materials.

iGC investigations using Alkane probes

When carbon number plots (plotting free enthalpies of adsorption versus the linear carbon number of the probe molecule) are considered, it is evident that although MOF samples show similar specific surface areas (SSA) and coordination numbers, their non-specific sorption behavior is clearly different. With increasing carbon number, polarizability and molar weight of n-alkanes are increased as well, leading to a linear relationship which can be used to determine the non-specific (dispersive) component γ_s^D of the surface energy.

Generally, due to rising temperature, molecular interaction gets suppressed. [310], [330], [331] For porous materials, this trend may contain local maxima and minima as a result of temperature dependent dynamical behavior in the framework, e.g. specific surfaces being inaccessible at lower temperatures. [260] A general trend is reflected in the thermal behavior of γ_s^D. Individual values are shown in Figure 52.

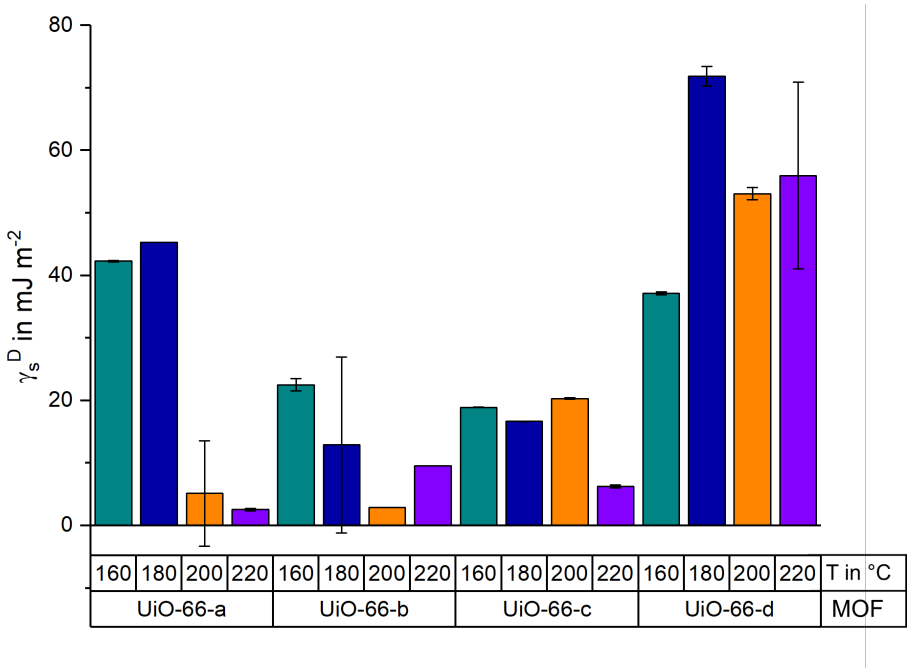

Figure 52. Dispersive component of the surface energy for UiO-66 type MOFs used in this study for 160, 180, 200 and 220 °C.

With respect to γ_s^D values, **UiO-66-c** showed the smallest errors in regression analysis and the most constant behavior with respect to temperature. At lower temperatures, it also features the lowest values throughout the series. In contrast, **UiO-66-d** shows the highest values, another deviation from the series. **UiO-66-b**, showing a similar specific surface area but slightly lower coordination numbers, shows only values that are approximately half the ones that were calculated for **UiO-66-d**. This could be explained by an excess amount of organic linkers due to poor activation (uncoordinated or only mono-coordinated) being present in the framework, effectively erroneously enlarging the coordination number as determined by TGA.

Plotting the derived enthalpies and entropies of adsorption versus the number of carbon atoms in the respective probe molecule, the adsorption enthalpy (α) and entropy (γ) per methylene group (-CH_2) can be derived from the slope of a linear fit. [307] The confinement factor Z can be calculated using both parameters:

$$Z = \frac{\gamma}{\alpha} \qquad (49)$$

In zeolite materials, larger confinement factors are found for microporous materials featuring smaller pores, e.g. 0.87 for Mordenite (7.0 x 6.5 Å pore size) or 1.26 for ZSM-23 (4.5 x 5.2 Å). [307]

In case of UiO-66 materials, values of 1.68 are found for **UiO-66-c** showing the highest coordination number. **UiO-66-a** (lowest coordination number) also shows a confinement factor of 1.43 while **UiO-66-d** exhibits only 0.78, which is primarily due to its poor entropy carbon number correlation (R^2 = 0.79). No meaningful values could be derived for **UiO-66-b**. Apparent from infrared spectroscopy, **UiO-66-b** has degraded to a certain extent during iGC measurements (appendix, Figure 67), therefore most certainly not having shown constant material behavior.

iGC investigations using BTEX compounds

BTEX compounds exhibit one aromatic ring complemented with differently arranged methylene-based groups. This results in different physicochemical properties. While the critical kinetic diameters of m- and o-xylene are 7.1 and 7.4 Å, ethylbenzene and p-xylene only exhibit 6.7 Å. [252] P-xylene also shows the lowest boiling point within the xylenes, 138.4 °C, followed by m-xylene (139.2 °C) and o-xylene (144.4 °C) and the lowest dipole moment (0.1 D) due to symmetry. Ethylbenzene shows an even lower boiling point than all xylene isomers (136.2 °C). [252]

Generally, **UiO-66** exhibits two types of microporous cages (tetrahedral 8 Å and octahedral 11 Å) connected by microporous, triangular windows of 5 to 7 Å. Especially the smaller tetrahedral pores are comparable to the critical diameters of xylenes and ethylbenzene leading to different adsorption behavior. [332]–[334]

A straightforward way to validate whether adsorption behavior is a result of steric features of the adsorbent and not due to physicochemical properties of the probe

molecules is plotting their logarithmized Henry constants (or retention volume) against their logarithmized saturation vapor pressures (Figure 53).

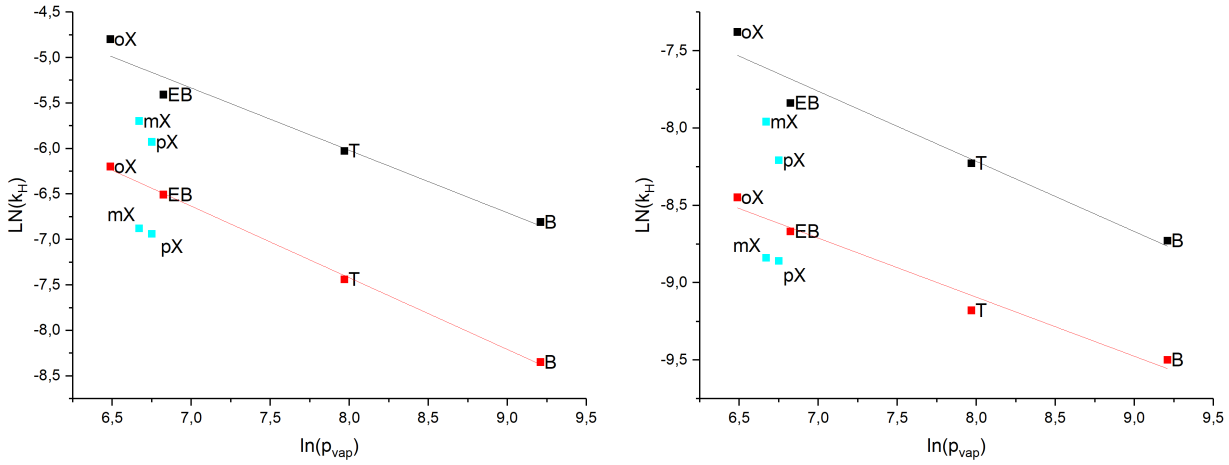

Figure 53. Plots of logarithmized Henry constants of UiO-66-c (black) and UiO-66-a (red) vs. logarithmized vapor pressure of the respective probe molecule at different temperatures (left 160 °C, right 220 °C). Data points with respect to vapor pressure: benzene (B: 9.21), toluene (T: 7.97), o-, m- and p-xylene (oX, mX and pX: 6.48, 6.67 and 6.75, respectively) and ethylbenzene (EB: 6.82). O- and m-xylene (cyan) are excluded from regression lines in both cases.

This way, it is evident that while there is an almost linear relationship for benzene, toluene, o-xylene and ethylbenzene, m- and o-xylene strongly deviate from this series. In case of **UiO-66-a**, the linear correlation is higher at both temperatures shown, while in case of **UiO-66-c** an additional discrimination between m- and p-xylene (with respect to regression line offset) is observed, which is not the case for **UiO-66-a**. This most probably due to steric effects and is reflected in the confinement factor *Z* derived from iGC investigations using n-alkanes. Furthermore, m- and p-xylene discrimination is increased with higher temperatures, indicating that accessibility or framework dynamics may be the driving factor for this behavior.

The thermodynamic compensation effect for all four UiO-66 samples is shown in Figure 54. This plot refers to the mode of adsorption, i.e. the specificity of adsorbent-adsorbate interaction in terms of the compensation between entropy (due to adsorbate degrees of

freedom lost upon adsorption) and enthalpy gained by the adsorbent in terms of kinetic energy upon adsorption.

In case n-alkanes are plotted in this fashion, the slope directly yields the respective confinement factor *Z*. The slopes in this plot are almost identical for three of four MOFs, indicating a similar kind of specific surface or adsorption site in their case. Interestingly, the deviating MOF is not the one with the lowest coordination number (**UiO-66-a**) but the one with the second highest one (**UiO-66-d**). As the synthesis as well as activation details and method of this commercial MOF is undisclosed, this observation cannot be further explained.

It is notable, that **UiO-66-d** showed the exact opposite behavior in alkane-derived confinement factors, namely the lowest confinement throughout the series. It underlines, that the adsorption mechanism deviates for both non-specific (n-alkanes) and specific (aromatics) interactions.

After all, it is obvious that neither specific surface area nor coordination numbers are the major factors influencing the behavior at zero coverage. The interaction sites being prevalent during this sorption processes (high surface energy) seem to be inaccessible by those rather macroscopic methods.

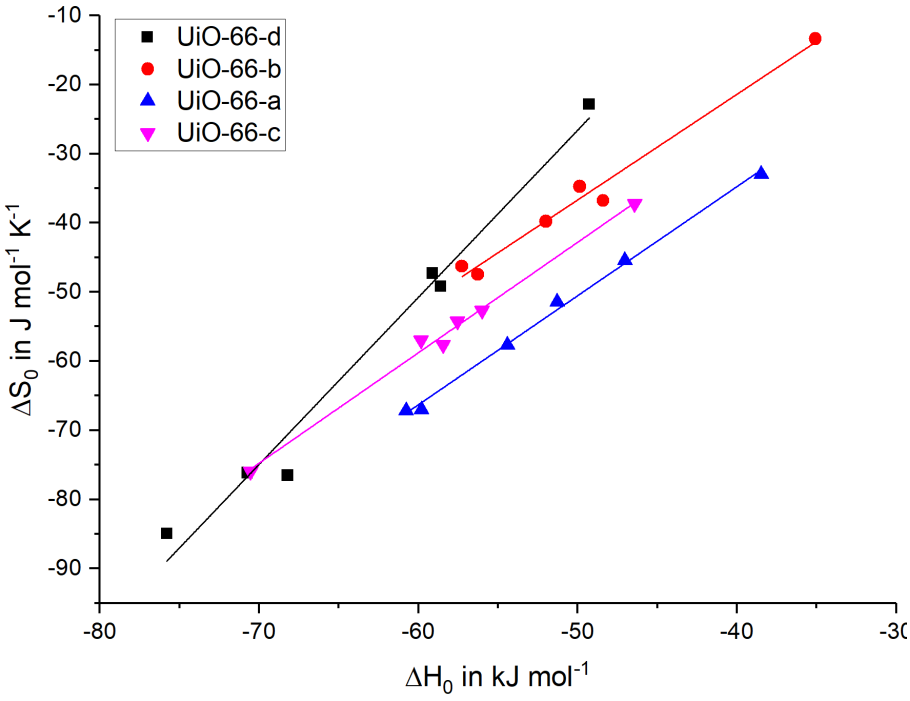

Figure 54. Thermodynamic compensation plot for BTEX compounds on four UiO-66 MOFs.

Due to sufficiently low errors in regression analysis in free enthalpy vs. carbon number plots, specific interactions of BTEX compounds with respect to alkane lines could only be derived for **UiO-66-c**. A temperature dependence was found, reaching a maximum for all compounds at 200 °C (7.2 to 9.9 kJ mol^{-1}), decreasing again at higher temperatures. An illustration for the derivation of specific interactions and their values on **UiO-66-c** is given in Figure 55.

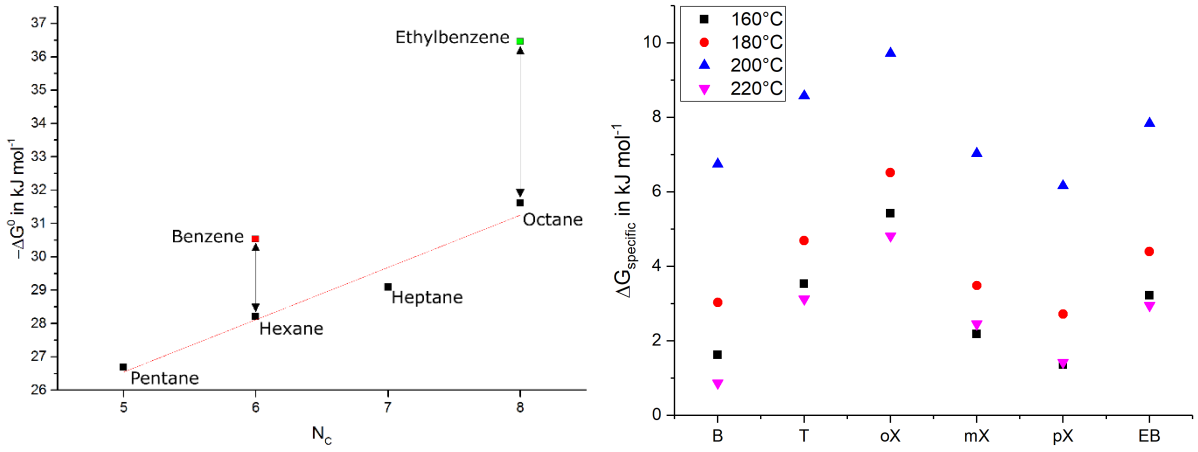

Figure 55. Specific interaction in terms of free adsorption enthalpy. Left: Example for specific interaction offset for benzene(red) and ethylbenzene or xylenes (green) with respect to the alkane line (black data points). Right: Specific interactions for all BTEX compounds at different temperatures for UiO-66-c.

The increase starting from 160 to 200 °C could be attributed to easier accessibility of pore system areas that probe molecules were not capable of at lower temperatures. [335]

As discrimination between xylene isomers also increased at elevated temperatures, it could more precisely relate to the tetrahedral pores, which were identified for xylene discrimination due to entropic effects (adsorbates rotational degrees of freedom). O-xylene, showing the highest specific interaction due to its molecular dimensions (small van der Waals volume and large kinetic diameter), is assumed to show an improved adsorption (retention) in both pores, the octahedral and the tetrahedral one. [334]

Looking at Figure 51, **UiO-66**s general favor of benzene over hexane due to linker adsorbate π-stacking [336]–[338] could be verified. The more general drop in specific interaction at 220 °C cannot be explained. A formation of the Zr_6O_6 clusters from existing $Zr_6O_x(OH)_{8-x}$ clusters is unlikely as this transition happens at 300 °C in vacuum. [151] However, dehydroxylation of **UiO-66** gradually starts at 200 °C. [151] If preconditioning UiO-66 samples at 200 °C for at least 24 h did not sufficiently remove all structural water molecules resulting in an undefined mixture of Zr_6O_8 and $Zr_6(OH)_8$, this would lead to different material properties and specific interactions with probe molecules.

In a recent publication, it was shown that three differently synthesized batches of IRMOF-1, all showing different specific surface areas, did show completely different properties in iGC experiments. [261] BET surface areas ranging from 208 to 1161 $m^2\ g^{-1}$ go along with confinement factors ranging from 0.99 to 1.12. They are calculated from therein reported linear alkanes enthalpies and entropies. It is not clear if the observed effect emerges from a lack of pore structure, defects or reactant molecules being present in the MOF structure. However, the effect is significant and shows that even small amounts of defects have a massive impact on adsorption behavior in the Henry region.

While the sample from continuous synthesis and high flow rates (**UiO-66-a**) shows a coordination number of 7.92, the one from batch synthesis (**UiO-66-b**) shows one of 10.53, which is about 1.5 below the maximum. The two commercial samples (**UiO-66-c** and **UiO-66-d**) show almost identical coordination numbers (11.71 and 11.53, respectively) however a difference of 100 $m^2 g^{-1}$ in specific surface area.

On the one hand, this can indicate a greater amount of mono- or uncoordinated terephthalic acid in **UiO-66-c**, effectively resulting in a lower micropore content and an erroneous coordination number calculated from TGA measurements. On the other hand, it could indicate a loss of tetrahedral pores in **UiO-66-d** and an increased percentage of octahedral pores, increasing the specific surface area. As the interaction with aromatic molecules (BTEX compensation plot, Figure 54) of **UiO-66-d** is clearly deviating from the other 3 samples, the latter hypothesis is supported. However, a pore-size distribution would be needed to confirm this.

4.2.5 Application of MOFs in a non-convective sensing system

As selective sensing is the goal, a differentiation in retention volumes at sampling and desorption temperature between the target analyte (benzene) and interferents (e.g. toluene) is mandatory. This differentiation is reflected in the enthalpies of adsorption of all BTEX compounds on the four **UiO-66**-type MOFs (a, b, c and d) as shown in Table 22 (appendix). **UiO-66-c** does show the second highest adsorption enthalpy for benzene, namely 46.4 kJ mol^{-1}. Clearly, **UiO-66-d** shows an even higher value, 68.2 kJ mol^{-1}, however this value is very close to the ones of its interferents, e.g. toluene with 70.7 kJ mol^{-1}. This will result in poor separation, i.e. selectivity, especially with the entropy values for benzene and toluene being almost identical, 76.5 and 76.2 J mol^{-1} K^{-1}, respectively. Therefore, **UiO-66-c** should be chosen for further deposition experiments in a non-convective setup, that is illustrated in Figure 56.

The following section reports on 1st generation Basolite MOFs being used in such a preconcentrator module. Application and evaluation of **UiO-66-c** in preconcentration modules is still an ongoing task and cannot be reported here, as project partners do have commercial claims on the preconcentrator designs and results of the whole setup.

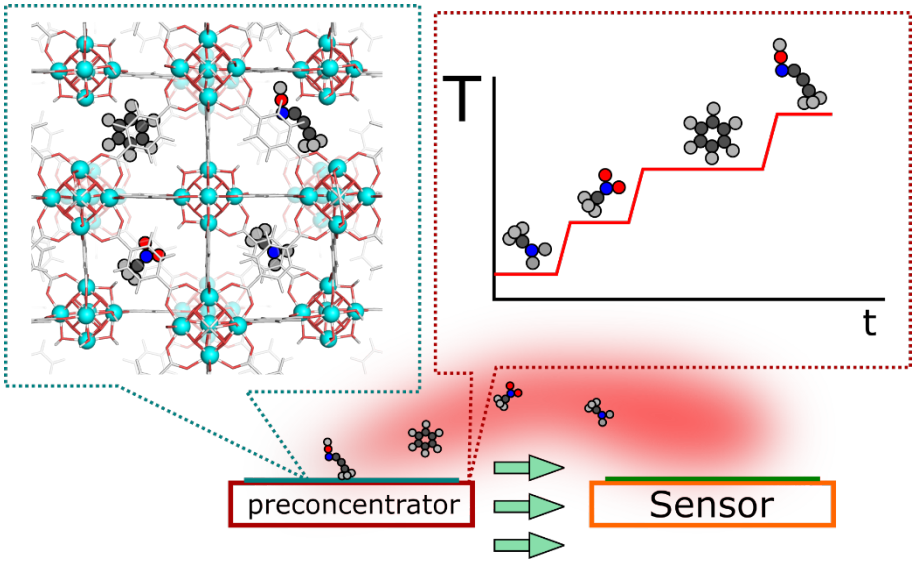

Figure 56. Concept of a diffusive sampling setup. After diffusive sampling in the adsorbent on top of the preconcentrator, the temperature is increased (once or stepwise). Via diffusion, the adsorbed molecules are transported to the sensor and detected.

Contrary to thermal desorption experiments shown in section 4.1 and 4.2, the preconcentration principle in this setup is based on diffusive mass transport. The adsorption of VOCs on the MOF material and its cyclic thermal desorption (by heating the preconcentrator, PC) is established by the individual VOC's diffusion in air.

As compared to active tube sampling, where a convection flow is used, this method creates losses in the amount of desorbed molecules with respect to the sensor: During desorption, analyte molecules will be distributed in all spatial dimensions, where the sensor only resembles one possible destination. This problem was avoided in the preconcentration setup as shown in 4.1 and 4.2 by a carrier-gas convection.

The sensor itself can be run in a so-called temperature cycling operation (TCO). [339], [340] This mode exploits the sensors different selectivities when operated at different

temperatures. Basically, a combination of temporally cycled virtual sensors is created as the sensors selectivities and sensitivities are temperature dependent.

Also, the preconcentrator itself could be run using a temperature program, effectively creating another dimension, comparable to a temperature ramp in gas chromatography, that can be used for algorithm development and component analysis. [66] In the following results, for the sake of parameter traceability, the preconcentrator was operated in cyclic on/off switching with a constant power supply, resulting in a constant desorption temperature.

Deposition of MOFs on heated elements, especially with high heating rates, is a challenging task as MOFs will in most cases not feature the same thermal expansion coefficients as the substrate or even negative ones. [341], [342] In addition, cohesion and adhesion were observed to be low for UiO-66-type MOFs if they are not directly grown on substrates. [343]

For the deposition experiments, no organic additives like adhesion increasing polymers can be used, as at elevated temperatures, their decomposition might create an unfavorable background, contaminate the MOF with decomposition products of delaminate the MOF layers. Therefore, MOFs were immersed in organic solvents, drop coated, and subsequently placed in an oven for the solvent to evaporate. Images of the typical substrates are shown in Figure 57. In these trials MIL-53 lead to unstable layers, often showing cracks and displacements after heating in the oven. Therefore, HKUST-1 was fourthly investigated in the non-convective setup. Substance amounts of approximately 30 mg were used in the following experiments.

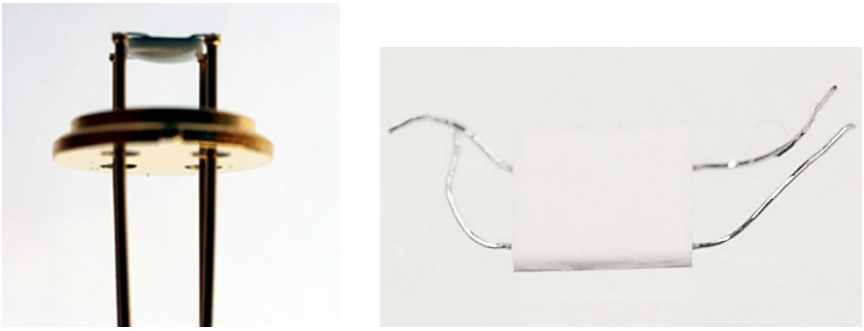

Figure 57. Left: Socket mounted (soldered) UST micro heater. Deposition on upper side. Right: UST-type micro heater detail. Dimensions of AlO_x part: 3x3 mm^2. Coating was done on the top side of the micro heater.

For concentration monitoring, due to better sensitivity and linearity, a mass spectrometer was used instead of the MOSFET. The mass spectrometer's linearity was evaluated by further diluting benzene carrier gas mixtures in gas sampling bags. Linearity from 100 ppb to 100 ppm was observed. A constant flow of carrier gas containing several concentrations of benzene was conducted through the measuring chamber (Figure 58), while the preconcentrators was switched off for a specific sampling time before being heated to 200 °C for 500 s by applying the respective voltage to its heating element.

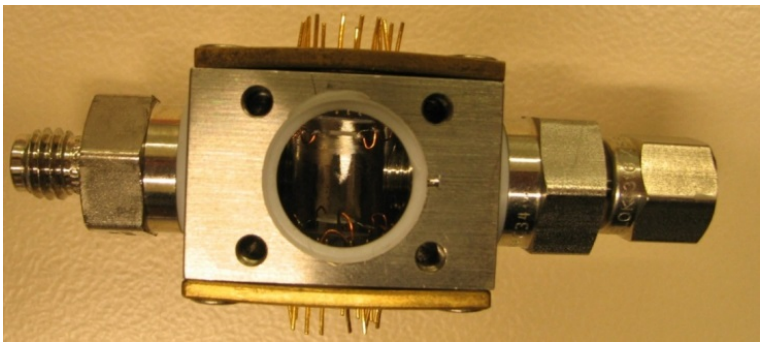

Figure 58. Measuring chamber (stainless steel) used for alumina-based preconcentrator testing, consisting of preconcentrator (top) and MOSFET sensor (bottom). Omitted: Gas sampling bags are on the right side, while mass spectrometer, mass flow controller and vacuum pump are installed on the right side of the measuring chamber.

The benzene-channel (m/z=78) of the mass spectrometer shows a clear peak when the preconcentrator is heated to 200 °C due to benzene desorption. Results using nitrogen 4.6 as background gas (Figure 59) are equal to investigations using zero-air as background gas.

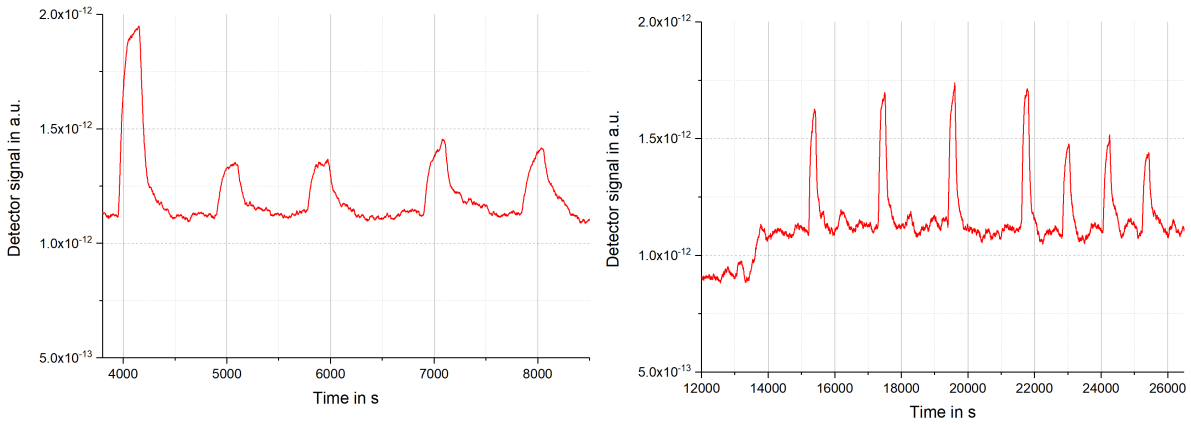

Figure 59. Left: Mass channel 78 (benzene) during HKUST-1 preconcentrator desorption at 200 °C after sampling times of 60, 10, 10, 15 and 10 minutes on a 1 ppm benzene source. Right: Sampling times of 30, 30, 30, 30, 15, 15 and 15 minutes on the same source of 1 ppm of benzene.

Below 20 minutes of sampling time, a linear relationship between sampling time and desorption peak area exists. On increasing the sampling time from 30 to 60 minutes, only a relative gain of 25% is observed ($7.9 \cdot 10^{-10}$ As for 60 min and $6.3 \cdot 10^{-10}$ As for 30 min). This indicates a beginning saturation of the MOF layer in the preconcentrator.

Using 10 ppm of benzene in zero air, enrichment factors of up to 7 (700%) were observed for sampling times of 60 minutes, 5.5 (550%) in case of 30 minutes. After each desorption cycle, a slight signal drop below the baseline can be observed. This is caused by re-adsorption of benzene as the hotplate is cooling to room temperature.

Repeatability of desorption experiments is neat, although peak height errors within 5-10% are observed. No clear trend in decreasing peak heights is seen that could indicate a degradation of HKUST-1 layers.

Using this setup, no sampling tubes containing MOFs have to be made and the atmosphere to be analyzed does not have to be conducted through a bed of adsorbent. In principle, no convection is needed for the preconcentrator to work. A bypassing convection was used to arrange for a constant background of benzene. Production of MOF-based preconcentrators this way is cheap and uncomplicated, as soon as the deposition method is developed. However, signal increases (enrichment factors) are orders of magnitude lower as compared to ones facilitated with convective tube sampling (section 4.2.3). This

is most certainly due to the overall design of diffusive sampling, where desorbed molecules are being distributed in all directions. In contrast, with tube sampling, all desorbed molecules are transported towards the detector in a small volume of carrier gas.

5 Conclusions and future work

This thesis had intention to incorporate novel, hybrid materials, namely metal-organic frameworks, into sensing and preconcentration applications for trace gas analysis. Thereby, a general concept for improving any sensor systems sensitivity and selectivity was sought. A possible technique to enhance both factors with respect to gas-phase sensing is thermal preconcentration.

A standardized technical and methodological basis to compare MOF materials with respect to guest molecules adsorption (at low concentration and room- or elevated temperature) was established. Inverse gas chromatography (iGC) was applied to study the MOF-analyte interaction at low coverage using various guest molecules from essentially two scenario-motivated families: Explosives and hazardous volatile organic compounds (VOCs). In both cases, additional analyte enrichment investigations by sampling and thermal desorption were done.

In the first part, a preconcentration concept for nitro-alkanes, for a sensitive sensing from the gas phase, using the commercially available archetype (type I) MOFs **HKUST-1** (Basolite C300), **MIL-53** (Basolite A100), **Fe-BTC** (Basolite F300) and **ZIF-8** (Basolite Z1200) was elaborated. The MOFs were utilized to adsorb and thereby increase the concentration of the analyte molecules. Inverse gas chromatography (iGC) turned out to be a suitable pre-screening method, where MOFs can easily be evaluated towards their affinity for target molecules in the gas phase (Henry constants as well as adsorption enthalpies and entropies). Archetype MOFs, and especially **HKUST-1** showed superior desorption peak heights as compared to **Tenax**.

Regarding nitro-alkanes, **HKUST-1** showed the largest ratios of low temperature (sampling) and high temperature (thermal desorption) Henry constants, reflected in the largest enthalpy of adsorption for the target molecule nitromethane. Using regular linear

hydrocarbon probes, the dispersive component of surface energies could be calculated for all MOFs. All MOFs investigated showed a decrease of this dispersive component at rising temperature with values ranging from 50 (**ZIF-8**) to above 100 mJ m^{-2} (**HKUST-1** and **Fe-BTC**).

Results from iGC experiments were correlated towards micro-breakthrough experiments with down streamed thermal desorption experiments. Again, **HKUST-1** showed remarkable enrichment factors (based on peak height and normalized towards sorbent mass) of above 2000 when sampling on a 1000 ppm_V nitromethane source, even though during sampling (breakthrough) the sorbent was heated to 100 °C. **MIL-53** and **Fe-BTC** showed values of around 300-500, whereas **ZIF-8** and **Tenax® TA** showed low enrichment factors of only 4 and 18, respectively. Using 1000 ppm_V nitromethane as sampling source, **HKUST-1** showed a more than 110-fold higher enrichment effect than the macroporous material **Tenax® TA**, the latter being a state-of-the-art adsorbent, while **Fe-BTC** and **MIL-53** showed about 18 to 30 times higher enrichment peak heights. Only **ZIF-8** showed lower results that lead to the conclusion that analyte molecules such as nitromethane cannot enter the microporous interior of **ZIF-8.**

In case of nitromethane and **HKUST-1**, the normalized enrichment factors were verified for sampling on a 1 ppm_V nitromethane source with subsequent thermal desorption in order to show the viability of this principle for low analyte concentrations. Preconcentration (or enrichment) factors were less than 5% lower than for sampling on a 1000 ppm_V source. In general, lowering the sampling temperature increases enrichment factors. However, it also allows for significant water adsorption in a relevant environment. In a possible relevant preconcentration scenario, e.g. using diffusive sampling with subsequent thermal desorption, enrichment factor losses due to lower initial gas concentrations can be compensated with increasing sampling intervals.

Under dry environment, Basolite MOFs can be re-used with a small decline in preconcentration capability for nitromethane. However, in realistic environments further problems might occur such as humidity posing a problem for **HKUST-1** at room temperature. Distinct solutions, such as sampling at 100 °C, can prevent water absorption and still provide enrichment factors that are only 30% less than for sampling at room temperature.

Thereby, the MOF-preconcentrator concept has been shown as a vital alternative for the direct analysis of low concentrations of nitroalkanes and alkanes. It can thereby enlarge the existing concepts of sensitive sensing, e.g. of explosives without being dependent on a special signal-transducing concept such as change in luminescence.

In the second part, the preconcentration setup and methodology was extended to the class of volatile organic compounds, in particular benzene from the class of BTEX compounds (benzene, toluene ethylbenzene and xylenes). This time, a range of type II MOFs was evaluated: **UiO-67**, **CAU-10-H**, **HKUST-1**, **MOF-177**, **ZIF-8**, **ZIF-67**. Also, four different batches of terephthalate **UiO-66**, both from own and commercial sources with varying textural properties, as well as an acetylene-linker-based linker version of **UiO-66** was included. As in the first part, comparisons towards the polymeric adsorbent **Tenax® TA** was drawn. Contrary to nitromethane sampling in part I, throughout the thermal desorption enrichment of benzene, **Tenax** proved the peak substance. This is most likely an effect of sampling times being too low for MOFs and humidity interfering with MOF-analyte interactions.

Enrichment factors were determined for benzene in concentration regimes of 1 ppm_V under dry and humid conditions by sampling for a defined period, followed by thermal desorption at 200 °C. Generally, **Tenax** outperformed all MOFs in both scenarios. Large-pore MOFs, such as **MOF-177** and **UiO-67** showed enrichment factors (EFs) being about

one order of magnitude lower than for **Tenax**. Especially **UiO-67** showed low relative decrease in EFs due to water background in subsequent desorption experiments.

The four different types of isostructural **UiO-66** type MOFs showed a strongly varying benzene enrichment behavior, although they share comparable textural properties, such as linker deficiency by TGA investigations and specific surface area as by the BET model. Using both parameters, no clear trend could be confirmed for the different **UiO-66** materials. Inverse gas chromatographic studies showed that linker coordination numbers did not correlate with varying dispersive surface energy values of these materials as determined by iGC with n-alkanes. Corresponding confinement factors as by iGC could partly be correlated with linker coordination numbers. Contrary to the first part of this work, no general trend in thermal desorption experiments could be explained by iGC investigations for the **UiO-66** subset of MOFs.

Altogether, this shows the major impact of synthesis and activation procedures on adsorption processes of organic molecules in the Henry region. This behavior was also observed in the literature and is most likely due to a degradation phase of **UiO-66** or non-coordinated reactants being located in or outside the pore system and showing a major impact on adsorption processes in the Henry region where the adsorbent-adsorbate interaction is strongly emphasized.

The strong impact of microscopic defects and structural features on the adsorption processes in the Henry region is a major challenge for MOF-based preconcentrators. As concentration quantification is in most cases required, strong variations in desorption peak heights due to non-standardized materials is to be avoided. Along with other problems, such as water retention and degradation of MOFs, especially thermal and mechanical layer stability have to be considered and optimized in a sensor system containing MOF-based preconcentrators.

The major conclusion of this work is that inverse gas chromatography proves to be a suitable screening and characterization method to study MOF-adsorbate interaction. It is not only possible to directly measure retention volumes at room temperatures, but also predicting these retention volumes at arbitrary temperatures once the adsorption enthalpy and entropy for this particular adsorbent-adsorbate combination are known. Using a range of chemically related compounds, even material constants such as the dispersive components of the surface energy can be determined, which allow for a characterization and comparison of MOFs from different sources as it is not accessible using traditional (TGA, BET, XRPD) methods.

6 Appendix

The appendix contains an overview of MOF synthesis methods and characterization techniques used in the scope of this thesis (6.1 and 6.2) as well as a review on selected MOF applications relevant for this thesis (6.3). Also, an explanation for the used ppm-notation and gas-sampling bag concentration calculation (6.4) is given. Finally, the appendix contains miscellaneous data and graphs for the two main result chapters (6.4 and 6.6).

6.1 MOF synthesis and handling

In order to achieve MOFs that do feature micropores and high specific surface area, their integrity during synthesis has to be maintained. [117] Due to self-assembly being the prevalent mechanism of their formation, MOF synthesis is in many cases very sensitive to changes in reactant ratios, temperature, pH value and solvent. [344] Also, the choice of the inorganic salt source is of crucial importance. The costs in MOF synthesis [345] are mainly driven by the reactant costs (metal salts, organic linkers and solvents) and the energy costs during synthesis. The additional solvent during successive washing steps as well as energy for the final activation are additional costs that increase the cost of commercially available MOFs.

A wide range of synthesis methods besides “traditional” solvothermal synthesis were reported. They are summarized in the following section (6.1.1).

6.1.1 Synthesis methods

In most cases, MOF syntheses are carried out in solution. Polar protic and non-protic solvents are used, for example alcohols, di-alkyl-formamides (namely dimethyl-formamide, DMF) or even water. In some cases, also so called modulators are used to

support the pre-arrangement of the building units prior to crystallization. [346] Reactions are heated in a convectional way and carried out at temperatures above 150 °C, i.e. solvothermal synthesis. Reaction times can range from several minutes (smaller particles and crystallites by trend) to two-digit hours or days. [139] As a practical example, the synthesis of Cobalt(II)-succinates yields no less than 7 different product phases depending on reactant ratios (also defining the pH) and reaction temperature. [347] The same was observed with the synthesis of ZIF-8 using microreaction technology (MRT). [348] As also reaction times were screened, this underlines the effort and costs that must expended in the optimization of typical MOF synthesis. [348]

Therefore, alternative synthesis methods were applied for MOFs, namely microwave-assisted, sonochemical, mechanochemical and electrochemical ones. [344] A different approach is the solvent free synthesis of MOFs by adding metal salts to melts of organic linkers. [349]–[352] Not only does it avoid the urge to use highly pure solvents, it also allows for MOF structures that are not accessible by solvent-based reactions. [350]

Co-doping of several metals within one MOF structure was also demonstrated with solvent free synthesis. [353]

Microwave (MW) assisted synthesis uses the direct interaction of microwaves (usually 300 MHz to 300 GHz) with the reaction mixture. Reportedly, only the magnetic component of the radiation itself shows a significant impact on the synthesis itself. [118] Molecules bearing a dipole will change their orientation in the electromagnetic field according to the applied frequency. On choosing an appropriate frequency, their collision probability will be increased, leading to an increase in overall kinetic energy. [344] This represents an efficient method of heating, with reaction times rarely exceeding 1 h, with particle sizes being generally smaller as for convectional heating.

The main mechanism that helps with sonochemical procedures are the cavitation-bubbles formed by largely alternating compression zones in the solvent while high-intensity acoustic waves (frequencies of 20 kHz to 10 MHz) are propagating through it. As opposed to MW-assisted synthesis, no direct interaction between the reactants and the acoustic wave does occur, as the wavelength is much larger than the molecular dimensions of the reactants. [139], [344]

However, in the close vicinity of these bubbles, high pressure and temperature gradients prevail, along with the fast release and re-capture of dissolved gases from the solvent. Heating and cooling rates in these cavitation bubbles lie above 10^{10} K s^{-1} with possible short-lived temperatures of about 5000 K and pressures of 1000 bars. [118] This mainly assists the nucleation, being the basic step for MOF crystal growth. [118] It also represents an energy efficient way to synthesize MOFs at mild conditions and room temperature. It has been recently shown that, by applying various ultrasound power-levels, the interpenetration of two MOF structures (CuTATB (TATB = 4,4′,4″-s-triazine-2,4,6-triyltribenzoate) could be tailored. Generally, high power-levels lead to more framework interpenetration. [354]

Mechanochemical (or mechanically-activated) synthesis of MOFs represents a relatively new strategy, being reported for the first time in 2006. [355] It involves the mechanical induced cleavage of chemical bonds within the reactants, followed by a chemical reaction. The hot-spot model suggests temperatures of above 1000 K lasting for 100 to 1000 μs, being local in nature. [118] The advantages are working mainly under solvent-free conditions and at room-temperature. [344] Reaction times are also usually below 1 hour, producing smaller particles as in solvothermal synthesis. Minimum amounts of solvent may be added to enhance the mobility of reactive species, effectively leading to higher reaction rates. Also, solvent molecules may exert a structure directing effect. Using

solvents, the process is referred to as liquid-assisted grinding (LAG). Recently, superparamagnetic Fe_3O_4/SiO_2 composite microparticles were coated with a luminescent MOF $_\infty^2[Ln_2Cl_6(bipy)_3]\cdot 2bipy$ (Ln = Eu, Tb and bipy = 4,4′-bipyridine) applying mechanochemistry. [356]

The key concept of electrochemical (EC) MOF synthesis is the introduction of metals by anodic dissolution during an electrochemical process. [118], [344] This anodic dissolution is carried out in a reaction solution containing dissolved linkers molecules. Also, a conducting salt is added. BASF used this concept to upscale the synthesis of their Basolite product families in 2005, being patented under WO 2005/049892. Inclusions of conductive salts in the MOF structure may pose a problem, as shown in a study comparing solvothermal and electrochemical synthesis of HKUST-1. [357] This method also provides the direct growth on suitable substrates, e.g. sensor coatings with tailorable thickness and strong adhesion. [358]

A different concept is liquid-phase epitaxy or layer-by-layer growth. It is not used for bulk-synthesis but for preparing MOF (mostly thin) films on various substrates. [359], [360] The reticular synthesis design is followed in terms of a stepwise routine, alternatingly exposing a surface towards solutions containing metal salts of organic linkers. Between each of these steps, the surface is washed with pure solvent, to remove excess reactants. Under ideal conditions, after one cycle, one unit cell of SURMOF (surface mounted MOF) is grown on the surface. If a transducing sensor element is being coated using this procedure, the growth of each layer can be monitored. [211], [361] However, in many cases substrates must be pre-functionalized to assist the MOF growth using self-assembled monolayers (SAMs). [362] In many cases, thiols or alkoxysilanes featuring amino or carboxylate groups are used. [211] This concept was already applied to the coating of GC capillary columns with HKUST-1. [363]

6.1.2 Activation

MOFs need to be activated before any application exploiting their pore volume in any way. Without activation, the void space within MOFs will be occupied by several families of guest molecules due to adsorption. Consequently, the active surface becomes inaccessible. Guest molecules can comprise solvent molecules, reactants of reaction products from the synthesis as well as humidity, CO_2 and other atmospheric components being adsorbed if an (partially) activated MOF is exposed to air. [136], [139]

The most common method is the removal of solvent and other guest molecules by a simple vacuum treatment, mostly at elevated temperature. This method is traditionally applied for zeolites or activated carbons as well. However, in case of MOFs, the transition of guest molecules from the liquid phase directly to the gas phase is accompanied by large surface tensions and capillary forces, that need to be compensated by the coordination bonds in the MOF structure. Therefore, this conventional activation may work in case of MOFs featuring strong bonds (e.g. UiO-66) but not for other ones. [136] A loss of crystallinity and pore volume are the immediate consequences of the pore system collapsing due to this effect. Post-synthetic thermal treatment in combination with vacuum can also be used to engineer mesoporosity into microporous MOFs, as it was demonstrated with $_{\infty}^{2}[Ln_2Cl_6(bipy)_3]\cdot 2bipy$ (Ln = Pr - Yb and bipy = 4,4′-bipyridine). [364] Without vacuum, an increasing formation of high-temperature phases in combination with bipyridine release was observed. [364]

An alternative method is a solvent exchange process with a more volatile and less polar solvent, prior to an activation featuring lower temperatures. Generally, the surface tension is minimized due to the exchanged solvent molecules featuring weaker interactions with the framework. [109]

Other methods for activating MOFs simply avoid the solvent molecules liquid-gas phase boundary after extraction. This can be achieved by two methods. One is using supercritical CO_2 and hence going from the liquid phase to the supercritical one, which is then used to wash or extract guest molecules from the framework. [136], [365] Afterwards, CO_2 goes directly from this supercritical state to the gaseous phase while leaving the framework. This method can be widely applied for many MOF systems. The other method is using a solvent that can easily be sublimated, preferably benzene. [366] After several heating and cooling cycles, the sample is kept at 0 °C and the remaining benzene is removed by vacuum, i.e. directly going from the solid phase to the gas phase. [136] It should be noted, that due to benzenes hazardous potential, the former method is more prevalent.

6.1.3 Post synthetic modification, calcination and processing

A further technique for tailoring MOFs is the application of post-synthetic modification (PSM) methods leading to further diversification in structure and functionality. [367] This modification may be carried out at the linkers or at the metal clusters. The former represents a covalent subdivision of PSM, often carried out at a nucleophilic amine group of the linkers, e.g. aldehyde condensation. [368] Although in most cases, this group is attached to the linkers prior to MOF synthesis, in case of very stable MOFs, it can be directly introduced (reaction taking place in the pores of the framework) via classical aromatic nitration, followed by a reduction towards the NH_2 group. [369] In case of the latter, the interaction is established by coordinative bonds of guest molecules towards vacancies of metal clusters in the framework. Using this strategy, dithiols, for example could be attached to the so called open metal sites of HKUST-1 with one thiol group. The other end of the dithiol vastly improved the capture of mercury ions from aqueous phase for HKUST-1 due to the strong interaction of sulfur and mercury. [137]

A different post-synthetic modification is the calcination of MOFs, yielding porous carbons containing metal oxides of mixed species. [195] Depending on the final temperature, temperature ramp and calcination time, this transformation may be carried out in a gradual way, leading to the exterior part of the MOF particles being calcinated, while the interior structure still remains a microporous MOF. [194] Using this routine, the hydrolysis stability of IRMOF-1, (MOF-5) was greatly improved.

With respect to industrial applications, MOF crystals need to be shaped either to processable powders or to particles being included within a matrix, e.g. membranes, composites or others. [225], [370]–[372] Also the coating of MOF particles on solid phase micro extraction (SPME) fibers [209], [373], [374] or their incorporation in respiratory cartridges [375]–[377] represents applications scenarios, where appropriate composite materials and processing methods are needed to be developed. [212], [374], [378] All these processing methods require additional activations as well as evaluating the MOFs integrity after all involved stages and in its final application.

6.2 Methods for MOF characterization

6.2.1 Thermogravimetric analysis

Thermogravimetric analysis (TGA) is a sub method of thermal analysis, where the sample mass is measured over time, while the temperature is changed (Figure 60). It may involve isothermal heating or heating ramps or more complex heating programs. Using this method, it is possible to detect or monitor physical phase change, adsorption, desorption as well as chemical processes such as chemisorption, decomposition and oxidation or reduction reactions including auxiliary gases. Usually, inert purge gases such as nitrogen, helium or air are used. The method can be complemented using FTIR or mass spectrometry at the exhaust of the TGA cell.

In the scope of this thesis, TGA was mostly used to assess thermal stabilities of adsorbents prior to iGC measurements. In case of UiO-66 based MOFs, e.g. average linker coordination per metal oxide node can be estimated using TGA (sections 4.2.2 and 6.6.1). TGA investigations were carried out on a Q5000 TA Instruments device. Mostly, samples were heated under air at a linear heating rate of 10 K min^{-1} up to 700 °C.

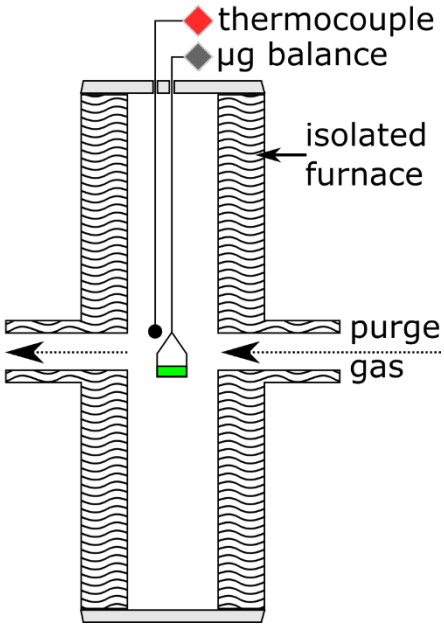

Figure 60. Schematic description of a TGA instrument. Within the isolated furnace (wavy pattern), the sample (green) is suspended and a flow of purge gas is passed over it towards the exhaust. While the heating is done, a µg balance (grey) is recording the weight while a thermocouple (red) is monitoring the current temperature.

6.2.2 Infrared spectroscopy

Infrared spectroscopy relies on the interaction of matter with infrared radiation. It exploits the fact that a molecule contains particular vibrational states. If the frequency of the radiation matches the energy represented by the energetic difference of vibrational states, resonance is observed, effectively resulting in significant absorption of infrared radiation.

A prerequisite is the Born-Oppenheimer approximation, i.e. the motion separation of atomic nuclei and electrons. Each bond can be modelled using a harmonic potential with the quantized vibrational states within the potential representing normal modes. A change in dipole moment during the vibrational excitation is also required for it being IR active. The frequency is influenced by the normal modes symmetry, kind (stretching, scissoring etc.), atom type (also isotopes) and bond strength. While linear molecules have $3N - 5$ normal modes, non-linear ones have $3N - 6$ normal modes (vibrational degrees of freedom) with N being the amount of atoms. Diatomic nitrogen does only have one

vibrational mode, which is IR inactive due to no changes in the dipole moment during excitation, whereas carbon monoxide is IR active. During the vibrational excitation of CO, its rotational modes, showing smaller energetic differences between states, do also change, resulting in a fine structure of the spectrum.

Infrared spectroscopy not only gives an indication for specific chemical groups, it also provides a fingerprint of the substance investigated. It can therefore be used to qualitatively assess if an adsorbent has undergone some significant change in its structure or if chemical groups were removed, added or altered. In this thesis, infrared spectra were recorded on a Nicolet™ iS™ 10 FT-IR-Spectrometer from Thermo Fisher Scientific Inc. For recording ATR spectra, a Durascope module from Smiths Detection was used. Measurements were done at ordinary lab conditions (25 °C, atmospheric pressure) for a wave number range of 600 to 4000 cm^{-1}, with a spectra resolution of 0.125 cm^{-1}.

6.2.3 Scanning electron microscopy

Scanning electron microscopy (SEM) is a variant of the electron microscope that uses a point type (1D) detector and an electron beam that is scanning a defined area in a raster fashion, like the image construction using a cathode ray tube in ancient displays. Therefore, SEM is not comparable to continuously image-forming techniques like a CCD camera. Furthermore, its resolution is neither diffraction limited, nor limited by fineness of lenses and mirrors (Figure 61). Depending on the nature of the emission, it provides different information about the samples surface.

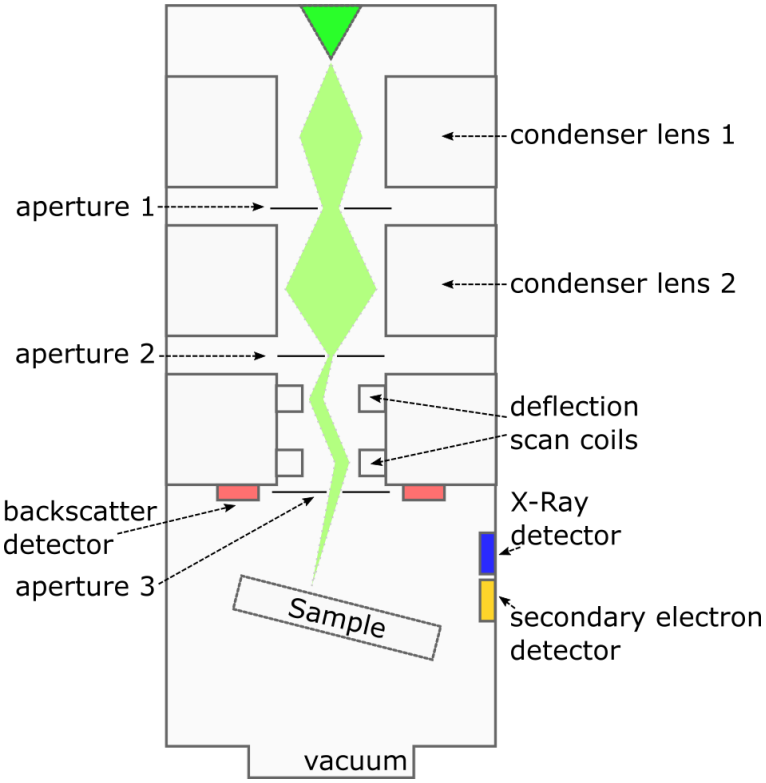

Figure 61. SEM schematic. Electrons (bright green) emitted from the electron gun (green triangle) pass several condenser lenses and apertures before being guided by the deflection (or scan) coils through the final aperture towards the sample. Backscatter, secondary electron and X-Ray detectors (for EDX) analyze the respective signals, while the whole microscope is (usually) operated under vacuum.

When the electrons collide with the sample, a consecutive, random series of absorption and scattering occurs, where effectively the kinetic energy of the electrons is decreased. This so-called interaction volume has a teardrop-like shape and reaches from 100 nm to 5 µm depth, depending on the sample (electrons kinetic energy, atomic number of the samples atoms and its density).

Mainly three different detectable phenomena result from this collision. The first one are elastic reflected beam-electrons, so-called backscattered electrons (BSE), by trend resulting from heavier elements. The second species are secondary electrons (SE) by inelastic scattering. It is the most widespread method that detects low-energy (below 50 eV) electrons from mostly the k-shell of sample atoms. The third species results from the emission of electromagnetic radiation, e.g. characteristic X-Ray (energy dispersive x-ray spectroscopy, EDX) or cathodoluminescence (CL).

Amplifiers are used to increase the signal and each position within this x-y plane is mapped in a pixel image, like in a surface plot, with pixel color representing intensity. While scattered electrons like Auger electrons result from low interaction depth (followed by secondary electrons), backscattered electrons result from larger interaction depth. Finally, characteristic X-ray (EDX), continuum X-Ray and cathodoluminescence (CL) result from interaction in depth of the sample material.

Due to the wave-particle duality, electrons carrying a specific kinetic energy as result of an electric or magnetic field can be assigned a wavelength. Typically, electrons are thermionically emitted by a tungsten electron gun. The electron beam contains electrons with kinetic energies from 0.2 to 50 keV and is guided by condenser lenses towards the deflector coils, that operate the electron beams raster scanning (rectangular area in x-y plane). Due to collisions with gas molecules, SEM is usually done under high vacuum (1-10 Pa), although there are methods like environmental SEM (ESEM) for non-conductive samples, that produce high pressure near the sample in order to neutralize or drain charge, that would otherwise accumulate on the sample.

In this study, scanning electron micrographs of MOF crystals were obtained using a Zeiss Supra microscope (55VP). The samples were observed by fixing the powder onto a double-sided carbon tape adhered on an aluminum specimen holder. Whenever necessary, the samples were coated with a thin layer of gold or palladium (Cressington high resolution sputter coater) prior to SEM investigation.

6.2.4 X-Ray powder diffraction

In X-Ray powder diffraction (XRPD) is considered, the diffraction pattern can be understood as a fingerprint from the according crystal, which does in this case work as a diffraction grating. [302]

Generally, as compared to amorphous materials, crystals exhibit a long-range order, their arrangement of the containing atoms follows a determined pattern. Plastics, glass or solid paraffins do not exhibit such a regular pattern. This can be verified using X-ray powder diffraction. XRPD can be used to identify phases, observe their transitions and assess crystallinity. It is also possible to obtain lattice parameters and derivatives with respect to temperature and pressure, like expansion tensors or the bulk modulus, respectively. [302], [379]

Practically, short wavelength, monochromatic X-rays (between 0.1 and 0.01 nm) are used as the wavelength is in the range of lattice distances within crystals. Lower wavelengths (higher energies) tend to show deeper penetration into the material, while larger wavelengths cause significant peak broadening which consequently may cause overlapping and therefore significant information loss.

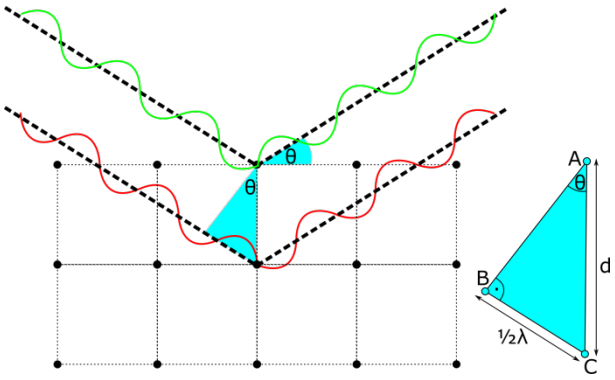

Figure 62. Bragg's condition for constructive interference on the crystals lattice or a powders crystal. ABC represents a right triangle, the distance BC needs to be λ/2 so that after passing this distance twice, positive interference will occur. At constructive interference, the signal will significantly increase.

Braggs condition for constructive interference is:

$$n \cdot \lambda = 2d \cdot \sin(\theta) \qquad (50)$$

And is schematically shown in Figure 62. Only in case of the red beams pathway being an integer value of λ, constructive interference will occur, with half values, destructive interference is observed. The angle θ defines the shape and edge lengths of the right triangle ABC. In combination with d, the distance BC is defined. Typically, X-rays will be

monochromatized, focused and collimated before irradiating the sample. While the incident X-ray forms a θ angle with the sample surface, the diffracted one will form a $2 \cdot \theta$ angle with respect to the incident one. The X-ray emitter and detector are therefore synchronized in a way that both parts are revolving in a circular fashion. For MOFs, typically values of 5-60° are used for $2 \cdot \theta$.

If an initial guess for the crystal structure is available, the theoretical model can be recursively fitted towards the XRPD pattern. However, it is extremely to construct an atomistic picture from a XRPD pattern without an initial structural guess due to reflection overlaps in a powder. The XRPD pattern is therefore characteristic for the crystal structure (position of the reflexes) and the texture (peak broadness and crystallite size). This method is therefore useful for identifying structural changes that modify the long-range order of the material. Amorphous changes (e.g. guest molecules in a porous crystal) were only apparent in XRPD if they exhibit a long-range order or indirectly by altering the long-range order of the crystalline host material.

In this thesis, X-ray powder diffraction analyses data were collected on a D8 Advance from Bruker AXS, equipped with a copper tube, two 2.5° Soller collimators, anti-scatter screen, flip-stick stage and silicon strip detector (LynxEye) in an angular range of 5, 10 or 12.5 to 65°2θ with a step size of 0.06°2θ.

6.2.5 Specific surface area by BET

The Brunauer-Emmet-Teller model is used to model the adsorption isotherm of porous materials by static volumetric or gravimetric adsorption investigations and derive the specific surface area from it. The underlying theories of adsorption isotherms, especially the BET isotherm are discussed in detail in section 2.2.2. In this thesis, specific surface areas based on the BET model were mainly used to assess sample stability prior, during and after iGC and thermal desorption investigations and trials.

For most investigations in this work, nitrogen adsorption isotherms were measured at -196 °C using a Quantachrome Nova 2000e surface area analyzer or a Quantachrome Autosorb iQ-MP-C-System. Samples were degassed in vacuum for 12-24 h at 100-200 °C prior to the analysis and the mass of the activated sample was recorded. BET pressure range varied between p/p_0 = 0.001 and p/p_0 = 0.1. In some cases, VectorDosing with ranges from $p/p_0 = 5\ 10^{-5}$ and p/p_0 = 0,2 was used as isotherm dosage mode. Suitable points for multipoint BET-analysis were selected with the Micropore-BET-Assistant tool and according to the Rouquerol method for microporous systems. If other conditions (devices and parameters) were used, it is directly indicated in the respective section of the results chapter.

6.3 Review of selected sorption-related MOF applications

The following section gives a brief summary of MOF-based applications, grouped by the respective application field.

6.3.1 Gas storage

Microporous materials play a significant role in small molecule (gases) storage and separation at medium to high pressures. The reason is the above-mentioned overlap of multiple adsorption potentials within the micropores, and therefore a strong interaction between adsorbate and adsorbent. This facilitates gas storage at lower pressures than in their liquefied state, energy savings, and increasing safety at the same time.

At current times, activated carbons are still predominant. They exhibit high surface areas at low costs as compared to zeolites and MOFs. However, being a natural product in most cases they lack chemical uniformity, resembled in variation in pore size distributions and impurities, causing in different chemical behavior.

In contrast, MOFs being crystalline and uniform from a pore-size point of view, are still a promising substance class to be utilized for (specialized) gas storage applications. Also, due to their high crystallinity, even higher surface areas and pore volumes, as compared to carbons, are available. It is furthermore possible to tailor MOFs for the specific purpose and screening them using molecular modelling beforehand.

Literature studies using virtual high throughput screening were done in the past, not only using existing experimental MOF structures but also using algorithm generated ones by using a library of SBUs. [172], [174], [187], [380] Not only hydrogen but also carbon dioxide, methane and acetylene and other gases are interesting guest molecules for storage applications. While the storage of hydrogen, methane and acetylene is interesting

for energy applications, the storage of CO_2, SO_2 and SO_3 as well as other sulfur compounds are relevant for environmental related applications. [102], [381]–[383]

Initially, hydrogen was a key target gas as it provides a "clean" alternative to fossil fuels. However, even in the liquefied state (70,8 g l^{-1}) the density is too low to provide for an efficient storage (desired value of 81 g l^{-1} or 9 wt%). [201], [384] The surface area was identified as a key parameter to enhance storage capacities of MOFs and has thus been optimized for several MOFs dealing with hydrogen adsorption. [201] The first hydrogen isotherm of MOF-5 (IRMOF-1) showed, evidenced by inelastic neutron scattering, that at room temperature the isotherm was linear and hydrogen molecules were preferentially adsorbed at the organic linkers with increasing pressure. An uptake of 1 wt% was achieved at 20 bars. [384] Therefore, MOFs with larger linkers were synthesized and loaded with hydrogen. Using molecular simulations, it could be shown that three different adsorption mechanisms, each correlated with a different pressure regime, were found for the IRMOF series of MOFs. [385]

In the low-pressure regime (below 0.1 bar), hydrogen gets adsorbed at the metal centers. The heat of adsorption at these sites drives the interaction. In the intermediate pressure zone (e.g. at 30 bar), hydrogen gets adsorbed at the pore walls, i.e. the linkers. The interaction is mainly driven by the surface area. In the high-pressure regime (e.g. at 100 bar), a pore-filling mechanism drives the interaction. In this case, the free volume within the framework is the key parameter.

Other possible strategies use the open-metal sites in HKUST-1 to form a dihydrogen complex or enrich MOF composites with platinum to maximize the hydrogen uptake. [386], [387]

More recent structures like NOTT-112 exhibiting a surface area of 3,800 m^2 g^{-1}, show a gravimetric hydrogen uptake of 10.0 wt% at 77 K and 77 bars. NOTT-112 consists of

Cu_2O_{10} nodes linked with hexatopic 1,3,5-tris(3',5'-dicarboxy[1,1'-biphenyl]-4-yl)benzene linkers. NOTT represents University of Nottingham. By extending the linker, 13.5 wt% for structures like NU-111 (YAGHI group, BET surface area 4,930 m^2 g^{-1}, NU relating to Northwestern University) could be achieved. NU-111 is also comprised of copper nodes (Cu_3L_2), connected by hexatopic linkers, resulting in the same topology as for NOTT-112. By furthermore extending the linker, leading to the NU-100 structure (BET surface area 6143 m^2 g^{-1}), even an uptake of 16.4 wt% could be shown. NU-100 is also copper based (Cu_3L_1) like NU-111, featuring a 5,5′,5″-(((benzene-1,3,5-triyltris(ethyne-2,1-diyl))tris(benzene-4,1-diyl))tris(ethyne-2,1-diyl))triisophthalic acid linker.

However, MOF-210 with a gravimetric uptake of 17.6 wt% and a BET surface area of above 6,200 m^2 g^{-1} is still the record holder to date. MOF-210 is a zinc-based MOF featuring two different linkers, $(Zn_4O)_3(BTE)_4(BPDC)_3$ (BTE = 4,4′,4″-(benzene-1,3,5-triyl-tris(ethyne-2,1-diyl))tribenzoic acid and BPDC = biphenyl-4,4′-dicarboxylic acid;). The concept of surface area and free volume being most important for intermediate to high pressure adsorption is maintained. [388]

Carbon dioxide capture in MOFs is also an application scenario for MOFs due to environmental greenhouse effect, as the conservative capture-method using mono-ethanol amine suffers from regeneration and degradation problems. [389] The thermal stabilities combined with large surface areas and polar nodes make MOFs promising candidates as reusable adsorbents for this subject.

The large pore (featuring a BTB linker) of MOF-177 showing an uptake of above 33 mmol g^{-1} or 147 wt% depicts a bright example for CO_2 capture at ambient conditions (and 42 bars). [390] Pore condensation at low pressures is the main reason for this outstanding uptake as compared to e.g. IRMOFs. [390], [391]

UiO-based MOFs, showing high thermal and water stability, can also be used for CO_2 capture, although generally being lower as compared to MOF-177. Values of 25.6 wt% at 0 °C are typical for compounds like UiO-66-$(CH_3)_2$, a dimethyl derivative of regular UiO-66. As compared to MOF-177, UiOs are far more robust, and therefore a comparison towards a typical industrial material like zeolite 13X (showing 26.4 wt% uptake) can be drawn. [325] By post-synthetic exchange of Zr with Ti, the CO_2 uptake can be further increased. [392] UiO-based MOFs (e.g. UiO-67 with a biphenyl dicarboxylate, BPDC linker) with larger linker show a similar behavior as the large-pore containing MOF-177. Values of 301 cm^3(STP) cm^{-3} (on a volumetric basis, i.e. V_{gas}/V_{MOF}) are observed for UiO-67, MOF-177 showing 357 and Zeolite 13X showing 185 cm^3(STP) cm^{-3}. [393]

6.3.2 Gas separation

It is evident that chemical substances strongly differ in boiling points, i.e. the adsorption-desorption equilibrium from their own liquid phase. Therefore, two substances will never show identical sorption properties on a given solid surface. Assuming that non-bonded interactions are expected to be similar, as for diatomic molecules, a correlation between uptake and boiling point is obvious, for example nitrogen adsorption will be stronger than hydrogen adsorption at 77 K. When going from idealized systems (inert homogeneous metal surface) towards a real system (heterogeneous, porous, confinement), the chemical structure of adsorbates starts to play an even more important roll. On choosing a suitable temperature and pressure regime, molecule separation can be adjusted in a dynamical fashion like in gas separation.

In case of a selective gas capture and storage, a prerequisite for CO_2 capture is its separation from its matrix beforehand. For most gases, as discussed in the adsorbents sections (1.1 and 1.2) the matrix is ambient air. Therefore, at industrial scale separation,

factors for gases like CO_2 as compared to the main component of the air background (i.e. N_2) is an important parameter.

Mechanisms for this separation task comprise thermodynamic equilibrium effects, kinetic effects as well as molecular sieving effects. [132], [253] In very confined situations, quantum sieving being a result of the transverse motion of the adsorbate being quantized is another mechanism that has to be considered. [95]

ZIFs show extraordinary CO_2 adsorption selectivities as compared to other light gases (such as methane or nitrogen), resembled in many applications of ZIFs for CO_2 separation. [394]–[396] Also, microporous metal formats ($M(HCO_2^-)_2$) show high selectivities for hydrogen over nitrogen and argon. This was attributed to the size-limiting passages in the zig-zag channels of these compounds in the range of 2.5 to 3.0 Å. According to the kinetic diameter of H_2, Ar and N_2 being 2.8, 3.4 and 3.64 Å, this effect can be classified as a size exclusion separation due to steric factors. [397]

For light gases, there are other more MOF specific separation mechanisms, namely size selectivity imposed by framework interpenetration, hydration-degree selective sorption as well as selectivity that is connected to framework flexibility or its dynamic behavior. [132] Notable examples are mixed-matrix membranes containing ZIF-8 particles: Ultem® hollow fibers CO_2/N_2 selectivity could be increased from 30 to 36 by incorporating 17 wt% of ZIF-8. [370]

It was furthermore demonstrated, that the CO_2/CH_4 selectivity in ZIF-67 isomorphs can be tailored (from 2.3 - 2.4 to 2.7 - 6.5) by varying the ratio of the regular linker (imidazolate) towards a second linker (functionalized imidazolate) during synthesis. [398] The concept of size exclusion can also be applied to larger adsorbates, e.g. hydrocarbons. Using both, molecular simulations as well as equilibrium adsorption isotherms, it could be shown that ZIF-8 exhibits larger Langmuir parameter as well as

Henry constants for linear hexane as compared to bulkier isomers. [399] This can be explained when the kinetic diameters of these alkanes are considered. For hexane, 2-methylpentane, 2,3-dimethylbutane and 2,2-dimethylbutane the kinetic diameters are 4.3, 5.0, 5.8 and 6.2, respectively. The Henry and Langmuir constants show a reciprocal correlation towards the kinetic diameters in this series.

6.3.3 Vapor sorption and separation

With increasing adsorbate size, thermodynamic and steric effects are constantly gaining more relevance, when MOF-based separation is considered. Especially, when heteroatoms of functional groups are present, not only steric effects due to these groups must be considered, but also specific interactions (hydrogen bonding and electrostatic effects) of these groups with the framework itself. An overview of different adsorption mechanisms and selected examples has been given in a recent review. [400]

A notable example is $[Cd(4\text{-btapa})_2(NO_3)_2]\cdot 6H_2O\cdot 2DMF$ (4-btapa=1,3,5-benzene tricarboxylic acid tris[N-(4-pyridyl)amide]), which loses its crystallinity (evidenced by XRPD) after DMF removal. [401] Although the activated MOF shows no significant nitrogen adsorption in BET measurements, a notable adsorption of short chain alcohols (up to n-butanol) has been revealed. The amide groups exposed in the pore channels are responsible for this particular sorption behavior. This effect could not be observed for the spatially similar molecules pentane and pentene due to a lack of hydrogen bonding. The amorphous state is transformed to a crystalline one by polar alcohol adsorption.

A different example, where organic vapors are favored over water, i.e. a hydrophobic effect, is [Zn(tbip)] (tbip=5-tert-butylisophthalate). [402] Bulky, non-polar tert-butyl groups within the channel generate this non-polar environment for guest molecules in the 4 Å channels. At lower pressures, dimethyl ether is favored over methanol and water. However, at increased pressure, methanol is adsorbed, which may be caused by a

capillary condensation process. This is because the interaction of adsorbent surface and adsorbate gains importance at lower pressures, but adsorbate-adsorbate interaction is emphasized at higher pressures.

A third possibility is the selectivity for functional groups in organic guest molecules. The separation of xylene isomers showing boiling points in the temperature range of 138 to 144 °C, is conducted at industrial scale using Zeolite X and Y. The vanadium based MOF MIL-47 also shows a selective adsorption for the three isomers o-, m- and p-xylene as well as ethylbenzene. [321], [403] This is evident when comparing the single component adsorption isotherms for these organic molecules. The trend of retention time follows the trend of slope of adsorption isotherms in this study. Theoretical studies imply that adsorbate sizes, i.e. kinetic diameters, are mostly responsible for this selective behavior. [294]

6.3.4 MOFs in chromatography

Separation of different adsorbates is not only of concern in industrial processes but also in terms of analytical methods. In chromatography, a substance specific separation is achieved resulting in different retention times for each molecule. As MOFs exhibit the afore mentioned structural features, namely size-exclusion effects, van-der-Waals and electrostatic interactions as well as hydrogen bonding combined with high specific surface areas and crystallinity (i.e. narrow pore-size distributions), they are promising candidates for chromatography and related topics such as sample enrichment.

Another, more general facet is the relatively low amounts of MOF materials needed for these applications (as compared to industrial scale applications such as gas storage applications). Typical application areas comprise gas (GC) and liquid (HPLC) chromatography as well as solid-phase microextraction (SPME). Overall, more studies of

MOFs in gas chromatography have been reported than for liquid (HPLC) chromatography. [404]

Generally, in chromatography the occurrence and parameters of a substance peak are the result of a complex interplay of thermodynamic, kinetic and equilibrium effects that are unique for a given combination of adsorbent (stationary) adsorbate (probe, analyte or guest molecule in the mobile phase, i.e. carrier gas in GC or solvent in HPLC).

Temperature in combination with enthalpies and entropies of adsorption will influence the retention time or retention volume of a peak, i.e. the first moment. Flow rates in combination with kinetic factors, such as mass transfer coefficients, diffusion constants etc. will influence the full width at half maximum (FWHM) as well as the skewness like fronting or tailing of chromatographic peaks (the second and higher moments of peaks, furtherly discussed in section 2.3).

In a chromatography experiment all these factors will contribute to one result, i.e. the peak position and shape. By separating and varying system parameters (temperature, flow, injection amount) these quantities can be determined.

Packed columns

With respect to gas chromatography, stationary phases can be sub-divided into packed columns and capillary columns.

In one of the first demonstrations of MOFs in packed columns, MOF-508 [Zn(BDC)(4,4'-bipy)$_{0,5}$·DMF·0,5H_2O], a pillared layer MOF featuring two linkers and a temperature stability up to 360 °C, was used to separate branched and linear alkanes in its 1D pore channels. [405] MOF-508s channels having dimensions of 4.0 by 4.0 Å are only slightly larger than the minimum projected dimensions of methane (3.8 by 3.8 Å). Therefore, linear alkanes being able to access the pore system show higher retention volumes as compared to their branched isomers. [405], [406]

A study involving isoreticular IRMOFs, namely IRMOF-1 (aka MOF-5, with terephthalate linker), IRMOF-8 (with 2,6-napthalene-dicarboxylate linker) and IRMOF-10 (with 4,4'-diphenyl-dicarboxylate linker), showed the pore-size effects for the retention of hydrocarbons and aromatics. [407] It could be shown that Henry constants (linear region isotherm slope, i.e. capacities at infinite dilution) as well as the adsorption enthalpies were correlated towards the cavity sizes resembled in the linker size. According to the study, this effect is mostly due to more carbon atoms being introduced into the pore system when going from IRMOF-1 to 8 to 10. This increases the overall non-specific interaction (explained in section 2.3.2), and (because of the aromaticity of the linkers) the specific interaction (in this case due to π-π interactions) is increased as well. The probability for defects is also correlated towards larger linkers being present in the framework. [164], [407] It was shown that rather the organic linkers were responsible for the specificity of interaction with guest (probe) molecules than the structure of the MOF itself.

As afore-mentioned, MIL-47(V) was also used to separate C8 aromatics which was achieved by their strongly different packing arrangements in MIL-47s pores. [321] Using inverse gas chromatography (iGC) resulting single component Henry constants as well as adsorption enthalpies did not show this trend as this method gives the picture at low coverage where adsorbate-adsorbate interactions are negligible. [313], [321] Adsorption selectivity is increased with higher partial pressures of the guest molecules.

Packed columns of HKUST-1(Cu) were also used for small Lewis-basic organic molecules such as diethyl ether or furan. As HKUST-1s interior is considered Lewis-acidic, increased retention times with increased polarity was observed. In case of some probe molecules (e.g. nitrobenzene) no elution was apparently possible. A conclusion was that the

adsorption was too strong. Also, the limited thermal stability of HKUST-1 in chromatographic systems of 220 °C was a major insight of this study. [408]

The zircon-based MOF UiO-66 was investigated for its chromatographic behavior with respect to cyclic and linear alkanes. [338] A rather unusual favor of more bulky cyclohexane as compared to linear hexane was observed. Other MOFs, like MIL-53, MIL-47 and HKUST-1, show a favor for linear hexane over cyclohexane. Between 200 and 300 °C the ratio of Henry constants (measurements from iGC at infinite dilution) only slightly drops from about 5.5 to 5. This inverse shape selective behavior can be explained by a combination of enthalpic and entropic effects. Due to a superior fitting of cyclohexane in UiO-66s pores (8 and 11 Å, respectively) and fewer loss of entropy (as cyclohexane does not have the conformational degrees of freedom as compared to linear hexane) cyclohexane shows higher retention volumes and resulting Henry constants as compared to linear hexane.

A general conclusion that can be drawn from these studies is, that packed MOF columns do not allow for low heights of theoretical plates (HETP) leading to a small amount of theoretical plates for a given column. [261], [310], [313], [321] This is not a MOF-specific issue because plate numbers of packed columns are usually considered below 10.000 per column, whereas wall-coated open tubular columns (WCOT) show plate numbers reaching from 30.000 to 300.000 plates per column. Low plate-numbers for packed columns are mostly an effect of high pressure drops along packed columns resulting in low carrier gas velocities. Also, the downsizing of particles is practically limited for packed columns. [52]

Capillary columns

The first application of interest for MOF coated capillary columns was about xylene isomers and ethylbenzene separation. One milligram of MIL-101 ($[Cr_3O(H_2O)_2F(BDC)_3]$)

was sufficient to create a 400 µm thick film in a 15 m long capillary column. [409] With a specific surface area of 5,900 $m^2 g^{-1}$, pores of 29 Å and 34 Å and open-metal sites, MIL-101 was chosen for this particular separation task.

A separation of all isomers was possible within 1.6 minutes and for p-xylene, an amount of 3,800 theoretical plates per m column was determined. Prior to capillary coating, MIL-101 was synthesized and stabilized via pyridine grafting. Suspensions of MIL-101 were purged through the column using a carrier gas. Another notable example is the preparation of UiO-66 coated capillary columns. [410] Similar as to above-mentioned packed columns of UiO-66 a reverse-shape selectivity was observed. Plate numbers of 1950 m^{-1} were obtained for hexane, whereas 2,3-dimethylbutane only showed 1,090 plates m^{-1}. 1,3,5-trimethylbenzene was excluded from the pore system (molecular sieving), whereas branched iso-propylbenzene was retained longer as compared to n-propylbenzene showing that the reverse-shape selectivity was also valid for aromatics. [410]

This so-called dynamic method is the primary coating method for manufacturing MOF coated capillary columns. [411], [412] This method lacks the so-called column bleeding, which is caused by displacement of MOF particles, referred to as spiking.

In order to improve the MOF coating stability, the controlled SBU approach (CSA), often referred to as layer-by-layer epitaxy, provides a solution. [130], [360], [361], [413] Alternately, metal-source and linker-source containing solutions (and optionally purge solvents) are being pumped through a blank column to yield ideally a unit cell extension of MOF film during each cycle. Improved adhesion, controlled layer-thicknesses and high crystallinity of the films are advantages of this method. [258], [414]

Liquid chromatography

In HPLC, especially the highly stable MIL family (MIL-53, MIL-47 and MIL-101) were demonstrated to show reasonable separation capabilities for alkyl aromatics but also for larger molecules like high-order fullerenes. [415] Especially for the flexible MIL-53 a temperature dependent pressure drop – a result of the breathing effect – could be observed leading to a temperature-based pressure control in the column. [416] With MOFs, high back-pressures at higher flows are obtained as compared to traditional stationary phases. Using organic dye mixtures in DMF and fluorescence confocal microscopy, it could be shown that the principle of liquid chromatography is even applicable in a single MOF crystal (1 to 2 mm of edge length). [246]

6.3.5 MOFs for purification of air and trapping of hazardous chemicals

Given their high surface area and tailorable pore sizes often combined with potentially reactive structural sites (metal-nodes as well as functional linkers), MOFs are not only candidates for reliable and stable storage or capture of guest molecules but also as detoxification agents (degradation or irreversible reaction partner for hazardous substances) in the gas phase. [376], [417]

Also, the capture of VOCs (like benzene, methanol or hexane) was studied and related to different adsorption mechanism such as pore-filling, unsaturated metal center, hydrogen bonding or breathing effects. [400]

An early demonstration of MOFs being used to trap or capture hazardous chemicals from the gas-phase was done in 2008. [418] Six different MOFs (mostly IRMOFs, such as IRMOF-1, 3 and 62 (all Zn) along with HKUST-1(Cu), MOF-74(Zn) and MOF-177(Zn)) were evaluated for their potential in adsorbing harmful gases including sulfur dioxide, ammonia, chlorine and carbon monoxide. Breakthrough investigations were used to

compare MOFs to state-of-the-art activated carbon. In almost all cases, MOFs outperformed the activated carbon, especially those MOFs having reactive chemical functionalities.

Dynamic adsorption capacities of up to 35% (HKUST-1 with tetrahydrothiophene, THT) were determined. MOF-177 and MOF-5 (IRMOF-1) showing the highest surface areas within this series did not show a beyond-carbon capture of guest molecules. IRMOF-3, i.e. MOF-5 carrying an amino group, showed increased breakthrough capacities for chlorine and ammonia. MOF-74, generally showing high affinities for any polar adsorbate, showed extraordinary uptakes for SO_2. HKUST-1 showed the best performance for THT, benzene, dichloromethane and ethylene oxide. Generally, this study showed that high surface area is not responsible for a high uptake of harmful gases, but open metal sites (like in HKUST-1 of MOF-74) and functionalized linkers (MOF-74 and IRMOF-3) are responsible for increased breakthrough volumes and uptakes of polar, reactive guest molecules.

Especially for MOF-74, it was shown that the different metal nodes directly drive the adsorption of polar molecules such as ammonia, cyanogen chloride, octane and SO_2. [419] Especially, the uptake behavior with respect to dry and humid conditions was investigated. Mg-MOF-74 turned out to be the peak substance for SO_2, ammonia and octane uptake, however showing also the strongest drop when tested under humid conditions. Using Co, Ni and Zn as metal nodes the drop in SO_2 capacity as a reason of humidity could be reduced.

Co-MOF-74 showed the highest capacity for cyanogen chloride. [419] In all cases, the octane adsorption was correlated with the specific surface area determined for the MOF-74 isomorphs and competitive water adsorption was always present thus emphasizing the lacking selectivity between water and other small polar adsorbates. With respect to CO adsorption a difference in metal nodes could also be observed for MOF-74. [420] Co,

Ni and Fe analogues were shown to adsorb almost one CO molecule per open-metal site. An uptake of 6 mmol g^{-1} of CO was reported for MOF-74(Fe) as well as binding energies of above 50 kJ mol^{-1} for MOF-74(Ni).

A theoretical study using several small molecules and various MOF-74 analogues showed that this substance class can be tailored for small molecules selectivity. [421] Overall, Cu and Cr containing MOF-74 showed diminished adsorption enthalpies as compared to others within the series, possibly a result of their d_{z2} electrons that form anti-bonding states with the adsorbates. Early transition metals like Ti or V showing unoccupied d_{z2} states are predicted to show strongly increased adsorption enthalpies as compared to the rest of the series. [421]

While MOF-74 type MOFs show excellent uptakes for small toxic industrial chemicals (TICs), their humidity stability is limited. [422], [423] An interesting MOF class for this application is the UiO-series due to their excellent chemical and humidity stability. This substance class was widely studied and evaluated for TIC capture recently.

A further example is NO_2 adsorption. In the dry state UiO-66 (BDC linker) shows almost the same NO_2 uptake (73 mg g^{-1}) as compared to the larger pore UiO-67 (79 mg g^{-1}) featuring a BPDC linker. [424] However, when humidity is introduced, this picture is changed. UiO-67, having larger pores as compared to UiO-66 (due to its biphenyl linker) shows triple uptake of NO_2 (118 mg g^{-1}) as compared to UiO-66 (40 mg g^{-1}) under humid conditions. This effect can be explained by the NO_2 dissolving in a physisorbed water film in UiO-67s pores, whereas UiO-66s pores are occupied by water molecules, effectively preventing the sequential dissolution of NO_2. [424]

A possibility to increase the NO_2 affinity of UiO-66s is the incorporation of vacant carboxylic acid residues into the pore network. [328] Using solvent assisted ligand incorporation (SALI), it was shown that the NO_2 uptake capacity was more than doubled

(from 3.8 to 8.4 mmol g^{-1}) when oxalic acid was introduced into defective UiO-66 crystals. This effect can be explained by an interaction of the free carboxylic acid and the NO_2 adsorbates. [328]

Similar effects of free carboxylic acid groups were seen for NH_3 capture. [383] However, using BDC linkers with two additional carboxylic acid groups (bulky in nature) tend to confine the pore system. This effectively leads to -COOH functionalized UiO-66 performing better than regular UiO-66 and ammonia capacities of 5.7 mmol g^{-1}. [383]

A possible reaction of NO_2 with amino functionalized linkers also provides an important strategy for TIC adsorption. [326] Three different major reaction mechanisms can be involved: The reaction of NO_2 with the $Zr_6O_{8-x}(OH)_x$ clusters, the linker nitration in position 4 to the amino group, and the diazonium-salt formation at the amino group. [326] A combination of the former and the latter seem to be essential parts of the mechanism combined with further reactions where water molecules are actively involved in.

Besides toxic industrial chemicals also the capture and catalytical degradation capabilities of MOFs towards chemical warfare agents (CWAs) were investigated using more complex reaction pathways. [162], [320], [376], [425]–[428] Usually, experiments were carried out using simulants such as dimethyl methylphosphonate (DMMP, for VX) or 2-chloro-ethyl ethyl sulfide (CEES, simulant for mustard gas). Widely employed reactions use either hydrolysis or oxidation to degrade CWAs.

A different application being related with air purification is particulate matter (PM) removal. Using an already upscaled layer-by-layer roll-to-roll hot-pressing manufacturing process, ZIF-8 particles were deposited on plastic mesh. This coated mesh was evaluated for its capabilities in particulate matter filtration of $PM_{2.5}$ and PM_{10} contaminated air samples. [429]

The high PM removal efficiency (almost 60% for both, $PM_{2.5}$ and PM_{10}) was attributed to PMs being mostly polar in nature (consisting of various ions such as nitrate, sulfate, ammonium, chloride along with elemental carbon) as well as the MOF surface containing various defects and a positive metal balance on the exterior surface area leading to polarization (of the PMs) and hence improved electrostatic interaction. [429] The retention was also assessed in a month trial with only 10% decrease in PM removal. Using electrospinning of MOFs to yield nanofibrous filters, the same group showed that even removal efficiencies of above 80% are possible. [430]

6.3.6 Selected optoelectronic sensing applications of MOFs

Many imaginable chemical functionalities that are known for non-porous materials, can also be incorporated into porous structures. A property change related to this functionality can be expected upon guest molecule adsorption. This property change can be transduced into an electrical signal that can be analyzed using e.g. pattern recognition or more sophisticated methods. MOFs involved in small molecule sensing, ion sensing, biomolecule sensing as well as humidity and temperature sensing applications have therefore been reported in several review articles. [431]–[434]

In matters of electronic sensing, signal transduction is still limited as many MOFs are insulators and show low electrical conductivity. [434] Nevertheless, progress was made and there are examples for impedance sensors, chemicapacitive sensors and chemiresistive sensors using MOF films. [434] An example for chemiresistive sensing using MOFs is the sensing of ppm levels of formaldehyde using ZIF-8 deposited on interdigitated electrodes. Response times were in the order of several minutes as formaldehyde diffusion in ZIF-8 is limited. [435] Temperatures of 150 °C were needed for the device, likely a result of the low electrical conductivity of ZIF-8.

In 2015 it was shown that by using the π-conjugated $Cu_3(HITP)_2$ (HITP = 2,3,6,7,10,11-hexaimino-triphenylene, a hexadentate linker) it was possible to fabricate chemiresistive sensors that can be operated at room temperature. Sub-ppm detection limits for ammonia were facilitated using $Cu_3(HITP)_2$ as coating for the electrodes. [436] Isostructural $Ni_3(HITP)_2$ did not show a sensitivity towards ammonia, thus demonstrating the selectivity that can be imposed by chemical synthesis. Finally, a sensor array made from three different 2D-MOFs ($Cu_3(HITP)_2$, $Ni_3(HITP)_2$, and $Cu_3(HHTP)_2$ (HHTP = 2,3,6,7,10,11-hexahydroxy-triphenylene, a hexadentate linker)) was able to discriminate between several VOCs using pattern recognition. [437] It is also possible to transduce a change in the work function of MOFs upon guest molecule adsorption using the Kelvin probe method. This setup avoids the high conductivity that is needed for MOFs to be used in field effect transistors (FETs). [438]–[440]

Other ways of transducing are the color change upon adsorption (solvato- or vaprochromism), luminescence (e.g. photoluminescence or radioluminescence), interferometry, surface plasmon resonance, surface-acoustic wave or electromechanical based methods (change in property due to adsorbate mass).

Colorimetric detection can, in the most basic case, be realized without any electronic equipment, as it is done in field explosive detection. [7], [441] This concept can also be transferred to MOFs. A sensor based on Mg-NDI (H_4NDI=N,N'-bis(5-isophthalic acid)naphthalene-diimide) showed reversible solvatochromic behavior with respect to the polarity of its interacting solvents. [442] Clearly, NDI depicts the chromophoric unit in this structure being electron deficient. Therefore, not only the solvatochromic effect due to polar guest molecules (e.g. methylamine (black) or acetonitrile (orange)) was an observed feature, but also the selective recognition of electron-rich organic amines as

compared to electron-deficient aromatics like chloro- or nitrobenzene by fluorescence quenching. [442]

Generally, luminescence detection exploits the changes in luminescent properties of a suitable host-material to detect the presence of a specific analyte. As the readout of this transduction mechanism is contact-free and easy to use, it is the most widely investigated one among MOFs.

The interactions involved in changing the photoluminescence in a fluorescent material can be subdivided into long range, short range, and complex/collision-driven interactions. [443] One mechanism is the long range radiative energy transfer (emission quenching), being range-independent.

An example for non-radiative energy transfer is Förster resonance energy transfer (FRET), which is based on dipole-dipole coupling of the excited state of the donor molecule towards the ground state of the acceptor molecule leading to either donor luminescence quenching (so-called turn-off response) or acceptor fluorescence stimulation (so-called turn-on response).

A donor-acceptor orbital overlapped-based mechanism is Dexter electron exchange (DEE) which results in in the transfer of an excited electron and its corresponding hole from the donor to the acceptor resulting in either quenching of the donor's fluorescence or induction of fluorescence in the acceptor.

A different mechanism is photoinduced electron transfer (PET), a redox process in which excited electrons are passed from the photo-excited donor to the lowest occupied molecular orbital (LUMO) of the acceptor. It results in photoluminescence quenching as the charge recombination produces excess heat.

Luminescence phenomena based on analyte-framework complexations can result from the frameworks highest occupied molecular orbital (HOMO) or the analytes lowest

unoccupied molecular orbital (LUMO) energy levels being shifted, resulting in altered emission wavelengths. The other possibility is the so called antenna-effect where the analyte complexation increases the photon absorption of the framework increasing the overall emission intensity of the framework (turn-on effect).

Combined with this multitude of charge transfer mechanisms, the donors and acceptors within the guest molecule containing MOF can vary. Charge transfers from metal-to-metal (MMCT), metal-to-ligand (MLCT), ligand-to-metal (LMCT) and ligand-to-ligand (LLCT) are, among the charge transfers of ligand or metal towards the analytes and vice versa, the most important ones.

Generally, sensitivities in terms of detection limits (LOD) are rarely stated in publications, quenching efficiencies are usually provided. This allows for some comparability among different MOF materials. This also goes for selectivity, being an arbitrarily complex phenomenon. In case of luminescence-based sensing, selectivity can arise from factors such as molecular dimensions (shape, functionality and rigidity) and electron deficiency. [444] Electron deficiency, i.e. the energetic position of the LUMO band in case of quenching as well as HOMO and LUMO in case of enhancement, does again have a interconnection with sensitivity: A guest molecule A being a more effective fluorescence quencher than molecule B, will also show a lower detection limit, as the total quenching is a product of quenching efficiency and concentration. This can make it almost impossible to detect RDX (1,3,5-trinitroperhydro-1,3,5-triazine) in the presence of DMNB (2,3-dimethyl-2,3-dinitrobutane), as the vapor pressure of DMNB is 6 orders of magnitude higher than for RDX. [445] Only if structural differences of linear DMNB and cyclic RDX can be transduced by the host material, a selective detection of both substances is possible. This is also the case for a selective low concentration detection of benzene in the

presence of toluene, xylenes and ethylbenzene, all being aromatic molecules and being diverse in spatial dimensions. [294]

However, MOFs being able to show fluorescence behavior change with respect to electron-deficient molecules are promising candidates for a sensitive explosives detection. An example is $Zn_2(BPDC)_2BPEE$ (BPDC = 4,4'-biphenyldicarboxylate; BPEE = 1,2-bipyridylethene) which was used for the detection of 1,4-dinitrotoluene (1,4-DNT) being a byproduct in 1,3,5-trinitrotoluene (TNT) production. Upon exposure to 180 ppb of 1,4-DNT the emission was significantly red-shifted with decreasing intensity as a result of the electron shift from the linkers towards the electron-deficient DNT. [446]

Using pillared-layer MOFs ($Zn_3(L)_3(DPB)_2$ (DPB = 1,4-dipyridylbenzene)) with increasingly conjugated linkers (with L ranging from 5-(benzyloxy)-isophthalic acid to 5-(pyren-1-ylmethoxy)-isophthalic acid) the limit of detection (LOD) was shifted from 3.6 to 0.9 ppb. This shows the neat correlation of the aromatic ring system of the pillars towards the efficiency in fluorescence quenching sensitivity. [444] This effect is commonly known and also exploited in amplifying conjugated fluorescent polymers (AFPs) used in explosive detection [447], [448]

Another notable example is the two-dimensional analysis of both change in emission sensitivity and wavelength-shift caused by the interaction of vapor-phase explosives using an interpenetrated MOF structure, namely $[Zn_2(NDC)_2(BPEE)]\cdot 2.25DMF\cdot 0.5H_2O$ (NDC = 2,6-naphthalenedicarboxylate). [445] Using this two parameters it was possible to discriminate between electron-deficient nitroaromatics (e.g. TNT), regular aromatics (e.g. toluene), nitroaliphatics (e.g. nitromethane) and interferents (e.g. methanol or water). Respective LUMO-levels of the analytes (e.g. lower as compared to the conduction band (CB) of the MOF as for nitrobenzene) will lead to a shift in the CB of the MOF (e.g. when increased leading to a blue shift in fluorescence). Also, compared to other

publications, analyte interactions were studied in the gas phase, not in solution. By further downsizing the particles from 50-120 μm to 1-5 μm, response times could be increased by factors of 4-5, allowing for sub-minute equilibration. [445]

In the last years, numerous articles related to MOF based luminescent and photonic materials have been published resulting in special review articles being dedicated to this emerging topic. [443], [449], [450] Analytes of interest comprise explosives, toxic sulfur compounds, amines and organophosphates, VOCs as well as metal ions and biomolecules. Also, humidity, oxygen and temperature sensors were using luminescent MOFs were put into practice. [443]

In case of MOF-based electromechanical sensors (quartz-crystal microbalance (QCM), surface acoustic wave (SAW) and micro cantilever (MCL)) the quantitative adsorption of guest molecules into the MOF structure is required to change the mechanical properties of the MOF layer that is being transduced by these methods. Also, it is required to prepare a tightly attached and defined MOF coating on top of the substrates.

With a detection limit of 1 ng QCMs are used to study MOF systems with respect to adsorption isotherms, diffusion constant determination but also for sensing purposes. An example is the electrospray deposition of HKUST-1 onto a QCM-chip being afterwards used as a sensor for acetone with detection limits of 10 ppm. [451] For SAW-based devices, layer uniformity is even more crucial, hence layer-by-layer epitaxy methods are used in most cases. Employing this coating method, a HKUST-1 based sensor for sub-ppm water monitoring was fabricated. [452] By coating HKUST-1 on a micro cantilever, water detection limits below 100 ppb were achieved. [453] The need for a uniform, tightly attached coating generally limits the number of applications facilitated using electromechanical transducers. To achieve an optimal coating several parameters, have

to be optimized and methods like liquid-phase epitaxy have to be used that are only applicable to a limited number of MOFs. [211], [359]

With respect to many sensing applications, MOF films in varying quality have to be created prior to sensing being possible. This generally limits the range of MOFs to be evaluated for their usage in such devices.

6.4 Details on gas sampling bags and concentrations

6.4.1 Explanation of the ppm notation

One ppm refers to the „parts per x“ notation, based on weight, pressure, volume or moles.

$$1\ ppm = \frac{1\ quantity}{10^6\ quantities} = \frac{1\ \mu l}{1\ l} = \frac{1\ mg}{1\ kg} \qquad (51)$$

The ideal gas law can be used to convert respective *ppms* into absolute values

$$p \cdot V = n \cdot R \cdot T \qquad (52)$$

Where p denotes pressure in Pa, V the volume in m^3, n the amount in moles, R the universal gas constant (8.31 J mol^{-1} K^{-1}) and T the temperature in K. On a volumetric basis, 1 ppm refers to 1 µl in 1 l or 1 ml in 1 m^3. At STP (273.15 K and 1 bar) one mole of ideal gas enfolds 22.69 l, at SATP (298 K and 1.013 bar) 24.46 l.

$$n = \frac{p \cdot V}{R \cdot T} \qquad (53)$$

Substituting 1000 ppm (red) into this equation results in:

$$n = \frac{1.013 \cdot 10^5\ Pa \left(\mathbf{1000} \cdot 10^{-6}\ \frac{l}{l} \cdot 1l \cdot 10^{-3}\ \frac{l}{m^3}\right)}{8.31\ \frac{J}{mol\ K} \cdot 298\ K} \qquad (54)$$

Where it is helpful to write explicit units (e.g. l/l) in order to avoid conversion errors. Within a volume of 1 l, 1.000 ppm_V refers to 1 ml, which equals 4.090 10^{-5} moles at SATP. Given in the mass per m^3 convention, 1.000 ppm of nitromethane in nitrogen equals 2.495 g/m^3. On a pressure basis, this term can be expressed as:

$$n = \frac{\left(\mathbf{1000} \cdot 10^{-6}\ \frac{Pa}{Pa}\right) \cdot 1.013 \cdot 10^5\ Pa \cdot \left(1\ l \cdot 10^{-3}\ \frac{l}{m^3}\right)}{8.31\ \frac{J}{mol\ K} \cdot 298\ K} \qquad (55)$$

Yielding the exact same result, namely 4.090 10^{-5} moles.

6.4.2 Calculation of gas sampling bag concentrations

By injecting a calculated amount of volatile analyte (in this case nitromethane) into a known volume of nitrogen, respective concentrations in ppm_p (similar to ppm_V see section 6.4.1) can be adjusted. The ideal gas law can be used for this purpose:

$$p \cdot V = n \cdot R \cdot T \qquad (56)$$

With a concentration of e.g. 100 ppm being $100 \cdot 10^{-6} \cdot 1.013 \cdot 10^5$ Pa (10.13 Pa) in total pressure of $1.013 \cdot 10^5$ Pa at 298 K, the term:

$$\frac{n_{an}}{V_{bag}} = \frac{p_{an}}{R \cdot T_{exp}} \qquad (57)$$

will yield a concentration of 4.09 10^{-3} mol m^{-3} as respective molar concentration. Multiplying it with the sampling bags volume (V_{bag}), it will yield the substance amount n_{an}. When n_{an} is finally multiplied by the molar mass of the respective analyte (61.01 g mol^{-1} for nitromethane) and divided by its density (1.14 ml g^{-1} for nitromethane) the volume to be injected can be calculated, in this case 2.19 µl (2.49 mg).

Alternatively, 100 ppm can be regarded as a fraction of V_{bag} with 100 ppm according to 1 ml in 10 l (100 10^{-6} 0.01 m^{-3}). The fractional volume V_{an} directly yields n_{an} using the following equation:

$$n_{an} = \frac{p_{exp} \cdot V_{an}}{R \cdot T_{exp}} \qquad (58)$$

As stated in section 6.4.1, it will yield the same results as using a pressure calculation.

6.5 Preconcentration of nitro alkanes with 1st generation MOFs

This appendix section contains tables with Henry constants, carbon number plots, tables containing the respective dispersive component of the surface energy and Henry constants, enthalpies and entropies of adsorption of all analyte-adsorbent combinations studied.

6.5.1 Logarithmised Henry constants of all probe molecules on all sorbents

The following tables show logarithmised (base e) Henry constants (in m) for combinations of various sorbents and nitro or regular alkanes.

Table 7. Logarithmised Henry constants for probe molecules (carbon numbers in lines) and HKUST-1. Color scale from low values (red) to high values (green).

$\ln(K_C)$ in ln(m)					
	T in °C	50	100	150	200
1	Nitromethane	1.94	0.11	-1.20	-2.07
2	Nitroethane	3.89	1.66	0.16	-1.48
3	1-Nitropropane	9.27	6.31	4.11	2.03
3	2-Nitropropane	3.93	1.58	-0.47	-1.82
5	Pentane	-	-1.11	-2.51	-3.83
6	Hexane	-	-0.22	-1.79	-3.21
7	Heptane	-	2.58	0.31	-1.41

Table 8. Logarithmised Henry constants for probe molecules (carbon numbers in lines) and ZIF-8. Color scale from low values (red) to high values (green).

$\ln(K_C)$ in ln(m)					
	T in °C	50	100	150	200
1	Nitromethane	-3.07	-3.46	-4.42	-4.83
2	Nitroethane	-2.07	-2.99	-4.60	-5.22
3	1-Nitropropane	1.03	-1.11	-2.35	-3.23
3	2-Nitropropane	-0.13	-1.29	-2.60	-3.92
5	Pentane	-	-3.26	-4.50	-5.53
6	Hexane	-	-1.97	-3.27	-4.67
7	Heptane	-	-0.80	-2.42	-3.88

Table 9. Logarithmised Henry constants for probe molecules (carbon numbers in lines) and Fe-BTC. Color scale from low values (red) to high values (green).

$\ln(K_C)$ / ln(m)					
	T in °C	50	100	150	200
1	Nitromethane	-0.68	-2.87	-3.46	-4.21
2	Nitroethane	-0.38	-1.16	-2.72	-3.53
3	1-Nitropropane	0.26	-2.06	-2.19	-3.42
3	2-Nitropropane	0.31	-1.75	-2.96	-3.25
5	Pentane	-	0.48	-1.86	-3.52
6	Hexane	-	0.71	-1.66	-4.12
7	Heptane	-	3.95	0.16	-2.12

Table 10. Logarithmised Henry constants for probe molecules (carbon numbers in lines) and MIL-53. Color scale from low values (red) to high values (green).

$\ln(K_C)$ / ln(m)					
	T in °C	50	100	150	200
1	Nitromethane	-0.06	-2.66	-2.91	-3.56
2	Nitroethane	3.69	-0.13	-1.18	-1.74
3	1-Nitropropane	3.78	2.10	-0.09	-1.72
3	2-Nitropropane	3.81	0.84	-0.36	-1.35
5	Pentane	-	-1.35	-2.32	-3.17
6	Hexane	-	-0.74	-2.45	-3.33
7	Heptane	-	2.16	-0.37	-1.29

Table 11. Logarithmised Henry constants for probe molecules (carbon numbers in lines) and Tenax TA. Color scale from low values (red) to high values (green).

$\ln(K_C)$ / ln(m)					
	T in °C	50	100	150	200
1	Nitromethane	-1.63	-2.84	-3.77	-3.61
2	Nitroethane	-5.20	-5.54	-6.63	-7.19
3	1-Nitropropane	-5.78	-6.70	-7.24	-7.52
3	2-Nitropropane	-6.88	-7.38	-7.75	-8.15

6.5.2 Enthalpies and entropies of adsorption

This table shows enthalpies and entropies of adsorption of respective adsorbent (column) and probe molecule (row) combinations for nitro and regular alkane molecules. Errors are given in absolute units.

Table 12. Enthalpies (ΔH_{ads} in kJ mol^{-1}) and entropies (ΔS_{ads} in J mol^{-1} K^{-1}) of adsorption of nitro and regular alkanes on all sorbents investigated.

Analyte	HKUST-1		ZIF-8		Fe-BTC		MIL-53		Tenax® TA	
	ΔH_{ads}	ΔS_{ads}	ΔH_{ads}	ΔS_{ads}	ΔH_{ads}	ΔS_{ads}	ΔH_{ads}	ΔS_{ads}	ΔH_{ads}	ΔS_{ads}
Nitromethane	31.0 ± 1.3	14.6 ± 3.3	12.4 ± 2.4	2.7 ± 6.2	25.9 ± 4.7	22.4 ± 12.1	25.2 ± 7.4	16.4 ± 19.3	14.9 ± 4.5	4.5 ± 11.6
Nitroethane	41.5 ± 1.6	30.3 ± 4.2	24.7 ± 3.3	27.0 ± 8.6	24.4 ± 3.6	11.6 ± 9.4	42.6 ± 10.4	40.6 ± 26.8	14.4 ± 3.2	20.6 ± 8.4
1-Nitropropane	57.5 ± 1.4	35.1 ± 3.6	32.9 ± 2.4	28.8 ± 6.2	25.7 ± 6.1	14.0 ± 15.8	43.8 ± 4.1	36.5 ± 10.6	11.7 ± 1.5	19.2 ± 3.8
2-Nitropropane	46.0 ± 1.0	43.9 ± 2.7	28.6 ± 3.1	22.6 ± 7.9	27.8 ± 4.8	19.9 ± 12.4	40.1 ± 5.3	29.4 ± 13.7	7.4 ± 0.4	14.3 ± 1.1
Pentane	36.2 ± 1.9	39.3 ± 4.5	29.7 ± 0.3	39.9 ± 0.7	55.2 ± 1.9	77.5 ± 4.5	23.2 ± 0.7	6.4 ± 1.7	-	-
Hexane	40.3 ± 1.7	42.7 ± 4.0	36.0 ± 3.4	45.6 ± 8.0	67.0 ± 5.4	106.0 ± 13.0	34.8 ± 4.5	33.2 ± 10.8	-	-
Heptane	55.0 ± 0.8	59.3 ± 1.9	41.6 ± 1.6	51.1 ± 3.7	86.1 ± 6.9	132.2 ± 16.4	47.9 ± 10.3	44.9 ± 24.6	-	-

6.5.3 Carbon number plots

These plots show the free enthalpies of adsorption as a function of carbon number (c#) at various temperatures (50 to 200 °C for nitro alkanes and 100 to 200 °C for regular alkanes).

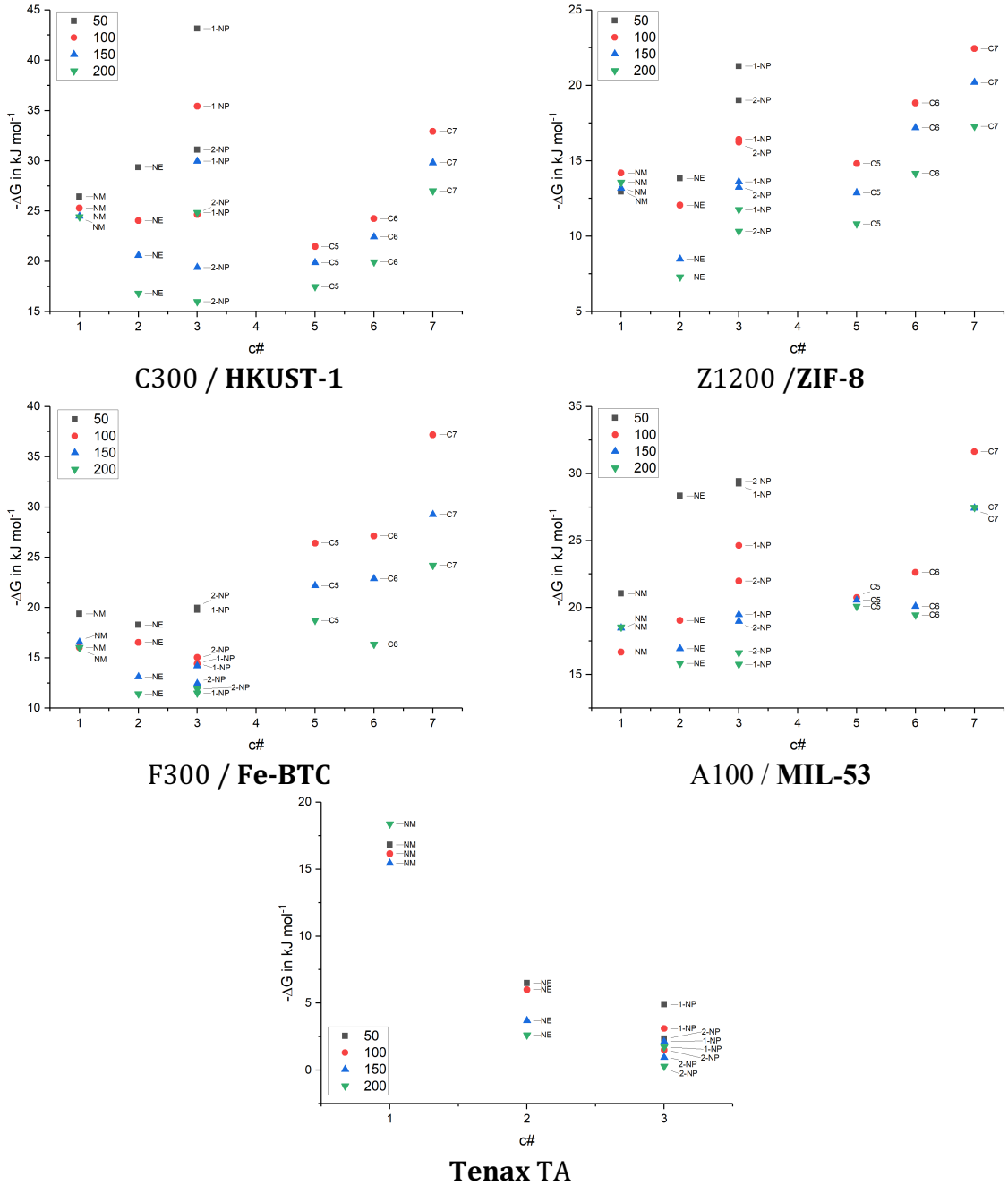

Figure 63. Carbon number vs. free enthalpy of adsorption plot for HKUST-1, ZIF-8, Fe-BTC, MIL-53 and Tenax TA. Temperatures in °C, free enthalpies of adsorption in kJ mol^{-1}. Carbon numbers refer to the total number of carbon atoms in the respective molecule. Carbon numbers 1-3: nitroalkanes, 5-7: regular saturated alkanes.

6.5.4 Dispersive components of surface energies as function of temperature

The following table shows the content of Figure 34, the dispersive component of the surface energy for all MOFs within this thesis.

Table 13. Dispersive components of the surface energy for various MOFs as function of temperature.

Sorbent	100 °C	150 °C	200 °C
HKUST-1	134.1 ± 11.8 mJ m^{-2}	107.6 ± 8.4 mJ m^{-2}	106.2 ± 8.4 mJ m^{-2}
ZIF-8	59.6 ± 0.1 mJ m^{-2}	58.4 ± 0.6 mJ m^{-2}	48.9 ± 0.1 mJ m^{-2}
Fe-BTC	118.8 ± 29.9 mJ m^{-2}	54.8 ± 11.9 mJ m^{-2}	35.0 ± 40.7 mJ m^{-2}
MIL-53	121.5 ± 17.3 mJ m^{-2}	51.4 ± 21.9 mJ m^{-2}	63.9 ± 29.1 mJ m^{-2}

6.5.5 Specific contribution of the nitro group

The following tables show either the specific contribution of nitromethane (Table 14, by comparison with hypothetical methane in terms of carbon number) or the nitro group (by regression line offset including 2-nitropropane, Table 15 and without 2-nitropropane, Table 16)

Table 14. Specific contributions of nitromethane to free enthalpies of adsorption.

Adsorbent	Temperature in °C	$\Delta G_{specific}$ in kJ mol^{-1}
HKUST-1	100	27.7 ± 12.0
HKUST-1	150	25.3 ± 9.8
HKUST-1	200	26.8 ± 9.5
ZIF-8	100	14.6 ± 0.9
ZIF-8	150	14.7 ± 2.7
ZIF-8	200	15.7 ± 0.5
Fe-BTC	100	12.7 ± 19.1
Fe-BTC	150	9.5 ± 11.6
Fe-BTC	200	9.9 ± 20.8
MIL-53	100	18.9 ± 14.5
MIL-53	150	12.9 ± 15.8
MIL-53	200	14.7 ± 17.6

Table 15. Specific contribution of the nitro group on free enthalpies of adsorption, including 2-nitropropane.

Adsorbent	Temperature in °C	$\Delta G_{specific,NO2}$ in kJ mol^{-1}
HKUST-1	100	15.8 ± 5.6
HKUST-1	150	8.0 ± 8.5
HKUST-1	200	2.8 ± 11.7
ZIF-8	100	4.8 ± 4.6
ZIF-8	150	2.1 ± 5.8
ZIF-8	200	-0.3 ± 7.6
Fe-BTC	100	-8.4 ± 11.5
Fe-BTC	150	-8.6 ± 9.3
Fe-BTC	200	-7.3 ± 8.7
MIL-53	100	11.4 ± 3.8
MIL-53	150	2.2 ± 5.4
MIL-53	200	-2.4 ± 8.9

Table 16. Specific contribution of the nitro group on free energies of adsorption, excluding 2-nitropropane.

Adsorbent	Temperature in °C	$\Delta G_{specific,NO2}$ in kJ mol^{-1}
HKUST-1	100	23.3 ± 1.2
HKUST-1	150	15.3 ± 4.2
HKUST-1	200	8.2 ± 8.5
ZIF-8	100	4.0 ± 5.1
ZIF-8	150	1.0 ± 6.4
ZIF-8	200	-0.6 ± 7.8
Fe-BTC	100	-8.5 ± 11.6
Fe-BTC	150	-7.8 ± 8.8
Fe-BTC	200	-8.3 ± 9.3
MIL-53	100	13.2 ± 2.8
MIL-53	150	2.0 ± 5.5
MIL-53	200	-3.6 ± 9.5

6.6 Appendix BTEX preconcentration with 2nd generation MOFs

The appendix contains the calculation of linker deficiency, tables with enrichment factors and their trend by a sequence, carbon number plots, thermodynamic properties and specific interactions from iGC measurements as well as a MOF stability section.

6.6.1 Coordination number calculation for UiO-66 samples

Coordination numbers for UiO-66 type MOFs can be calculated using different metal nodes($Zr_6O_4(OH)_4$, Zr_6O_8, and Zr_6O_6). After complete decomposition and oxidation only Zr_6O_{12} is assumed to remain as all organic materials (linker: $C_8O_4H_4$) will decompose to CO_2, CO and water. Table 17 shows the molar weights of the discussed fragments.

Table 17. Molar weights (in g mol^{-1}) of hypothetical UiO-66 components.

Fragment	Mw in g mol^{-1}
Zr_6O_6	643.3
$Zr_6O_4(OH)_4$	679.37
Zr_6O_8	675.34
Zr_6O_{12}	739.34
$C_8O_4H_4$	164.12

Table 18 shows the molar weight of a hypothetical cluster (nodes: $Zr_6O_4(OH)_4$, Zr_6O_8, and Zr_6O_6) with n BDC linkers. It should be noted that n=6 in this case represents a fully coordinated cluster (12 linkers). This is due to symmetry reasons, i.e. n=5.5 means 11 linkers per node.

Table 18. Molar weight of a hypothetical cluster (nodes: $Zr_6O_4(OH)_4$, Zr_6O_8, and Zr_6O_6) with n BDC linkers in g mol^{-1}.

n BDC	Zr_6O_8	$Zr_6O_4(OH)_4$	Zr_6O_6
0	675.34	679.37	643.30
1	839.46	843.49	807.42
2	1003.58	1007.61	971.54
3	1167.70	1171.73	1135.66
4	1331.82	1335.85	1299.78
5	1495.94	1499.97	1463.90
6	1660.06	1664.09	1628.02
Total mass of specific node + n-BDC linkers in g mol^{-1}.			

Table 19 shows the pre-decomposition plateau heights (relative to Zr_6O_{12}) as a function of coordination number.

Table 19. Pre-decomposition plateau height (in %, relative to Zr_6O_{12}, which is set to 100%) as a function of coordination number per node. Again 11 linkers per node would result in n=5.5.

n BDC	Zr_6O_8	$Zr_6O_4(OH)_4$	Zr_6O_6
0	91.34%	91.89%	87.01%
1	113.54%	114.09%	109.21%
2	135.74%	136.29%	131.41%
3	157.94%	158.48%	153.60%
4	180.14%	180.68%	175.80%
5	202.33%	202.88%	198.00%
6	224.53%	225.08%	220.20%
(Total mass – $M(Zr_6O_{12})$)/$M(Zr_6O_{12})$ in %.			

Table 20 shows the coordination numbers of the four UiO-66 type MOFs as determined by this method.

Table 20. Coordination numbers calculated from TGA investigations using different hypothetical nodes ($Zr_6O_4(OH)_4$, Zr_6O_8, and Zr_6O_6). m_{rel} denotes the relative mass determined at the plateau before the main decomposition (500 °C).

MOF	m_{rel}	linkers per node			
		$Zr_6O_4(OH)_4$	Zr_6O_8	Zr_6O_6	Average
UiO-66-c	220	11.54	11.59	11.98	11.71
UiO-66-d	218	11.36	11.41	11.80	11.53
UiO-66-b	207	10.37	10.42	10.81	10.53
UiO-66-a	178	7.76	7.81	8.20	7.92

6.6.2 Table with enhancement factors

Table 21. Enhancement factors (in a.u.) for water (mass channel 18) and benzene (mass channel 78) under dry and humid investigations for all adsorbents used in this study.

MOF	Benzene, dry	Benzene, humid	Water, dry	Water, humid
UiO-66-a	2368 ± 74	1156 ± 36	2385 ± 629	30770 ± 3011
UiO-66-b	2033 ± 171	1103 ± 16	1624 ± 732	18781 ± 1931
UiO-66-c	1003 ± 90	1364 ± 61	2836 ± 2002	25863 ± 2142
UiO-66-d	1273 ± 359	916 ± 64	1391 ± 717	14138 ± 106
UiO-67	9830.3 ± 1515	7983 ± 170	2756 ± 2659	8934 ± 346
UiO-66(ADC)	2607 ± 168	955 ± 33	2171 ± 78	19116 ± 4521
CAU-10	2199 ± 113	1632 ± 46	852 ± 21	14242 ± 1100
HKUST-1	1938 ± 94	895 ± 22	4218 ± 1155	23636 ± 1633
MOF-177	10056 ± 441	7217 ± 262	798 ± 124	5152 ± 633
ZIF-8	1215 ± 158	889 ± 21	225 ± 43	1655 ± 133
ZIF-67	1664 ± 189	1026 ± 4	452 ± 76	3147 ± 214
Tenax	16502 ± 3785	11630 ± 1695	120 ± 15	717 ± 16

6.6.3 Enrichment factor behavior in consecutive runs

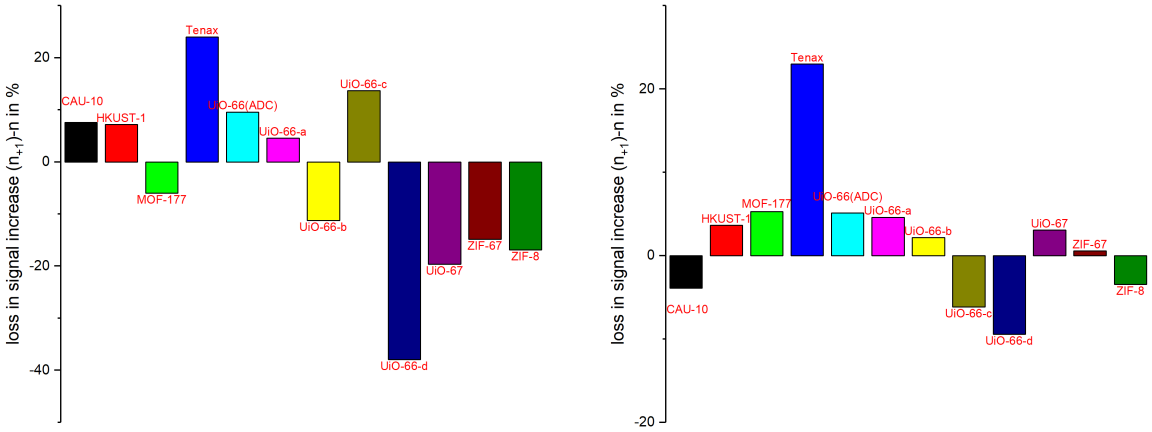

Figure 64. Benzene EFs for a sequence of desorption experiments. Left: Under dry conditions. Right: Under humid conditions. The EFs of the first measurement are subtracted from the second one and divided by the first one.

6.6.4 Enrichment factors of water during thermal desorption

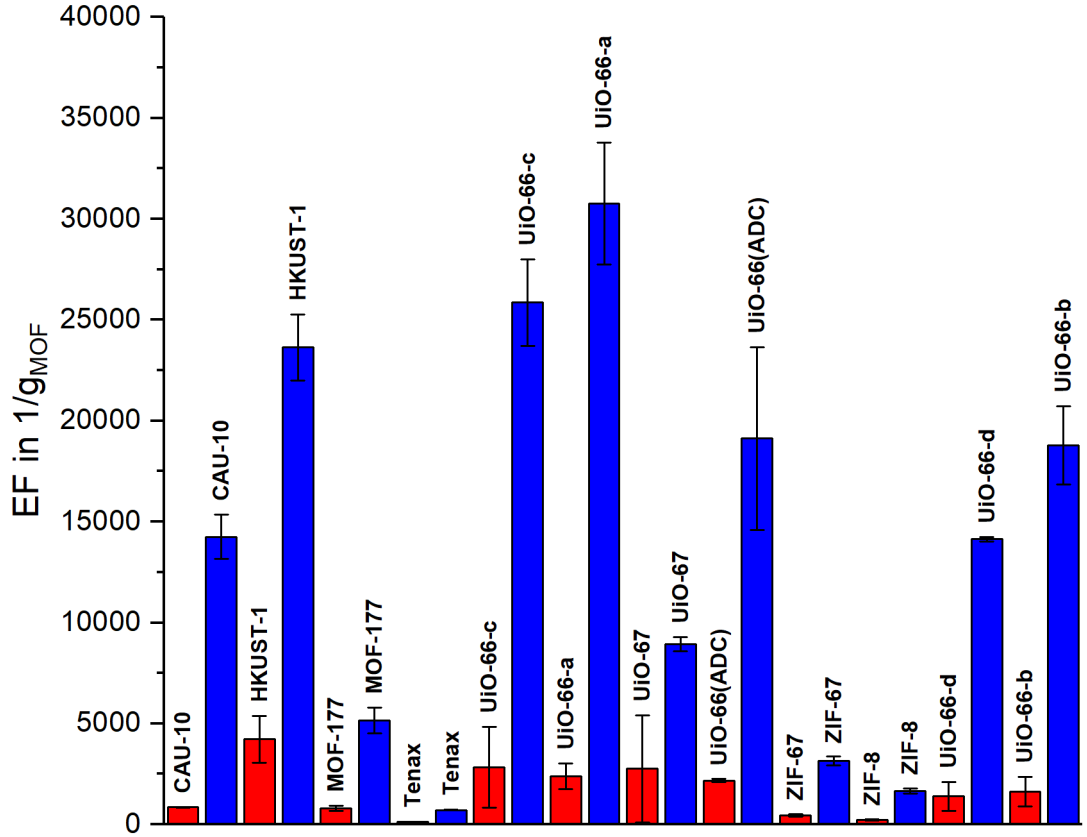

Figure 65. Enrichment factors (EFs) in terms of mass channel 18 (water) during thermal desorption investigations under dry (red) and humid (blue) conditions.

6.6.5 Carbon number plots for UiO-66 type MOFs

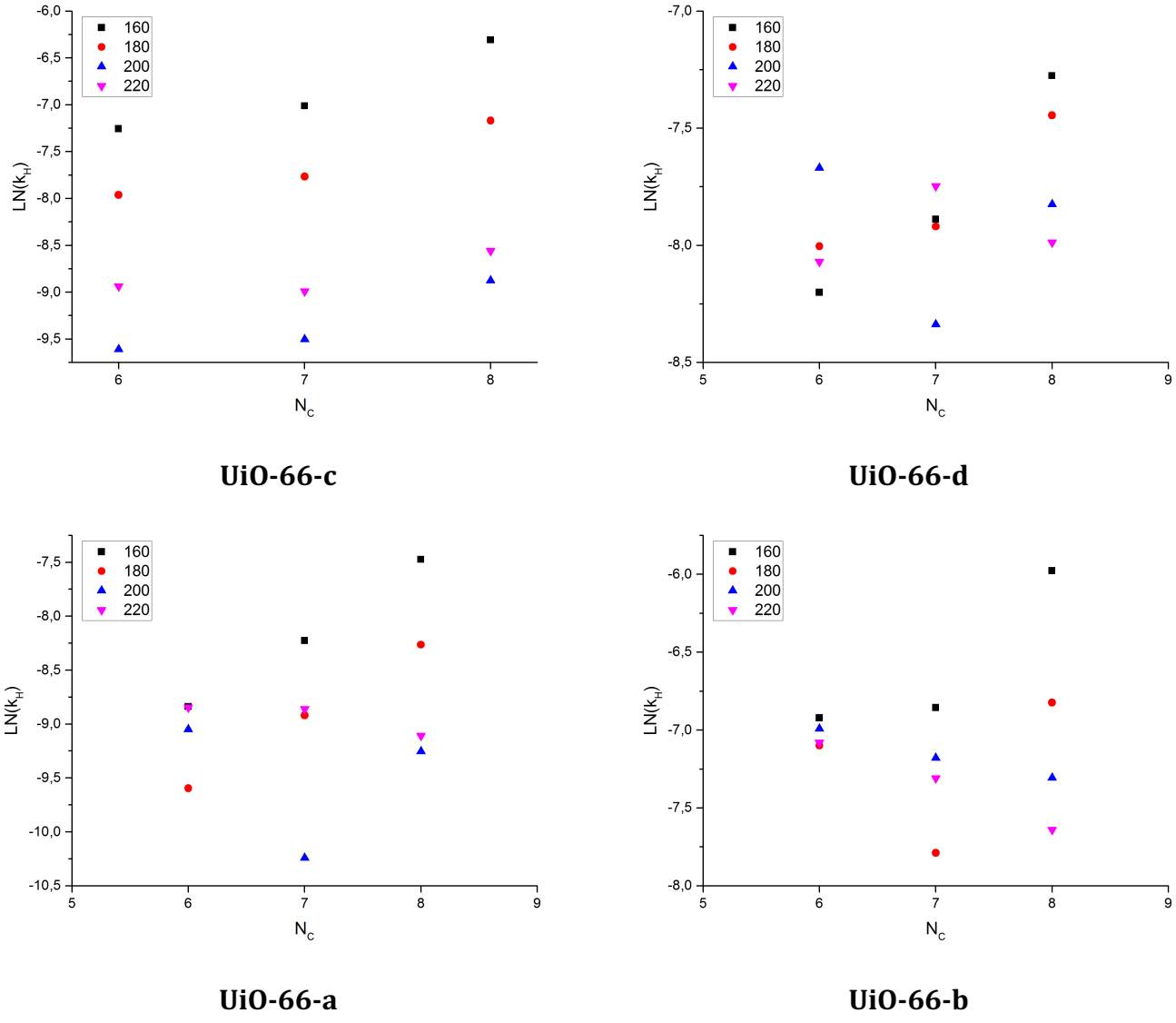

Figure 66. Carbon number plots for UiO-66 type MOFs in this study. Ordinate shows natural logarithm of Henry constants ( ) while abscissa shows amount of carbon atoms in the n-alkane.

6.6.6 Enthalpies and entropies of adsorption for BTEX compounds on UiO-66 MOFs

Table 22. Enthalpies of adsorption (in kJ mol^{-1}) of BTEX compounds on UiO-66 type MOFs.

MOF	Benzene	Toluene	o-Xylene	m-Xylene	p-Xylene	Ethylbenzene
UiO-66-b	35.1 ± 4.5	48.4 ± 7.0	57.3 ± 1.9	49.9 ± 4.9	51.9 ± 3.6	56.3 ± 3.3
UiO-66-a	38.5 ± 4.2	47.0 ± 2.2	60.8 ± 2.5	54.4 ± 2.6	51.3 ± 3.6	59.8 ± 1.9
UiO-66-d	68.2 ± 1.8	70.7 ± 1.4	49.3 ± 2.4	75.8 ± 9.8	58.6 ± 10.4	59.1 ± 0.5
UiO-66-c	46.4 ± 10.9	55.9 ± 10.8	70.5 ± 10.3	57.5 ± 7.5	58.4 ± 12.0	59.8 ± 9.9

Table 23. Entropies of adsorption (in J mol^{-1} K^{-1}) of BTEX compounds on UiO-66 type MOFs.

MOF	Benzene	Toluene	o-Xylene	m-Xylene	p-Xylene	Ethylbenzene
UiO-66-b	13.4 ± 9.8	36.8 ± 15.2	46.3 ± 4.1	34.7 ± 10.7	39.8 ± 7.6	47.5 ± 7.1
UiO-66-a	32.9 ± 9.3	45.4 ± 4.6	67.2 ± 5.3	57.7 ± 5.6	51.5 ± 7.5	67.1 ± 4.1
UiO-66-d	76.5 ± 4.1	76.2 ± 3.1	22.9 ± 5.2	84.9 ± 22.4	49.2 ± 22.4	47.3 ± 1.2
UiO-66-c	37.3 ± 23.8	52.7 ± 23.5	75.9 ± 22.2	54.2 ± 16.1	57.6 ± 26.3	57.0 ± 21.7

6.6.7 Specific interaction of BTEX compounds on UiO-66-c

Table 24. Specific interaction (free enthalpies basis, $\Delta G_{specific}$ in kJ mol^{-1}) of BTEX compounds on UiO-66 type MOF UiO-66-c.

T in °C	160	180	200	220
Benzene	1.6	3.0	6.7	0.9
Toluene	3.5	4.7	8.6	3.1
o-Xylene	5.4	6.5	9.7	4.8
m-Xylene	2.2	3.5	7.0	2.5
p-Xylene	1.4	2.7	6.2	1.4
Ethylbenzene	3.2	4.4	7.8	2.9

6.6.8 MOF stability by infrared spectroscopy

Before and after iGC investigations

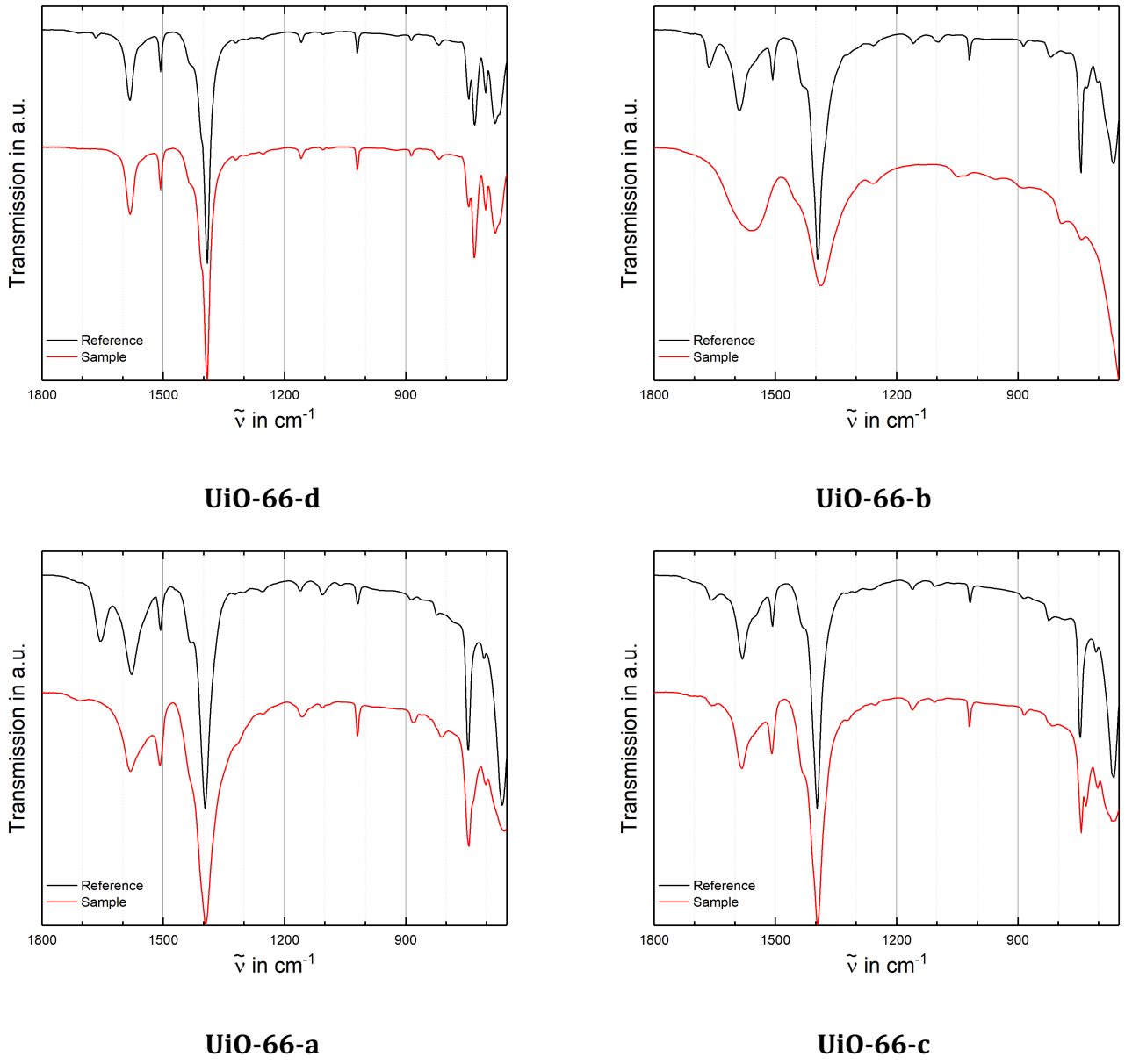

Figure 67. Infrared spectra of MOFs before (black) and after iGC investigations. MOF names under spectra.

Before and after humid thermal desorption

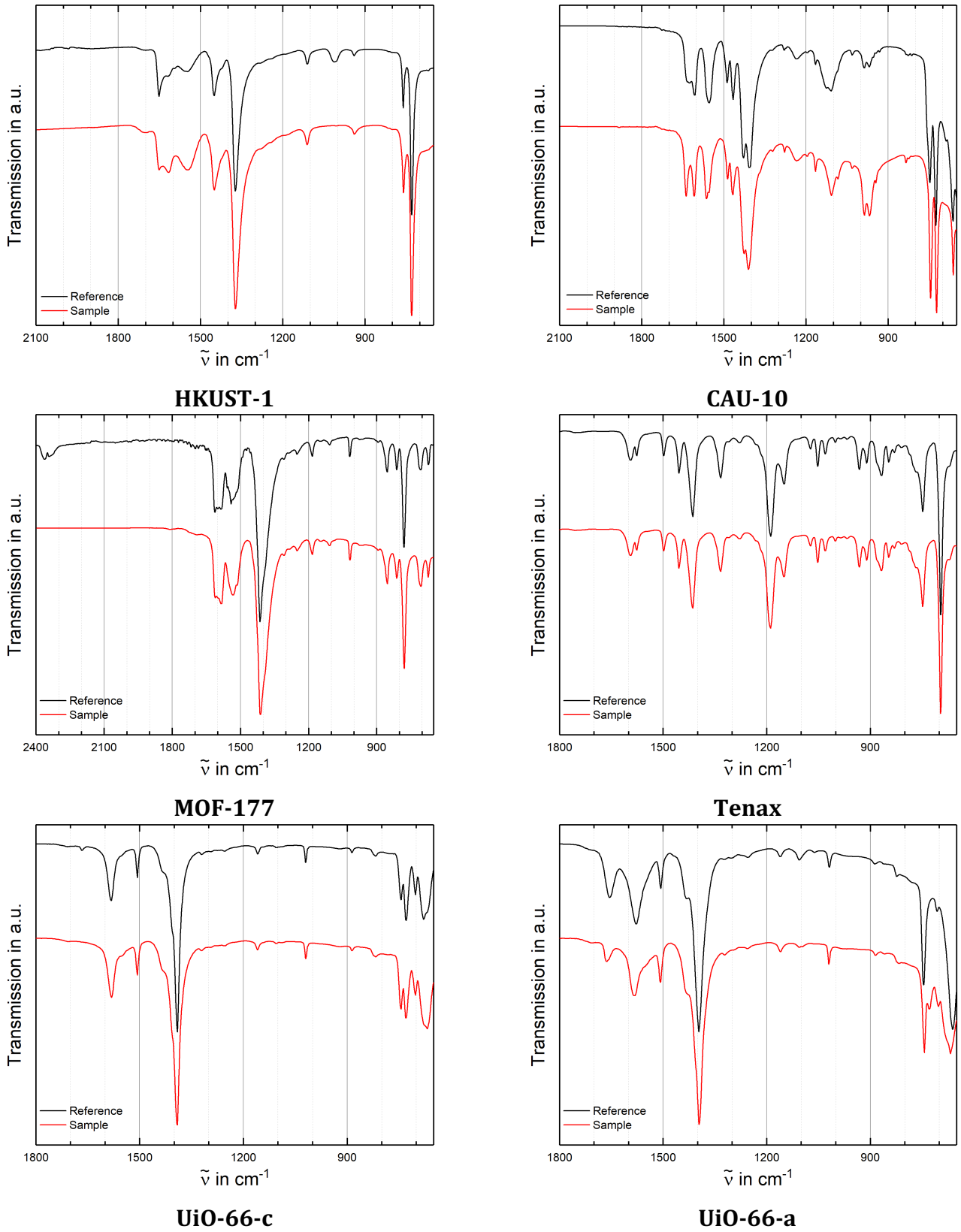

Figure 68. First part of infrared spectra of MOFs before (black) and after sampling and thermal desorption experiments. Adsorbent names under spectra.

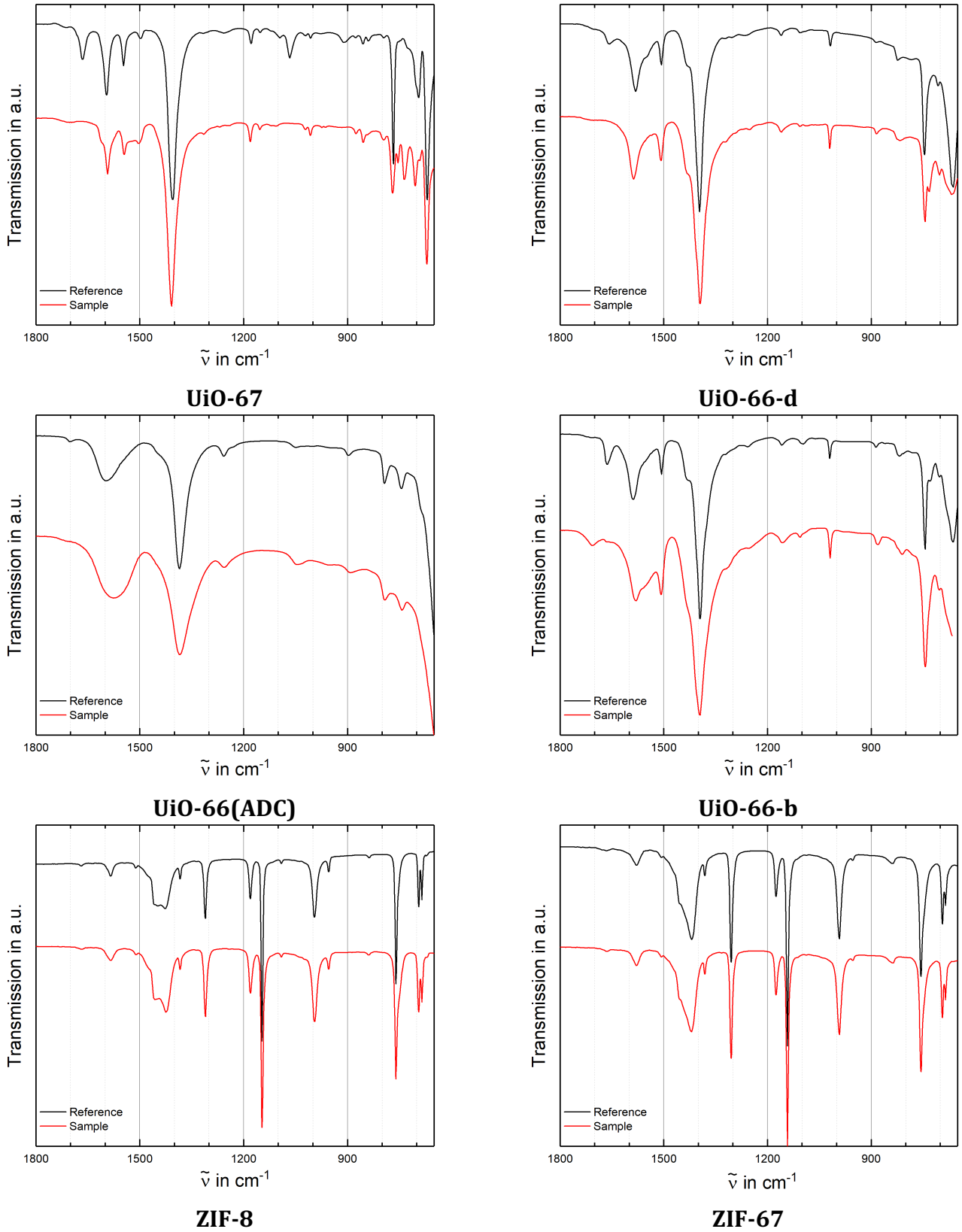

Figure 69. Second part of infrared spectra of MOFs before (black) and after sampling and thermal desorption experiments. MOF names directly under spectra.

7 Publications

The section “Preconcentration of nitro alkanes with archetype 1st generation MOFs” (4.1) was submitted to Advanced Functional Materials (AFM) at the 26th of July 2017 and was published at the 1st of December 2’017 under the title “Preconcentration of Nitroalkanes with Archetype Metal–Organic Frameworks (MOFs) as Concept for a Sensitive Sensing of Explosives in the Gas Phase”. [293] Co-authors were: Michael Wittek, Philip Scherer, Stefan Löbbecke and Klaus Müller-Buschbaum

Parts of subsection 4.2.5 were published in different engineering-focused journals and conference proceedings. [67], [314], [315], [322], [340], [454] In all cases, results were produced in close cooperation with researchers from the “Lehrstuhl für Messtechnik” of the Saarland University, namely Tilman Sauerwald and Martin Leidinger. MOF-coatings using drop coating, air brush as well as the characterization using scanning electron and visible light microscopy were within the contributions for this publications as well as analyte gas mixing, basic preconcentrator testing and iGC-measurements for benzene and toluene.

8 References

[1] J. E. Parmeter, G. A. Eiceman, and J. E. Rodriguez, "Trace detection of narcotics using a preconcentrator/ion mobility spectrometer system," *Juv. Justice*, vol. 602, 2001.

[2] R. Schulte-Ladbeck, P. Kolla, and U. Karst, "Trace analysis of peroxide-based explosives.," *Anal. Chem.*, vol. 75, no. 4, pp. 731–5, Feb. 2003.

[3] L. Senesac and T. G. Thundat, "Nanosensors for trace explosive detection," *Mater. Today*, vol. 11, no. 3, pp. 28–36, Mar. 2008.

[4] National Consortium for the Study of Terrorism and Responses to Terrorism, "Global Terrorism Database, incidents by weapon type," 2016. [Online]. Available: http://www.start.umd.edu/gtd/search/Results.aspx?charttype=pie&chart=weapon&casualties_type=&casualties_max=&start_year=2016&start_month=1&start_day=1&end_year=2016&end_month=12&end_day=31. [Accessed: 08-Jan-2018].

[5] Airports Council international, "Preliminary world airport traffic rankings 2015," 2015. [Online]. Available: http://www.aci.aero/News/Releases/Most-Recent/2016/04/04/ACI-releases-preliminary-world-airport-traffic-rankings-. [Accessed: 08-Jan-2018].

[6] H. Schubert, *Detection of Liquid Explosives and Flammable Agents in Connection with Terrorism*. Dordrecht: Springer Netherlands, 2008.

[7] J. S. Caygill, F. Davis, and S. P. J. Higson, "Current trends in explosive detection techniques.," *Talanta*, vol. 88, pp. 14–29, Jan. 2012.

[8] S. Singh, "Sensors - an effective approach for the detection of explosives.," *J. Hazard. Mater.*, vol. 144, no. 1–2, pp. 15–28, Jun. 2007.

[9] J. R. Conder and C. L. Young, *Physicochemical Measurement by Gas Chromatography*. Hoboken, New Jersey: John Wiley & Sons, Ltd, 1979.

[10] J. Richardson, "Gas Chromatography," *Org. Chem. CU Boulder*, vol. 23, 2015.

[11] O. Yaghi, G. Li, and H. Li, "Selective binding and removal of guests in a microporous metal-organic framework," *Nature*, vol. 378, pp. 703–706, 1995.

[12] Y. He, S. Xiang, and B. Chen, "A microporous hydrogen-bonded organic framework for highly selective C2H2/C2H4 separation at ambient temperature.," *J. Am. Chem. Soc.*, vol. 133, no. 37, pp. 14570–3, Sep. 2011.

[13] A. Díaz Aguilar *et al.*, "A hybrid nanosensor for TNT vapor detection," *Nano Lett.*, vol. 10, no. 2, pp. 380–4, Feb. 2010.

[14] X. Yang, X. X. Du, J. Shi, and B. Swanson, "Molecular recognition and self-assembled polymer films for vapor phase detection of explosives.," *Talanta*, vol. 54, no. 3, pp. 439–45, May 2001.

[15] M. Szultka, J. Szeliga, M. Jackowski, and B. Buszewski, "Development of novel molecularly imprinted solid-phase microextraction fibers and their application for the determination of antibiotic drugs in biological samples by SPME-LC/MS n," *Anal. Bioanal. Chem.*, vol. 403, pp. 785–796, 2012.

[16] V. Ramanathan, R. J. Cicerone, H. B. Singh, and J. T. Kiehl, "Trace gas trends and their potential role in climate change," *J. Geophys. Res.*, vol. 90, no. D3, p. 5547, 1985.

[17] "Earth System Research Laboratory." [Online]. Available: https://www.esrl.noaa.gov/gmd/hats/insitu/cats/cats_conc.html. [Accessed: 11-Mar-2018].

[18] D. Menning and H. Östmark, "Detection of liquid and homemade explosives: What do we need to know about their properties?," *NATO Sci. Peace Secur. Ser. B Phys. Biophys.*, pp. 55–70, 2008.

[19] R. G. Ewing, M. J. Waltman, D. a. Atkinson, J. W. Grate, and P. J. Hotchkiss, "The vapor pressures of explosives," *TrAC Trends Anal. Chem.*, vol. 42, pp. 35–48, Jan. 2013.

[20] K. E. Brown, M. T. Greenfield, S. D. McGrane, and D. S. Moore, "Advances in explosives analysis—part II: photon and neutron methods," *Anal. Bioanal. Chem.*, 2015.

[21] K. E. Brown, M. T. Greenfield, S. D. McGrane, and D. S. Moore, "Advances in explosives analysis—part I: animal, chemical, ion, and mechanical methods," *Anal. Bioanal. Chem.*, vol. 408, no. 1, pp. 35–47, Jan. 2016.

[22] H. Östmark, S. Wallin, and H. G. Ang, "Vapor Pressure of Explosives: A Critical Review," *Propellants, Explos. Pyrotech.*, vol. 37, no. 1, pp. 12–23, Feb. 2012.

[23] A. FAINBERG, "Explosives Detection for Aviation Security," *Science (80-.).*, vol. 255, no. 5051, pp. 1531–1537, Mar. 1992.

[24] J. Yinon, "Field detection and monitoring of explosives," *TrAC Trends Anal. Chem.*, vol. 21, no. 4, pp. 292–301, Apr. 2002.

[25] H. Sohn and J. Steinhanses, "Use of Ion Mobility Spectrometry for the Preliminary Evaluation of Hazardous Military Waste Sites - Opportunities and Limitations," in *International Society for Ion Mobility Spectrometry*, 1998, pp. 1–14.

[26] A. Zalewska, W. Pawłowski, and W. Tomaszewski, "Limits of detection of explosives as determined with IMS and field asymmetric IMS vapour detectors.," *Forensic Sci. Int.*, vol. 4000, pp. 1–5, Jan. 2013.

[27] P. Guerra-Diaz, S. Gura, and J. R. Almirall, "Dynamic planar solid phase microextraction-ion mobility spectrometry for rapid field air sampling and analysis of illicit drugs and explosives.," *Anal. Chem.*, vol. 82, no. 7, pp. 2826–35, Apr. 2010.

[28] J. Lee *et al.*, "Analysis of explosives using corona discharge ionization combined with ion mobility

spectrometry–mass spectrometry," *Talanta*, vol. 120, pp. 64–70, Mar. 2014.
[29] R. A. Fox, "Indoor Air Quality and Health," *J. Nutr. Environ. Med.*, vol. 6, no. 4, pp. 339–340, Jan. 1996.
[30] J. Ten Brinke *et al.*, "Development of New Volatile Organic Compound (VOC) Exposure Metrics and their Relationship to 'Sick Building Syndrome' Symptoms," *Indoor Air*, vol. 8, no. 3, pp. 140–152, Sep. 1998.
[31] P. Konieczka, *Handbook of Trace Analysis*. 2016.
[32] The European Parliament and the council of the European Union, "Directive 2008/50/EC of the European Parliament and of the council," 2008.
[33] A. P. Jones, "Indoor air quality and health," *Atmos. Environ.*, vol. 33, no. 28, pp. 4535–4564, Dec. 1999.
[34] P. S. Burge, "Sick building syndrome," *Occup. Environ. Med.*, vol. 61, no. 2, pp. 185–190, Feb. 2004.
[35] WHO, "Guidelines for indoor air quality," 2010.
[36] H. Hofmann, G. Erdmann, and A. Müller, "Zielkonflikt energieeffiziente Bauweise und gute Raumluftqualität – Datenerhebung für flüchtige organische Verbindungen in der Innenraumluft von Wohn- und Bürogebäuden (Lösungswege)," Springe-Eldagsen, 2014.
[37] T. C. Pearce, S. S. Schiffman, H. T. Nagle, and J. W. Gardner, *Handbook of Machine Olfaction*. Weinheim, FRG: Wiley-VCH Verlag GmbH & Co. KGaA, 2002.
[38] W. Groves, "Analyzing organic vapors in exhaled breath using a surface acoustic wave sensor array with preconcentration: Selection and characterization of the preconcentrator adsorbent," *Anal. Chim. Acta*, vol. 371, no. 2–3, pp. 131–143, Oct. 1998.
[39] K. Fiedler, E. Schütz, and S. Geh, "Detection of microbial volatile organic compounds (MVOCs) produced by moulds on various materials," *Int. J. Hyg. Environ. Health*, vol. 204, no. 2–3, pp. 111–121, Jan. 2001.
[40] K. Dettmer and W. Engewald, "Ambient air analysis of volatile organic compounds using adsorptive enrichment," *Chromatographia*, vol. 57, no. S1, pp. S339–S347, Jan. 2003.
[41] K. Dettmer and W. Engewald, "Adsorbent materials commonly used in air analysis for adsorptive enrichment and thermal desorption of volatile organic compounds," *Anal. Bioanal. Chem.*, vol. 373, no. 6, pp. 490–500, Jul. 2002.
[42] J. Namiesnik, T. Gorecki, E. Kozlowski, L. Torres, and J. Mathieu, "Passive dosimeters — an approach to atmospheric pollutants analysis," *Sci. Total Environ.*, vol. 38, pp. 225–258, Sep. 1984.
[43] T. Górecki and J. Namieśnik, "Passive sampling," *TrAC Trends Anal. Chem.*, vol. 21, no. 4, pp. 276–291, Apr. 2002.
[44] S. . Krupa and A. . Legge, "Passive sampling of ambient, gaseous air pollutants: an assessment from an ecological perspective," *Environ. Pollut.*, vol. 107, no. 1, pp. 31–45, Jan. 2000.
[45] M. Harper, "Evaluation of solid sorbent sampling methods by breakthrough volume studies," *Ann. Occup. Hyg.*, vol. 37, no. 1, pp. 65–88, 1993.
[46] P. P. Ylä-Mäihäniemi and D. R. Williams, "A Comparison of Frontal and Nonfrontal Methods for Determining Solid–Liquid Adsorption Isotherms Using Inverse Liquid Chromatography," *Langmuir*, vol. 23, no. 7, pp. 4095–4101, Mar. 2007.
[47] J. F. Pankow, "Overview of the gas phase retention volume behavior of organic compounds on polyurethane foam," *Atmos. Environ.*, vol. 23, no. 5, pp. 1107–1111, 1989.
[48] V. Camel and M. Caude, "Trace enrichment methods for the determination of organic pollutants in ambient air," *J. Chromatogr. A*, vol. 710, no. 1, pp. 3–19, Aug. 1995.
[49] K. Dettmer, T. Bittner, and W. Engewald, "Adsorptive enrichment and thermal desorption of low-boiling oxygenated compounds—possibilities and limitations," *Chromatographia*, vol. 53, no. S1, pp. S322–S326, Jan. 2001.
[50] S. Mariné, M. Pedrouzo, R. Maria Marcé, I. Fonseca, and F. Borrull, "Comparison between sampling and analytical methods in characterization of pollutants in biogas," *Talanta*, vol. 100, pp. 145–152, Oct. 2012.
[51] Z. Ni, J. P. Jerrell, K. R. Cadwallader, and R. I. Masel, "Metal-organic frameworks as adsorbents for trapping and preconcentration of organic phosphonates.," *Anal. Chem.*, vol. 79, no. 4, pp. 1290–3, Feb. 2007.
[52] K. Dettmer-Wilde and W. Engewald, *Practical Gas Chromatography*. Berlin, Heidelberg: Springer Berlin Heidelberg, 2014.
[53] M. Schneider and K. U. Goss, "Systematic investigation of the sorption properties of tenax TA, chromosorb 106, porapak n, and carbopak f," *Anal. Chem.*, vol. 81, no. 8, pp. 3017–3021, 2009.
[54] S. Takada *et al.*, "Micro Gas Preconcentrator Made of a Film of Single-Walled Carbon Nanotubes," *IEEJ Trans. Sensors Micromachines*, vol. 130, no. 6, pp. 207–211, 2010.
[55] J. McCaffrey, C.A and MacLachlan, "Adsorbent Tube Evaluation for the Preconcentration of Volatile Organic Compounds in Air for Analysis by Gas Chromatography-Mass Spectrometry," *Analyst*, vol. 119, no. May, p. 897, 1994.
[56] C. Jia, S. Batterman, and C. Godwin, "Continuous, intermittent and passive sampling of airborne VOCs.," *J. Environ. Monit.*, vol. 9, no. 11, pp. 1220–1230, 2007.
[57] MARKES, "EPA Method TO-17 for monitoring 'air toxics' in ambient air using sorbent tubes and automated, cryogen- free thermal desorption," *Markes Appl. Notes*.
[58] MARKES, "Analytical thermal desorption : History , technical aspects and application range," *Markes Appl. Notes*.
[59] MARKES, "Selection of gas flows and split ratios during thermal desorption," *Markes Appl. Notes*.
[60] F. Zheng, D. L. Baldwin, L. S. Fifield, N. C. Anheier, C. L. Aardahl, and J. W. Grate, "Single-walled carbon nanotube paper as a sorbent for organic vapor preconcentration.," *Anal. Chem.*, vol. 78, no. 7, pp. 2442–6, Apr. 2006.
[61] I. Voiculescu *et al.*, "Micropreconcentrator for enhanced trace detection of explosives and chemical agents,"

Sensors Journal, IEEE, vol. 6, no. 5, pp. 1094–1104, 2006.
[62] F. Almazán *et al.*, "Zeolite based microconcentrators for volatile organic compounds sensing at trace-level: fabrication and performance," *J. Micromechanics Microengineering*, vol. 26, no. 8, p. 084010, 2016.
[63] I. Gràcia *et al.*, "Sub-ppm gas sensor detection via spiral μ-preconcentrator," *Sensors Actuators B Chem.*, vol. 132, no. 1, pp. 149–154, May 2008.
[64] J. Yeom *et al.*, "Enhanced toxic gas detection using a MEMS preconcentrator coated with the metal organic framework absorber," in *2008 IEEE 21st International Conference on Micro Electro Mechanical Systems*, 2008, no. c, pp. 232–235.
[65] S. Semancik *et al.*, "Microhotplate platforms for chemical sensor research," *Sensors Actuators B Chem.*, vol. 77, no. 1–2, pp. 579–591, Jun. 2001.
[66] A. Schütze *et al.*, "Highly Sensitive and Selective VOC Sensor Systems Based on Semiconductor Gas Sensors: How to?," *Environments*, vol. 4, no. 1, p. 20, Mar. 2017.
[67] A. Schütze, M. Leidinger, B. Schmitt, T. Sauerwald, M. Rieger, and C. Alépée, "A novel low-cost pre-concentrator concept to boost sensitivity and selectivity of gas sensor systems," in *Proceedings IEEE Sensors 2015*, 2015.
[68] Supelco, "Application Note 141: Air Sampling of VOCs by SPME for Analysis by Capillary GC," vol. 141, no. Table 2.
[69] R. Maleki, K. Farhadi, and R. Tahmasebi, "Preparation of a Sol–Gel Titania Based Coating for HS-SPME of Aliphatic Alcohols from Non-Alcoholic Beer Samples," *Chromatographia*, vol. 69, no. 7, pp. 775–778, 2009.
[70] J. L. Liu, L. Li, Z. Ning, P. Zhao, and H. Fan, "Multi-layer Cartridges Filled with Multi-Walled Carbon Nanotubes for the Determination of Volatile Organic Compounds in Indoor Air," *Anal Chem*, vol. 24, no. April, pp. 515–519, 2008.
[71] W. Yao *et al.*, "Absorption and desorption characteristic of zeolites in gas sensor system," *2008 9th Int. Conf. Solid-State Integr. Technol.*, pp. 2589–2592, Oct. 2008.
[72] G. Bunte, J. Hürttlen, H. Pontius, K. Hartlieb, and H. Krause, "Gas phase detection of explosives such as 2,4,6-trinitrotoluene by molecularly imprinted polymers.," *Anal. Chim. Acta*, vol. 591, no. 1, pp. 49–56, May 2007.
[73] A. V. Kiselev and Y. I. Yashin, *Gas-Adsorption Chromatography*, vol. 1. Boston, MA: Springer US, 1969.
[74] E. Matisová and S. Škrabáková, "Carbon sorbents and their utilization for the preconcentration of organic pollutants in environmental samples," *J. Chromatogr. A*, vol. 707, no. 2, pp. 145–179, Jul. 1995.
[75] Y. Mohsen *et al.*, "Selection and characterization of adsorbents for the analysis of an explosive-related molecule traces in the air," *Sensors Actuators, B Chem.*, vol. 176, pp. 124–131, 2013.
[76] J. Zhao, T. Luo, X. Zhang, Y. Lei, K. Gong, and Y. Yan, "Highly Selective Zeolite Membranes as Explosive Preconcentrators.," *Anal. Chem.*, Jul. 2012.
[77] X. Xu, J. Wang, and Y. Long, "Zeolite-based Materials for Gas Sensors," *Sensors*, vol. 6, no. 12, pp. 1751–1764, Dec. 2006.
[78] G. Korotcenkov, *Handbook of Gas Sensor Materials. Properties, Advantages and Shortcomings for Applications. Volume 2: New Trends and Technologies*, vol. 2. New York, NY: Springer New York, 2014.
[79] G. Walsh and S. Hamilton, "Adsorption of 2,4,6-Trinitrotoluene on MFI Zeolite," *Propellants, Explos. Pyrotech.*, vol. 36, no. 2, pp. 182–186, Apr. 2011.
[80] T. G. Glover, K. I. Dunne, R. J. Davis, and M. D. LeVan, "Carbon–silica composite adsorbent: Characterization and adsorption of light gases," *Microporous Mesoporous Mater.*, vol. 111, no. 1–3, pp. 1–11, Apr. 2008.
[81] E. J. Cha and D. S. Lee, "Poly(dimethylsiloxane) mini-disk extraction," *Bull. Korean Chem. Soc.*, vol. 32, no. 10, pp. 3603–3609, 2011.
[82] S. Lordel, F. Chapuis-Hugon, V. Eudes, and V. Pichon, "Selective extraction of nitroaromatic explosives by using molecularly imprinted silica sorbents," *Anal. Bioanal. Chem.*, pp. 1–10, 2011.
[83] S. Lordel, F. Chapuis-Hugon, V. Eudes, and V. Pichon, "Development of imprinted materials for the selective extraction of nitroaromatic explosives.," *J. Chromatogr. A*, vol. 1217, no. 43, pp. 6674–80, Oct. 2010.
[84] G. Bunte, M. Heil, D. Röseling, J. Hürttlen, H. Pontius, and H. Krause, "Trace Detection of Explosives Vapours by Molecularly Imprinted Polymers for Security Measures," *Propellants, Explos. Pyrotech.*, vol. 34, no. 3, pp. 245–251, Jun. 2009.
[85] A. McCluskey, C. I. Holdsworth, and M. C. Bowyer, "Molecularly imprinted polymers (MIPs): sensing, an explosive new opportunity?," *Org. Biomol. Chem.*, vol. 5, no. 20, pp. 3233–44, Oct. 2007.
[86] D. L. Rathbone, D. Su, Y. Wang, and D. C. Billington, "Molecular recognition by fluorescent imprinted polymers," *Tetrahedron Lett.*, vol. 41, no. 1, pp. 123–126, Jan. 2000.
[87] B. Sellergren, "Shaping enzyme inhibitors," vol. 2, no. January, pp. 7–8, 2010.
[88] B. Okutucu, A. Akkaya, and N. K. Pazarlioglu, "Molecularly imprinted polymers for some reactive dyes.," *Prep. Biochem. Biotechnol.*, vol. 40, no. 4, pp. 366–76, Oct. 2010.
[89] CAMSCO, "CAMSCO sorbent selection chart." [Online]. Available: https://camsco.com/public/resources/sorbents.html. [Accessed: 10-Mar-2018].
[90] V. Simon, M.-L. Riba, A. Waldhart, and L. Torres, "Breakthrough volume of monoterpenes on Tenax TA: influence of temperature and concentration for α-pinene," *J. Chromatogr. A*, vol. 704, no. 2, pp. 465–471, Jun. 1995.
[91] K. Schoene, J. Steinhanses, and A. K&#xFFFD;nig, "The sorptive efficiency of Tenax for binary vapour mixtures," *Fresenius. J. Anal. Chem.*, vol. 336, no. 2, pp. 114–119, 1990.
[92] B. Alfeeli, V. Jain, R. K. Johnson, F. L. Beyer, J. R. Heflin, and M. Agah, "Characterization of poly(2,6-diphenyl-p-phenylene oxide) films as adsorbent for microfabricated preconcentrators," *Microchem. J.*, vol. 98, pp. 240–245, 2011.
[93] K. E. Murray, "Concentration of headspace, airborne and aqueous volatiles on chromosorb 105 for

examination by gas chromatography and gas chromatography-mass spectrometry," *J. Chromatogr. A*, vol. 135, no. 1, pp. 49–60, May 1977.
[94] T. C. Thomas and Y. A. Nishioka, "Sampling of airborne pesticides using Chromosorb 102," *Bull. Environ. Contam. Toxicol.*, vol. 35, no. 1, pp. 460–465, Jul. 1985.
[95] R. T. Yang, *Adsorbents: Fundamentals and Applications*. Hoboken, NJ, USA: John Wiley & Sons, Inc., 2003.
[96] C. Prado, M. J. Alcaraz, A. Fuentes, J. Garrido, and J. F. Periago, "Storage stability of ketones on carbon adsorbents," *J. Chromatogr. A*, vol. 1129, no. 1, pp. 82–87, Sep. 2006.
[97] W. R. BETZ, S. G. MAPOLDO, G. D. WACHOB, and M. C. FIRTH, "Characterization of Carbon Molecular Sieves and Activated Charcoal for Use in Airborne Contaminant Sampling," *Am. Ind. Hyg. Assoc. J.*, vol. 50, no. 4, pp. 181–187, Apr. 1989.
[98] K. Dettmer, T. Knobloch, and W. Engewald, "Stability of reactive low boiling hydrocarbons on carbon based adsorbents typically used for adsorptive enrichment and thermal desorption," *Fresenius. J. Anal. Chem.*, vol. 366, no. 1, pp. 70–78, Jan. 2000.
[99] A. Kumar and I. Víden, "Volatile organic compounds: Sampling methods and their worldwide profile in ambient air," *Environ. Monit. Assess.*, vol. 131, no. 1–3, pp. 301–321, 2007.
[100] K. S. Novoselov, "Electric Field Effect in Atomically Thin Carbon Films," *Science (80-.).*, vol. 306, no. 5696, pp. 666–669, Oct. 2004.
[101] A. Oberlin, M. Endo, and T. Koyama, "Filamentous growth of carbon through benzene decomposition," *J. Cryst. Growth*, vol. 32, no. 3, pp. 335–349, Mar. 1976.
[102] M. Eddaoudi *et al.*, "Systematic design of pore size and functionality in isoreticular MOFs and their application in methane storage.," *Science*, vol. 295, no. 5554, pp. 469–72, Jan. 2002.
[103] A. K. Cheetham, G. Férey, and T. Loiseau, "Open-Framework Inorganic Materials," *Angew. Chemie Int. Ed.*, vol. 38, no. 22, pp. 3268–3292, Nov. 1999.
[104] S. S. Chui, "A Chemically Functionalizable Nanoporous Material [Cu3(TMA)2(H2O)3]n," *Science (80-.).*, vol. 283, no. 5405, pp. 1148–1150, Feb. 1999.
[105] C. S. Diercks and O. M. Yaghi, "The atom, the molecule, and the covalent organic framework," *Science (80-.).*, vol. 355, no. 6328, p. eaal1585, Mar. 2017.
[106] E. A. Tomic, "Thermal stability of coordination polymers," *J. Appl. Polym. Sci.*, vol. 9, no. 11, pp. 3745–3752, Nov. 1965.
[107] C. Biondi, M. Bonamico, L. Torelli, and A. Vaciago, "On the structure and water content of copper(II) tricyanomethanide," *Chem. Commun.*, no. 10, p. 191, 1965.
[108] B. F. Hoskins and R. Robson, "Design and construction of a new class of scaffolding-like materials comprising infinite polymeric frameworks of 3D-linked molecular rods. A reappraisal of the zinc cyanide and cadmium cyanide structures and the synthesis and structure of the diamond-rela," *J. Am. Chem. Soc.*, vol. 112, no. 4, pp. 1546–1554, Feb. 1990.
[109] H. Li *et al.*, "Design and synthesis of an exceptionally stable and highly porous metal-organic framework," *Nature*, vol. 402, no. 6759, pp. 276–279, Nov. 1999.
[110] O. M. Yaghi and H. Li, "Hydrothermal Synthesis of a Metal-Organic Framework Containing Large Rectangular Channels," *J. Am. Chem. Soc.*, vol. 117, no. 41, pp. 10401–10402, Oct. 1995.
[111] M. Kondo, T. Yoshitomi, H. Matsuzaka, S. Kitagawa, and K. Seki, "Three-Dimensional Framework with Channeling Cavities for Small Molecules:{[M2(4, 4?-bpy)3(NO3)4]?xH2O}n(M? Co, Ni, Zn)," *Angew. Chemie Int. Ed. English*, vol. 36, no. 16, pp. 1725–1727, Sep. 1997.
[112] G. Férey *et al.*, "A chromium terephthalate-based solid with unusually large pore volumes and surface area.," *Science*, vol. 309, no. 5743, pp. 2040–2, Sep. 2005.
[113] CCDC, "How many MOFs are there in the CSD?," 2016. [Online]. Available: https://www.ccdc.cam.ac.uk/support-and-resources/support/case/?caseid=9833bd2c-27f9-4ff7-8186-71a9b415f012. [Accessed: 10-Jan-2018].
[114] CCDC, "The Cambridge Structural Database Data Update - May 2017," 2017. [Online]. Available: https://www.ccdc.cam.ac.uk/support-and-resources/ccdcresources/csd-2017-updates/%0D. [Accessed: 01-Jun-2018].
[115] H. Furukawa *et al.*, "Ultrahigh porosity in metal-organic frameworks.," *Science*, vol. 329, no. 5990, pp. 424–8, Jul. 2010.
[116] S. R. Batten *et al.*, "Terminology of metal–organic frameworks and coordination polymers (IUPAC Recommendations 2013)," *Pure Appl. Chem.*, vol. 85, no. 8, pp. 1715–1724, 2013.
[117] J. L. C. Rowsell and O. M. Yaghi, "Metal–organic frameworks: a new class of porous materials," *Microporous Mesoporous Mater.*, vol. 73, no. 1–2, pp. 3–14, Aug. 2004.
[118] V. V Butova, M. A. Soldatov, A. A. Guda, K. A. Lomachenko, and C. Lamberti, "Metal-organic frameworks: structure, properties, methods of synthesis and characterization," *Russ. Chem. Rev.*, vol. 85, no. 3, pp. 280–307, 2016.
[119] O. M. Yaghi *et al.*, "Reticular synthesis and the design of new materials.," *Nature*, vol. 423, no. 6941, pp. 705–14, Jun. 2003.
[120] H.-C. "Joe" Zhou and S. Kitagawa, "Metal–Organic Frameworks (MOFs)," *Chem. Soc. Rev.*, vol. 43, no. 16, pp. 5415–5418, Jul. 2014.
[121] H. Furukawa, K. E. Cordova, M. O'Keeffe, and O. M. Yaghi, "The chemistry and applications of metal-organic frameworks.," *Science*, vol. 341, no. 6149, p. 1230444, Aug. 2013.
[122] M. E. Kosal, J.-H. Chou, S. R. Wilson, and K. S. Suslick, "A functional zeolite analogue assembled from metalloporphyrins," *Nat. Mater.*, vol. 1, no. 2, pp. 118–121, Oct. 2002.

[123] B. Chen, F. R. Fronczek, and A. W. Maverick, "Porous Cu?Cd Mixed-Metal?Organic Frameworks Constructed from Cu(Pyac) 2 {Bis[3-(4-pyridyl)pentane-2,4-dionato]copper(II)}," *Inorg. Chem.*, vol. 43, no. 26, pp. 8209–8211, Dec. 2004.
[124] L. J. Wang *et al.*, "Synthesis and Characterization of Metal–Organic Framework-74 Containing 2, 4, 6, 8, and 10 Different Metals," *Inorg. Chem.*, vol. 53, no. 12, pp. 5881–5883, Jun. 2014.
[125] N. L. Rosi, M. Eddaoudi, J. Kim, M. O'Keeffe, and O. M. Yaghi, "Advances in the chemistry of metal–organic frameworks," *CrystEngComm*, vol. 4, no. 68, pp. 401–404, 2002.
[126] O. K. Farha and J. T. Hupp, "Rational design, synthesis, purification, and activation of metal-organic framework materials.," *Acc. Chem. Res.*, vol. 43, no. 8, pp. 1166–75, Aug. 2010.
[127] H. Wu *et al.*, "Metal-organic frameworks with exceptionally high methane uptake: where and how is methane stored?," *Chemistry*, vol. 16, no. 17, pp. 5205–14, May 2010.
[128] A. D. Burrows, "Mixed-component metal-organic frameworks (MC-MOFs): enhancing functionality through solid solution formation and surface modifications," *CrystEngComm*, vol. 13, no. 11, p. 3623, 2011.
[129] H. Deng *et al.*, "Multiple Functional Groups of Varying Ratios in Metal-Organic Frameworks," *Science (80-.).*, vol. 327, no. 5967, pp. 846–850, Feb. 2010.
[130] D. Zacher *et al.*, "Liquid-Phase Epitaxy of Multicomponent Layer-Based Porous Coordination Polymer Thin Films of [M(L)(P)0.5] Type: Importance of Deposition Sequence on the Oriented Growth," *Chem. - A Eur. J.*, vol. 17, no. 5, pp. 1448–1455, Feb. 2011.
[131] L. Heinke, M. Tu, S. Wannapaiboon, R. a. Fischer, and C. Wöll, "Surface-mounted metal-organic frameworks for applications in sensing and separation," *Microporous Mesoporous Mater.*, pp. 1–16, 2015.
[132] L. R. MacGillivra, *Metal-Organic Frameworks*. Hoboken, NJ, USA: John Wiley & Sons, Inc., 2010.
[133] S. L. James, "Metal-organic frameworks," *Chem. Soc. Rev.*, vol. 32, no. 5, p. 9377, Jul. 2003.
[134] M. Haouas, C. Volkringer, T. Loiseau, G. Férey, and F. Taulelle, "The extra-framework sub-lattice of the metal-organic framework MIL-110: a solid-state NMR investigation.," *Chemistry*, vol. 15, no. 13, pp. 3139–46, Jan. 2009.
[135] S. Kitagawa and K. Uemura, "Dynamic porous properties of coordination polymers inspired by hydrogen bonds," *Chem. Soc. Rev.*, vol. 34, no. 2, p. 109, 2005.
[136] J. E. Mondloch, O. Karagiaridi, O. K. Farha, and J. T. Hupp, "Activation of metal–organic framework materials," *CrystEngComm*, vol. 15, no. 45, p. 9258, 2013.
[137] F. Ke *et al.*, "Thiol-functionalization of metal-organic framework by a facile coordination-based postsynthetic strategy and enhanced removal of Hg2+ from water.," *J. Hazard. Mater.*, vol. 196, pp. 36–43, Nov. 2011.
[138] M. Meilikhov, K. Yusenko, and R. a. Fischer, "The adsorbate structure of ferrocene inside [Al(OH)(bdc)]x (MIL-53): a powder X-ray diffraction study," *Dalt. Trans.*, vol. 53, no. 4, p. 600, 2009.
[139] A. J. Howarth, A. W. Peters, N. A. Vermeulen, T. C. Wang, J. T. Hupp, and O. K. Farha, "Best Practices for the Synthesis, Activation, and Characterization of Metal–Organic Frameworks," *Chem. Mater.*, p. acs.chemmater.6b02626, Sep. 2016.
[140] A. Schaate, P. Roy, T. Preuße, S. J. Lohmeier, A. Godt, and P. Behrens, "Porous interpenetrated zirconium-organic frameworks (PIZOFs): A chemically versatile family of metal-organic frameworks," *Chem. - A Eur. J.*, vol. 17, no. 34, pp. 9320–9325, 2011.
[141] J. Zhang, L. Wojtas, R. W. Larsen, M. Eddaoudi, and M. J. Zaworotko, "Temperature and Concentration Control over Interpenetration in a Metal-Organic Material," *J. Am. Chem. Soc.*, vol. 131, no. 47, pp. 17040–17041, Dec. 2009.
[142] M. Alhamami, H. Doan, and C.-H. Cheng, "A Review on Breathing Behaviors of Metal-Organic-Frameworks (MOFs) for Gas Adsorption," *Materials (Basel).*, vol. 7, no. 4, pp. 3198–3250, Apr. 2014.
[143] G. Férey, "Hybrid porous solids: past, present, future," *Chem. Soc. Rev.*, vol. 37, no. 1, pp. 191–214, 2008.
[144] W. Lu *et al.*, "Tuning the structure and function of metal-organic frameworks via linker design.," *Chem. Soc. Rev.*, pp. 5561–5593, Mar. 2014.
[145] T. Loiseau *et al.*, "A Rationale for the Large Breathing of the Porous Aluminum Terephthalate (MIL-53) Upon Hydration," *Chem. - A Eur. J.*, vol. 10, no. 6, pp. 1373–1382, Mar. 2004.
[146] S. Kaskel, *The Chemistry of Metal-Organic Frameworks: Synthesis, Characterization, and Applications*. Weinheim, Germany: Wiley-VCH Verlag GmbH & Co. KGaA, 2016.
[147] J. M. Castillo, T. J. H. Vlugt, and S. Calero, "Understanding Water Adsorption in Cu–BTC Metal–Organic Frameworks," *J. Phys. Chem. C*, vol. 112, no. 41, pp. 15934–15939, Oct. 2008.
[148] A. Dhakshinamoorthy *et al.*, "Comparison of porous iron trimesates basolite F300 and MIL-100(Fe) as heterogeneous catalysts for lewis acid and oxidation reactions: Roles of structural defects and stability," *ACS Catal.*, vol. 2, no. 10, pp. 2060–2065, 2012.
[149] M. Sanchez-Sanchez, I. de Asua, D. Ruano, and K. Diaz, "Direct Synthesis, Structural Features, and Enhanced Catalytic Activity of the Basolite F300-like Semiamorphous Fe-BTC Framework," *Cryst. Growth Des.*, vol. 15, no. 9, pp. 4498–4506, Sep. 2015.
[150] J. H. Cavka *et al.*, "A New Zirconium Inorganic Building Brick Forming Metal Organic Frameworks with Exceptional Stability," *J. Am. Chem. Soc.*, vol. 130, no. 42, pp. 13850–13851, Oct. 2008.
[151] L. Valenzano *et al.*, "Disclosing the Complex Structure of UiO-66 Metal Organic Framework: A Synergic Combination of Experiment and Theory," *Chem. Mater.*, vol. 23, no. 7, pp. 1700–1718, Apr. 2011.
[152] P. Ghosh, Y. J. Colón, and R. Q. Snurr, "Water adsorption in UiO-66: the importance of defects," *Chem. Commun.*, vol. 50, no. 77, pp. 11329–11331, 2014.
[153] H. Wu *et al.*, "Unusual and highly tunable missing-linker defects in zirconium metal-organic framework UiO-66 and their important effects on gas adsorption," *J. Am. Chem. Soc.*, vol. 135, no. 28, pp. 10525–10532, 2013.

[154] M. J. Katz *et al.*, "A facile synthesis of UiO-66, UiO-67 and their derivatives.," *Chem. Commun. (Camb).*, vol. 49, no. 82, pp. 9449–51, Oct. 2013.
[155] K. S. Park *et al.*, "Exceptional chemical and thermal stability of zeolitic imidazolate frameworks.," *Proc. Natl. Acad. Sci. U. S. A.*, vol. 103, no. 27, pp. 10186–91, Jul. 2006.
[156] M. Etter and R. E. Dinnebier, "A Century of Powder Diffraction: a Brief History," *Zeitschrift für Anorg. und Allg. Chemie*, vol. 640, no. 15, pp. 3015–3028, Dec. 2014.
[157] S. Brunauer, P. H. Emmett, and E. Teller, "Adsorption of Gases in Multimolecular Layers," *J. Am. Chem. Soc.*, vol. 60, no. 2, pp. 309–319, Feb. 1938.
[158] S. Devautour-Vinot, G. Maurin, F. Henn, C. Serre, and G. Férey, "Water and ethanol desorption in the flexible metal organic frameworks, MIL-53 (Cr, Fe), investigated by complex impedance spectroscopy and density functional theory calculations.," *Phys. Chem. Chem. Phys.*, vol. 12, no. 39, pp. 12478–85, Oct. 2010.
[159] J. E. Mondloch *et al.*, "Are Zr6-based MOFs water stable? Linker hydrolysis vs. capillary-force-driven channel collapse.," *Chem. Commun. (Camb).*, Jun. 2014.
[160] S. Couck, J. F. M. Denayer, G. V Baron, T. Re, and J. Gascon, "An Amine-Functionalized MIL-53 Metal - Organic Framework with Large Separation Power for CO2 and CH4," *J. Am. Chem. Soc.*, vol. 53, pp. 6326–6327, 2009.
[161] I. Senkovska, F. Hoffmann, M. Fröba, J. Getzschmann, W. Böhlmann, and S. Kaskel, "New highly porous aluminium based metal-organic frameworks: Al(OH)(ndc) (ndc = 2,6-naphthalene dicarboxylate) and Al(OH)(bpdc) (bpdc = 4,4′-biphenyl dicarboxylate)," *Microporous Mesoporous Mater.*, vol. 122, no. 1–3, pp. 93–98, 2009.
[162] Y. Liu, S. Moon, J. T. Hupp, and O. K. Farha, "Dual-Function Metal–Organic Framework as a Versatile Catalyst for Detoxifying Chemical Warfare Agent Simulants," *ACS Nano*, vol. 9, no. 12, pp. 12358–12364, Dec. 2015.
[163] S. Mukherjee, B. Joarder, A. V. Desai, B. Manna, R. Krishna, and S. K. Ghosh, "Exploiting Framework Flexibility of a Metal–Organic Framework for Selective Adsorption of Styrene over Ethylbenzene," *Inorg. Chem.*, vol. 54, no. 9, pp. 4403–4408, May 2015.
[164] J. Canivet, M. Vandichel, and D. Farrusseng, "Origin of highly active metal–organic framework catalysts: defects? Defects!," *Dalt. Trans.*, vol. 45, no. 10, pp. 4090–4099, 2016.
[165] F. Stallmach *et al.*, "NMR Studies on the Diffusion of Hydrocarbons on the Metal-Organic Framework Material MOF-5," *Angew. Chemie Int. Ed.*, vol. 45, no. 13, pp. 2123–2126, Mar. 2006.
[166] M. Wehring, J. Gascon, D. Dubbeldam, F. Kapteijn, R. Q. Snurr, and F. Stallmach, "Self-diffusion studies in CuBTC by PFG NMR and MD simulations," *J. Phys. Chem. C*, vol. 114, no. 23, pp. 10527–10534, 2010.
[167] X. Cheng *et al.*, "Size- and morphology-controlled NH2-MIL-53(Al) prepared in DMF–water mixed solvents," *Dalt. Trans.*, vol. 42, no. 37, p. 13698, 2013.
[168] J.-C. Rybak *et al.*, "Metal–Organic Framework Luminescence in the Yellow Gap by Codoping of the Homoleptic Imidazolate ∞ Europium 3 [Ba(Im)2] with Divalent," *J. Am. Chem. Soc.*, vol. 135, no. 18, pp. 6896–902, May 2013.
[169] J.-R. Li, J. Sculley, and H.-C. Zhou, "Metal–Organic Frameworks for Separations," *Chem. Rev.*, vol. 112, no. 2, pp. 869–932, Feb. 2012.
[170] E. Deniz, F. Karadas, H. A. Patel, S. Aparicio, C. T. Yavuz, and M. Atilhan, "A combined computational and experimental study of high pressure and supercritical CO2 adsorption on Basolite MOFs," *Microporous Mesoporous Mater.*, vol. 175, pp. 34–42, Jul. 2013.
[171] T. Düren, F. Millange, G. Férey, K. S. Walton, and R. Q. Snurr, "Calculating Geometric Surface Areas as a Characterization Tool for Metal–Organic Frameworks," *J. Phys. Chem. C*, vol. 111, no. 42, pp. 15350–15356, Oct. 2007.
[172] C. E. Wilmer *et al.*, "Large-scale screening of hypothetical metal–organic frameworks," *Nat. Chem.*, vol. 4, no. 2, pp. 83–89, Nov. 2011.
[173] D. Wu, C. Wang, B. Liu, D. Liu, Q. Yang, and C. Zhong, "Large-scale computational screening of metal-organic frameworks for CH4/H2 separation," *AIChE J.*, vol. 00, no. 0, 2011.
[174] M. Fernandez, T. K. Woo, C. E. Wilmer, and R. Q. Snurr, "Large-Scale Quantitative Structure–Property Relationship (QSPR) Analysis of Methane Storage in Metal–Organic Frameworks," *J. Phys. Chem. C*, vol. 117, no. 15, pp. 7681–7689, Apr. 2013.
[175] D. Wu *et al.*, "Revealing the structure-property relationships of metal-organic frameworks for CO2 capture from flue gas.," *Langmuir*, vol. 28, no. 33, pp. 12094–9, Aug. 2012.
[176] M. Kandiah *et al.*, "Synthesis and stability of tagged UiO-66 Zr-MOFs," *Chem. Mater.*, vol. 22, no. 24, pp. 6632–6640, 2010.
[177] N. C. Burtch, H. Jasuja, and K. S. Walton, "Water Stability and Adsorption in Metal-Organic Frameworks.," *Chem. Rev.*, Sep. 2014.
[178] K. a Cychosz and A. J. Matzger, "Water stability of microporous coordination polymers and the adsorption of pharmaceuticals from water.," *Langmuir*, vol. 26, no. 22, pp. 17198–202, Nov. 2010.
[179] K. Leus *et al.*, "Systematic study of the chemical and hydrothermal stability of selected 'stable' Metal Organic Frameworks," *Microporous Mesoporous Mater.*, vol. 226, no. JANUARY, pp. 110–116, May 2016.
[180] M. Bosch, M. Zhang, and H. Zhou, "Increasing the Stability of Metal-Organic Frameworks," *Adv. Chem.*, vol. 2014, pp. 1–8, 2014.
[181] A. U. Czaja, N. Trukhan, and U. Müller, "Industrial applications of metal-organic frameworks.," *Chem. Soc. Rev.*, vol. 38, no. 5, pp. 1284–93, May 2009.
[182] B. Van de Voorde *et al.*, "Improving the mechanical stability of zirconium-based metal–organic frameworks by incorporation of acidic modulators," *J. Mater. Chem. A*, vol. 3, no. 4, pp. 1737–1742, 2015.
[183] I. Senkovska and S. Kaskel, "Ultrahigh porosity in mesoporous MOFs: promises and limitations.," *Chem.*

Commun. (Camb)., vol. 50, no. 54, pp. 7089–98, Jun. 2014.
[184] J. Canivet, A. Fateeva, Y. Guo, B. Coasne, and D. Farrusseng, "Water adsorption in MOFs: fundamentals and applications.," *Chem. Soc. Rev.*, pp. 5594–5617, May 2014.
[185] A. J. Howarth *et al.*, "Chemical, thermal and mechanical stabilities of metal–organic frameworks," *Nat. Rev. Mater.*, no. 15018, p. 15018, 2016.
[186] Y. Bai, Y. Dou, L.-H. Xie, W. Rutledge, J.-R. Li, and H.-C. Zhou, "Zr-based metal–organic frameworks: design, synthesis, structure, and applications," *Chem. Soc. Rev.*, 2016.
[187] J. J. Low, A. I. Benin, P. Jakubczak, J. F. Abrahamian, S. A. Faheem, and R. R. Willis, "Virtual high throughput screening confirmed experimentally: porous coordination polymer hydration.," *J. Am. Chem. Soc.*, vol. 131, no. 43, pp. 15834–42, Nov. 2009.
[188] K. Schwitzgebel, P. S. Lowell, T. B. Parson, and K. J. Sladek, "Estimation of heats of formation of binary oxides," *J. Chem. Eng. Data*, vol. 16, no. 4, pp. 418–423, Oct. 1971.
[189] J. J. Bravo-Suárez, E. A. Páez-Mozo, and S. T. Oyama, "Review of the synthesis of layered double hydroxides: a thermodynamic approach," *Quim. Nova*, vol. 27, no. 4, Aug. 2004.
[190] C. Yang *et al.*, "Fluorous Metal–Organic Frameworks with Superior Adsorption and Hydrophobic Properties toward Oil Spill Cleanup and Hydrocarbon Storage," *J. Am. Chem. Soc.*, vol. 133, no. 45, pp. 18094–18097, Nov. 2011.
[191] T. Wu *et al.*, "Enhancing the stability of metal-organic frameworks in humid air by incorporating water repellent functional groups," *Chem. Commun. (Camb).*, vol. 46, no. 33, pp. 6120–6122, Sep. 2010.
[192] F. Vermoortele *et al.*, "Synthesis modulation as a tool to increase the catalytic activity of MOFs: the unique case of UiO-66 (Zr)," *J. Am. Chem. Soc.*, vol. 66, pp. 0–3, 2013.
[193] L. Zhou, X. Zhang, and Y. Chen, "Modulated synthesis of zirconium metal–organic framework UiO-66 with enhanced dichloromethane adsorption capacity," *Mater. Lett.*, 2017.
[194] S. J. Yang and C. R. Park, "Preparation of Highly Moisture-Resistant Black-Colored Metal Organic Frameworks," *Adv. Mater.*, vol. 24, no. 29, pp. 4010–4013, Aug. 2012.
[195] Z. Hasan, D. Cho, I. Nam, C. Chon, and H. Song, "Preparation of Calcined Zirconia-Carbon Composite from Metal Organic Frameworks and Its Application to Adsorption of Crystal Violet and Salicylic Acid," *Materials (Basel).*, vol. 9, no. 4, p. 261, Mar. 2016.
[196] X. Yan, X. Li, Z. Yan, and S. Komarneni, "Porous carbons prepared by direct carbonization of MOFs for supercapacitors," *Appl. Surf. Sci.*, vol. 308, no. July, pp. 306–310, Jul. 2014.
[197] Y. V. Kaneti *et al.*, "Nanoarchitectured Design of Porous Materials and Nanocomposites from Metal-Organic Frameworks," *Adv. Mater.*, p. 1604898, Dec. 2016.
[198] H. Yoo, H. D. Mai, and K. Rafiq, "Nano Metal-Organic Framework-derived Inorganic Hybrid Nanomaterials: Synthetic Strategies and Applications," *Chem. - A Eur. J.*, Nov. 2016.
[199] N. L. Torad *et al.*, "Facile synthesis of nanoporous carbons with controlled particle sizes by direct carbonization of monodispersed ZIF-8 crystals," *Chem. Commun.*, vol. 49, no. 25, p. 2521, 2013.
[200] W. Zhang, Y. Hu, J. Ge, H. Jiang, and S. Yu, "A Facile and General Coating Approach to Moisture/Water-Resistant Metal–Organic Frameworks with Intact Porosity," *J. Am. Chem. Soc.*, vol. 136, pp. 16978–16981, 2014.
[201] D. J. Collins and H.-C. Zhou, "Hydrogen storage in metal–organic frameworks," *J. Mater. Chem.*, vol. 17, no. 30, p. 3154, 2007.
[202] R. E. Morris and P. S. Wheatley, "Gas storage in nanoporous materials," *Angew. Chemie - Int. Ed.*, vol. 47, no. 27, pp. 4966–4981, 2008.
[203] M. D. Allendorf, A. Schwartzberg, V. Stavila, and a A. Talin, "A roadmap to implementing metal-organic frameworks in electronic devices: challenges and critical directions.," *Chemistry*, vol. 17, no. 41, pp. 11372–88, Oct. 2011.
[204] Z.-Y. Gu, G. Wang, and X.-P. Yan, "MOF-5 metal-organic framework as sorbent for in-field sampling and preconcentration in combination with thermal desorption GC/MS for determination of atmospheric formaldehyde.," *Anal. Chem.*, vol. 82, no. 4, pp. 1365–70, Feb. 2010.
[205] Y.-H. Kim, P. Kumar, E. E. Kwon, and K.-H. Kim, "Metal-organic frameworks as superior media for thermal desorption-gas chromatography application: A critical assessment of MOF-5 for the quantitation of airborne formaldehyde," *Microchem. J.*, vol. 132, pp. 219–226, 2017.
[206] L. Xie *et al.*, "Amine-functionalized MIL-53(Al)-coated stainless steel fiber for efficient solid-phase microextraction of synthetic musks and organochlorine pesticides in water samples," *Anal. Bioanal. Chem.*, vol. 53, 2017.
[207] L. Xie *et al.*, "Preparation and characterization of metal-organic framework MIL-101(Cr)-coated solid-phase microextraction fiber," *Anal. Chim. Acta*, vol. 853, no. 1, pp. 303–310, 2015.
[208] Y.-Y. Wu, C.-X. Yang, and X.-P. Yan, "Fabrication of metal-organic framework MIL-88B films on stainless steel fibers for solid-phase microextraction of polychlorinated biphenyls.," *J. Chromatogr. A*, vol. 1334, pp. 1–8, Mar. 2014.
[209] G.-H. Wang and Y.-Q. Lei, "Fabrication of Metal–Organic Framework MOF-177 Coatings on Stainless Steel Fibers for Head-Space Solid-Phase Microextraction of Phenols," *Bull. Environ. Contam. Toxicol.*, vol. 0, no. 0, p. 0, 2017.
[210] J. Rowsell, "Metal organic frameworks: a new class of porous materials," *Microporous Mesoporous Mater.*, vol. 73, no. 1–2, pp. 3–14, Aug. 2004.
[211] O. Shekhah, J. Liu, R. a Fischer, and C. Wöll, "MOF thin films: existing and future applications.," *Chem. Soc. Rev.*, vol. 40, no. 2, pp. 1081–106, Feb. 2011.
[212] P. Falcaro, R. Ricco, C. M. Doherty, K. Liang, A. J. Hill, and M. J. Styles, "MOF positioning technology and device

fabrication.," *Chem. Soc. Rev.*, vol. 43, no. 16, pp. 5513–60, Jul. 2014.
[213] B. Liu, "Metal–organic framework-based devices: separation and sensors," *J. Mater. Chem.*, pp. 10094–10101, 2012.
[214] P. Kumar, A. Deep, and K.-H. Kim, "Metal organic frameworks for sensing applications," *TrAC Trends Anal. Chem.*, vol. 73, pp. 39–53, 2015.
[215] Z. Huang and H. K. Lee, "Micro-solid-phase extraction of organochlorine pesticides using porous metal-organic framework MIL-101 as sorbent," *J. Chromatogr. A*, vol. 1401, pp. 9–16, 2015.
[216] Y. Wang, Y. Wu, H. Ge, H. Chen, G. Ye, and X. Hu, "Fabrication of metal-organic frameworks and graphite oxide hybrid composites for solid-phase extraction and preconcentration of luteolin.," *Talanta*, vol. 122, pp. 91–6, May 2014.
[217] E. García, R. Medina, M. Lozano, I. Hernández Pérez, M. Valero, and A. Franco, "Adsorption of Azo-Dye Orange II from Aqueous Solutions Using a Metal-Organic Framework Material: Iron- Benzenetricarboxylate," *Materials (Basel).*, vol. 7, no. 12, pp. 8037–8057, Dec. 2014.
[218] M. O. Rodrigues, M. V. de Paula, K. a. Wanderley, I. B. Vasconcelos, S. Alves, and T. a. Soares, "Metal organic frameworks for drug delivery and environmental remediation: A molecular docking approach," *Int. J. Quantum Chem.*, vol. 112, no. 20, pp. 3346–3355, Oct. 2012.
[219] P. A. P. Mendes, A. E. Rodrigues, P. Horcajada, C. Serre, and J. A. C. Silva, "Single and multicomponent adsorption of hexane isomers in the microporous ZIF-8," *Microporous Mesoporous Mater.*, vol. 194, no. August, pp. 146–156, 2014.
[220] R. Manurung *et al.*, "Tunable Porosity through Cooperative Diffusion in a Multicomponent Porous Molecular Crystal," *J. Phys. Chem. C*, p. 150918154818007, 2015.
[221] S. Lowell and J. E. Shields, *Powder Surface Area and Porosity*, vol. 1. Dordrecht: Springer Netherlands, 1991.
[222] H. G. Karge and J.Weitkamp, *Molecular Sieves*. Springer Heidelberg, 2008.
[223] J. Comyn, *Polymer Permeability*. Dordrecht: Springer Netherlands, 1985.
[224] Y. Zhang, I. H. Musselman, J. P. Ferraris, and K. J. Balkus, "Gas permeability properties of Matrimid® membranes containing the metal-organic framework Cu–BPY–HFS," *J. Memb. Sci.*, vol. 313, no. 1–2, pp. 170–181, Apr. 2008.
[225] R. Abedini, M. Omidkhah, and F. Dorosti, "Highly permeable poly(4-methyl-1-pentyne)/NH2-MIL 53 (Al) mixed matrix membrane for CO2/CH4 separation," *RSC Adv.*, vol. 4, no. 69, pp. 36522–36537, 2014.
[226] P. R. Tremaine and D. G. Gray, "Determination of Brunauer-Emmett-Teller monolayer capacities by gas-solid chromatography," *Anal. Chem.*, vol. 48, no. 2, pp. 380–382, 1976.
[227] J. M. Zielinski and L. Kettle, "Physical Characterization : Surface Area and Porosity," 2013.
[228] U. Atkins, Peter Fellow of Lincoln College, University of Oxford, Oxford and U. Julio de Paula Professor of Chemistry, Lewis & Clark College, Portland, Oregon, *Physical Chemistry*, 10th ed. 2014.
[229] S. Lowell, J. E. Shields, M. A. Thomas, and M. Thommes, *Characterization of Porous Solids and Powders: Surface Area, Pore Size and Density*, vol. 16. Dordrecht: Springer Netherlands, 2004.
[230] F. Thielmann and E. Baumgarten, "Characterization of Microporous Aluminas by Inverse Gas Chromatography," *J. Colloid Interface Sci.*, vol. 229, no. 2, pp. 418–422, 2000.
[231] M. Thommes *et al.*, "Physisorption of gases, with special reference to the evaluation of surface area and pore size distribution (IUPAC Technical Report)," *Pure Appl. Chem.*, vol. 87, no. 9–10, pp. 1051–1069, Jan. 2015.
[232] H. Y. Erbil, *Surface Chemistry of Solid And Liquid Interfaces*. Wiley-Blackwell, 2006.
[233] V. Bolis, "Fundamentals in Adsorption at the Solid-Gas Interface. Concepts and Thermodynamics," in *Calorimetry and Thermal Methods in Catalysis*, vol. 154, 2013, p. 561.
[234] Nick Kanellopoulos, *Nanoporous Materials: Advanced Techniques for Characterization, Modeling, and Processing*. CRC Press, 2011.
[235] F. O. Mertens, "Determination of absolute adsorption in highly ordered porous media," *Surf. Sci.*, vol. 603, no. 10–12, pp. 1979–1984, Jun. 2009.
[236] K. Sing, "The use of nitrogen adsorption for the characterisation of porous materials," *Colloids Surfaces A Physicochem. Eng. Asp.*, vol. 187–188, pp. 3–9, Aug. 2001.
[237] M. Leistner, W. Grählert, and S. Kaskel, "Screening of Porous Materials by Thermal Response Measurements," *Chemie Ing. Tech.*, vol. 85, no. 5, pp. 747–752, May 2013.
[238] O. K. Farha *et al.*, "Metal-organic framework materials with ultrahigh surface areas: is the sky the limit?," *J. Am. Chem. Soc.*, vol. 134, no. 36, pp. 15016–21, Sep. 2012.
[239] H. Qiu, L. Lv, B. Pan, Q. Zhang, W. Zhang, and Q. Zhang, "Critical review in adsorption kinetic models," *J. Zhejiang Univ. Sci. A*, vol. 10, no. 5, pp. 716–724, May 2009.
[240] D. Yan, D. D. Gang, N. Zhang, and L. Lin, "Adsorptive Selenite Removal Using Iron-Coated GAC: Modeling Selenite Breakthrough with the Pore Surface Diffusion Model," *J. Environ. Eng.*, vol. 139, no. 2, pp. 213–219, Feb. 2013.
[241] E. Beerdsen and B. Smit, "Understanding diffusion in nanoporous materials," *Stud. Surf. Sci. Catal.*, vol. 170, no. B, pp. 1646–1651, 2007.
[242] T. R. Marrero and E. A. Mason, "Gaseous Diffusion Coefficients," *J. Phys. Chem. Ref. Data*, vol. 1, no. 1, pp. 3–118, Jan. 1972.
[243] N. W. Taylor, "Diffusion in and through Solids," *J. Phys. Chem.*, vol. 46, no. 4, pp. 533–534, Apr. 1942.
[244] R. Krishna, "Diffusion in porous crystalline materials," *Chem. Soc. Rev.*, vol. 41, p. 3099, 2012.
[245] D. I. Kolokolov, L. Diestel, J. Caro, D. Freude, and A. G. Stepanov, "Rotational and Translational Motion of Benzene in ZIF-8 Studied by 2 H NMR: Estimation of Microscopic Self-Diffusivity and Its Comparison with Macroscopic Measurements," *J. Phys. Chem. C*, vol. 118, no. 24, pp. 12873–12879, Jun. 2014.

[246] S. Han *et al.*, "Chromatography in a Single Metal-Organic Framework (MOF) Crystal," *J. Am. Chem. Soc.*, vol. 132, no. 46, pp. 16358–16361, Nov. 2010.
[247] D. Frenkel, *Understanding Molecular Simulation*. 2001.
[248] Y. Jiang, S. Kirmizialtin, and I. C. Sanchez, "Dynamic void distribution in myoglobin and five mutants," *Sci. Rep.*, vol. 4, no. 1, p. 4011, May 2015.
[249] A. W. Thornton, T. Hilder, A. J. Hill, and J. M. Hill, "Predicting gas diffusion regime within pores of different size, shape and composition," *J. Memb. Sci.*, vol. 336, no. 1–2, pp. 101–108, 2009.
[250] J. U. Keller and R. Staudt, *Gas Adsorption Equilibria*. Boston: Kluwer Academic Publishers, 2005.
[251] D. D. Do, *Adsorption Analysis: Equilibria and Kinetics*, vol. 2. Imperial College Press, 1998.
[252] Z. Bao, G. Chang, H. Xing, R. Krishna, Q. Ren, and B. Chen, "Potential of microporous metal–organic frameworks for separation of hydrocarbon mixtures," *Energy Environ. Sci.*, vol. 9, no. 12, pp. 3612–3641, 2016.
[253] J.-R. Li, R. J. Kuppler, and H.-C. Zhou, "Selective gas adsorption and separation in metal–organic frameworks," *Chem. Soc. Rev.*, vol. 38, no. 5, p. 1477, 2009.
[254] J. J. van Deemter, F. J. Zuiderweg, and A. Klinkenberg, "Longitudinal diffusion and resistance to mass transfer as causes of nonideality in chromatography," *Chem. Eng. Sci.*, vol. 5, no. 6, pp. 271–289, Sep. 1956.
[255] N. A. Katsanos, R. Thede, and F. Roubani-Kalantzopoulou, "Diffusion, adsorption and catalytic studies by gas chromatography," *J. Chromatogr. A*, vol. 795, no. 2, pp. 133–184, Feb. 1998.
[256] N. a. Katsanos, A. Lycourghiotis, and A. Tsiatsios, "Thermodynamics of adsorption based on gas–solid chromatography," *J. Chem. Soc. Faraday Trans. 1 Phys. Chem. Condens. Phases*, vol. 74, p. 575, 1978.
[257] J. H. DEBOER, "The Dynamical Character of Adsorption," *Soil Sci.*, vol. 76, no. 2, p. 166, Aug. 1953.
[258] A. S. Münch and F. O. R. L. Mertens, "The Lewis acidic and basic character of the internal HKUST-1 surface determined by inverse gas chromatography," *CrystEngComm*, vol. 17, no. 2, pp. 438–447, 2015.
[259] A. S. Münch and F. O. R. L. Mertens, "HKUST-1 as an open metal site gas chromatographic stationary phase—capillary preparation, separation of small hydrocarbons and electron donating compounds, determination of thermodynamic data," *J. Mater. Chem.*, vol. 22, no. 20, p. 10228, 2012.
[260] I. Gutiérrez *et al.*, "Hydrocarbons adsorption on metal trimesate MOFs: Inverse gas chromatography and immersion calorimetry studies," *Thermochim. Acta*, vol. 602, no. August, pp. 36–42, 2015.
[261] M. T. Luebbers, T. Wu, L. Shen, and R. I. Masel, "Trends in the Adsorption of Volatile Organic Compounds in a Large-Pore Metal–Organic Framework, IRMOF-1," *Langmuir*, vol. 26, no. 13, pp. 11319–11329, Jul. 2010.
[262] M. T. Luebbers, "Adsorption Behavior of Volatile Organic Compounds in Metal- Organic Frameworks," University of Illinois at Urbana-Champaign, 2010.
[263] R. Surana, L. Randall, A. Pyne, N. M. Vemuri, and R. Suryanarayanan, "Determination of Glass Transition Temperature and in Situ Study of the Plasticizing Effect of Water by Inverse Gas Chromatography," *Pharm. Res.*, vol. 20, no. 10, pp. 1647–1654, 2003.
[264] Y. Yampolskii and N. Belov, "Investigation of Polymers by Inverse Gas Chromatography," *Macromolecules*, vol. 48, no. 19, pp. 6751–6767, 2015.
[265] L. M. Blumberg, "Properties of James-Martin compressibility correction factor," *Chromatographia*, vol. 44, no. 5–6. pp. 326–329, 1997.
[266] J. Schultz, L. Lavielle, and C. Martin, "The Role of the Interface in Carbon Fibre-Epoxy Composites," *J. Adhes.*, vol. 23, no. February 2015, pp. 45–60, 1987.
[267] M. Pérez-Mendoza, M. C. Almazán-Almazán, L. Méndez-Liñán, M. Domingo-García, and F. J. López-Garzón, "Evaluation of the dispersive component of the surface energy of active carbons as determined by inverse gas chromatography at zero surface coverage," *J. Chromatogr. A*, vol. 1214, no. 1–2, pp. 121–127, Dec. 2008.
[268] A. Voelkel, B. Strzemiecka, K. Adamska, and K. Milczewska, "Inverse gas chromatography as a source of physiochemical data," *J. Chromatogr. A*, vol. 1216, no. 10, pp. 1551–1566, 2009.
[269] A. Voelkel, B. Strzemiecka, K. Milczewska, and Z. Okulus, "Inverse Gas Chromatographic Examination of Polymer Composites," *Open Chem.*, vol. 13, no. 1, pp. 893–900, 2015.
[270] T. Duerinck *et al.*, "Understanding Hydrocarbon Adsorption in the UiO-66 Metal–Organic Framework: Separation of (Un)saturated Linear, Branched, Cyclic Adsorbates, Including Stereoisomers," *J. Phys. Chem. C*, vol. 117, no. 24, pp. 12567–12578, Jun. 2013.
[271] G. M. Dorris and D. G. Gray, "Adsorption of n-alkanes at zero surface coverage on cellulose paper and wood fibers," *J. Colloid Interface Sci.*, vol. 77, no. 2, pp. 353–362, Oct. 1980.
[272] F. Tihminlioglu, R. K. Surana, R. P. Danner, and J. L. Duda, "Finite Concentration Inverse Gas Chromatography : Diffusion and Partition Measurements," *J. Polym. Sci. Part B Polym. Phys.*, vol. 35, no. 8, pp. 1279–1290, 1996.
[273] F. Thielmann and D. Pearse, "Determination of surface heterogeneity profiles on graphite by finite concentration inverse gas chromatography," *J. Chromatogr. A*, vol. 969, no. 1–2, pp. 323–327, 2002.
[274] H. Balard, a Saada, E. Papirer, and B. Siffert, "Energetic Surface Heterogeneity of Illites and Kaolinites," *Langmuir*, vol. 13, no. 5, pp. 1256–1259, 1997.
[275] H. Balard, "Estimation of the Surface Energetic Heterogeneity of a Solid by Inverse Gas Chromatography †," *Langmuir*, vol. 13, no. 3, pp. 1260–1269, 1997.
[276] Surface Measurement Systems, "Characterisation of Microporous Materials by Finite Concentration Inverse Gas Chromatography," pp. 1–7, 2001.
[277] F. Thielmann, "Introduction into the characterisation of porous materials by inverse gas chromatography," *J. Chromatogr. A*, vol. 1037, no. 1–2, pp. 115–123, 2004.
[278] K. Bielicka-Daszkiewicz and A. Voelkel, "Theoretical and experimental methods of determination of the breakthrough volume of SPE sorbents," *Talanta*, vol. 80, no. 2, pp. 614–621, 2009.
[279] P. P. Ylä-Mäihäniemi, J. Y. Y. Heng, F. Thielmann, and D. R. Williams, "Inverse gas chromatographic method for

measuring the dispersive surface energy distribution for particulates.," *Langmuir*, vol. 24, no. 17, pp. 9551–7, 2008.
[280] R. R. Smith, D. R. Williams, D. J. Burnett, and J. Y. Y. Heng, "A new method to determine dispersive surface energy site distributions by inverse gas chromatography.," *Langmuir*, vol. 30, no. 27, pp. 8029–35, 2014.
[281] A. Voelkel, *Physicochemical Measurements (Inverse Gas Chromatography)*. Elsevier, 2012.
[282] M. Herrmann *et al.*, "Characterization of Metal-Organic Frameworks Using X-ray Diffraction," *Chemie Ing. Tech.*, no. 7, pp. 1–5, 2016.
[283] R. M. Stephenson and S. Malanowski, *Handbook of the Thermodynamics of Organic Compounds*. Dordrecht: Springer Netherlands, 1987.
[284] D. R. Stull, "Vapor Pressure of Pure Substances. Organic and Inorganic Compounds," *Ind. Eng. Chem.*, vol. 39, no. 4, pp. 517–540, Apr. 1947.
[285] W. M. Jones and W. F. Giauque, "The Entropy of Nitromethane. Heat Capacity of Solid and Liquid. Vapor Pressure, Heats of Fusion and Vaporization," *J. Am. Chem. Soc.*, vol. 69, no. 5, pp. 983–987, May 1947.
[286] RAE Systems, *The PID Handbook - Theory and Applications of Direct-Reading Photoionization Detectors*, Third Edit. 2013.
[287] P. A. Smith, C. J. Lepage, K. L. Harrer, and P. J. Brochu, "Hand-Held Photoionization Instruments for Quantitative Detection of Sarin Vapor and for Rapid Qualitative Screening of Contaminated Objects," *J. Occup. Environ. Hyg.*, vol. 4, no. 10, pp. 729–738, Aug. 2007.
[288] P. L. Patterson, "Recent advantages in thermoionic detection for gas chromatography," *J. Chromatogr. Sci.*, vol. 24, 1986.
[289] T. Fujii and H. Arimoto, "Thermionic Ionization Detector with Lanthanum Hexaboride/Silicon Dioxide Thermionic Emitter Material for Gas Chromatography," *Anal. Chem.*, vol. 57, no. 2, pp. 490–493, Feb. 1985.
[290] S. Mohammadi-Jam and K. E. Waters, "Inverse gas chromatography applications: A review," *Adv. Colloid Interface Sci.*, vol. 212, pp. 21–44, 2014.
[291] F. Ragon *et al.*, "In situ energy-dispersive x-ray diffraction for the synthesis optimization and scale-up of the porous zirconium terephthalate UiO-66," *Inorg. Chem.*, vol. 53, no. 5, pp. 2491–2500, 2014.
[292] A. Polyzoidis, M. Schwarzer, S. Loebbecke, and C. G. Piscopo, "Continuous synthesis of UiO-66 in microreactor: Pursuing the optimum between intensified production and structural properties," *Mater. Lett.*, vol. 197, pp. 213–216, 2017.
[293] M. Rieger, M. Wittek, P. Scherer, S. Löbbecke, and K. Müller-Buschbaum, "Preconcentration of Nitroalkanes with Archetype Metal-Organic Frameworks (MOFs) as Concept for a Sensitive Sensing of Explosives in the Gas Phase," *Adv. Funct. Mater.*, vol. 28, no. 2, p. 1704250, 2018.
[294] F. D. Lahoz-Martín, A. Martín-Calvo, and S. Calero, "Selective separation of BTEX mixtures using metal-organic frameworks," *J. Phys. Chem. C*, vol. 118, no. 24, pp. 13126–13136, 2014.
[295] J. A. Greathouse, N. W. Ockwig, L. J. Criscenti, T. R. Guilinger, P. Pohl, and M. D. Allendorf, "Computational screening of metal-organic frameworks for large-molecule chemical sensing.," *Phys. Chem. Chem. Phys.*, vol. 12, no. 39, pp. 12621–9, Oct. 2010.
[296] R. A. Ocakoglu, J. F. M. Denayer, G. B. Marin, J. A. Martens, and G. V. Baron, "Tracer Chromatographic Study of Pore and Pore Mouth Adsorption of Linear and Monobranched Alkanes on ZSM-22 Zeolite," *J. Phys. Chem. B*, vol. 107, no. 1, pp. 398–406, Jan. 2003.
[297] H. E. Newell, G. Buckton, D. a. Butler, F. Thielmann, and D. R. Williams, "The use of inverse phase gas chromatography to measure the surface energy of crystalline, amorphous, and recently milled lactose," *Pharm. Res.*, vol. 18, no. 5, pp. 662–666, 2001.
[298] A. J. Vukov and D. G. Gray, "Adsorption of n -Alkanes on Carbon Fibers at Zero Surface Coverage," no. 7, 1988.
[299] A. Van Asten, N. Van Veenendaal, and S. Koster, "Surface characterization of industrial fibers with inverse gas chromatography," *J. Chromatogr. A*, vol. 888, no. 1–2, pp. 175–196, 2000.
[300] D. R. Williams, "Particle Engineering in Pharmaceutical Solids Processing : Surface Energy Considerations," *Curr. Pharm. Des.*, vol. 21, pp. 2677–2694, 2015.
[301] F. Thielmann and C. Levoguer, "iGC – A new instrumental technique for characterising the phyisco-chemical properties of pharmaceutical materials," 2001. .
[302] P. Scherrer, "Bestimmung der inneren Struktur und der Größe von Kolloidteilchen mittels Röntgenstrahlen," in *Kolloidchemie Ein Lehrbuch*, Berlin, Heidelberg: Springer Berlin Heidelberg, 1912, pp. 387–409.
[303] M. K. Bhunia, J. T. Hughes, J. C. Fettinger, and A. Navrotsky, "Thermochemistry of paddle wheel MOFs: Cu-HKUST-1 and Zn-HKUST-1.," *Langmuir*, vol. 29, no. 25, pp. 8140–5, Jun. 2013.
[304] A. Zukal, M. Opanasenko, M. Rubeš, P. Nachtigall, and J. Jagiello, "Adsorption of pentane isomers on metal-organic frameworks Cu-BTC and Fe-BTC," *Catal. Today*, vol. 243, no. C, pp. 69–75, Apr. 2015.
[305] Sigma Aldrich, "Tenax® Porous Polymer Adsorbent Datasheet." [Online]. Available: http://www.sigmaaldrich.com/catalog/product/supelco/11982. [Accessed: 11-Mar-2018].
[306] C. Volkringer, T. Loiseau, N. Guillou, G. Férey, E. Elkaïm, and A. Vimont, "XRD and IR structural investigations of a particular breathing effect in the MOF-type gallium terephthalate MIL-53(Ga).," *Dalt. Trans.*, vol. 53, no. 12, pp. 2241–2249, 2009.
[307] J. F. M. Denayer and G. V. Baron, "The Confinement Factor: A Thermodynamic Parameter to Characterize Microporous Adsorbents," *Adsorption*, vol. 11, no. S1, pp. 85–90, Jul. 2005.
[308] D. M. Ruthven and B. K. Kaul, "Compensation Theory of Adsorption: Correlation and Prediction of Henry Constants for Linear Paraffins on Zeolite Adsorbents," *Adsorption*, vol. 4, no. 3/4, pp. 269–273, 1998.
[309] G. Kortüm, W. Vogel, and K. Andrussow, "Disssociation constants of organic acids in aqueous solution," *Pure Appl. Chem.*, vol. 1, no. 2–3, Jan. 1960.

[310] M. T. Luebbers, T. Wu, L. Shen, and R. I. Masel, "Effects of molecular sieving and electrostatic enhancement in the adsorption of organic compounds on the zeolitic imidazolate framework ZIF-8.," *Langmuir*, vol. 26, no. 19, pp. 15625–33, Oct. 2010.
[311] M. Phukan, K. J. Borah, and R. Borah, "Henry reaction in environmentally benign methods using imidazole as catalyst," *Green Chem. Lett. Rev.*, vol. 2, no. 4, pp. 249–253, 2009.
[312] S. Couck, T. Rémy, G. V Baron, J. Gascon, F. Kapteijn, and J. F. M. Denayer, "A pulse chromatographic study of the adsorption properties of the amino-MIL-53 (Al) metal–organic framework," *Phys. Chem. Chem. Phys.*, vol. 12, no. 32, p. 9413, 2010.
[313] V. Finsy *et al.*, "Low-coverage adsorption properties of the metal-organic framework MIL-47 studied by pulse chromatography and Monte Carlo simulations.," *Phys. Chem. Chem. Phys.*, vol. 11, no. 18, pp. 3515–3521, 2009.
[314] M. Leidinger, M. Rieger, T. Sauerwald, C. Alépée, and A. Schütze, "Integrated pre-concentrator gas sensor microsystem for ppb level benzene detection," *Sensors Actuators B Chem.*, vol. 236, pp. 988–996, Nov. 2016.
[315] M. Leidinger *et al.*, "Trace gas VOC Detection Using Metal-organic Frameworks as Pre-concentrators and Semiconductor Gas Sensors," *Procedia Eng.*, vol. 120, pp. 1042–1045, 2015.
[316] Q. Wang *et al.*, "Metal-Organic Framework Templated Synthesis of Copper Azide as the Primary Explosive with Low Electrostatic Sensitivity and Excellent Initiation Ability," *Adv. Mater.*, May 2016.
[317] S. A. Sotnik, K. S. Gavrilenko, A. S. Lytvynenko, and S. V. Kolotilov, "Catalytic activity of copper(II) benzenetricarboxylate (HKUST-1) in reactions of aromatic aldehydes condensation with nitromethane: Kinetic and diffusion study," *Inorganica Chim. Acta*, vol. 426, pp. 119–125, Feb. 2015.
[318] S. a Sotnik, I. L. Eremenko, V. V Pavlishchuk, and K. S. Gavrilenko, "trans-Stereoselective Catalysis of the Henry Reaction by a New Metal–Organic Framework of Iron(III) with 1,3,5-Benzenetricarboxylic Acid," *Theor. Exp. Chem.*, vol. 49, no. 2, pp. 103–108, May 2013.
[319] S. Patai, Ed., *Amino, Nitrosco and Nitro Compounds and Their Derivatives: Vol. 2 (1982)*. Chichester, UK: John Wiley & Sons, Ltd., 1982.
[320] C. Montoro *et al.*, "Capture of nerve agents and mustard gas analogues by hydrophobic robust MOF-5 type metal-organic frameworks.," *J. Am. Chem. Soc.*, vol. 133, no. 31, pp. 11888–91, Aug. 2011.
[321] V. Finsy *et al.*, "Pore-Filling-Dependent Selectivity Effects in the Vapor-Phase Separation of Xylene Isomers on the Metal–Organic Framework MIL-47," *J. Am. Chem. Soc.*, vol. 130, no. 22, pp. 7110–7118, Jun. 2008.
[322] M. Leidinger, T. Sauerwald, M. Rieger, C. Alépée, and A. Schütze, "Integrated pre-concentrator gas sensor micro system for trace gas detection," in *12. Dresdner Sensor-Symposium*, 2015, pp. 72–77.
[323] P. Krokidas *et al.*, "ZIF-67 Framework: A Promising New Candidate for Propylene/Propane Separation. Experimental Data and Molecular Simulations," *J. Phys. Chem. C*, vol. 120, no. 15, pp. 8116–8124, Apr. 2016.
[324] Q. Yang, A. D. Wiersum, P. L. Llewellyn, V. Guillerm, C. Serre, and G. Maurin, "Functionalizing porous zirconium terephthalate UiO-66(Zr) for natural gas upgrading: a computational exploration," *Chem. Commun.*, vol. 47, no. 34, p. 9603, 2011.
[325] Y. Huang, W. Qin, Z. Li, and Y. Li, "Enhanced stability and CO2 affinity of a UiO-66 type metal–organic framework decorated with dimethyl groups," *Dalt. Trans.*, vol. 41, no. 31, p. 9283, 2012.
[326] G. W. Peterson, J. J. Mahle, J. B. DeCoste, W. O. Gordon, and J. A. Rossin, "Extraordinary NO2 Removal by the Metal-Organic Framework UiO-66-NH2," *Angew. Chemie Int. Ed.*, pp. 1–5, Apr. 2016.
[327] M. A. Browe, A. Napolitano, J. B. DeCoste, and G. W. Peterson, "Filtration of Chlorine and Hydrogen Chloride Gas by Engineered UiO-66-NH2 Metal-Organic Framework," *J. Hazard. Mater.*, Feb. 2017.
[328] J. B. DeCoste, T. J. Demasky, M. J. Katz, O. K. Farha, and J. T. Hupp, "A UiO-66 analogue with uncoordinated carboxylic acids for the broad-spectrum removal of toxic chemicals," *New J. Chem.*, vol. 39, no. 4, pp. 2396–2399, 2015.
[329] D. Saha and S. Deng, "Structural stability of metal organic framework MOF-177," *J. Phys. Chem. Lett.*, vol. 1, no. 1, pp. 73–78, 2010.
[330] A. Voelke, E. Andrzejewska, R. Maga, and M. Andrzejewski, "Examination of surfaces of solid polymers by inverse gas chromatography: 1. Dispersive properties," *Polymer (Guildf).*, vol. 37, no. 3, pp. 455–462, 1996.
[331] K. Yusuf, A. Y. Badjah-Hadj-Ahmed, A. Aqel, T. Aouak, and Z. A. ALOthman, "Zeolitic imidazolate framework-methacrylate composite monolith characterization by inverse gas chromatography," *J. Chromatogr. A*, vol. 1443, pp. 233–240, Apr. 2016.
[332] Q. Yang *et al.*, "Understanding the Thermodynamic and Kinetic Behavior of the CO 2 /CH 4 Gas Mixture within the Porous Zirconium Terephthalate UiO-66(Zr): A Joint Experimental and Modeling Approach," *J. Phys. Chem. C*, vol. 115, no. 28, pp. 13768–13774, Jul. 2011.
[333] N. A. Ramsahye *et al.*, "Adsorption and Diffusion of Light Hydrocarbons in UiO-66(Zr): A Combination of Experimental and Modeling Tools," *J. Phys. Chem. C*, vol. 118, no. 47, pp. 27470–27482, Nov. 2014.
[334] P. S. Bárcia *et al.*, "Reverse shape selectivity in the adsorption of hexane and xylene isomers in MOF UiO-66," *Microporous Mesoporous Mater.*, vol. 139, no. 1–3, pp. 67–73, 2011.
[335] D. I. Kolokolov, A. G. Stepanov, V. Guillerm, C. Serre, B. Frick, and H. Jobic, "Probing the dynamics of the porous Zr terephthalate UiO-66 framework using 2H NMR and neutron scattering," *J. Phys. Chem. C*, vol. 116, no. 22, pp. 12131–12136, 2012.
[336] N. A. Ramsahye *et al.*, "The effect of pore shape on hydrocarbon selectivity on UiO-66(Zr), HKUST-1 and MIL-125(Ti) metal organic frameworks: Insights from molecular simulations and chromatography," *Microporous Mesoporous Mater.*, vol. 189, pp. 222–231, May 2014.
[337] S. Van der Perre, B. Bozbiyik, J. Lannoeye, D. E. De Vos, G. V. Baron, and J. F. M. Denayer, "Experimental Study of Adsorptive Interactions of Polar and Nonpolar Adsorbates in the Zeolitic Imidazolate Framework ZIF-68 via Pulse Gas Chromatography," *J. Phys. Chem. C*, vol. 119, no. 4, pp. 1832–1839, Jan. 2015.

[338] B. Bozbiyik, T. Duerinck, J. Lannoeye, D. E. De Vos, G. V. Baron, and J. F. M. Denayer, "Adsorption and separation of n-hexane and cyclohexane on the UiO-66 metal–organic framework," *Microporous Mesoporous Mater.*, vol. 183, pp. 143–149, Jan. 2014.
[339] M. Leidinger, J. Huotari, T. Sauerwald, J. Lappalainen, and A. Schütze, "Selective detection of naphthalene with nanostructured WO3 gas sensors prepared by pulsed laser deposition," *J. Sensors Sens. Syst.*, vol. 5, no. 1, pp. 147–156, 2016.
[340] M. Leidinger, T. Baur, T. Sauerwald, W. Reimringer, L. Spinelle, and A. Schütze, "Highly sensitive benzene detection with MOS gas sensors."
[341] Y. Wu *et al.*, "Negative Thermal Expansion in the Metal-Organic Framework Material Cu3(1,3,5-benzenetricarboxylate)2," *Angew. Chemie*, vol. 120, no. 46, pp. 9061–9064, Nov. 2008.
[342] S. S. Han and W. A. Goddard, "Metal–Organic Frameworks Provide Large Negative Thermal Expansion Behavior," *J. Phys. Chem. C*, vol. 111, no. 42, pp. 15185–15191, Oct. 2007.
[343] I. Stassen *et al.*, "Electrochemical Film Deposition of the Zirconium Metal–Organic Framework UiO-66 and Application in a Miniaturized Sorbent Trap," *Chem. Mater.*, vol. 27, no. 5, pp. 1801–1807, Mar. 2015.
[344] N. Stock, S. Biswas, and M. O. F. Topologies, "Synthesis of Metal-Organic Frameworks (MOFs): Routes to Various MOF Topologies, Morphologies, and Composites," *Synthesis (Stuttg).*, vol. 112, no. 2, pp. 933–969, Feb. 2012.
[345] P. A. Julien, C. Mottillo, and T. Friščić, "Metal-organic frameworks meet scalable and sustainable synthesis," *Green Chem.*, vol. 19, no. 12, pp. 2729–2747, 2017.
[346] W. Morris *et al.*, "Role of Modulators in Controlling the Colloidal Stability and Polydispersity of the UiO-66 Metal–Organic Framework," *ACS Appl. Mater. Interfaces*, p. acsami.7b01040, 2017.
[347] P. M. Forster, N. Stock, and A. K. Cheetham, "A High-Throughput Investigation of the Role of pH, Temperature, Concentration, and Time on the Synthesis of Hybrid Inorganic-Organic Materials," *Angew. Chemie Int. Ed.*, vol. 44, no. 46, pp. 7608–7611, Nov. 2005.
[348] A. Polyzoidis, M. Etter, M. Herrmann, S. Loebbecke, and R. E. Dinnebier, "Revealing the Initial Reaction Behavior in the Continuous Synthesis of Metal–Organic Frameworks Using Real-Time Synchrotron X-ray Analysis," *Inorg. Chem.*, vol. 56, no. 10, pp. 5489–5492, May 2017.
[349] C. J. Höller and K. Müller-Buschbaum, "The First Dinitrile Frameworks of the Rare Earth Elements: ∞3[LnCl3(1,4-Ph(CN)2)] and ∞3[Ln2Cl6(1,4-Ph(CN)2)], Ln = Sm, Gd, Tb, Y; Access to Novel Metal-Organic Frameworks by Solvent Free Synthesis in Molten 1,4-Benzodinitrile," *Inorg. Chem.*, vol. 47, no. 21, pp. 10141–10149, Nov. 2008.
[350] K. Müller-Buschbaum and Y. Mokaddem, "MOFs by solvent free high temperature synthesis exemplified by ∞3[Eu3(Tz∗)6(Tz∗H)2]," *Solid State Sci.*, vol. 10, no. 4, pp. 416–420, Apr. 2008.
[351] A. Zurawski *et al.*, "Alkaline earth imidazolate coordination polymers by solvent free melt synthesis as potential host lattices for rare earth photoluminescence: x∞[AE(Im)2(ImH)2–3], Mg, Ca, Sr, Ba, x = 1–2," *Dalt. Trans.*, vol. 41, no. 14, p. 4067, 2012.
[352] K. Müller-Buschbaum and F. Schönfeld, "The Utilisation of Solvent-Free Synthesis for the Reaction of Cobalt with Imidazole: MOF Conversion from [Co3(Im)6(ImH)2] via [Co4(Im)8(ImH)] to [Co(Im)2]," *Zeitschrift für Anorg. und Allg. Chemie*, vol. 637, no. 7–8, pp. 955–960, Jun. 2011.
[353] A. Zurawski *et al.*, "Alkaline earth imidazolate coordination polymers by solvent free melt synthesis as potential host lattices for rare earth photoluminescence: (x)(∞)[AE(Im)2(ImH)(2-3)], Mg, Ca, Sr, Ba, x = 1-2.," *Dalton Trans.*, vol. 41, no. 14, pp. 4067–78, Apr. 2012.
[354] J. Kim, S.-T. Yang, S. B. Choi, J. Sim, J. Kim, and W.-S. Ahn, "Control of catenation in CuTATB-n metal-organic frameworks by sonochemical synthesis and its effect on CO2 adsorption," *J. Mater. Chem.*, vol. 21, no. 9, p. 3070, 2011.
[355] A. Pichon, A. Lazuen-Garay, and S. L. James, "Solvent-free synthesis of a microporous metal-organic framework," *CrystEngComm*, vol. 8, no. 3, p. 211, 2006.
[356] T. Wehner, K. Mandel, M. Schneider, G. Sextl, and K. Müller-Buschbaum, "Superparamagnetic Luminescent MOF@Fe3O4 /SiO2 Composite Particles for Signal Augmentation by Magnetic Harvesting as Potential Water Detectors," *ACS Appl. Mater. Interfaces*, vol. 8, no. 8, pp. 5445–5452, Mar. 2016.
[357] M. Schlesinger, S. Schulze, M. Hietschold, and M. Mehring, "Evaluation of synthetic methods for microporous metal–organic frameworks exemplified by the competitive formation of [Cu2(btc)3(H2O)3] and [Cu2(btc)(OH)(H2O)]," *Microporous Mesoporous Mater.*, vol. 132, no. 1–2, pp. 121–127, Jul. 2010.
[358] R. Ameloot, L. Stappers, J. Fransaer, L. Alaerts, B. F. Sels, and D. E. De Vos, "Patterned Growth of Metal-Organic Framework Coatings by Electrochemical Synthesis," *Chem. Mater.*, vol. 21, no. 13, pp. 2580–2582, Jul. 2009.
[359] D. Zacher, O. Shekhah, C. Wöll, and R. a Fischer, "Thin films of metal-organic frameworks.," *Chem. Soc. Rev.*, vol. 38, no. 5, pp. 1418–29, May 2009.
[360] B. Liu *et al.*, "Chemistry of SURMOFs: Layer-Selective Installation of Functional Groups and Post-synthetic Covalent Modification Probed by Fluorescence Microscopy.," *J. Am. Chem. Soc.*, pp. 1734–1737, Jan. 2011.
[361] O. Shekhah, "Layer-by-Layer Method for the Synthesis and Growth of Surface Mounted Metal-Organic Frameworks (SURMOFs)," *Materials (Basel).*, vol. 3, no. 2, pp. 1302–1315, Feb. 2010.
[362] M. Kind and C. Wöll, "Maßgeschneiderte Organische Oberflächen. Dünnstschichten," *Chemie unserer Zeit*, vol. 42, no. 2, pp. 128–141, Apr. 2008.
[363] A. S. Münch *et al.*, "Room temperature preparation method for thin MOF-5 films on metal and fused silica surfaces using the controlled SBU approach," *Microporous Mesoporous Mater.*, vol. 159, pp. 132–138, Sep. 2012.
[364] P. Matthes, F. Schönfeld, S. Zottnick, and K. Müller-Buschbaum, "Post-Synthetic Shaping of Porosity and

Crystal Structure of Ln-Bipy-MOFs by Thermal Treatment," *Molecules*, vol. 20, no. 7, pp. 12125–12153, Jul. 2015.
[365] A. P. Nelson, O. K. Farha, K. L. Mulfort, and J. T. Hupp, "Supercritical Processing as a Route to High Internal Surface Areas and Permanent Microporosity in Metal-Organic Framework Materials," *J. Am. Chem. Soc.*, vol. 131, no. 2, pp. 458–460, Jan. 2009.
[366] M. R. Lohe, M. Rose, and S. Kaskel, "Metal-organic framework (MOF) aerogels with high micro- and macroporosity," *Chem. Commun.*, no. 40, p. 6056, 2009.
[367] S. M. Cohen, "Postsynthetic methods for the functionalization of metal-organic frameworks.," *Chem. Rev.*, vol. 112, no. 2, pp. 970–1000, Feb. 2012.
[368] S. J. Garibay, Z. Wang, K. K. Tanabe, and S. M. Cohen, "Postsynthetic Modification: A Versatile Approach Toward Multifunctional Metal-Organic Frameworks," *Inorg. Chem.*, vol. 48, no. 15, pp. 7341–7349, Aug. 2009.
[369] S. Bernt, V. Guillerm, C. Serre, and N. Stock, "Direct covalent post-synthetic chemical modification of Cr-MIL-101 using nitrating acid," *Chem. Commun.*, vol. 47, no. 10, p. 2838, 2011.
[370] Y. Dai, J. R. Johnson, O. Karvan, D. S. Sholl, and W. J. Koros, "Ultem®/ZIF-8 mixed matrix hollow fiber membranes for CO2/N2 separations," *J. Memb. Sci.*, vol. 401–402, pp. 76–82, May 2012.
[371] S. Basu, A. Cano-Odena, and I. F. J. Vankelecom, "Asymmetric Matrimid®/[Cu3(BTC)2] mixed-matrix membranes for gas separations," *J. Memb. Sci.*, vol. 362, no. 1–2, pp. 478–487, Oct. 2010.
[372] H. B. Tanh Jeazet, C. Staudt, and C. Janiak, "Metal–organic frameworks in mixed-matrix membranes for gas separation," *Dalt. Trans.*, vol. 41, no. 46, 2012.
[373] X.-F. Chen *et al.*, "Metal-organic framework MIL-53(Al) as a solid-phase microextraction adsorbent for the determination of 16 polycyclic aromatic hydrocarbons in water samples by gas chromatography-tandem mass spectrometry.," *Analyst*, vol. 137, no. 22, pp. 5411–9, Nov. 2012.
[374] S. Zhang, Z. Du, and G. Li, "Metal-organic framework-199/graphite oxide hybrid composites coated solid-phase microextraction fibers coupled with gas chromatography for determination of organochlorine pesticides from complicated samples.," *Talanta*, vol. 115, pp. 32–9, Oct. 2013.
[375] G. W. Peterson, G. Wagner, and C. J. Karwacki, "Evaluation of MOF-74, MOF-177, and ZIF-8 for the Removal of Toxic Industrial Chemicals.," no. November, 2008.
[376] N. S. Bobbitt *et al.*, "Metal–organic frameworks for the removal of toxic industrial chemicals and chemical warfare agents," *Chem. Soc. Rev.*, 2017.
[377] J. Zhao *et al.*, "Highly Adsorptive, MOF-Functionalized Nonwoven Fiber Mats for Hazardous Gas Capture Enabled by Atomic Layer Deposition," *Adv. Mater. Interfaces*, vol. 1, no. 4, p. n/a-n/a, Jul. 2014.
[378] T. Bandosz and C. Petit, "Nanocomposite materials comprising metal-organic-framework units and methods of using same," *US Pat. 8,633,331*, vol. 2, no. 12, 2014.
[379] R. Dinnebier, "93 years after Debye and Scherrer: powder diffraction in the 21st century," *Acta Crystallogr. Sect. A Found. Crystallogr.*, vol. 65, no. a1, pp. s6–s6, 2009.
[380] B. J. Sikora, C. E. Wilmer, M. L. Greenfield, and R. Q. Snurr, "Thermodynamic analysis of Xe/Kr selectivity in over 137 000 hypothetical metal–organic frameworks," *Chem. Sci.*, vol. 3, no. 7, p. 2217, 2012.
[381] R. B. Getman, Y.-S. Bae, C. E. Wilmer, and R. Q. Snurr, "Review and analysis of molecular simulations of methane, hydrogen, and acetylene storage in metal-organic frameworks.," *Chem. Rev.*, vol. 112, no. 2, pp. 703–23, Feb. 2012.
[382] K. Tan *et al.*, "Trapping gases in metal-organic frameworks with a selective surface molecular barrier layer," *Nat. Commun.*, vol. 7, p. 13871, 2016.
[383] H. Jasuja, G. W. Peterson, J. B. Decoste, M. a. Browe, and K. S. Walton, "Evaluation of MOFs for air purification and air quality control applications: Ammonia removal from air," *Chem. Eng. Sci.*, vol. 124, pp. 118–124, Aug. 2014.
[384] N. L. Rosi, "Hydrogen Storage in Microporous Metal-Organic Frameworks," *Science (80-.).*, vol. 300, no. 5622, pp. 1127–1129, May 2003.
[385] H. Frost, T. Düren, and R. Q. Snurr, "Effects of surface area, free volume, and heat of adsorption on hydrogen uptake in metal-organic frameworks.," *J. Phys. Chem. B*, vol. 110, pp. 9565–9570, 2006.
[386] Y. Li and R. T. Yang, "Significantly Enhanced Hydrogen Storage in Metal–Organic Frameworks via Spillover," *J. Am. Chem. Soc.*, vol. 128, no. 3, pp. 726–727, Jan. 2006.
[387] C. Prestipino *et al.*, "Local Structure of Framework Cu(II) in HKUST-1 Metallorganic Framework: Spectroscopic Characterization upon Activation and Interaction with Adsorbates," *Chem. Mater.*, vol. 18, no. 5, pp. 1337–1346, Mar. 2006.
[388] B. Li, H.-M. Wen, W. Zhou, and B. Chen, "Porous Metal – Organic Frameworks for Gas Storage and Separation: What, How, and Why?," *J. Phys. Chem. C*, vol. 5, p. 3468–3479, 2014.
[389] D. M. D'Alessandro, B. Smit, and J. R. Long, "Carbon Dioxide Capture: Prospects for New Materials," *Angew. Chemie Int. Ed.*, vol. 49, no. 35, pp. 6058–6082, Aug. 2010.
[390] A. R. Millward and O. M. Yaghi, "Metal-organic frameworks with exceptionally high capacity for storage of carbon dioxide at room temperature.," *J. Am. Chem. Soc.*, vol. 127, no. 51, pp. 17998–9, Dec. 2005.
[391] K. S. Walton *et al.*, "Understanding inflections and steps in carbon dioxide adsorption isotherms in metal-organic frameworks.," *J. Am. Chem. Soc.*, vol. 130, no. 2, pp. 406–7, Jan. 2008.
[392] C. Hon Lau, R. Babarao, and M. R. Hill, "A route to drastic increase of CO2 uptake in Zr metal organic framework UiO-66," *Chem. Commun.*, vol. 49, no. 35, p. 3634, 2013.
[393] Q. Yang *et al.*, "CH4 storage and CO2 capture in highly porous zirconium oxide based metal–organic frameworks," *Chem. Commun.*, vol. 48, no. 79, p. 9831, 2012.
[394] L. Hertäg *et al.*, "Diffusion of CH4 and H2 in ZIF-8," *J. Memb. Sci.*, vol. 377, no. 1–2, pp. 36–41, Jul. 2011.

[395] S. R. Venna and M. a Carreon, “Highly permeable zeolite imidazolate framework-8 membranes for CO2/CH4 separation.,” *J. Am. Chem. Soc.*, vol. 132, no. 1, pp. 76–8, Jan. 2010.
[396] T. Chokbunpiam, S. Fritzsche, C. Chmelik, J. Caro, W. Janke, and S. Hannongbua, “Gate Opening, Diffusion, and Adsorption of CO2 and N2 Mixtures in ZIF-8,” *J. Phys. Chem. C*, p. acs.jpcc.6b05506, 2016.
[397] D. N. Dybtsev, H. Chun, S. H. Yoon, D. Kim, and K. Kim, “Microporous Manganese Formate: A Simple Metal–Organic Porous Material with High Framework Stability and Highly Selective Gas Sorption Properties,” *J. Am. Chem. Soc.*, vol. 126, no. 1, pp. 32–33, Jan. 2004.
[398] D. Peralta, G. Chaplais, A. Simon-Masseron, K. Barthelet, and G. D. Pirngruber, “Synthesis and adsorption properties of ZIF-76 isomorphs,” *Microporous Mesoporous Mater.*, vol. 153, pp. 1–7, May 2012.
[399] A. F. P. Ferreira, M. C. Mittelmeijer-Hazeleger, M. A. Granato, V. F. D. Martins, A. E. Rodrigues, and G. Rothenberg, “Sieving di-branched from mono-branched and linear alkanes using ZIF-8: experimental proof and theoretical explanation.,” *Phys. Chem. Chem. Phys.*, vol. 15, no. 22, pp. 8795–804, 2013.
[400] K. Vellingiri, P. Kumar, and K.-H. Kim, “Coordination polymers: Challenges and future scenarios for capture and degradation of volatile organic compounds,” *Nano Res.*, pp. 1–28, Sep. 2016.
[401] S. Hasegawa *et al.*, “Three-Dimensional Porous Coordination Polymer Functionalized with Amide Groups Based on Tridentate Ligand: Selective Sorption and Catalysis,” *J. Am. Chem. Soc.*, vol. 129, no. 9, pp. 2607–2614, Mar. 2007.
[402] L. Pan, B. Parker, X. Huang, D. H. Olson, Lee, and J. Li, “Zn(tbip) (H2tbip=5-tert-Butyl Isophthalic Acid): A Highly Stable Guest-Free Microporous Metal Organic Framework with Unique Gas Separation Capability,” *J. Am. Chem. Soc.*, vol. 128, no. 13, pp. 4180–4181, Apr. 2006.
[403] L. Alaerts *et al.*, “Selective adsorption and separation of xylene isomers and ethylbenzene with the microporous vanadium(IV) terephthalate MIL-47,” *Angew. Chemie - Int. Ed.*, vol. 46, no. 23, pp. 4293–4297, 2007.
[404] Y. Yu, Y. Ren, W. Shen, H. Deng, and Z. Gao, “Applications of metal-organic frameworks as stationary phases in chromatography,” *TrAC Trends Anal. Chem.*, vol. 50, no. 0, pp. 33–41, 2013.
[405] B. Chen *et al.*, “A Microporous Metal–Organic Framework for Gas-Chromatographic Separation of Alkanes,” *Angew. Chemie*, vol. 118, no. 9, pp. 1418–1421, Feb. 2006.
[406] N. Chang, C. Yang, and X. Yan, “Applications of Metal-Organic Frameworks to Analytical Chemistry,” 2014.
[407] I. Gutiérrez, E. Díaz, A. Vega, and S. Ordóñez, “Consequences of cavity size and chemical environment on the adsorption properties of isoreticular metal-organic frameworks: An inverse gas chromatography study,” *J. Chromatogr. A*, vol. 1274, no. August, pp. 173–180, 2013.
[408] S. D. Harvey, A. D. Eckberg, and P. K. Thallapally, “Evaluation of copper-1,3,5-benzenetricarboxylate metal-organic framework (Cu-MOF) as a selective sorbent for Lewis-base analytes,” *J. Sep. Sci.*, vol. 34, no. 18, pp. 2418–2426, Sep. 2011.
[409] Z.-Y. Gu and X.-P. Yan, “Metal-organic framework MIL-101 for high-resolution gas-chromatographic separation of xylene isomers and ethylbenzene.,” *Angew. Chem. Int. Ed. Engl.*, vol. 49, no. 8, pp. 1477–80, Feb. 2010.
[410] N. Chang and X.-P. Yan, “Exploring reverse shape selectivity and molecular sieving effect of metal-organic framework UIO-66 coated capillary column for gas chromatographic separation.,” *J. Chromatogr. A*, vol. 1257, pp. 116–24, Sep. 2012.
[411] K. Yusuf, A. Aqel, and Z. ALOthman, “Metal-organic frameworks in chromatography,” *J. Chromatogr. A*, vol. 1348, pp. 1–16, 2014.
[412] J. G. Nikelly, “Preparation of porous layer open tubular columns by the dynamic method,” *Anal. Chem.*, vol. 44, no. 3, pp. 623–625, Mar. 1972.
[413] J.-L. Zhuang, A. Terfort, and C. Wöll, “Formation of oriented and patterned films of metal–organic frameworks by liquid phase epitaxy: A review,” *Coord. Chem. Rev.*, vol. 307, pp. 391–424, 2015.
[414] A. S. Münch, J. Seidel, A. Obst, E. Weber, and F. O. R. L. Mertens, “High-separation performance of chromatographic capillaries coated with MOF-5 by the controlled SBU approach.,” *Chemistry*, vol. 17, no. 39, pp. 10958–64, Sep. 2011.
[415] C.-X. Yang, Y.-J. Chen, H.-F. Wang, and X.-P. Yan, “High-Performance Separation of Fullerenes on Metal-Organic Framework MIL-101(Cr),” *Chem. - A Eur. J.*, vol. 17, no. 42, pp. 11734–11737, Oct. 2011.
[416] W. De Malsche *et al.*, “Unusual pressure-temperature dependency in the capillary liquid chromatographic separation of C8 alkylaromatics on the MIL-53(Al) metal–organic framework,” *Microporous Mesoporous Mater.*, vol. 162, pp. 1–5, Nov. 2012.
[417] J. DeCoste and G. Peterson, “Metal–Organic Frameworks for Air Purification of Toxic Chemicals,” *Chem. Rev.*, 2014.
[418] D. Britt, D. Tranchemontagne, and O. M. Yaghi, “Metal-organic frameworks with high capacity and selectivity for harmful gases,” *Proc. Natl. Acad. Sci.*, vol. 105, no. 33, pp. 11623–11627, Aug. 2008.
[419] T. Grant Glover, G. W. Peterson, B. J. Schindler, D. Britt, and O. Yaghi, “MOF-74 building unit has a direct impact on toxic gas adsorption,” *Chem. Eng. Sci.*, vol. 66, no. 2, pp. 163–170, Jan. 2011.
[420] E. D. Bloch *et al.*, “Reversible CO Binding Enables Tunable CO/H 2 and CO/N 2 Separations in Metal–Organic Frameworks with Exposed Divalent Metal Cations,” *J. Am. Chem. Soc.*, vol. 136, no. 30, pp. 10752–10761, Jul. 2014.
[421] K. Lee, J. D. Howe, L. C. Lin, B. Smit, and J. B. Neaton, “Small-molecule adsorption in open-site metal-organic frameworks: A systematic density functional theory study for rational design,” *Chem. Mater.*, vol. 27, no. 3, pp. 668–678, 2015.
[422] K. Tan *et al.*, “Water Reaction Mechanism in Metal Organic Frameworks with Coordinatively Unsaturated

Metal Ions: MOF-74," *Chem. Mater.*, vol. 26, no. 23, pp. 6886–6895, Dec. 2014.
[423] S. Zuluaga *et al.*, "Understanding and controlling water stability of MOF-74," *J. Mater. Chem. A*, vol. 4, no. 14, pp. 5176–5183, 2016.
[424] A. M. Ebrahim, B. Levasseur, and T. J. Bandosz, "Interactions of NO2 with Zr-Based MOF: Effects of the Size of Organic Linkers on NO2 Adsorption at Ambient Conditions," *Langmuir*, vol. 29, no. 1, pp. 168–174, Jan. 2013.
[425] S.-Y. Moon *et al.*, "Detoxification of Chemical Warfare Agents Using a Zr6 -Based Metal-Organic Framework/Polymer Mixture," *Chem. - A Eur. J.*, pp. 1–6, 2016.
[426] R. Gil *et al.*, "Chemical Warfare Agents Detoxification Properties of Zirconium Metal-Organic Frameworks by Synergistic Incorporation of Nucleophilic and Basic Sites Chemical Warfare Agents Detoxification Properties of Zirconium Metal-Organic Frameworks by Synergistic Inc," 2017.
[427] J. Zhao *et al.*, "Ultra-Fast Degradation of Chemical Warfare Agents Using MOF-Nanofiber Kebabs," *Angew. Chemie*, pp. 1–6, 2016.
[428] J. E. Mondloch *et al.*, "Destruction of chemical warfare agents using metal–organic frameworks," *Nat. Mater.*, no. March, pp. 1–5, 2015.
[429] Y. Chen *et al.*, "Roll-to-Roll Production of Metal-Organic Framework Coatings for Particulate Matter Removal," *Adv. Mater.*, p. 1606221, Jan. 2017.
[430] Y. Zhang, S. Yuan, X. Feng, H. Li, J. Zhou, and B. Wang, "Preparation of Nanofibrous Metal–Organic Framework Filters for Efficient Air Pollution Control," *J. Am. Chem. Soc.*, vol. 138, no. 18, pp. 5785–5788, May 2016.
[431] V. Stavila, a a Talin, and M. D. Allendorf, "MOF-based electronic and opto-electronic devices.," *Chem. Soc. Rev.*, pp. 5994–6010, May 2014.
[432] H.-L. Jiang, F.-Y. Yi, D. Chen, M.-K. Wu, and L. Han, "Metal-organic frameworks based chemical sensors," *Chempluschem*, pp. 1–11, Apr. 2016.
[433] L. E. Kreno, K. Leong, O. K. Farha, M. Allendorf, R. P. Van Duyne, and J. T. Hupp, "Metal-organic framework materials as chemical sensors.," *Chem. Rev.*, vol. 112, no. 2, pp. 1105–25, Feb. 2012.
[434] M. Campbell and M. Dincă, "Metal–Organic Frameworks as Active Materials in Electronic Sensor Devices," *Sensors*, vol. 17, no. 5, p. 1108, 2017.
[435] E.-X. Chen, H. Yang, and J. Zhang, "Zeolitic Imidazolate Framework as Formaldehyde Gas Sensor," *Inorg. Chem.*, vol. 53, no. 11, pp. 5411–5413, Jun. 2014.
[436] M. G. Campbell, D. Sheberla, S. F. Liu, T. M. Swager, and M. Dincă, "Cu 3 (hexaiminotriphenylene) 2 : An Electrically Conductive 2D Metal-Organic Framework for Chemiresistive Sensing," *Angew. Chemie*, vol. 127, no. 14, pp. 4423–4426, Mar. 2015.
[437] M. G. Campbell, S. F. Liu, T. M. Swager, and M. Dincă, "Chemiresistive Sensor Arrays from Conductive 2D Metal–Organic Frameworks," *J. Am. Chem. Soc.*, vol. 137, no. 43, pp. 13780–13783, Nov. 2015.
[438] P. Davydovskaya, A. Ranft, B. V Lotsch, and R. Pohle, "Analyte detection with Cu-BTC Metal-Organic Framework thin films by means of mass sensitive and work function based readout.," *Anal. Chem.*, Jun. 2014.
[439] P. Davydovskaya, R. Pohle, A. Tawil, and M. Fleischer, "Metal-Organic-Frameworks as an aldehyde sensing layer in work-function based gas sensing devices," in *IMCS 2012 – The 14th International Meeting on Chemical Sensors*, 2012, pp. 323–326.
[440] V. Pentyala, P. Davydovskaya, R. Pohle, G. Urban, and O. Yurchenko, "Mg-MOF74 and Co-MOF74 as Sensing Layers for CO2 Detection," *Procedia Eng.*, vol. 87, pp. 1071–1074, 2014.
[441] A. Larki, M. R. Nasrabadi, and N. Pourreza, "Sensitive Colorimetric Detection of Explosive 2,6-Bis(picrylamino)pyridine after Preconcentration by Dispersive Liquid-Liquid Microextraction," *Propellants, Explos. Pyrotech.*, vol. 41, no. 1, pp. 166–171, Feb. 2016.
[442] E. Article *et al.*, "Solid state organic amine detection in a photochromic porous metal organic framework," *Chem. Sci.*, vol. 6, pp. 1420–1425, 2015.
[443] W. P. Lustig, S. Mukherjee, N. D. Rudd, A. V. Desai, J. Li, and S. K. Ghosh, "Metal–organic frameworks: functional luminescent and photonic materials for sensing applications," *Chem. Soc. Rev.*, 2017.
[444] B. Gole, A. K. Bar, and P. S. Mukherjee, "Modification of Extended Open Frameworks with Fluorescent Tags for Sensing Explosives: Competition between Size Selectivity and Electron Deficiency," *Chem. - A Eur. J.*, p. n/a-n/a, Jan. 2014.
[445] Z. C. Hu *et al.*, "Selective, Sensitive and Reversible Detection of Vapor-Phase RDX and Other High Explosives via 2D Mapping: A New Strategy for MOF Based Sensors," *Cryst. Growth Des*, vol. 13, pp. 4204–4207, 2013.
[446] A. Lan *et al.*, "A luminescent microporous metal-organic framework for the fast and reversible detection of high explosives.," *Angew. Chem. Int. Ed. Engl.*, vol. 48, no. 13, pp. 2334–8, Jan. 2009.
[447] S. W. Thomas, J. P. Amara, R. E. Bjork, and T. M. Swager, "Amplifying fluorescent polymer sensors for the explosives taggant 2,3-dimethyl-2,3-dinitrobutane (DMNB).," *Chem. Commun. (Camb).*, no. 36, pp. 4572–4, Sep. 2005.
[448] S. W. Thomas, G. D. Joly, and T. M. Swager, "Chemical sensors based on amplifying fluorescent conjugated polymers.," *Chem. Rev.*, vol. 107, no. 4, pp. 1339–86, Apr. 2007.
[449] M. D. Allendorf, C. a Bauer, R. K. Bhakta, and R. J. T. Houk, "Luminescent metal-organic frameworks.," *Chem. Soc. Rev.*, vol. 38, no. 5, pp. 1330–52, May 2009.
[450] Y. Cui, Y. Yue, G. Qian, and B. Chen, "Luminescent Functional Metal-Organic Frameworks.," *Chem. Rev.*, Jun. 2011.
[451] A. H. Khoshaman and B. Bahreyni, "Application of Metal Organic Framework crystals for sensing of volatile organic Gases," in *2011 IEEE SENSORS Proceedings*, 2011, pp. 1101–1104.
[452] A. L. Robinson *et al.*, "Ultrasensitive Humidity Detection Using Metal–Organic Framework-Coated Microsensors," *Anal. Chem.*, vol. 84, no. 16, pp. 7043–7051, Aug. 2012.

[453] I. Ellern *et al.*, "HKUST-1 coated piezoresistive microcantilever array for volatile organic compound sensing," vol. 8, pp. 766–769, 2013.
[454] I. Wilhelm *et al.*, "Novel Low-Cost Selective Pre-Concentrators Based on Metal Organic Frameworks," *Procedia Eng.*, vol. 168, pp. 151–154, 2016.